TOWARD BIOLOGICALLY REALISTIC COMPUTATIONAL MEMBRANE PROTEIN STRUCTURE PREDICTION AND DESIGN

by

Rebecca F. Alford

A dissertation submitted to The Johns Hopkins University
in conformity with the requirements for the degree of
Doctor of Philosophy

Baltimore, Maryland
June, 2020

Abstract

Membrane proteins function as gates and checkpoints that control the transit of molecules and information across the lipid bilayer. Understanding their structures will provide mechanistic insights in how to keep cells healthy and defend against disease. However, experimental difficulties have slowed the progress of structure determination. Previous work has demonstrated the promise of computational modeling for elucidating membrane protein structures. A remaining challenge is to model proteins coupled with the heterogeneous cell membrane environment. In the first half of this dissertation, I detail the development, testing and integration of a biologically realistic implicit lipid bilayer model in Rosetta. First, I describe the initial iteration of the implicit model that captures the anisotropic structure, shape of water-filled pores, and nanoscale dimensions of membranes with different lipid compositions. Second, I explain my approach to energy function benchmarking and optimization given the challenge of sparse and low-quality experimental data. Third, I outline the second generation that incorporates a new electrostatics and pH model. All of these developments have advanced the accuracy of Rosetta membrane protein structure prediction and design. In the second half of this dissertation, I investigate three challenging biological and engineering applications involving membrane proteins. In the first application, I examine mutation-induced stability changes in the integral

membrane zinc metalloprotease ZMPSTE24: a protein with a large voluminous chamber that is not captured by current implicit models. In the second application, I model interactions between the SERCA2a calcium pump and the regulatory transmembrane protein phospholamban: a key membrane protein-protein interaction implicated in the heart's response to adrenaline. Finally, I explore the challenge of membrane protein design to engineer a self-assembling transmembrane protein pore for nanotechnology applications. These applications highlight the next steps required to improve computational membrane protein modeling tools. Taken together, my work in both methods development and applications has advanced our understanding and ability to model and design membrane protein structures.

Thesis Committee

Jeffrey J. Gray (Primary Advisor)
Professor
Department of Chemical & Biomolecular Engineering
Johns Hopkins Whiting School of Engineering

Karen G. Fleming
Professor
T.C. Jenkins Department of Biophysics
Johns Hopkins Krieger School of Arts and Sciences

Jamie Spangler
Assistant Professor
Department of Chemical & Biomolecular Engineering
Johns Hopkins Whiting School of Engineering

Paulette Clancy
Professor, Department Head
Department of Chemical & Biomolecular Engineering
Johns Hopkins Whiting School of Engineering

Albert Lau
Associate Professor
Department of Biophysics & Biophysical Chemistry
Johns Hopkins School of Medicine

Acknowledgments

First and foremost, thank you to my advisor Jeff Gray. Jeff is a thoughtful mentor and excellent role model. Jeff provided a rich environment for creativity, a place I enjoyed working every day. Thank you for helping me to grow as both a scientist and a person. I am truly grateful to have been part of the lab!

Next, thank you to my co-mentor Karen Fleming. I admire Karen's strong leadership as both a scientist and advocate. During graduate school, Karen challenged me to be more confident, to dig deep into the data, and to constantly strive for better. Thank you Karen for being an excellent mentor.

Further, thank you to my thesis committee for providing critical feedback on my research: Professors Jamie Spangler, Albert Lau, and Paulette Clancy.

I am grateful for the National Science Foundation Graduate Research Fellowship Program and the Hertz Foundation for generously funding my graduate research. In particular, thank you to my Hertz Mentors Dr. Phillip Welkoff and Dr. Jessica Seeliger for providing critical career support and inspiration during my tenure as an in-school fellow. I want to thank Kathy Young, Kaarin Grahm, and Robbee Kosak for cultivating the rich and vibrant Hertz community: I have had great experiences and made many lifelong friends! Thank you also to the ChemBE department staff, especially Kourtney Roussey, Alisha Wells, and NIkeya Campbell, for supporting my

graduate school experiences.

Thank you to the past and present Gray Lab members for creating a fun and supportive lab environment. I would especially like to recognize Dr. Julia Koehler and Dr. Brian Weitzner who were my first mentors in the lab. They both challenged me to think critically, be patient, and pay attention to detail. It has been a pleasure to share an office with Dr. Rahel Frick and Dr. Jing Zhou: our lunches and chats always brightened my day. I am grateful to Sergey Lyskov and Matt Mulqueen who helped me debug many hardware and software problems. Finally, thank you to all of the bright undergraduate, masters, and Ph.D. rotation students that I had the pleasure to work with: Cameron White, Brita Ostermeier, Peter Murray, Morgan Beckett, Brittany Lasher, Aleexan Adal, Ashton Ohmdal, Margaret Luo, and Priya Prathima.

Thank you to my collaborators for sharing your exciting biological questions and design problems: Dr. Susan Michaelis, Dr. Eric Spear, Dr. Seth Robia, Dr. Howard Young, Dr. Rebecca Schulman, Dr. Judy Savitkaya and Dr. John Deuber. Our projects have challenged the capabilities of RosettaMP and inspired many improvements. I want to thank Dr. Vladimir Yarov-Yaravoy for providing critical feedback on the design of both RosettaMP and the *franklin* energy function. In addition, I am grateful to be part of the Rosetta Commons: It has been amazing to learn from such a diverse group of scientists. Within the Rosetta Commons, I want to give a special thank you to Dr. Una Natterman, Dr. Ora Furman, and Dr. Deanne Sammond who have been excellent scientific role models for me.

There are countless mentors who have touched my journey, many who graciously gave their time during off hours to advise and guide me. First, thank you to Debbie Lapidus for encouraging me to advocate for myself. Thank you to my high school

research teachers Richard Kurtz, Jeanette Colette, and Renata Arceri for teaching me critical skills that laid a sturdy foundation for my research career. Thank you to Dr. Richard Bonneau for welcoming me into your lab as a high school student and enabling me to do research that fueled my excitement for science. Further, thank you to Drs. Nancy and Pete Torpey and Dr. Bonnie Swenor who have mentored me in overcoming barriers of being a visually impaired scientist.

My graduate school experience was enriched by many friendships, especially within my ChemBE cohort. We made great memories outside the lab, from dressing up as Hogwarts students at the first year halloween party to Thanksgiving potluck celebrations. I will truly miss lunch and coffee meetups with Natalia Majewska, Caleb Anderson, and Josh DiGiacomo. Thank you for being great friends!

Thank you to my wonderful family. Emily - I am so proud to be your sister and am excited for our future experiences together. Grandma Jeanne - thank you for inspiring me to be a strong and smart woman, and for always being there to listen. Thank you to all of the Alford & Miller Aunts, Uncles, and Cousins for keeping me laughing, especially during our recent quarantine zoom chats. I am very grateful to make memories with my new family who has welcomed me with open arms: Joan, Danny, and Aliza Ross. Finally, thank you to Ollie for keeping me on my toes and for adding joy to life during this crazy time.

Thank you to my amazing husband Andrew Ross. Since January 29th, 2017 you have been the brightest light in my life. You make me want to be a better person every single day, and even our hardest days are better because we are together. Thank you for your love, your kindness, your patience, your humility, your support, and for always believing in me. I am so excited for our future together!

Finally, my dissertation is dedicated to my loving parents, Marjorie and Steven Alford. My parents always encouraged me to dream big and live without limitations. My mom spent countless hours advocating for me to ensure I had the same opportunities to learn as my fully sighted peers. She is an incredible role model and has empowered me to become a strong person. My dad inspired my curiosity and hunger for problem solving. When you took us to the computer show as kids, even though I did not seem interested, you definitely planted the engineering seed. I love you both so much and I am so grateful to be your daughter. Thank you for all of your encouragement and support!

To Mom & Dad

Table of Contents

List of Tables

List of Figures

Chapter 1

Introduction

1.1 Overview

In a common analogy, *"A cell is like a fortified city where lipid membranes form the defensive walls and membrane proteins function as gates and checkpoints that control the transit of molecules and information across these walls"* [1]. Membrane proteins are critically important: they constitute 30% of all proteins [2] and are targets for over 50% of pharmaceuticals on the market [3]. Understanding membrane protein structure and function is essential to keep cells healthy and defend against disease. However, the "defensive walls" present many challenges for wet lab experiments, resulting in a scarcity of experimental information [4].

Computational methods are promising for elucidating membrane protein structures. Over the past decade, computational tools have predicted structures with a resolution as low as 2.0 Å and enabled the design of membrane proteins with new functions for therapeutic and nanotechnology applications [5]. These methods capture the protein fold; yet, a remaining challenge is to capture the heterogeneous lipid environment that influences both the structure and function of resident proteins. This challenge is further complicated by the fact that the membrane lipid composition is diverse and varies across different cell types, organelles, and species [6]. In this dissertation, I focus on developing and applying computational tools with novel lipid bilayer representations for membrane protein structure prediction and design.

1.2 Structural properties of membrane proteins

Membrane proteins share basic properties with proteins in the cytoplasm or extracellular space, herein referred to as "soluble proteins." Both membrane and soluble proteins are folded polymers composed from the twenty canonical amino acids. These polymer chains fold into α-helices, β-sheets, and loops that further assemble into tertiary and quaternary structures. Their cores are stabilized by non-polar interactions, except in the case of pore-forming proteins [7]. Further, amino acid side chains pack in similar configurations [8].

Membrane proteins associate with the lipid bilayer in various ways. Some membrane proteins can be anchored to the cytosolic surface by an amphipathic α-helix. An example of the membrane anchored protein annexin is shown in (Figure 1.1a). Alternatively, most transmembrane proteins extend across the bilayer as a bundle of α-helices or a rolled-up β sheet (a β-barrel) [9]. Most open reading frames in the

human genome encode for α-helical proteins that are predominantly found in the plasma membrane [10]. An example of the multi-pass membrane protein bacteriorhodopsin is shown in (Fig. 1.1b) [11]. In contrast, β-barrel proteins are found in the outer membrane of gram-negative bacteria, mitochondria, and chloroplasts. An example of the β-barrel protein lysozyme OmpF is shown in (Fig. 1.1c) [12].

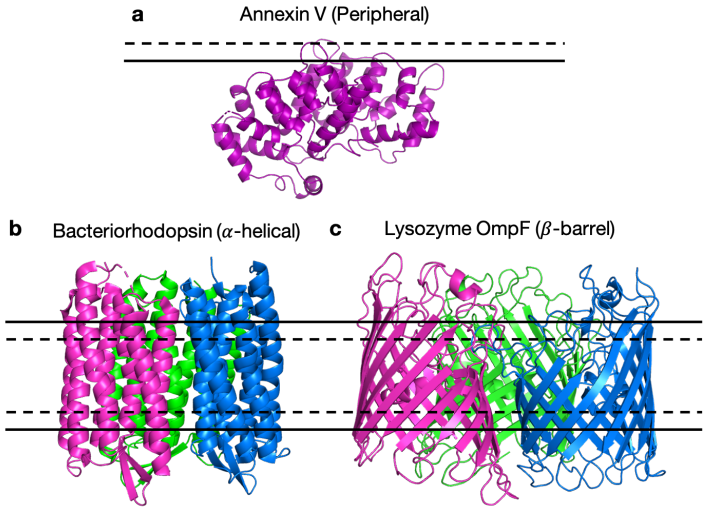

Figure 1.1: Proteins associated with the lipid bilayer anchor to the surface or extend through the bilayer. (a) The protein Annexin V (PDB: 1A8A) associates with the bilayer surface. (b) Bacteriorhodopsin (PDB: 1PY6) is an example of the α-helical fold. (c) Outer membrane protein F (PDB: 3POQ) is an example of a β-barrel fold.

Additionally, membrane proteins occupy precise orientations in the lipid bilayer, controlled in part by the hydrophobicity of transmembrane domains and the position of cytosolic domains. This position is defined by three degrees of freedom: the distance between the protein center and bilayer center d, the rotation of the protein relative to the membrane normal, α, and the procession of the protein around the normal axis τ. Characterizing membrane protein orientation provides a key first glance to how membrane protein structures are coupled with the structure of the lipid bilayer.

1.3 Biophysical properties of lipid membranes

Biological membranes are mainly composed of phospholipids that self-assemble to form a bilayer [13]. Each phospholipid molecule has a hydrophilic head-group and two hydrophobic acyl tails. The membrane also includes non-bilayer lipids such as cholesterol and non-structural lipids for signaling. When assembled, the bilayer can be described as three phases: (1) a hydrocarbon core of lipid tails, (2) an interfacial region of head-groups, and (3) the surrounding cytosol or extracellular space (Fig. 1.2). The lipid composition of biological membranes varies greatly across cell types, organelles, and species [6].

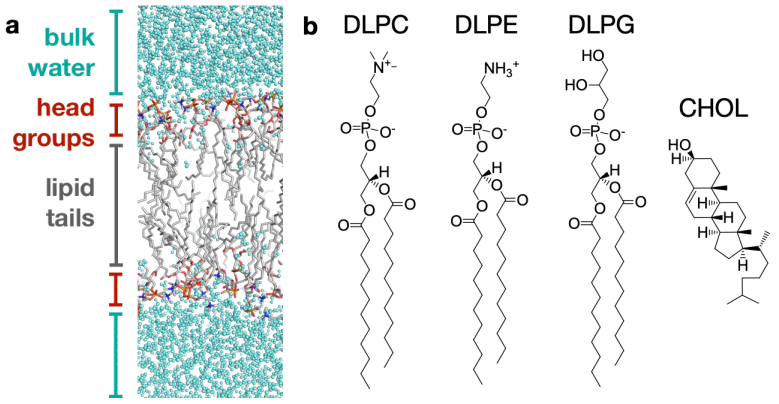

Figure 1.2: Membrane proteins reside in a bilayer with diverse lipid composition. (A) Biological membranes are mainly composed of phospholipids that self-assemble to form a bilayer. Each phospholipid molecule has a hydrophilic head-group and two hydrophobic acyl tails. Thus, the bilayer can be described by three phases: (1) a hydrocarbon core of lipid tails, (2) an interfacial region of head-groups, and (3) a layer of aqueous solvent. (B) Phospholipid molecules can vary significantly in their chemical composition, specifically in the head-group type, length of the hydrocarbon tails, and the degrees of saturation in the hydrocarbon tails. Shown are three different head-groups: choline (DLPC), ethanol-amine (DLPE), and glycerol (DLPG). Membranes also contain cholesterol (CHOL) which are part of the sterol class of lipids.

In 1972, Singer and Nicholson proposed the fluid mosaic model of cell membrane organization [14]. This model describes biological membranes as a phospholipid bilayer with a "mosaic" of embedded proteins and carbohydrates. Nearly 50 years

later, this model has persisted with a few key modifications. First, the bilayer contains up to 60% protein by mass [15] in contrast to prior thinking that the bilayer is mostly lipids [16]. Second, biological membranes include hundreds of different lipid types, mixed non-uniformly near a miscibility critical point [17]. In fact, cells invest significant resources into generating thousands of different lipids, many of which populate the bilayer [18, 19]. Further, the bilayer can separate into different phases at physiological conditions [20]. For instance, cholesterol rafts form that alter the rigidity of the bilayer [21].

The biochemically diverse lipid composition gives rise to physical properties that influence membrane protein function. Hydrocarbon chain length tunes the hydrophobic thickness of the bilayer. Hydrophobic thickness is an important variable because proteins will re-orient themselves to maximize contact between the hydrophobic surface of the protein and bilayer [22, 23]. The footprint of a phospholipid is influenced by the size and shape of the head group [24]. For instance, a choline head group results in a cylindrical footprint whereas a smaller or larger head group results in a conical footprint. This difference in shape can give rise to bilayer curvature [25]. Properties of the membrane are also influenced by the environment. For example, osmotic pressure on the bilayer surface cause the bilayer to expand and contract, a key mechanism for the function of mechano-sensitive channels [26].

1.4 Approaches to membrane protein structure determination

Determining membrane protein structures at high-resolution is critical to understanding their function and role in disease. Historically, membrane protein structure determination has been ridden with challenges. Even though the first soluble protein

structures were solved in 1960 [27, 28] the first membrane protein structure was not resolved at atomic resolution until 25 years later [29]. Many of the challenges persist, as membrane protein structures constitute only 2% of the protein databank [30]. As an encouraging sign of progress, 80% of these structures have been determined in the last decade (Fig. 1.3).

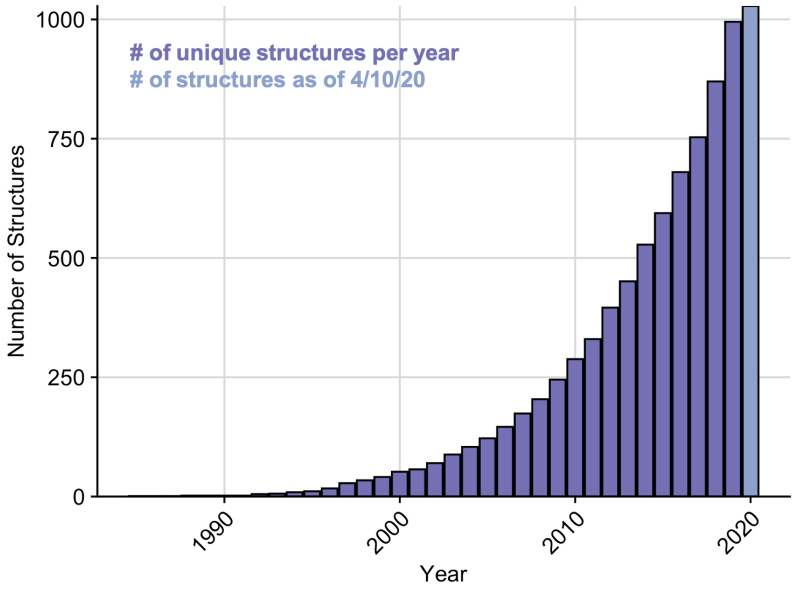

Figure 1.3: Growth in unique membrane proteins of known structure between 1985-present. Each bar represents the cumulative number of unique structures known in a given year. The light purple bar represents the cumulative number of structures in 2020 as of April 10th, 2020.

Currently, there are three main approaches to membrane protein structure determination: (1) X-ray crystallography, (2) Nuclear magnetic resonance (NMR) Spectroscopy, and (3) Cryo-electron microscopy. Each method is discussed below.

1.4.1 X-Ray Crystallography

X-Ray crystallography is a powerful tool for macromolecular structure determination and has been highly successful for soluble proteins. To determine a structure, X-Rays are diffracted from a crystal, which has an ordered and regularly repeating arrangement of atoms. Then, the diffraction pattern is used to reconstruct the electron density of the macromolecule [31]. With membrane proteins, a critical challenge for this technique is amassing a large quantity of stable protein in crystals. This step is complicated by the fact that few membrane proteins are naturally abundant [32]. Further, several membrane proteins cannot be solubilized in detergents because they will aggregate and/or denature. This is especially true for membrane proteins in higher eukaryotes. Despite these challenges, X-Ray crystallography has been the dominant tool for membrane protein structure determination. In particular, the technique has been applied to G-protein coupled receptors, which account for a large fraction of membrane protein drug targets [33, 34].

1.4.2 Nuclear Magnetic Resonance (NMR) Spectroscopy

NMR spectroscopy provides an alternate route to membrane protein structure determination. The technique uses the magnetic spin properties of atomic nuclei in a molecule to identify atoms that are close in space, either because they are bonded or because folds in a protein chain bring them together [35]. A unique benefit of NMR is that it can accommodate a wide variety of membrane mimetics including soluble detergent micelles, detergent-free lipid bilayer membranes, and native cell envelope preparations [36]. This permissively is in stark contrast to X-ray crystallography and cryo-EM (discussed below), which require non-lipid amphiphiles such as detergents

or amphiphilic polymers [37]. NMR is adept at determining intrinsically disordered regions of membrane proteins [38]. Further, NMR is sensitive enough to capture weak ligand binding, enabling the detection of structure-activity correlations for binding events or conformational changes [39]. Importantly, NMR still imposes the same limitation as X-ray crystallography of requiring a highly concentrated sample.

1.4.3 Cryo-Electron Microscopy

Cryo-electron microscopy (Cryo-EM) uses a transmission electron microscope (TEM) to examine macromolecular structures. A beam of electrons passes through a sample embedded in a thin layer of vitreous ice, projecting an image of the sample onto a detector. The electron micrographs are then averaged to reveal a structure [40]. In 1975, the first membrane protein structure was determined at helix-resolving resolution in a native lipid bilayer with this technique [41]. Once limited by resolution, improvements to detector accuracy have elevated Cryo-EM as a leading method [42]. Today, Cryo-EM is beneficial for membrane proteins because it requires less sample. As a result, we have accessed several milestone structures including the Sec61 translocon [43], TRPV1 [44], and a glutamate receptor [45]. There are still two limits to Cryo-EM: proteins must be biochemically well-behaved and over 100 kDa [46].

1.5 Computational membrane models

Computational protein structure prediction and design tools provide a promising route to improving our understanding of membrane protein structure and function. An extensive review of membrane protein modeling methods has recently written by Koehler Leman *et al.* [5]. There are two key steps in computational modeling: (1)

sampling possible conformations and (2) *scoring* sampled conformations to identify near-native conformations. Many of the sampling techniques developed for soluble proteins are also applicable to membrane proteins. The central challenge is devising energy functions that capture the heterogeneous lipid environment.

Over the past 20 years, the field has developed a collection of methods to model the lipid bilayer. The most popular approach is an explicit model that represents molecules directly (Fig. 1.4a). All-atom models are the most detailed methods and represent every atom in the system, whereas coarse-grained methods map atoms onto representative beads to capture properties of chemical groups. Explicit models can provide detailed representations of different lipid compositions. However, calculations with explicit lipid bilayers are computationally expensive.

Alternatively, implicit models represent the membrane as a continuum that differentiates between the aqueous, interfacial, and hydrophobic phases (Fig. 1.4b). In exchange for a more approximate bilayer representation, implicit models offer a 50-100 fold sampling speedup [47]. The most detailed implicit model is the Poisson-Boltzmann (PB) equation that relates electrostatic potential to dielectric properties of the solute through a second-order partial differential equation [48]. However, the PB model is too expensive for long biomolecular simulations. There are several alternatives to the PB model including a Generalized Born (GB) model, an empirical implicit model, and a knowledge-based model. All of these approaches provide tradeoffs and will be discussed in further detail throughout this dissertation. Importantly, the choice of model has significant implications on membrane protein modeling results.

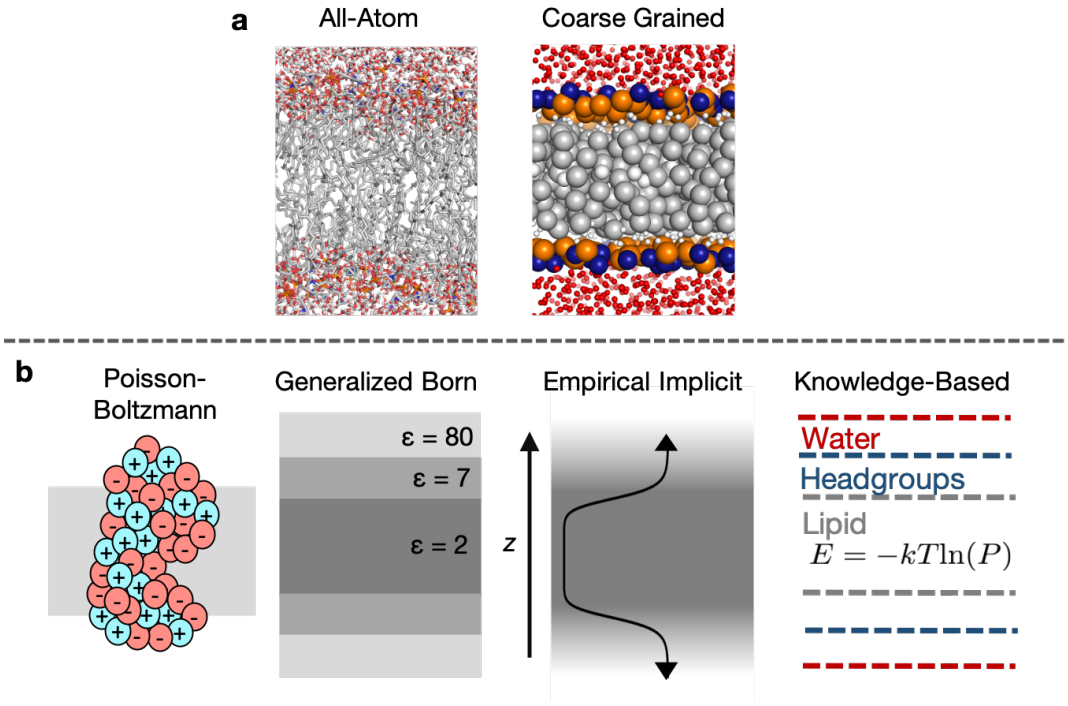

Figure 1.4: Computational explicit and implicit approaches to modeling the heterogeneous lipid bilayer.]. (a) Explicit membrane models represent every atom in the biomolecular system and rely on molecular mechanics to capture atomic interactions. All-atom models (left) represent every atom in the system whereas coarse-grained models (right) map 4-6 atoms onto to beads that represent various chemical groups. (B) Implicit membrane models represent the heterogeneous lipid environment as a continuous medium with variable properties. From left-to-right, the four most common approaches are the Poisson-Boltzmann model, the Generalized-Born approximation of the Poisson-Boltzmann model, empirical implicit models and knowledge-based models.

1.6 Macromolecular modeling with Rosetta

The Rosetta macromolecular modeling suite was originally developed for *ab initio* protein folding [49, 50]. Since its inception, Rosetta has evolved into an integrated toolkit for biomolecular structure prediction and design [51] that can be applied to wide ranging tasks such as docking [52] and design [53, 54] as well as systems such as sugars [55] and RNA [56]. Rosetta follows the premise that the observed conformations of folded proteins are almost always the low free-energy states [57, 58].

Therefore, structure prediction is the problem of finding the lowest-energy structure given the sequence of a protein. Design is often posed as the problem of finding the lowest-energy sequence given a target structure [59]. To tackle both problems, Rosetta relies on a diverse library of scoring and sampling modules.

1.6.1 Sampling

Rosetta accomplishes sampling through a Monte Carlo plus minimization scheme. In this setup, the system degrees of freedom are perturbed, energy minimized, and then changes are accepted or rejected according to the Metropolis criteria: given that $A = \min(1, \exp(\Delta E / k_B T))$, where ΔE is the change in energy, T is temperature, and k_B is Boltzmann's constant, accept if $A \geq U(0,1)$ where $U(0,1)$ is a random number between zero and one (inclusive); otherwise reject the changes. Rosetta samples macromolecular degrees of freedom as internal coordinates (ϕ,ψ,ω) rather than Cartesian coordinates (x,y,z). Bond lengths and angles can be sampled but are usually kept fixed. Sampling relevant conformations is a stochastic process: meaning that the program is run many times and an ensemble of models is required to identify a solution.

1.6.2 Scoring

Energy functions are based on Anfinsen's hypothesis that native-like protein conformations represent unique, low-energy, thermodynamically stable conformations. These folded states reside in minima on the energy landscape, and they have a net favorable change in Gibbs free energy of each biomolecule conformation, which is the sum of contributions from both enthalpy (ΔH) and entropy ($-T\Delta S$) relative to the unfolded state. To follow this heuristic, Rosetta uses a mathematical model that can

discriminate between unfolded, folded, and native-like conformations. This function is a weighted linear combination of terms that compute energies E_i as a function of various degrees of freedom Θ (Eq. 1.1).

$$\Delta E_{\text{total}} = \sum_i w_i E_i(\Theta_i) \tag{1.1}$$

The energy terms include a combination of classical molecular mechanics terms, empirically-derived terms, and knowledge-based terms derived from structures in the Protein Databank. The weights on each term were determined through a Nelder-Mead optimization scheme [60]. The energy terms are as follows: van der Waals attractive energy, Pauli-Exclusion repulsive energy, Gaussian exclusion Lazaridis-Karplus implicit solvation energy (EEF1), Coulomb electrostatics energy, geometry of hydrogen and disulfide bonds, rotamer probabilities, backbone-dependent amino acid probabilities and propensities, amino acid reference energies, and empirical penalties to enforce the ω peptide angle, planarity of the tyrosine hydroxyl χ angle, and proper torsions in the proline ring. Each term is reviewed extensively in Alford *et al.* [61].

1.6.3 Accounting for the lipid bilayer

Rosetta had two pioneering membrane protein modeling applications: RosettaMembrane *ab initio* and *relax*. The RosettaMembrane *ab initio* protocol was one of the first methods for *ab initio* structure prediction of membrane proteins. It combines the *ab initio* structure prediction protocol for soluble proteins [49] with a low-resolution score function derived from a database of structures of membrane proteins [62]. This method was later updated to include a high-resolution refinement stage [63] that

uses an all-atom score function based on the Lazaridis implicit Gaussian-exclusion solvation model (IMM1) for atoms in the membrane [64].

Since the creation of the RosettaMembrane *ab initio* protocol in 2006, Rosetta has been reorganized into a set of object-oriented libraries ("Rosetta3") [51] while RosettaMembrane remained in its original implementation. Rosetta3 is now a cohesive, flexible software suite that includes separate objects for conformation and scoring, interaction graphs, score functions organized by multi-body dependencies, kinematics managed through a fold tree, maps to identify flexible portions of the molecule(s), job distribution, and scripting interfaces. To leverage this flexible platform for membrane proteins, we developed RosettaMP.

As an undergraduate, I developed RosettaMP with my mentor Dr. Julia Koehler Leman [65]. The framework has central building blocks to represent the membrane bilayer, and to sample and score both conformations and sequences. An overview of the architecture of RosettaMP is shown in Fig 1.5. Initially, the methods were tested with four proof-of-concept applications: (1) prediction of free energy changes upon mutation, (2) high-resolution structural refinement, (3) protein—protein docking, and (4) assembly of symmetric complexes, all in the membrane bilayer. The protocols can be accessed via command line, PyRosetta [66], and RosettaScripts [67], with various levels of customizability for both developers and users. Collectively, the applications demonstrate how RosettaMP and existing Rosetta protocols can be combined to quickly create powerful new methods to answer a broad range of scientific questions. Importantly, RosettaMP also provided a platform to identify the next scientific challenges, many of which I address in my thesis.

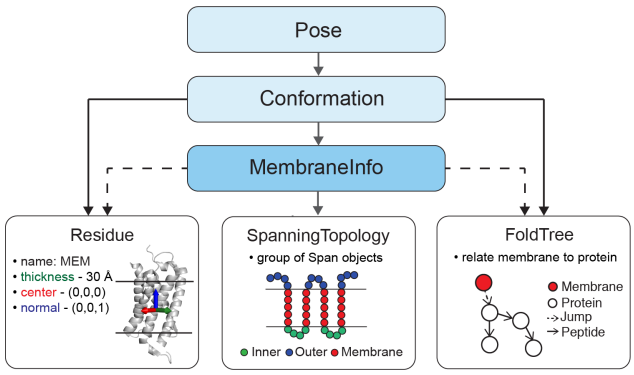

Figure 1.5: Detailed architecture of RosettaMP. RosettaMP represents the membrane bilayer using three main components connected to a central MembraneInfo object (blue). MembraneInfo stores information needed to represent the membrane (line arrows) and tracks information present in the Pose (dotted arrows). A special Residue type is added to the Pose, describing the geometry of the membrane bilayer by coordinates storing the center, normal and thickness of the bilayer. A SpanningTopology object describes the transmembrane regions of the Pose. The FoldTree uses a jump edge to establish the connection between the membrane residue and the protein.

1.7 Dissertation Outline

This dissertation is presented in two parts. The first three chapters describe the development of computational tools for biologically-realistic membrane protein modeling. In Chapter 2, I describe a new biologically-realistic implicit membrane energy function. The chapter details the theory of the energy function, evaluation, and design anecdotes. In Chapter 3, I describe my approach to evaluating implicit membrane energy functions with multiple scientific benchmark tests. In Chapter 4, I describe the next round of energy function improvements: accounting for electrostatics and pH changes in the membrane environment. The remaining thee chapters describe the application of computational modeling to biological systems involving membrane proteins. In Chapter 5, I investigate the effects of mutations linked to pre-mature aging diseases on stability of the integral membrane zinc metalloprotease. In Chapter 6, I apply membrane protein-protein docking to explore the interaction between

the SERCA2a calcium pump and phospholamban in cardiac muscle cells. Then, in Chapter 7 I describe the application of the new membrane protein tools to the design of a protein channel. Finally, in Chapter 8 I describe my contributions to the field and map future directions.

Chapter 2

A biologically realistic implicit membrane model for protein structure prediction and design

With permission from the publisher, this chapter includes material from Alford RF, Fleming PJ, Fleming KG, and Gray JJ, "Protein structure prediction and design in a biologically realistic implicit membrane" *Biophysical Journal* 118(8):2024-2055.

2.1 Overview

Protein design is a powerful tool for elucidating mechanisms of function and engineering new therapeutics and nanotechnologies. While soluble protein design has advanced, membrane protein design remains challenging due to difficulties in modeling the lipid bilayer. In this work, we developed an implicit approach that captures the anisotropic structure, shape of water-filled pores, and nanoscale dimensions of membranes with different lipid compositions. The model improves performance in computational benchmarks against experimental targets including prediction of protein orientations in the bilayer, $\Delta\Delta G$ calculations, native structure discrimination,

and native sequence recovery. When applied to *de novo* protein design, this approach designs sequences with an amino acid distribution near the native amino acid distribution in membrane proteins, overcoming a critical flaw in previous membrane models that were prone to generating leucine-rich designs. Further, the proteins designed in the new membrane model exhibit native-like features including interfacial aromatic side chains, hydrophobic lengths compatible with bilayer thickness, and polar pores. Our method advances high-resolution membrane protein structure prediction and design toward tackling key biological questions and engineering challenges.

2.2 Introduction

Membrane proteins partner with the surrounding lipid environment to perform essential life processes. They constitute 30% of all proteins [68] and are targets for over 60% of pharmaceuticals [3]. However, experimental difficulties have limited our insights into their molecular mechanisms of function. Protein design tools are powerful for elucidating biological mechanisms and developing new therapeutics. Over the past 20 years, soluble protein design has advanced to atomic level accuracy [54]. A remaining challenge is to create robust tools for membrane proteins [69]. There have been several achievements in membrane protein design including a zinc-transporting tetramer Rocker [70], an ion-conducting protein based on the *Escherichia coli* Wza transporter [71], β-barrel pores with increased selectivity [72], receptors with new ligand-binding properties [73, 74], and designed *de novo* α-helical bundles that insert into the membrane [75]. A critical limitation is capturing the heterogeneous membrane environment: models are either too computationally expensive or severely approximate the bilayer. In fact, has been common for membrane protein structure

prediction and design to be carried out in a 30Å hydrophobic slab. A slab is a poor proxy for the heterogeneous membranes found in biology with varying lipid composition across different organelles, cell types, and species. To apply membrane protein design to addressing biological questions, tools must sample a realistic distribution of amino acids tied with the diverse lipid composition.

The foundation of computational modeling and design tools is the energy function: a mathematical model of the physical rules that distinguish native from non-native membrane protein conformations and sequences. Currently, most computational studies of membrane proteins are molecular dynamics simulations with an all-atom lipid bilayer. In this conception, the lipid molecules are represented explicitly using force fields such as AMBER[76], CHARMM [77], or GROMOS [78], and the protein-lipid interactions are scored with a molecular mechanics energy function. All-atom models are attractive because they can feature hundreds of lipid types toward approximating the composition of biological membranes. With current technology, detailed all-atom models can be used to explore membrane dynamics for hundreds of nanoseconds [79]: the time scale required to achieve equilibrated properties on a bilayer with approximately 250 lipids [80]. Coarse-grained representations such as MARTINI [81] and SIRAH [82] reduce computation time by mapping atoms onto representative beads. As a result, simulations have explored dynamics up to the millisecond time scale to access features of membrane organization and large protein domain motions [83].

Implicit solvent models enable simulations to reach longer timescales required to investigate biologically-relevant conformational and sequence changes. Instead of using explicit molecules, implicit methods represent the solvent as a continuous

medium [84, 85], resulting in a 50-100-fold sampling speedup [86]. The most detailed implicit model is the Poisson-Boltzmann (PB) equation, which relates electrostatic potential to dielectric properties of the solvent and solute through a second-order partial differential equation [87]. Numerical solvers have enabled PB calculations on biomolecular systems [88]; however, these calculations do not scale well. To reduce computational cost, the Generalized Born (GB) approximation of the PB equation treats atoms as charged spheres [89]. GB methods represent the low-dielectric membrane through various treatments ranging from a simple switching function [90] to heterogeneous dielectric approaches [91]. However, evaluating the GB formalism is still computationally expensive.

A popular approach to overcoming the computational cost of solvent electrostatics models is the Lazaridis implicit membrane model (IMM1; [64]): a Gaussian solvent-exclusion model that uses experimentally measured transfer energies of side-chain analogues in organic solvents to emulate amino acid preferences in the bilayer [92]. IMM1 has been applied to various biomolecular modeling problems including studies of antimicrobial peptides [93], *de novo* folding [63], and *de novo* design of transmembrane helical bundles [75]. However, organic solvent slabs differ from phospholipid bilayers because lipids are thermodynamically constrained to a bilayer configuration, resulting in a unique polarity gradient that influences side chain preferences [94, 95]. An alternative is to directly calculate amino acid preferences by deriving statistical potentials from a database of known membrane protein structures [62, 96–98]. Yet, statistical potentials do not capture varying physiochemical properties of the membrane.

In this work, we developed a biologically realistic implicit membrane model for

protein structure prediction and design. We first developed the model from experimental and computational modeling of phospholipid bilayers to capture biologically-important membrane features. Next, we tested the model on four benchmarks: (1) prediction of protein orientations in the membrane, (2) $\Delta\Delta G$ of mutation calculations, (3) native structure discrimination and (4) native sequence recovery. We applied the model to protein design and investigated properties of the *in silico* designed membrane proteins including the amino acid composition. Finally, we share several design anecdotes that exhibit native-like membrane protein features including interfacial aromatic side chains, hydrophobic lengths compatible with different lipid compositions, and polar pores.

2.3 Methods

2.3.1 Development of the implicit membrane model

2.3.1.1 Derivation of $\Delta G^{\mathbf{atom}}_{\mathbf{w,l}}$ values

The Moon & Fleming hydrophobicity scale provides a set of water-to-bilayer transfer energies $\Delta G^{\mathrm{aa}}_{\mathrm{w,l}}$ for the 20 canonical amino acids [99] measured in the reversibly folding OmpLA scaffold. Note, the default ionization state for Histidine in Rosetta is neutral and Glu and Asp are protonated because the Moon & Fleming scale was measured at pH 3.8. We used regression to derive energies that correspond to atom types (Table S5), called $\Delta G^{\mathrm{atom}}_{\mathrm{w,l}}$. Specifically, least-squares fitting was applied solve the equation $\mathbf{Ax} = \mathbf{b}$; where, $\mathbf{A}$ is a matrix of atom type stoichiometric coefficients (Table S6), $\mathbf{b}$ is the vector of $\Delta G^{\mathrm{aa}}_{\mathrm{w,l}}$ values, and $\mathbf{x}$ is the desired vector of $\Delta G^{\mathrm{atom}}_{\mathrm{w,l}}$ values. Matrix rows for glycine, alanine, and proline were excluded to avoid over fitting. The resulting $\Delta G^{\mathrm{atom}}_{\mathrm{w,l}}$ values are in Table S7.

2.3.1.2 Molecular dynamics simulations of phospholipid bilayers

All-atom molecular dynamics simulations were performed to extract properties of membranes with different phospholipid compositions. We simulated phospholipid bilayers with hydrocarbon tails between 12-18 carbons long and either a phosphatidylethanolamine (PE), phosphatidylcholine (PC) or phosphatidylglycerol (PG) head group (Table S1). The exceptions were DPPC and DMPG because the liquid-to-gel phase transition temperatures are above physiological temperature [100, 101]. CHARMM-GUI [102] was used to configure each bilayer system with 75 lipids in each leaflet, 22.5Å of water on each side, and 0.1 M NaCl. Simulations were performed using the NAMD molecular dynamics engine [103] at a constant pressure of 1 atm and a temperature of 37°C. We used the CHARMM36 [77] force field for lipid and the TIP3 model for water. The simulations were equilibrated with restraints according to the procedure outlined by Jo *et al.* [102]. Then, each system was simulated for 50 ns.

2.3.1.3 Derivation of water density profiles

MDAnalysis [104] was used to extract water density information from each bilayer simulation. For each frame, the system was first re-centered on the lipid center-of-mass. Then, we computed a normalized histogram of TIP3 z-coordinates with 1Å bins to capture the distribution of water molecules. The histogram was recentered at $z = 0$ by fitting the histogram to a cosine function to estimate the midpoint. The time-averaged histogram was computed by averaging the histograms representing each frame (Fig. S9).

To generate analytic profiles, we used nonlinear regression to fit each histogram

to the logistic function, f_{thk}:

$$f_{\text{thk}} = \frac{1}{1 + \tau \exp(-\kappa z)}. \tag{2.1}$$

The function f_{thk} depends on membrane depth (z) and has two adjustable parameters: steepness κ and width τ. We derived κ and τ for all simulated lipid compositions. The resulting parameters are in Table S2 and the analytic water density profiles are in Fig. S10.

2.3.1.4 Calculation of water-filled pore shapes

For proteins with more than three transmembrane segments, we introduced a pore into the implicit membrane model. To determine the pore shape, we created a new method to transform discrete structural information into a smooth geometry described by differentiable functional forms. First, we used the convex-hull algorithm described in Koehler Leman *et al* [105] to identify backbone and side chain atoms that are in the transmembrane region ($|z| \leq T$), face the protein interior, and are not buried. A side-chain was defined as buried if it had 23 or more neighboring atoms within 12 Å of its C_α atom [106]. Next, we computed a histogram of the z-coordinates of pore facing atoms with a bin size of $\frac{1}{3}T$. For each bin, the (x, y) coordinates of the atoms were collected. Then, the Khachiyan algorithm [107] was used to compute the minimum-area ellipse that bounds these coordinates. Each ellipse is defined with the following parameters: major radius (a), minor radius (b), rotation angle (θ), and center (x_0,y_0). The radius of the ellipse, g_{radius}, is calculated using rotation matrix M:

$$M = \begin{bmatrix} \sin(\theta(z)) & \cos(\theta(z)) \\ \cos(\theta(z)) & -\sin(\theta(z)) \end{bmatrix} \tag{2.2}$$

$$g_{\text{radius}} = M \cdot \left[\left(\frac{(x - x_0(z))}{a(z)} \right)^2 ; \left(\frac{(y - y_0(z))}{b(z)} \right)^2 \right] \tag{2.3}$$

Cubic spline interpolation was used to fit polynomials to describe the depth-dependence of each parameter. The result is five continuous and differentiable parametric functions: $a(z)$, $b(z)$,$\theta(z)$, $x_0(z)$, and $y_0(z)$. The transition between the water-filled pore and lipid phase is defined by g_{radius} given the transition steepness n:

$$f_{\text{pore}} = 1 - \frac{g_{\text{radius}}^n}{1 + g_{\text{radius}}^n}. \tag{2.4}$$

2.3.2 Validation of model parameters

2.3.2.1 $\Delta G_{\text{w,l}}^{\text{atom}}$ values

To verify $\Delta G_{\text{w,l}}^{\text{atom}}$ values, we first recalculated the side chain transfer energies by solving $\mathbf{Ax} = \mathbf{b}$. The Pearson correlation coefficient between the calculated and experimentally measured side chain transfer energies was $R^2 = 0.99$ (Fig. S13). In addition, we used the procedure outlined in the *Scientific Benchmarks* section of *Methods* to estimate the $\Delta\Delta G_{\text{mut}}$ values from Moon & Fleming [99]. Specifically, we sought to verify that $\Delta G_{\text{w,l}}^{\text{aa}}$ trends were preserved in context of the full energy function. The correlation between predicted and experimentally measured $\Delta\Delta G^{\text{mut}}$ values was $R^2 = 0.84$ (Fig. S11) and the residuals are listed in Table S8. Note, the $\Delta\Delta G^{\text{mut}}$ for proline was excluded from the correlation coefficients because steric clashes resulted large energies.

2.3.2.2 Membrane thickness

We validated the water-density profiles computed from Molecular Dynamics by comparing the derived membrane thickness parameters with thickness measured at various temperatures via x-ray and neutron scattering experiments [108]. First, we computed the membrane half thickness t from each logistic curve as the Gibbs dividing surface between the water and lipid phases ($f(z) = 0.5$). We then calculated a line of best fit through the measured thickness values at each temperature (Fig. S14).

2.4 Results

2.4.1 Biologically realistic realistic implicit membrane model

We developed a biologically realistic implicit membrane model inspired by Lazaridis' implicit model (IMM1; [64]). Similar to IMM1, the membrane is modeled as a continuum of three phases: an isotropic phase representing bulk lipids, an isotropic phase representing bulk water, and an anisotropic phase representing the interfacial region. To accurately model the polarity gradient and dimensions of native membranes, we derived new equations and parameters from biophysical measurements. The result is a new energy term called ΔG_{memb} that computes protein stability given the water-to-bilayer transfer energy $\Delta G^{\text{atom}}_{\text{w}\to\text{l}}$ of atomic groups a and the fractional hydration f_{hyd}:

$$\Delta G_{\text{memb}} = \sum_{r=1}^{N_{\text{res}}} \sum_{a=1}^{N_{\text{atom}}(r)} (1 - f_{\text{hyd}})(\Delta G^{\text{atom}}_{\text{w,l (a)}}). \tag{2.5}$$

The parameter $\Delta G^{\text{atom}}_{\text{w,l}}$ captures the thermodynamics of protein-lipid interactions.

We derived $\Delta G_{w,l}^{atom}$ from the Moon & Fleming side-chain hydrophobicity scale [99] because the energies were measured in bilayers with phospholipids, a major component of biological membranes [6]. Further, we chose this scale because the measurements capture the stability of the final folded protein relative to the fully hydrated, unfolded state. Side-chain burial vs. solvent exposure is accounted for through neighbor count calculations in the Rosetta energy functions. Then, following Lazaridis' formalism [109], the function f_{hyd} captures the three-dimensional shape of the implicit membrane as a dimensionless number that describes the phase given the position of an atomic group. When an atomic group is exposed to the lipid phase, $f_{hyd} = 0$; whereas when an atomic group is exposed to the water phase, $f_{hyd} = 1.0$. The transition between the two isotropic phases is modeled by a composition of two functions: f_{thk} captures the membrane thickness and f_{pore} captures the geometry of a water-exposed pore:

$$f_{hyd} = f_{thk} + f_{pore} - f_{thk} f_{pore}. \tag{2.6}$$

The function f_{thk} (Eq. 2.1, see Methods) models the transition between the water and lipid phase along the z-axis, and is thus an implicit representation of the hydrophobic thickness. We developed parameters for f_{thk} by fitting to molecular dynamics simulations and scattering density profiles of phospholipid bilayers. The result is a logistic curve that depends on two parameters. We derived parameters for thirteen phospholipid bilayer compositions (Table S1-2, see SI Appendix). The membrane thickness can be derived by setting $f_{thk} = 0.5$ (Fig. 2.1A-B). Thus, the user can perform simulations with any of these thirteen different phospholipid compositions, or in principle, with any mix of membrane components by using a molecular

dynamics run and extracting the hydration profile parameters.

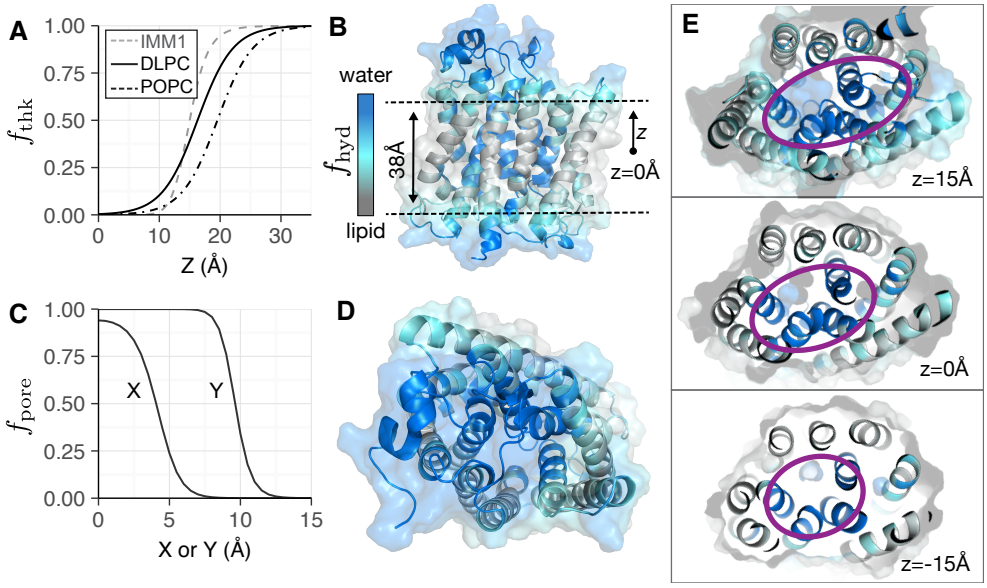

Figure 2.1: Features of the biologically realistic implicit membrane model. The implicit membrane is modeled as three phases: two isotropic phases for water and lipid and a transition region that represents the interfacial head groups. (A) The transition between phases in the z-dimension is modeled by a logistic curve which can be parameterized for different lipid compositions. Example curves for DLPC (solid, black) and POPC (dot-dash, black) are shown in comparison to the sigmoid curve used in IMM1 (dashed, gray). (B) Implicit solvent phases for the Ammonium transporter Amt-1 (PDB 2b2f) in the z-dimension. The water phase is shown in blue, the interface is in teal, and the lipid is in gray. (C) The transition between phases due to an elliptical pore is modeled by a sigmoid curve. (D) Top view of implicit solvent phases due to a pore in Amt-1 with the same coloring scheme as B. The three panels of (E) demonstrate the variation in pore shape (purple) for different cross sections in the x, y plane along the z-axis.

The function f_{pore} defines the shape of a water-exposed pore (Fig. 2.1C-E). Previously, Lazaridis developed a cylindrical model of pores for β-barrel proteins [109]. This geometric assumption is straightforward for β-barrel proteins; however, α-helical protein pores require varied geometric descriptors such as cones, cylinders, and ellipses [110]. To accommodate, we created a model that approximates pores as an elliptical tube with varying cross sections. This parameterization allows the model to describe cavities that do not penetrate through the membrane and pores that constrict,

expand, or twist relative to z. The energy function accounts for the pore by first calculating a relative radius, g_{radius} (Eqs. 2.2 and 7.1, see Methods). The transition between the two phases is modeled by a sigmoid curve f_{pore} (Eq. 7.2, see Methods) with two parameters: g_{radius} and the transition steepness n (default $n = 10$). Additional examples for larger proteins with multiple pores and proteins with ellipsoidal architecture are shown in Supplemental Fig. 12.

We integrated our model into the current all-atom energy function for modeling soluble proteins in Rosetta, called REF15 [61]. REF15 computes macromolecular energies through a linear combination of terms for van der Waals, solvation, electrostatics, hydrogen bonding, backbone- and side-chain interactions. To account for the membrane environment, we added ΔG_{memb} with an empirically determined weight of 0.5. The resulting energy function, called *franklin2019*, is given by $\Delta E_{\text{franklin2019}} = \Delta E_{\text{REF15}} + \Delta G_{\text{memb}}$.

2.4.2 Computational benchmark performance of the biologically realistic implicit membrane

We evaluated the accuracy of *franklin2019* using four computational benchmark tests against experimental targets. The tests were designed to evaluate an energy function's ability to replicate measured membrane protein stabilities and perform accurate structure prediction and design. We compared the performance of *franklin2019* to three existing models: (1) an implicit membrane parameterized from the behavior of side-chain analogues in organic solvents (**M07**; [63]), (2) a knowledge-based model that captures depth-dependent amino acid preferences (**M12**; [111]), and (3) the Rosetta all-atom energy function for soluble proteins (**R15**; [60, 61]). For brevity, we will refer to *franklin2019* as **M19**. We chose these models because the low computational cost

enabled evaluation with structure prediction and design tests. Additional details describing the benchmark tests and command lines are provided in the SI Appendix.

2.4.2.1 Test #1: Prediction of membrane protein orientation and insertion energy

Membrane proteins are thermodynamically stable in the bilayer due to a favorable orientation and insertion energy. Therefore, implicit membrane energy functions must accurately estimate these quantities. First, we evaluated the partitioning properties of oligomeric proteins into the implicit membrane. Here, we chose to study oligomers because the single-TM peptides may be marginally hydrophobic with insertion depending on the sequence context. We performed calculations for the acetylcholine receptor (pentamer, Fig. 2.2) and the influenza A M2 proton channel (tetramer, Fig. S2). Remarkably, **M19** was the only model to predict a favorable insertion energy for both proteins. The mapping of peptide orientation to energies is shown for the acetylcholine receptor in Fig. 2.2. The **M07** energy landscape (Fig. 2.2C) has three small, low energy wells, and they are isoenergetic with the water phase (since **M07** was not parameterized for the water environment). This behavior is not physical. In contrast, the lipid phase is more thermodynamically favorable than the water phase for both **M12** (Fig. 2.2D) and **M19** (Fig. 2.2E). This result is quantified by a favorable transfer energy from the water phase (G_1) to the lipid phase (G_3; Fig. 2.2F). Ultimately, **M19** is the most native-like because the model accurately captures the aqueous reference state relative to the bilayer phase.

In addition, we predicted the tilt angle for five proteins with single transmembrane spans: influenza A M2 (1mp6), acetylcholine receptor segment 2 (1a11), NR1 subunit of the NMDA receptor (2nr1), VPU domain of HIV-1 (1pje) and WALP (WALP23). We chose the first four biological peptides from Ulmschneider *et al.* [47] because

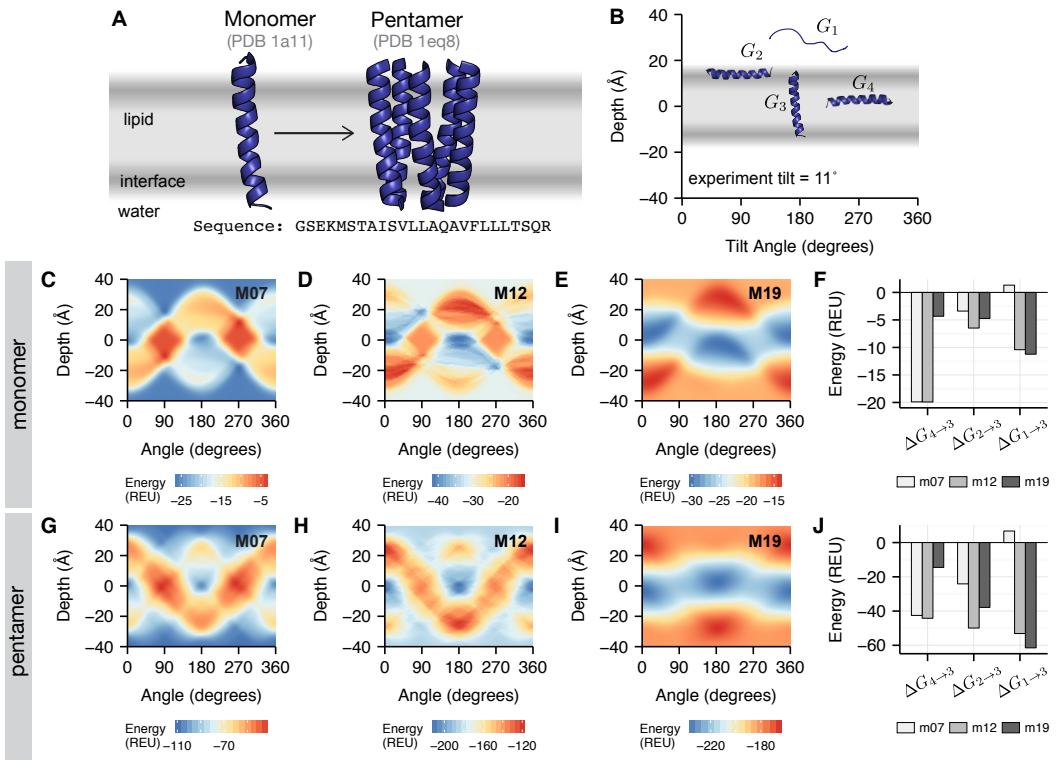

Figure 2.2: Prediction of membrane insertion and orientation for acetylcholine receptor. (A) Sequence of the monomer and structures of both the monomer (PDB 1a11) and pentamer (PDB 1eq8). (B) Important conformations given as a function of peptide depth (z) and tilt angle (θ): G_1 is the energy of the unfolded state in solution ($z = 30, \theta = 90°$). G_2 is the energy of the folded state at the interface, parallel to the plane of the interface ($z = 15, \theta = 90°$), G_3 is the energy of the peptide oriented vertically ($z = 0, \theta = 0°$), and G_4 is the energy of a peptide buried in the membrane ($z = 0, \theta = 90°$). The mapping of protein orientations to energies calculated by the M07, M12, and M19 energy function respectively is shown in panels C-E for the monomer and G-I for the pentamer. The partitioning energies between two lipid-buried conformations ($\Delta G_{4\to3}$), from interface to lipid ($\Delta G_{2\to3}$) and from water to lipid ($\Delta G_{1\to3}$) are shown in (F) for the monomer and (J) for the pentamer.

the sequences are less than 35% homologous and tilt angles have been measured by solid-state NMR spectroscopy. We also included WALP because the sequence was rationally designed [112]. The dependence of energy on orientation is shown in Fig. 2.2C-E for 1a11 and Fig. S2 and S3 for the remaining targets. The dependence of energy on tilt angle is shown in Fig. S1 and the low energy tilt angles are listed in Table S3. We found that **M19** predicted tilt angles within $\pm 10°$of the experimentally

measured value for four of the five peptides. Further, **M19** predicted tilt angles closest to the measured value in contrast to **M07** and **M12**. Together, these results demonstrate that **M19** is both predictive for insertion and orientation.

2.4.2.2 Test #2: Predicting the $\Delta\Delta G$ of mutation

Predicting changes in protein stability upon single amino acid substitutions at lipid exposed positions informs predictions of the effects of genetic mutations and *de novo* protein design. We evaluated the ability of **M19** to capture the change in protein stability upon mutation, called $\Delta\Delta G^{\text{mut}}$, by comparing experimentally measured values with computational predictions. Here, we used a dataset of mutations at position 111 on outer membrane palmitoyl transferase (PagP) [113]. The dataset contains mutations from the host amino acid (alanine) to all 19 other canonical amino acids. Therefore, the $\Delta\Delta G$ computed in this test represents side chain stability relative to alanine. A summary of prediction accuracy relative to the experimentally measured values is given in Fig. 2.3. The raw predicted values are also listed in Table S4. Calculated energies are given in Rosetta Energy Units (REU).

The correlation between **M19** predicted and experimentally measured $\Delta\Delta G^{\text{mut}}$ values was $R^2 = 0.85$. Note, the $\Delta\Delta G^{\text{mut}}$ for proline was excluded for all three energy functions because steric clashes resulted in large values. While prediction accuracy was improved relative to **M12** ($R^2 = 0.77$), accuracy was comparable to **M07** ($R^2 = 0.84$). We were surprised that **M07** and **M19** demonstrated similar predictive ability. This is because a second set of measurements in OmpLA [99] correlates well with PagP measurements but not with **M07** predictions [65]. According to Marx *et al.*, the largest deviations were for side chains containing polar atoms. We therefore recalculated the correlation coefficient for polar and charged side chains. Here, the

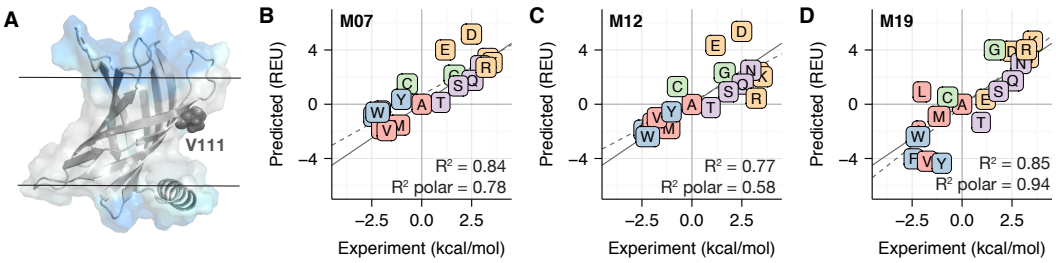

Figure 2.3: Comparison between computationally predicted and experimentally measured $\Delta\Delta G^{\text{mut}}$ for mutations in PagP. For all correlation plots (B-D), proline is not shown due to steric clashes resulting in a large $\Delta\Delta G^{\text{mut}}$ value. The dotted gray line is the line of best fit and the solid gray line is $y = x$. In addition, amino acids are colored according to the following categories: charged (orange), nonpolar (red), aromatic (blue), polar (purple), special case (green). (A) Structure of the PagP scaffold (PDB 3gp6) with the mutation site V111 highlighted in dark grey. The implicit solvent phases in A are colored in a similar manner to Fig 2.1. The $\Delta\Delta G^{\text{mut}}$ predictions for mutations in PagP by M07, M12, and M19 are shown in panels B, C, and D respectively.

correlations were 0.78, 0.58, and 0.94 for **M07**, **M12**, and **M19** respectively. Note, this is mainly due to Asp and Glu as the overall correlation coefficients without these side chains are 0.90, 0.87, and 0.85 for **M07**, **M12**, and **M19** respectively. Nonetheless, we were encouraged by these results because they demonstrate the ability of our model to capture the behavior of polar side chains in the bilayer.

We examined $\Delta\Delta G^{\text{mut}}$ predictions that deviate more than 1.5 REU from the measured value. For **M19**, this included predictions for G, T, V, Y, and L. To investigate, we analyzed contributions of the component energies to the overall $\Delta\Delta G^{\text{mut}}$ (Fig. S4-6). From the component energies, we found that glycine, threonine, and valine had errors arising from over- or under-estimation of van der Waals energy. This suggests double counting between the physics-based terms and the water-to-bilayer energy that captures all of the enthalpic contributions to $\Delta\Delta G^{\text{mut}}$. On the other hand, tyrosine was predicted to be too favorable due to a large attractive van der Waals and water-to-bilayer energy, also suggesting double counting. We were most surprised

by the prediction of leucine as less favorable relative to alanine since it is typically one of the most common side chains in the bilayer. This difference arises from a large positive contribution from the two-body solvation term (fa_sol), a term we have not yet refit for the membrane because of insufficient experimental data.

2.4.2.3 Test #3: Native structure discrimination

Identification of native-like structures in an ensemble of candidate structures is a key function of biomolecular modeling energy functions. To evaluate native structure discrimination, we refined ensembles of candidate structures generated by molecular dynamics [114] and then computed the root-mean-squared-deviation (RMSD) between the native crystal and the candidate models. We performed the analysis for five targets: bacteriorhodopsin (Brd7), fumarate reductase (Fmr5), lactose permease (LtpA), rhodopsin (RhoD), and V-ATPase (Vatp). To quantify decoy discrimination, we computed the Boltzmann-weighted average RMS value, called W_{RMS}, for all targets (Table 2.1, see SI Appendix for definition of W_{RMS}). In addition, a mapping of energy vs. RMSD for each target is shown in Fig. S7.

Table 2.1: Weighted RMSD of refined and rescored candidate models by each energy function

Target	R15 (Å)	M07 (Å)	M12 (Å)	M19 (Å)
Brd7	1.95	3.21	5.89	2.59
Fmr5	3.33	3.62	3.50	3.11
LtpA	2.25	1.65	1.69	2.20
RhoD	1.88	1.77	1.62	1.93
Vatp	1.38	1.52	1.36	1.55
Average	2.16	2.81	2.35	2.28

On average, all of the energy functions distinguished near-native from non-native conformations up to 2.1-2.3 Å from the native crystal structure, except **M12** which

distinguished conformations at 2.8 Å from the native crystal structure. In addition, for all targets except LtpA, all energy models score the native conformation as lower energy than the decoy structures. Upon examination of individual targets, we also found that no specific energy model was consistently better or worse.

We were surprised that the new implicit membrane model did not have an impact on native structure discrimination. Further, **R15** which does not consider the membrane, was able to distinguish near-native from non-native decoys at similar resolution. This result suggests while membrane environment energy terms are important, most of the high-resolution discrimination is driven by van der Waals and side chain packing at high-resolution. This finding complements recent work by Mravic *et al.* [115] that demonstrates side-chain packing is a key driver for stability.

2.4.2.4 Test #4: Native sequence recovery

A fourth test evaluates sequence recovery: the fraction of amino acids recovered after performing complete redesign on naturally occurring proteins. High sequence recovery has long been correlated with strong energy function performance for soluble proteins [106]. We therefore performed this test in the context of our membrane protein energy function. In this work, we used a test set of 133 α-helical and β-barrel membrane proteins. The test set is a subset of the 222-member dataset from Koehler Leman *et al.* [105] and was chosen because it is the largest possible subset of high-resolution structures with diverse sequences, further filtered for proteins with known host lipid compositions.

To perform redesign, we used a Monte Carlo fixed-backbone design protocol which samples possible sequences using a full protein rotamer-and-sequence optimization and a multi-cool annealer-simulated annealing protocol [116]. Each protein

is initialized in the orientation computed from the Orientations of Proteins in Membranes database [117] and the orientation is kept fixed during sequence search. Then, we computed two metrics: (a) the fraction of all amino acids recovered and (b) the fraction of amino acid types with individual recovery rates greater than 0.05, the same probability of choosing an amino acid at random. Overall, 31.8% of the amino acids designed by **M19** were identical to the native amino acid (Fig. 2.4A). The soluble protein energy function **R15** recovered the second highest percentage of amino acid positions at 29.9%. In contrast, the two existing implicit membrane models lagged behind with **M07** at 26.5% and **M12** at 26.7%. The individual amino acid recovery rates were also revealing. Here, **M19** and **R15** recovered all 20 amino acids at rates above random; whereas **M12** recovered 19 and **M07** recovered 14.

To examine the influence of different solvent environments, we recomputed sequence recovery over subsets of residues. First, we compared buried vs. solvent-exposed side chains (Fig. 2.4B). For all energy functions, recovery was significantly higher for buried side chains than solvent-exposed side chains, as noted in previous studies due to higher packing density [106]. On the surface, **M12** recovered 25% of acid positions, slightly higher than the 22% recovery rate by **M19**. However, **M19** recovered 16 amino acids at rates above random; whereas, **M12** recovered only 12 amino acids. In essence, **M19** gets the overall answer correct slightly less frequently; however, it is better at getting more amino acid types correct.

Next, we examined sequence recovery differences between side chains facing the water and lipid phases (Fig. 2.4C). In the lipid phase, all membrane energy functions recovered nearly the same fraction of amino acids. The main differentiating feature is the number of amino acids recovered with greater than random probability. Whereas

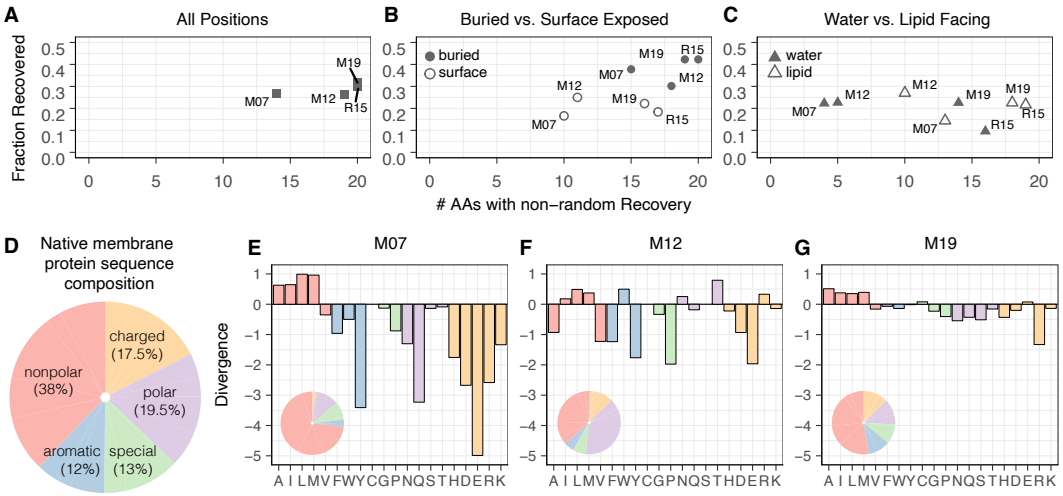

Figure 2.4: Properties of designed membrane protein sequences relative to their native counterparts. Panels A-C rank the performance of each energy function by two metrics: the fraction of all amino acids recovered on the y-axis and the fraction of amino acid types with individual recovery rates greater than 0.05 on the x-axis. An accurate energy function would have a high sequence recovery rate both overall and for the individual amino acid types. The results are shown for all positions in panel (A), buried vs. surface-exposed positions in (B) and water vs. lipid exposed positions in (C). Panel D shows the amino acid composition of the native sequences in the benchmark set. Panels E-G show the Kullback-Leibler (KL) divergence of the amino acid distribution of the designed proteins relative to the distribution in native membrane proteins. The designs by M07, M12, and M19 are shown in panels E, F, and G respectively. A positive value indicates that an amino acid is over-enriched, whereas a negative value indicates that an amino acid is under-enriched. Values are given on a logarithmic scale. An amino acid composition pie chart for sequence designed by each candidate energy function is also shown in the bottom left hand corner of the divergence plots.

M07 and **M12** recovered four and five amino acids respectively, **M19** recovered 14 amino acids. We observed a similar trend in the water phase. Here, **M12** has the highest overall sequence recovery rate of 27%, next to **M19** with a recovery rate of 23%. However, **M12** only recovered 10 amino acid types whereas M19 recovers 14. These results reveal that early energy functions used a rudimentary design strategy: prioritizing only some amino acid types. In contrast, **M19** is capable of designing more chemically diverse sequences.

Looking ahead, there are many ways to expand this benchmark to provide more insight. Here, we used a fixed-backbone design algorithm to generate new sequences. An interesting future area is to use flexible-backbone design to enable a larger range of possible sequences. This is an easy extension because the pore shape calculation plus energy evaluation is efficient. In addition, we can compute sequence logos for each design relative to homologous sequences. This provides insight into recovered positions that are also conserved. Thus, our sequence recovery test provides a foundation for learning more about energy function features in the future.

2.4.2.5 Comparison with ref15_memb

While this work was in revision, another membrane energy function was published by Weinstein *et al.* [118] (*ref15_memb*, **R15M**). This presented a good opportunity to compare performance of *franklin2019* with a more recent Rosetta model. We ran all four benchmark tests and the results are reported in Supplementary Fig. S8. Overall, **M19** outperformed **R15M** on all tests. The largest discrepancy was performance on the $\Delta\Delta G$ of mutation test, with **R15M** incorrectly predicting $\Delta\Delta G$ values for both OmpLA and PagP. The predicted tilt angles were correct for only one of five targets. The resolution of decoy discrimination was overall higher than for **M19**. Specifically, for R15M, the weighted RMS values were 6.00, 7.22, 2.47, 3.26, and 2.99 for brd7, fmr5, ltpa, rhod, and vatp respectively. Further, while both methods predicted a more near-native distribution of amino acids during design, **M19** outperformed in both KL divergence and recovery metrics, especially for lipid facing residues.

We were surprised about the discrepancy between **M19** and **R15M** because both energy functions use the same foundation (**R15**) and the transfer energies in **R15M** from the dSTβL assay [119] have been shown to correlate with the Moon & Fleming

scale. We hypothesize that the main challenge is consideration of side chain exposure. **R15M** does not account for lipid composition or pores and cavities. Further, the method was predominantly benchmarked on docking and folding of single-span dimers, whereas the benchmarks in this paper are larger and quantitatively more diverse. Therefore, these results suggest that while **R15M** may be specialized for single-TM dimers, **M19** is capable of handling more complex membrane protein topologies.

2.4.3 Designed membrane proteins exhibit native-like features

The sequence recovery experiment enables us to study properties of *in silico* designed membrane proteins. These properties are crucial for demonstrating that the implicit model has native membrane properties and is capable of facilitating realistic design experiments. Below, we examine various sequence and structural features important for membrane protein stability and function.

2.4.3.1 Amino acid distribution in designed proteins mirrors the native distribution

We examined the distribution of amino acids in design protein sequences relative to their native counterparts. Specifically, we measured the Kullback-Leilber (D_{KL}) divergence (Eq. S2, see SI Appendix) on our membrane protein dataset. A negative D_{KL} value indicates that sequences are under-enriched in specific amino acid types; whereas, a positive D_{KL} value indicates that sequences are over-enriched. An ideal KL value is zero. Remarkably, sequences designed by **M19** are near-native with $D_{\mathrm{KL}} = -2.7$. This is in stark contrast to sequences designed by **M07** and **M12** which are strongly divergent from native membrane protein sequences, with $D_{\mathrm{KL}} = -24.6$

and $D_{\mathrm{KL}} = -26.6$ respectively.

To learn more about the design implications of each energy function, we computed the KL for each amino acid type (Fig. 2.4D-G) and compared to the composition of amino acids in the native set. The **M07** sequences are over-enriched in non-polar amino acids and under-enriched in all other categories. The deficits are large with under-enrichment values ranging from 10^{-2} to 10^{-4}. The **M12** sequences are less skewed with the magnitude of under-enrichment deficits ranging between 10^{-1} and 10^{-2}. However, there is still a large over-enrichment of non-polar amino acids including I, L, and M, as well as W and T. In contrast, the distribution of amino acids in **M19** sequences is comparable to the native distribution, with the magnitude of under- and over-enrichment values ranging between 10^{1} and 10^{-1}. Thus, **M07** and **M12** employ a rudimentary design strategy: only choosing non-polar amino acids guaranteed to be compatible with the greasy membrane environment. The **M19** model does not rely on this assumption and can design every amino acid type within each phase. As a result, **M19** designs proteins with an amino acid distribution that is close to the native membrane protein sequence composition. We thus expect that **M19** will more accurately evaluate the effects of genetic mutations on protein stability. Further, the diversified sequences will enable designed membrane proteins to achieve a broader range of architectures and functions.

2.4.3.2 Three-dimensional membrane geometry enables design of polar pores

We were interested to see whether a three-dimensional implicit membrane shape facilitates accurate protein design. To do so, we investigated the native and designed sequence of the scaffold protein voltage-dependent anion channel 1 (VDAC1; PDB 3emn; Fig. 2.5). The native sequence of this β-barrel protein pore is rich in

charged amino acids. In the two-dimensional membranes used by **M07** and **M12**, the pore-facing residues are designed as if they are in the lipid phase; and as a result, the designed sequences are rich in non-polar amino acids. In contrast, the three-dimensional implicit membrane geometry treats pore-facing residues as exposed to the water phase; thus, the designed sequence contains both polar and charged amino acids. These positive features are reflected in the sequence for this specific target. Here, **M19** exhibits the highest recovery over all surface residues, lipid-facing, and aqueous-facing residues when compared with other energy functions. This result suggests the potential of **M19** to perform accurate design on both the lipid-facing and water-filled-pore facing surfaces.

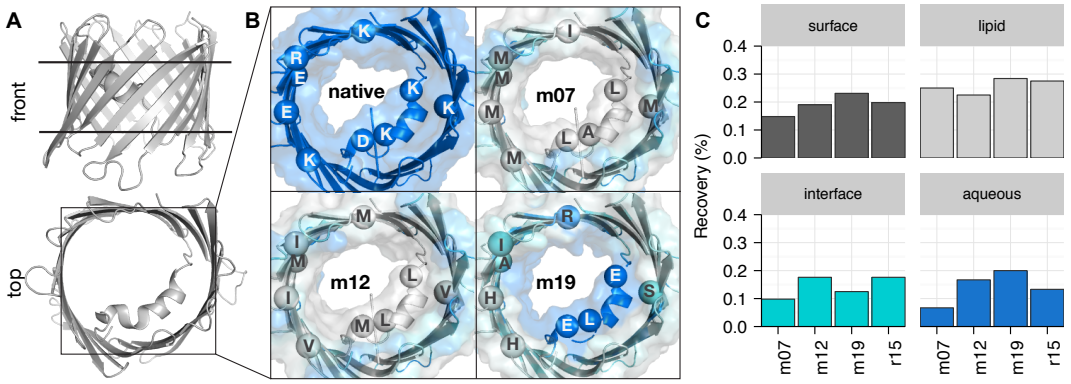

Figure 2.5: An *in silico* redesigned β-barrel membrane protein with a polar aqueous pore. (A) Structure of the design scaffold protein voltage-dependent anion channel VDAC1 (PDB 3emn) from a lateral and top view. The horizontal black lines denote the approximate position of the membrane. (B) Sequence composition and solvation properties of the pore redesigned by the M07 (top right), M12 (bottom left), and M19 (bottom right) energy functions in contrast to the native sequence (top left). The M07 and M12 treat the pore as lipid-exposed resulting in a non polar sequence. In contrast, the M19 energy function calculates a custom pore shape resulting in a polar pore sequence. (C) Recovery of the native 3EMN sequence upon redesign. In contrast to other energy functions, the M19 recovers the most native sequence for the total surface, lipid-exposed, and aqueous-solvated residues.

An unexpected result was that **M19** outperformed **R15** in the aqueous pore of VDAC1. In fact, we expected the performance of R15 to match M19 because in the

pore region, $f_{\text{hyd}} = 0$. We hypothesize that the pore size and transition steepness were underestimated and thus the calculation was influenced by M19. While it is hard to draw a quantitative conclusion about the improved performance, we suggest a future step of investigating the amino acid composition of a larger set of β-barrel pores to understand the result.

2.4.3.3 Biologically-relevant lipid composition parameters improve per-target sequence recovery

Finally, we were eager to explore whether implicit membrane parameters for different lipid compositions can improve design outcomes. This question is difficult to evaluate because the host membrane composition of proteins is not always known. At the same time, this question is crucial because of the long-standing criticism that implicit membrane models do not accurately capture the properties of different lipid membrane compositions. In this work, we investigated this question anecdotally by examining two examples from our membrane protein design dataset.

First, we examined the β-barrel protein scaffold outer membrane transporter FecA from *Escherichia coli*. The outer membranes of gram-negative bacteria are significantly thinner than eukaryotic plasma membranes. We therefore hypothesized that sequence recovery of lipid-facing residues in this protein would be higher in a thinner membrane. To test this hypothesis, we again searched for low energy sequences in an **M19** membrane with either DLPC or POPC parameters. Encouragingly, the recovery of lipid facing residues in this protein was 33% in DLPC in contrast to 28% in POPC. We also repeated this test on the α-helical protein scaffold VCX1 calcium/proton exchanger from *Saccharomyces cerevisiae*. Here, we expected the reverse trend: improved design in a POPC membrane over DLPC. Again, the design results followed: 22%

sequence recovery in DLPC and 29% in POPC. These results demonstrate that lipid composition parameters facilitate more biologically realistic structure prediction and design.

In addition, there was an inevitable question that we wanted to ask about our β-barrel protein scaffold. Experimental studies have long demonstrated that β-barrel membrane proteins have high concentrations of aromatic side chains near the interfacial head groups [120]. While the thermodynamics of this phenomena are not completely understood, it is suggested that stacking of the aromatics nearby polar head-groups stabilizes the protein [121]. Thus, we asked the questions: does **M19** also design aromatics near the anisotropic phase representing interfacial head groups? To answer, we calculated the apparent membrane thickness according to the average positions of aromatic side chains in native and designed FecA (Fig. 2.6). We found that **M19** designed with a larger apparent thickness in POPC rather than DLPC membranes. Notably, the DLPC aromatic thickness is near the native aromatic thickness. While still anecdotal, these results suggest that **M19** designs proteins with native-like features.

2.5 Discussion

In this work, we developed, implemented, and tested a new energy function for membrane protein structure prediction and design. The energy function, called *franklin2019*, uses an implicit approach to represent the anisotropic structure and nanoscale dimensions of membranes with varied phospholipid composition, a key component of biological membranes. Through computational benchmarking, we demonstrated that the model can replicate experimentally measured protein stabilities

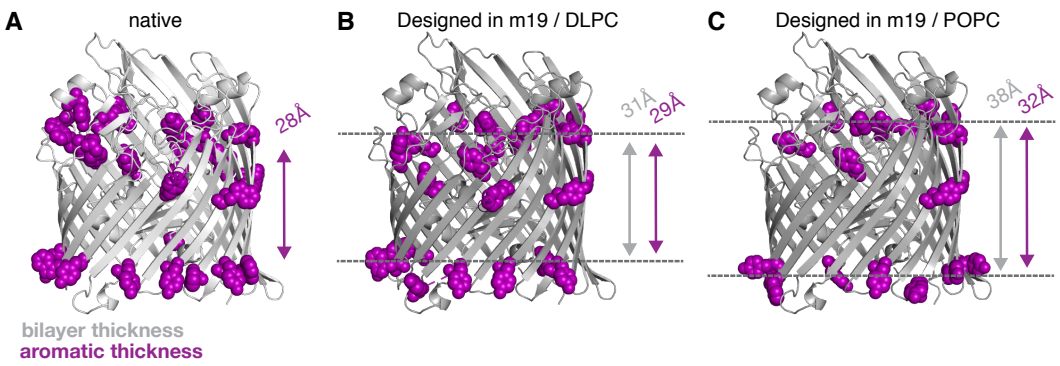

Figure 2.6: *In silico* redesigned β-barrel membrane proteins in native-like lipid compositions. (A) Structure of the design scaffold Outer Membrane Transporter FecA (PDB 1kmo) from *Escherichia coli*. The backbones redesigned by the M19 energy function with DLPC and POPC parameters are shown in panels (B) and (C) respectively. The native scaffold is colored in light grey and the design scaffolds are colored in dark grey. Aromatic amino acids near the interface (>7 and < 25 from the center) are colored in light pink. The grey arrow shows the bilayer thickness and the pink arrow shows the thickness according to the average position of interfacial aromatic residues. The dotted lines denote the approximate position of the bilayer. The thickness from the DLPC design best matches the native and results in the highest recovery of lipid facing residues in the transmembrane region. DLPC is closest to the thickness in *E. coli*.

and orientations. With multiple diverse benchmark sets, we demonstrated that *franklin2019* improves modeling and design of membrane proteins with complex topologies, pores, and juxta-membrane domains. Further, proteins designed by *franklin2019* exhibit native-like features including amino acid distribution, aromatic amino acids near interfacial head groups, and hydrophobic match with specific lipid compositions. Together, these features demonstrate the potential of *franklin2019* to advance high-resolution membrane protein structure prediction and design.

Through the goal of developing a new energy function, our study interrogated fundamental questions about the design rules for native membrane proteins. First, the implicit model is based on transfer energies from a thermodynamic hydrophobicity scale measured in a phospholipid bilayer. The high sequence recovery rate demonstrates the importance of thermostability and bulk phospholipid chemistry in

constraining membrane protein sequences. Further, previous work relied on narrow membrane protein design rules such as enrichment of leucine side-chains in the hydrophobic core. We demonstrated that native membrane protein sequences are diverse and not constrained to hydrophobic amino acids. Accordingly, our energy function uses the full palette of amino acid chemistries during design.

This work was enabled by the Moon & Fleming [99] hydrophobicity scale. While there has been extensive work to quantify transfer energies [122], the Moon & Fleming scale captures the actual equilibrium change in free energy in the context of a membrane protein in a phospholipid bilayer [123]. Thus, the implicit model captures more biologically realistic context relative to prior models that approximated the membrane as a slab of non-polar organic solvent. One consideration of using the Moon & Fleming scale is that *franklin2019* would not capture non-thermodynamic (kinetic) end-states of *ab initio* folding where chaperones are required. For example, in α-helical membrane protein folding, the intermediate states in the two-stage folding process may not be captured [124]. However, because the goal of Rosetta calculations is to capture the free energy minima, this does not impose limitations. Second, the measurements were taken at pH 3.8. As a result, the energetics of Asp and Glu are undervalued because the side chains are protonated. This may affect estimates of transfer energies for soluble proteins and marginally hydrophobic proteins. Accurately assigning the protonation states of Asp and Glu is an ongoing challenge due to membrane-induced pKa shifts that alter the protonation equilibrium [125].

Next, we sought to develop a model that describes bilayers with different lipid compositions. We were inspired by prior studies that added more detail to implicit

"slab" models, including anionic lipid parameters [126] and adjustable bilayer thickness [91]. In this work, we focused on single-component phospholipid bilayers for two reasons: (1) there is significant SAXS and neutron scattering data available for validation, and (2) many experiments are performed in single-component bilayers, enabling easy comparison. We coined our model "biologically realistic" to highlight the advance of using phospholipid models over prior organic slab models. Importantly, there are many future steps required to achieve a "biologically accurate" model. First, native membranes include hundreds of lipid types, distributed non-uniformly [6]. While all-atom models remain difficult, there has been excellent progress in coarse-grained modeling of native lipid bilayers [127]. Thus, a possible step is to develop model parameters from these coarse-grained models. Another important step is to generate parameters for the asymmetric lipid composition to emulate the outer membrane of gram-negative bacteria [128]. Additionally, the membrane bends and curves to accommodate the hydrophobic surface of proteins [129]. A further challenge is accounting for local properties such as specific protein interactions with lipids and cholesterol, which may be captured by a hybrid implicit-explicit approach such as SPadES [130] or HMMM [131]. Finally, an open question is how to account for mechanical properties such as lateral pressure and strain due to local curvature. In these scenarios, it is most likely that implicit membrane simulations will compliment information from emerging membrane protein modeling tools and molecular dynamics simulations to investigate structure, dynamics, and function.

Another important methodological step is modeling of membrane protein pores and cavities. Previously, implicit models approximated pores as cylinders [109] or segregated side chains using grid-based approaches [132]. In contrast, *franklin2019*

uses continuous functions to model a wide range of pore geometries. We chose this approach over solvent-accessible surface area calculations to reduce computational cost, enabling scalability for more sophisticated molecular modeling applications such as flexible backbone design. For future work, we aim to capture membrane deformations [133] through the integration of continuum elastic models [24, 134] or hybrid continuum-atomistic models [135]. Additionally, more work is needed to account for fenestrations that alter the solvent exposure of lipid accessible residues [48]. Ultimately, these features will advance *franklin2019* from capturing static membrane features to incorporate dynamics important for protein function.

We evaluated our implicit membrane model using sparse, high-resolution experimental data. This approach contrasts soluble protein energy function evaluation, where there is an abundance of thermodynamic and spectroscopic measurements of small molecules [136] and high-resolution protein structures [137]. To overcome the possibility of over-fitting, we limited the validation data to high-quality measurements. For instance, we did not use crystal structures ≥ 3 Å resolution or $\Delta\Delta G_{\text{mut}}$ values that were not measured in a reversible system. Further, we benchmarked our energy function against both thermodynamic and structure prediction data. Previous studies have evaluated membrane energy functions on a single test such as tilt angles [47], native structure discrimination [114, 138], predicting hydrophobic lengths [132], $\Delta\Delta G$ prediction [139] and sequence recovery [140]. Simultaneously performing the benchmarks enables a well-rounded evaluation of the energy function for diverse biomolecular modeling tasks.

Looking ahead, a larger benchmark set will enable broader energy function development and optimization. This work focused on developing a single empirical term

that captures water-to-bilayer transfer energetics that could be added to the existing Rosetta energy function. Naturally, this introduces double-counting between the new term and existing physics-based terms such as solvation and electrostatics. Previous work on the soluble protein energy function used a Nelder-Mead optimization scheme [60] to remove double counting. While there is currently insufficient data to apply this approach, we envision that as more data emerges we will be able to apply more robust fitting techniques including machine learning. Further, additional benchmark data will enable adding membrane dependence to the solvation and electrostatic terms, which will improve modeling of local side chain environments. Important future requirements for a larger benchmark set include more diverse modeling tasks, such as capturing multiple conformation states and diverse data sources such as models from X-Ray Crystallography, Cryo-EM, and NMR spectroscopy.

An important remaining task is to compare the performance of *franklin2019* with the latest methods in other molecular modeling packages. Currently, there are several technical hurdles: (1) alternate membrane representations are not implemented within the Rosetta package and (2) other packages cannot generate all of the requisite data for each benchmark (e.g., design is computationally expensive for classical molecular dynamics packages). Notably, the latest energy functions for membrane protein modeling use a wide-range of physical, empirical, and statistical models for energy calculations. Therefore, direct comparison will provide important information to the community about the best strategies for membrane protein structure prediction and design.

In summary, we developed a biologically realistic energy function for membrane protein structure prediction and design. The energy function is implemented within

the Rosetta software and can be used for a wide range of macromolecular modeling tools. By pursuing a balance of efficiency and accuracy, we anticipate that the implicit membrane will enable high-throughput and high-resolution membrane protein structure prediction and design. Importantly, this model transforms once protein-centric tools to techniques that can predict and design structures tied with varied biologically relevant lipid compositions.

2.6 Appendix

2.6.1 Test #1 Methods: Prediction of transmembrane peptide orientation

Dataset curation. We computed energy landscapes for five transmembrane helical peptides [47]: acetylcholine receptor segment (1a11), M2 proton channel segment (1mp6) NMDA glutamate receptor (2nr1), VPU-forming domain of HIV-1 (1pje), and WALP23. Coordinates for the first four peptides were downloaded from the Protein Data Bank [141]. The structure of WALP23 was modeled as an ideal helix with $\phi = -47°$and $\psi = -57°$. For calculations with the new implicit membrane model, we chose lipid composition parameters that were consistent with the lipid composition used for the experimental measurement (Table 2.12).

Protocol Information. Low-free-energy peptide orientations were identified by calculating an energy landscape: a mapping between all possible peptide orientations relative to the membrane and their energies. Orientation was defined by two coordinates: (1) distance between the membrane center and peptide center of mass, d and (2) angle between the membrane normal and helical axis, θ. For the oligomeric forms of the M2 proton channel and acetylcholine receptor, the helical axis was defined as the average of the helical axis for each transmembrane segment.

To compute the mapping, we first applied side-chain packing and minimization to resolve steric clashes in the peptide structure. Then, we applied rigid-body moves to sample all combinations of θ and d values. Membrane depths were sampled between -60 Å and 60 Å with a 1 Å step size and tilt angles were sampled between $0° - 360°$ with a $1°$ step size. In addition, the water-to-bilayer transfer energy $\Delta G_{\mathrm{w,l}}$ was computed for each peptide as the difference in energy between the aqueous phase (ΔG_{w}: peptide at (60 Å,270 °)) and the lipid phase (ΔG_{l}: peptide at (0 Å, 270°)): $\Delta G_{\mathrm{w,l}} = \Delta G_{\mathrm{l}} - \Delta G_{\mathrm{w}}$.

Detailed command lines. The `MembraneEnergyLandscapeSampler` samples and scores all peptide orientations within the specified range of membrane depth values and tilt angles. The protocol is captured by the XML script listed below.

```
<ROSETTASCRIPTS>
  <SCOREFXNS>
    <ScoreFunction name="s" weights="%%sfxn_weights%%"/>
  </SCOREFXNS>
  <TASKOPERATIONS>
    <RestrictToRepacking name="rtrp"/>
    <ExtraRotamersGeneric name="extra_chi" ex1="1"
       ex2="1" extrachi_cutoff="0"/>
  </TASKOPERATIONS>
  <MOVERS>
    <AddMembraneMover name="add_memb" />
    <TransformIntoMembraneMover name="transform_into_memb" />
    <PackRotamersMover name="pack_rotamers" scorefxn="s"
      task_operations="rtrp"/>
    <MinMover name="minimize_struc" scorefxn="s" chi="1"
      bb="1" jump="0" type="dfpmin_armijo_nonmonotone"
      tolerance="0.01" />
    <MembraneEnergyLandscapeSampler name="landscape_test"
      scorefxn="s" interface="0" />
  </MOVERS>
  <PROTOCOLS>
    <Add mover_name="add_memb"/>
    <Add mover_name="transform_into_memb"/>
    <Add mover_name="pack_rotamers"/>
    <Add mover_name="minimize_struc"/>
    <Add mover_name="landscape_test"/>
  </PROTOCOLS>
</ROSETTASCRIPTS>
```

The protocol is deterministic and outputs a single file with a mapping between orientations and energies. To run the protocol, we ran the following command line for each peptide:

```
/path/to/Rosetta/main/source/bin/rosetta_scripts.macosclangrelease
  -in:file:s 1a11.pdb                # Input PDB File
  -mp:setup:spanfiles 1a11.span        # Input span file
  -parser:protocol                 # Name of XML script file
    sample_energy_landscape.xml
  -parser:script_vars          # Energy function to use
    sfxn_weights=franklin2019
  -mp:lipids:composition DLPC       # Lipid composition (for f19)
```

2.6.2 Test #2 Methods: $\Delta\Delta G^{\mathbf{mut}}$ predictions

Protocol information. $\Delta\Delta G^{\text{mut}}$ values were computed using the protocol described in Alford *et al.* [65]. Here, a mutation is introduced at the host site and the side chains are optimized within 8Å of the mutated residue. The $\Delta\Delta G^{\text{mut}}$ was calculated as the difference in energy between the mutant (ΔG^{mutant}) and native (ΔG^{native}) conformations: $\Delta\Delta G^{\text{mut}} = \Delta G^{\text{mutant}} - \Delta G^{\text{native}}$. $\Delta\Delta G^{\text{mut}}$ prediction was evaluated on mutations in position 111 in outer membrane palmitoyl transferase (PagP; 3qd6) [113]. The dataset included mutations from the native amino acid to all 19 other canonical amino acids. For calculations with the new implicit membrane model, parameters for DLPC membranes at 20°C were chosen to match experimental conditions.

Detailed command lines. To calculate $\Delta\Delta G^{\text{mut}}$ values, we used the MPddG protocol described in Alford *et al.* [65]. The protocol combines the RosettaMP framework with a fixed-backbone $\Delta\Delta G$ prediction protocol similar to the method described in Kellogg *et al*. [142]. The MPddG protocol is captured in a PyRosetta script [66]. The following command line and options were used for prediction of $\Delta\Delta G_{\text{mut}}$ values for mutations in the OmpLA and PagP scaffolds:

```
python predict_ddG.py
  --pdb sample.pdb                  # Input PDB file
  --spanfile sample.span            # Input spanfile
  --out_ddGs ddGs.txt               #  Predicted ddGs
  --out_breakdown decomposed.sc     # Predicted per-term ddGs
  --lipid_composition DLPC          # Lipid composition
  --res ##                          # Host site
  --repack_radius 8.0               # Repack radius
```

The script will predict $\Delta\Delta G_{\text{mut}}$ values for all canonical amino acids. The first output file, `ddGs.txt` includes the predicted $\Delta\Delta G_{\text{mut}}$ values. The second output file, `decomposed.sc` includes the contribution of each energy term to the overall $\Delta\Delta G_{\text{mut}}$.

2.6.3 Test #3 Methods: Native structure discrimination

Protocol information. Native structure discrimination is the ability of an energy function to distinguish near-native from non-native conformations. To measure discrimination, we used ensembles of five α-helical proteins generated by Dutagaci *et al.* [114]: bacteriorhodopsin (BRD7; 1py6), fumarate reductase (FMR5; 1qla), lactose permease (LTPA; 1pv6), rhodopsin (RHOD; 1u19), and V-ATPase (VATP; 2bl2). Structures in each ensemble were between 1-11Å from the coordinates of the crystal structure. We refined each conformation using RosettaMPRelax [65] with constraints to the starting C_α coordinates. For structures refined using the new implicit membrane model, we used POPC parameters for eukaryotic targets and DLPC for targets from bacteria. The root-mean-squared-deviation (RMS) between the C_α coordinates of the native and refined models was computed with the MMTSB package [143]. Then, we computed the Boltzmann-weighted average RMS W_{RMS} [144]. Here, W_{RMS} is computed over N refined candidates with scores ΔG and distances from the native

RMS at a given temperature T (Eq. 2.7):

$$W_{\text{rms}} = \frac{\sum_i^N (\text{RMS}_i) \exp\left(\frac{\Delta G_i}{kT}\right)}{\sum_i^N \exp\left(\frac{\Delta G_i}{kT}\right)}. \tag{2.7}$$

Detailed command lines. To measure native structure discrimination, we refined decoys using the `mp_relax` protocol [65]. The `mp_relax` protocol combines the RosettaMP Framework with FastRelax [145]: a protocol that perturbs the protein using small backbone torsion moves, followed by side-chain repacking and energy minimization along all torsion angles (ϕ, ψ, ω). The protocol is captured by the Rosetta XML script `mp_relax.xml` listed below:

```
<ROSETTASCRIPTS>
  <SCOREFXNS>
    <ScoreFunction name="memb_hires" weights="%%sfxn_weights%%" />
  </SCOREFXNS>
  <MOVERS>
    <AddMembraneMover name="add_memb"/>
    <MembranePositionFromTopologyMover name="init_pos"/>
    <FastRelax name="fast_relax" scorefxn="memb_hires" repeats="8"/>
  </MOVERS>
  <PROTOCOLS>
    <Add mover="add_memb"/>
    <Add mover="init_pos"/>
    <Add mover="fast_relax"/>
  </PROTOCOLS>
  <OUTPUT scorefxn="memb_hires" />
</ROSETTASCRIPTS>
```

To execute the program, we ran the following command line on the decoy set for each target:

```
/path/to/Rosetta/main/source/bin/rosetta_scripts.linuxgccrelease
  -in:file:native sample_native.pdb   # Native PDB coordinates
  -in:file:l sample_candidates.list   # List of candidate models
  -mp:setup:spanfiles sample.span     # Spanning topology file
  -parser:script_vars
        sfxn_weights=franklin2019       # Name of candidate energy function
  -parser:protocol mp_relax.xml       # XML script for relax protocol
  -out:file:scorefile model_scores.sc # File with energies and RMS values
  -out:path:all /path/to/output/pdbs  # Refined models
  -mp:lipids:composition DLPC         # Choose phospholipid composition
```

To compute the RMSD between the native and refined models, we used the `score_jd2` application with the following options:

```
/path/to/Rosetta/main/source/bin/score_jd2.linuxgccrelease
  -in:file:l refined_models.list    # List of refined models
  -in:file:native native.pdb        # Native structure
  -in:file:spanfile sample.span     # Input spanfile
  -in:membrane                      # Use RosettaMP
  -score:weights franklin2019       # Energy function
  -mp:lipid:composition DLPC        # Lipid composition
```

Finally, we estimated the native structure discrimination score, W_{rms} using `score_energy_landscape.py`:

```
/path/to/Rosetta/bakerlab_scripts/boinc/score_energy_landscape.py
  -terms rms total_score              # Name of rms and energy term
  -abinitio_scorefile candidates.sc   # Energies and rms values
```

2.6.4 Test #4 Methods: Native sequence recovery

Dataset curation. To evaluate recovery, we used a benchmark set curated by Koehler Leman *et al.* [105] of α-helical and β-barrel proteins, each between 40-10,000 residues with less than 25% sequence identity and better than 3.0 Åresolution. While the

original dataset included 222 proteins, we reduced the set to 133 proteins with a known host lipid composition in the Orientations of Proteins in Membranes database [117]. We chose this approach to dataset curation because it resulted in the largest possible set of high-resolution membrane protein structures with diverse sequences and known host lipid composition. For design with the new implicit membrane model, all targets were designed with DOPC membrane parameters. This is because it was difficult to assign a lipid composition to all targets given inconsistencies in the membrane environments used for expression and structure determination. The protein coordinates were downloaded from the Orientations of Proteins in Membranes database [117].

Protocol Information. The fixed-backbone Rosetta Design protocol [116] was used to search for low-free energy-sequences. Sequence recovery, R_{seq}, was calculated as the number of correct positions N_{correct} relative to the number of available positions N_{all}:

$$R_{\text{seq}} = \frac{N_{\text{correct}}}{N_{\text{all}}}. \tag{2.8}$$

In addition, we examined sequence recovery rates for individual amino acid types, relative the background probability of guessing a random amino acid type (1 in 20 types, or 5%). This metric, N_{AA} is the fraction of amino acid types recovered with rates higher than random.

Detailed command lines. To measure native sequence recovery, we used an adapted version of the fixed-backbone design protocol from Leaver-Fay *et al.* [116]. Here, we combined this protocol with the RosettaMP framework to keep proteins oriented in the bilayer during design. Each protein in our dataset was redesigned

using the following command line:

```
/path/to/Rosetta/main/source/bin/fixbb.linuxgccrelease
  -in:file:s sample.pdb               # Input PDB coordinates
  -mp:setup:spanfiles sample.span     # Input spanfile
  -score:weights candidate_efxn       # Energy function weights file
  -in:membrane                        # Load the membrane framework
  -out:path:all                       # Output redesigned structures
  -in:ignore_unrecognized_res         # Ignore unknown residues
  -mp:lipids:composition DOPC         # Lipid composition
```

Then, we computed sequence recovery with the `mp_seqrecov` application using the command line given below:

```
/path/to/Rosetta/main/source/bin/mp_seqrecov.linuxgccrelease
  -native_pdb_list natives.list       # List of native protein PDBs
  -redesign_pdb_list redesigned.list  # List of redesigned protein PDBs
  -seq_recov_filename seqrecov.txt    # File for sequence recovery data
```

2.6.5 Computing properties of *in silico* designs

Sequence divergence. We examined properties of the *in silico* designed proteins using the Kullback-Leibler (KL) divergence. This metric quantifies the divergence between the distribution of amino acid types (i) in the native ($N_{\text{nat},i}$) and designed ($N_{\text{des},i}$) sequences:

$$D_{\text{KL}} = -\sum \ln\left(\frac{N_{\text{des},i}}{N_{\text{nat},i}}\right). \tag{2.9}$$

Aromatic thickness. To compute aromatic thickness, the aromatic carbon center-of-mass (m) was computed for all tyrosine and tryptophan side chains. Side chains were assigned to two bins: if the z-coordinate of m was less than 5Å , the coordinate

was assigned to the lower bin, and if the z coordinate of m was greater than 5Åthe coordinate was assigned to the upper bin. The ring center-of-mass M was computed as the center-of-mass of each bin. Then, the aromatic thickness was calculated as the distance between the z-coordinate of M_{upper} and M_{lower}.

2.6.6 Supplemental Figures

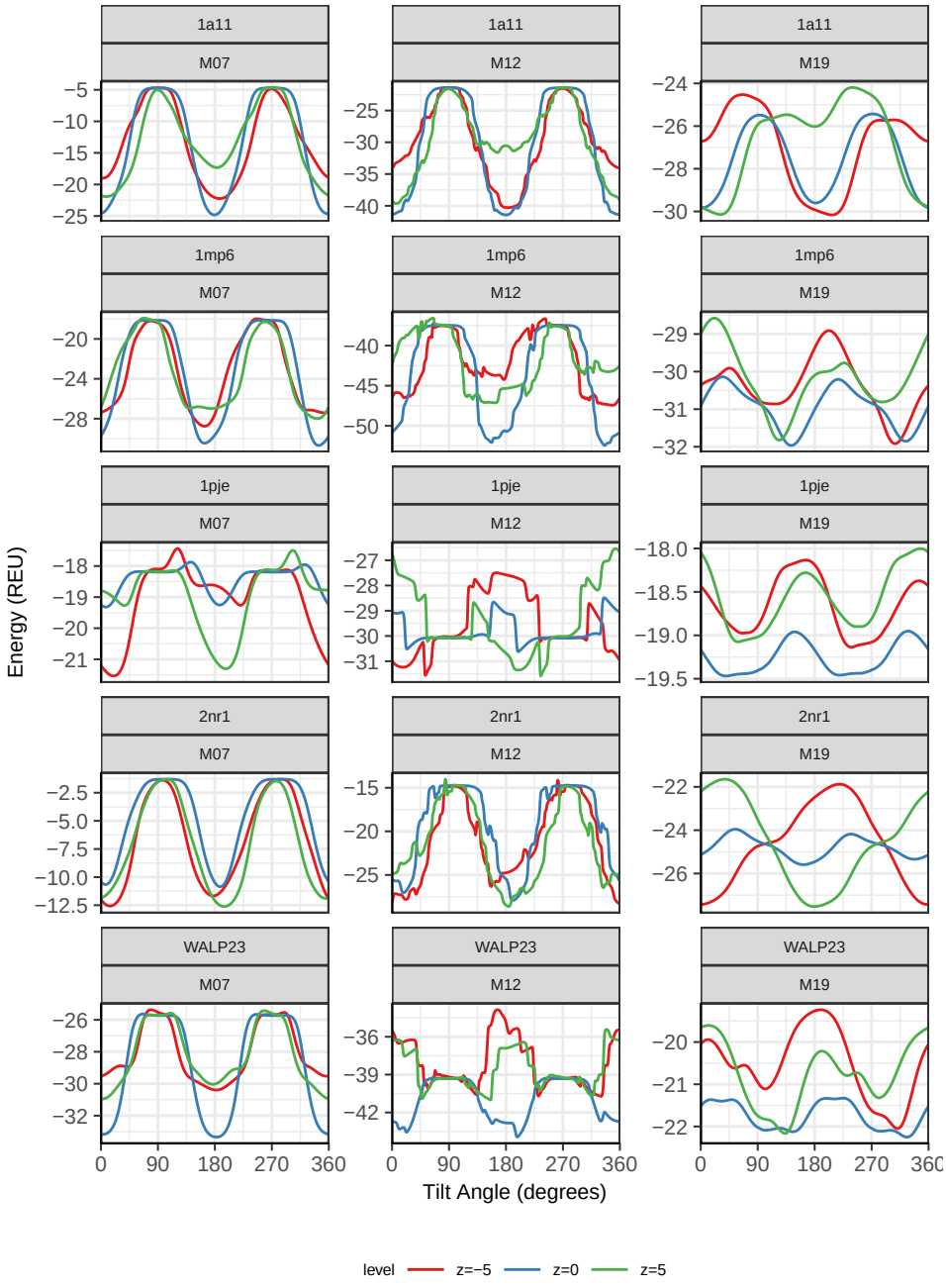

Figure 2.7: Dependence of total energy on tilt angle. Dependence of total energy on the peptide tilt angle for three depths: $z = 0$Å (blue), $z = -5$Å (red), $z = 5$Å (green).

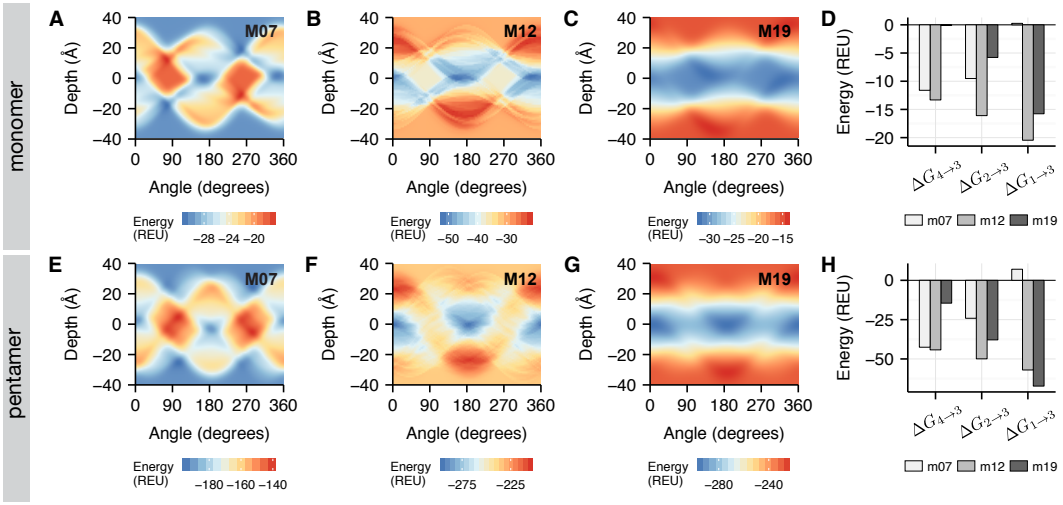

Figure 2.8: Prediction of insertion and orientation for monomeric and tetrameric M2 proton channel. The mapping of protein orientations to energies calculated by the M07, M12, and M19 energy function respectively is shown in panels A-C for the monomer and E-G for the pentamer. The partitioning energies between two lipid-buried conformations ($\Delta G_{4\to3}$), from interface to lipid ($\Delta G_{2\to3}$) and from water to lipid ($\Delta G_{1\to3}$) are shown in (D) for the monomer and (H) for the tetramer. Here, G_1 is the energy of the unfolded state in solution ($z = 30, \theta = 90°$). G_2 is the energy of the folded state at the interface, parallel to the plane of the interface ($z = 15, \theta = 90°$), G_3 is the energy of the peptide oriented vertically ($z = 0, \theta = 0°$), and G_4 is the energy of a peptide buried in the membrane ($z = 0, \theta = 90°$).

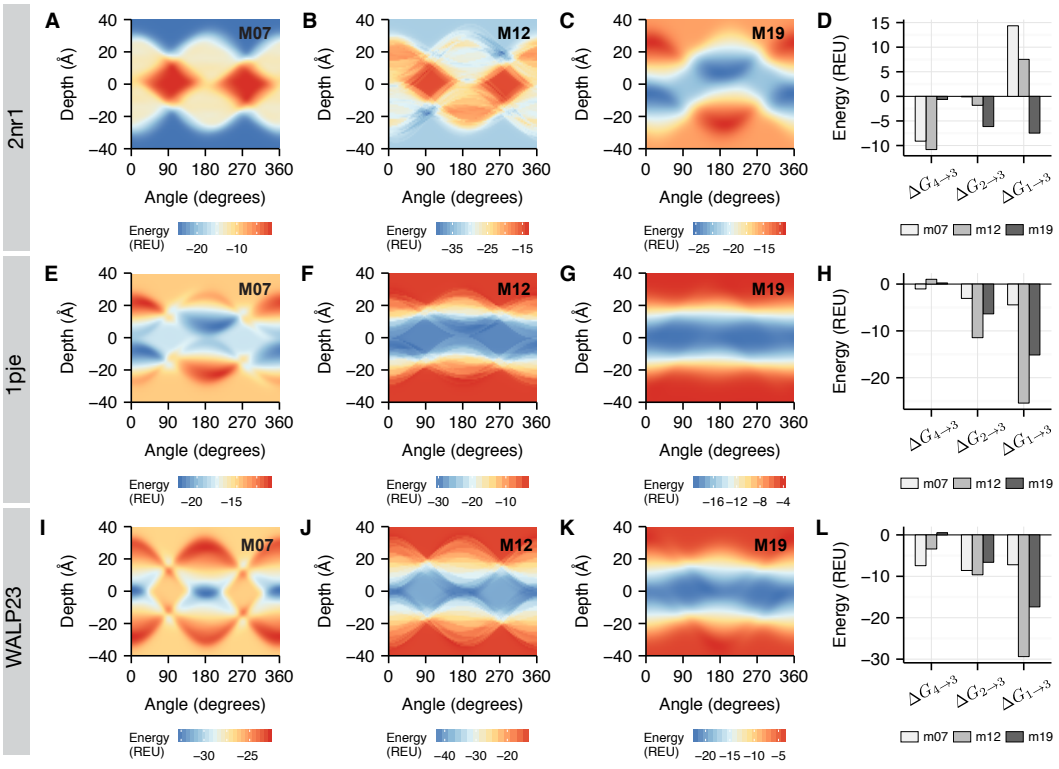

Figure 2.9: Prediction of peptide orientation for VPU-forming domain, NMDA-receptor, and WALP23. Prediction of peptide orientation for the remaining three peptides in the test set: the NR1 subunit of NMDA glutamate receptor (2nr1, top row), the VPU-forming domain of HIV-1 (1pje, middle row), and a rationally designed WALP peptide (WALP23, bottom row). The mapping of protein orientations to energies calculated by the M07, M12, and M19 energy function respectively is shown in panels A-C for 2nr1, E-G for 1pje, and I-K for WALP23. The partitioning energies between two lipid-buried conformations ($\Delta G_{4\to3}$), from interface to lipid ($\Delta G_{2\to3}$) and from water to lipid ($\Delta G_{1\to3}$) are shown in (D) for 2nr1, (H) for 1pje, and (J) for WALP23. Here, G_1 is the energy of the unfolded state in solution ($z = 30, \theta = 90°$). G_2 is the energy of the folded state at the interface, parallel to the plane of the interface ($z = 15, \theta = 90°$), G_3 is the energy of the peptide oriented vertically ($z = 0, \theta = 0°$), and G_4 is the energy of a peptide buried in the membrane ($z = 0, \theta = 90°$).

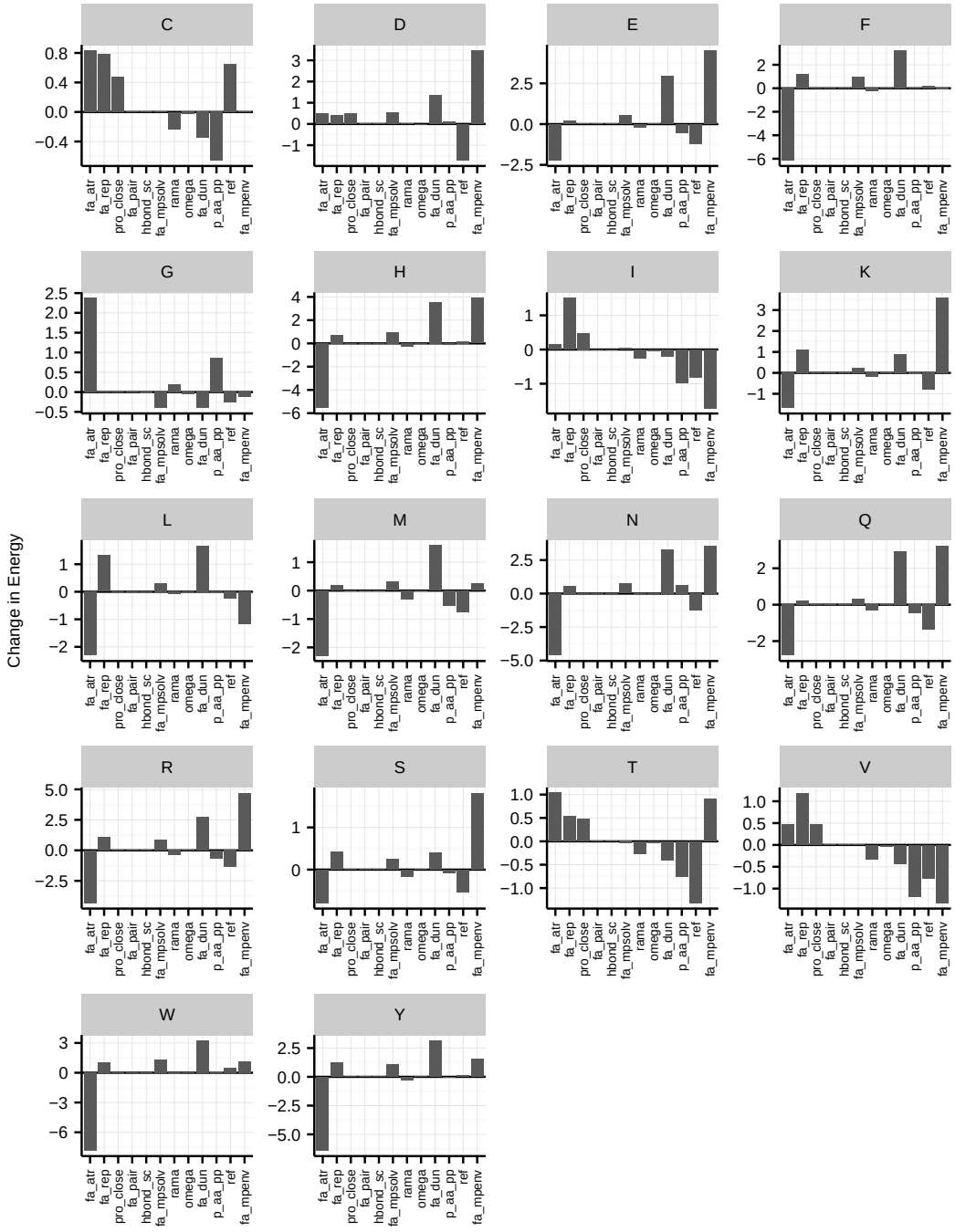

Figure 2.10: Contributions of M07 component energies to the $\Delta\Delta G^{\mathbf{mut}}$ for each mutation in PagP. Energies are only listed for contributions > 0.1 REU to the $\Delta\Delta G_{\text{mut}}$.

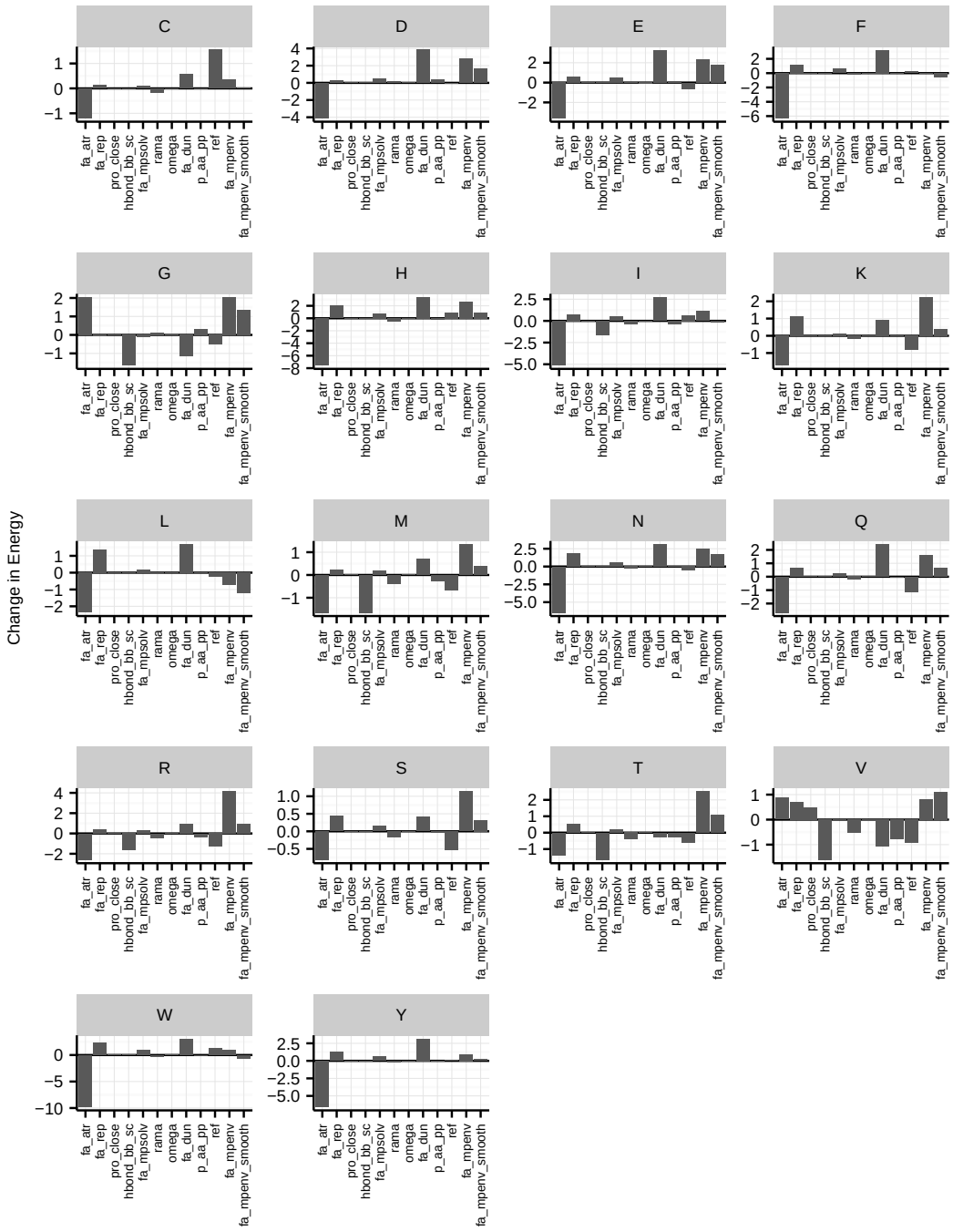

Figure 2.11: Contributions of M12 component energies to the $\Delta\Delta G^{\mathbf{mut}}$ for each mutation in PagP. Energies are only listed for contributions > 0.1 REU to the $\Delta\Delta G_{\text{mut}}$.

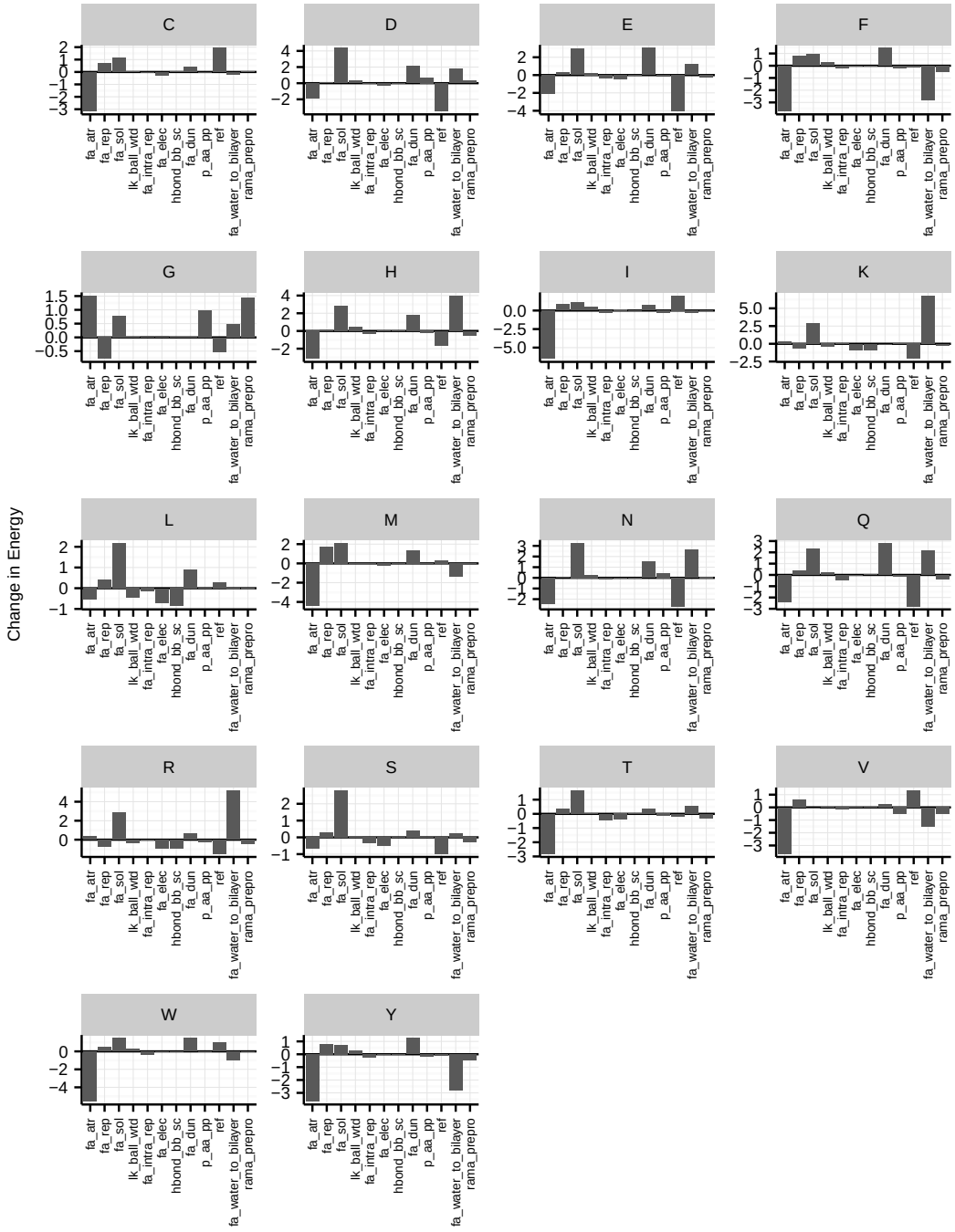

Figure 2.12: Contributions of M19 component energies to the $\Delta\Delta G^{\mathbf{mut}}$ for each mutation in PagP. Energies are only listed for contributions > 0.1 REU to the $\Delta\Delta G_{\text{mut}}$.

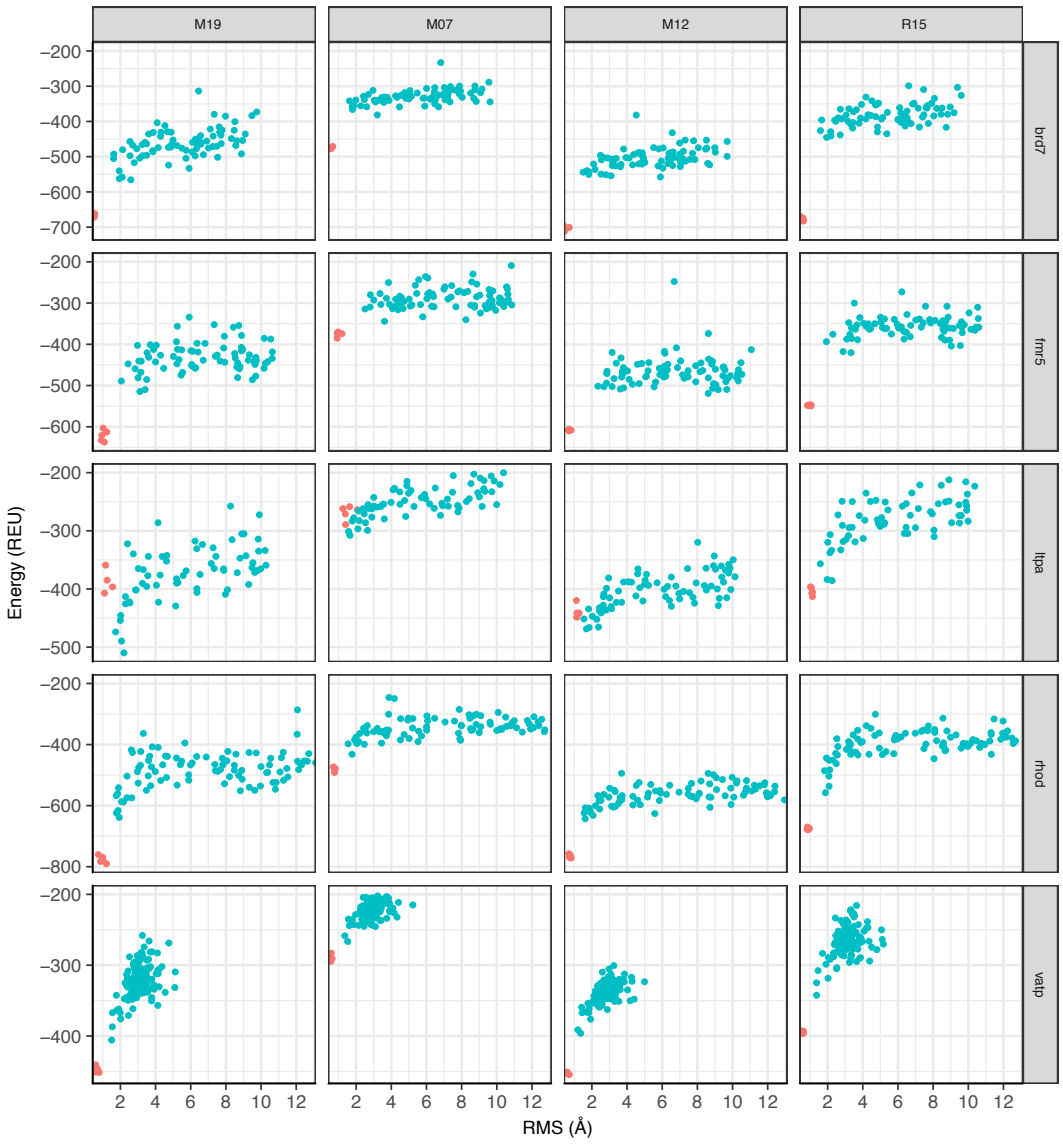

Figure 2.13: Discrimination of candidate conformations from the native crystal structure. Each panel is a plot of the score in Rosetta energy units (REU) vs. the root-mean-squared-deviation between the C_α coordinates of the model and native crystal structure. The refined decoy models are shown in blue and the refined natives are shown in pink.

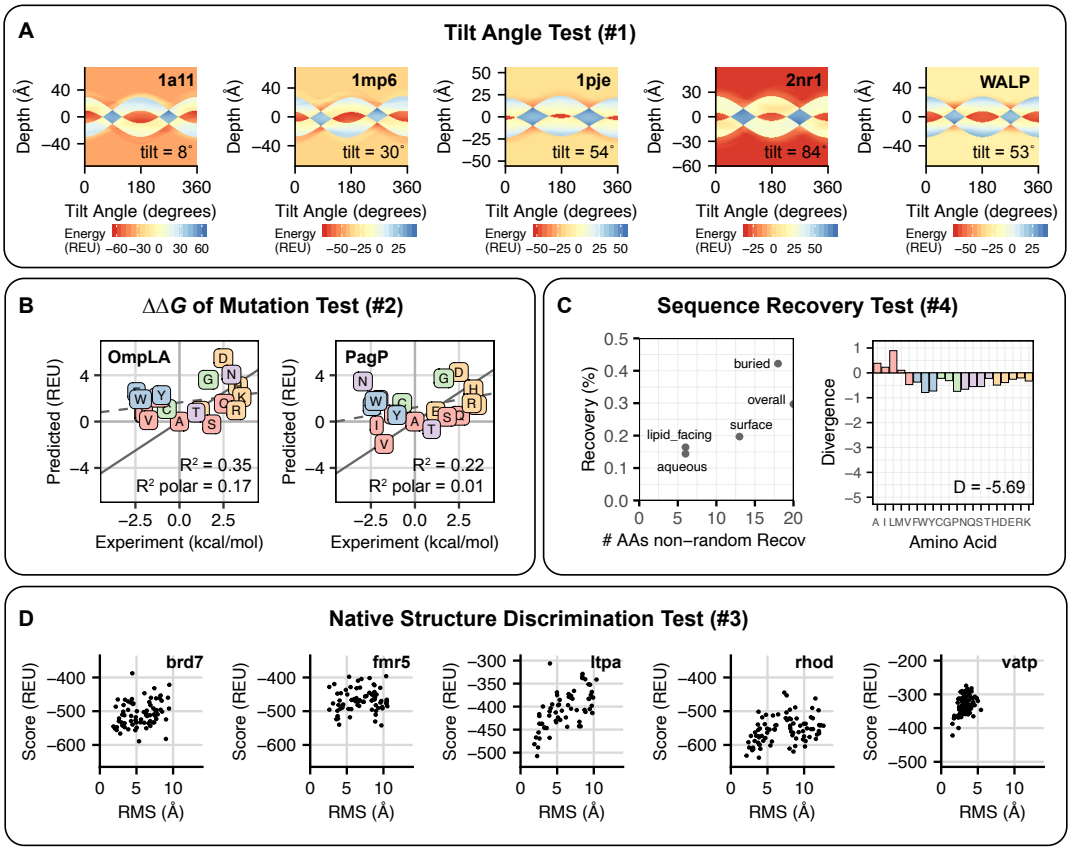

Figure 2.14: Performance of the Weinstein energy function (ref15_memb) on four scientific benchmarks. (A) *Tilt angle test* - Mapping of protein orientation to energies for five target peptides: 1a11, 1mp6, 1pje, 2nr1, and WALP23. The minimum energy peptide tilt angle is annotated in the bottom right corner of each panel. (B) $\Delta\Delta G$ *of mutation test* - Comparison between experimentally measured and predicted values for mutations in OmpLA and PagP. For both correlation plots, proline is not shown due to steric clashes resulting in large energies. The dotted gray line is the line of best fit and the solid gray line is $y = x$. In addition, amino acids are colored according to the following categories: charged (orange), nonpolar (red), aromatic (blue), polar (purple), special case (green). (C) *Sequence recovery test* - The left panel ranks the performance of ref15_memb by two metrics: the fraction of all amino acids recovered on the y-axis and the fraction of amino acid types with individual recovery rates greater than 0.05 on the x-axis. Each point represents a different subset of amino acids. The right panel shows the Kullback-Leibler (KL) divergence of the amino acid distribution of the designed protiens relative to the distribution in native membrane proteins. Values are given on a logarithmic scale and the bars are colored according to same scale in (B). (D) *Decoy discrimination test* - Ranking of models by total score in Rosetta Energy Units (REU) and root-mean-squared-deviation (RMS) from the Cα coordinates of the native crystal structure.

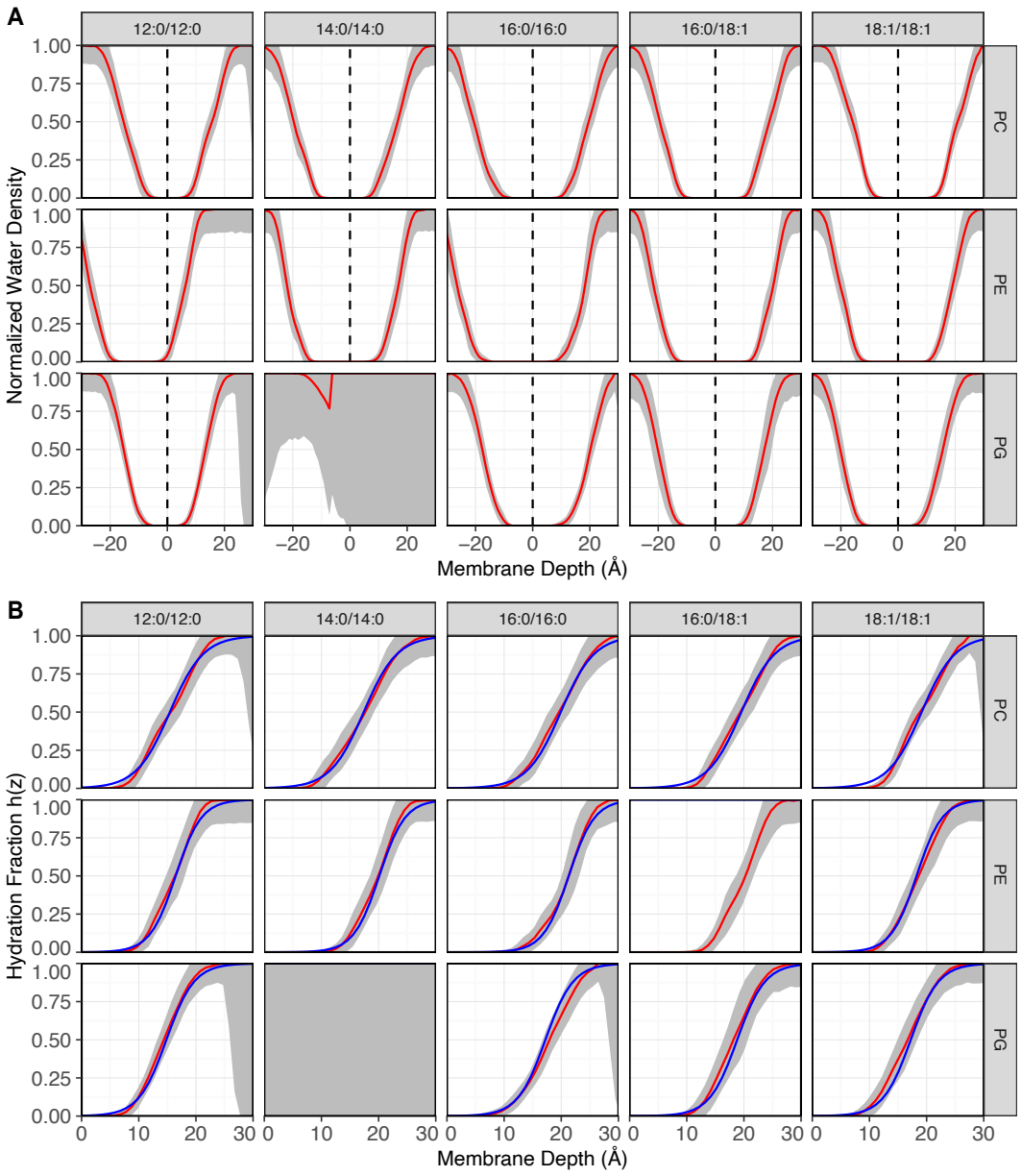

Figure 2.15: Numeric and analytic profiles of depth-dependent water density for 15 lipid compositions. (A) The raw time-averaged water density for 15 different lipid compositions is shown in red and the standard deviation across time steps is shaded in gray. Note that for DMPG lipids, the bilayer is in the liquid-crystalline phase [100]. As a result, it does not form a cohesive bilayer, resulting in high error rates when estimating the fractional hydration. (B) The raw histograms were centered at $z = 0$ and fitted to a logistic function (see Main Text eq. 1). The re-centered raw histogram is shown in red and the analytic fit is shown in blue.

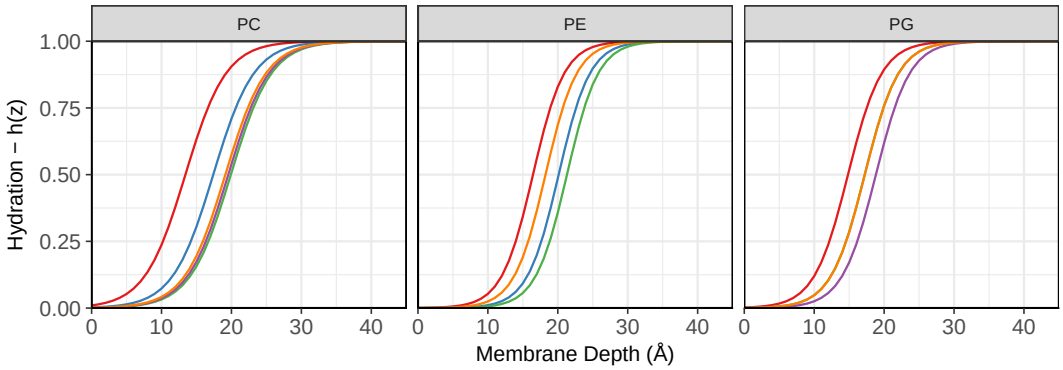

Figure 2.16: Hydration profiles along the membrane normal for simulated phospholipid bilayers at physiological temperature. Each profile is colored by acyl chain type with 12:0/12:0 in red, 14:0/14:0 in blue, 16:0/16:0 in green, 18:1/18:1 in purple, and 16:0/18:1 in orange. For each lipid composition, membrane thickness increases with increasing acyl chain length. The exception is for 16:0/18:1 where the degree of saturation makes the chains more rigid and thins the bilayer.

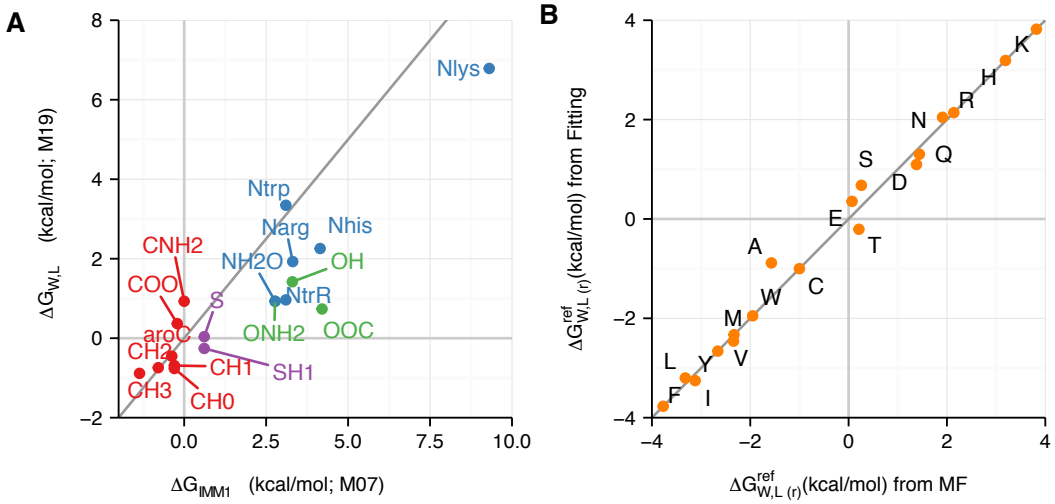

Figure 2.17: Comparison of derived per-atom transfer energies for *franklin2019* with prior computational models (M07/IMM1) and experimental measurements. (A) Comparison of derived per-atom transfer energies with values from the Implicit Membrane Model 1. Carbon atom types are in red, nitrogen in blue, oxygen in green, and sulfur in purple. The mean absolute error (MAE) between IMM1 and derived values is 1.20 kcal/mol. (B) Comparison of calculated per-residue transfer energies with experimental values from Moon & Fleming. The MAE between calculated and experimental values is 0.15 kcal/mol.

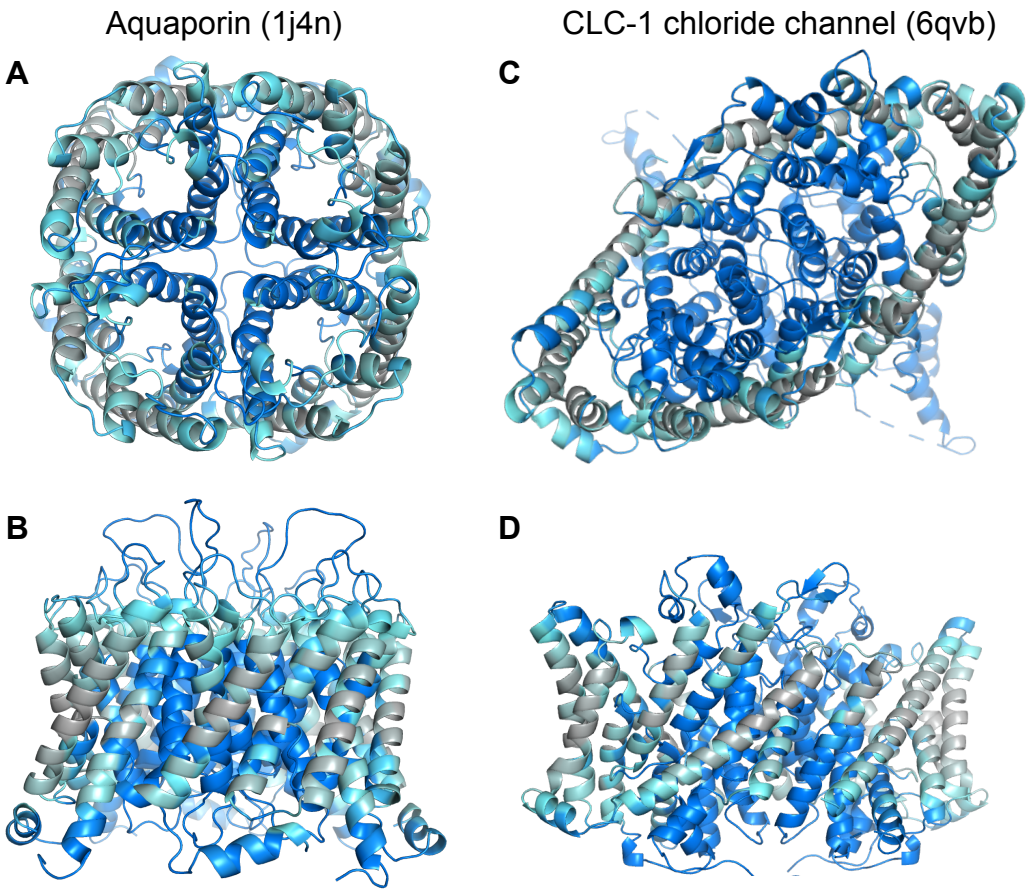

Figure 2.18: Example calculations for a protein with multiple pores and a protein with ellipsoidal architecture. The pore geometry is illustrated by coloring each side chain by implicit solvent phase. The water phase is shown in blue, the interface is in teal, and lipid exposed positions are in gray. Panels (A) and (B) show a top and membrane view of the aquaporin-1 channel (1j4n). Aquaporin-1 is a tetramer with four pores. Panels (C) and (D) show a top and membrane view of the CLC-1 chloride channel (6qvb) which has an elliptical architecture.

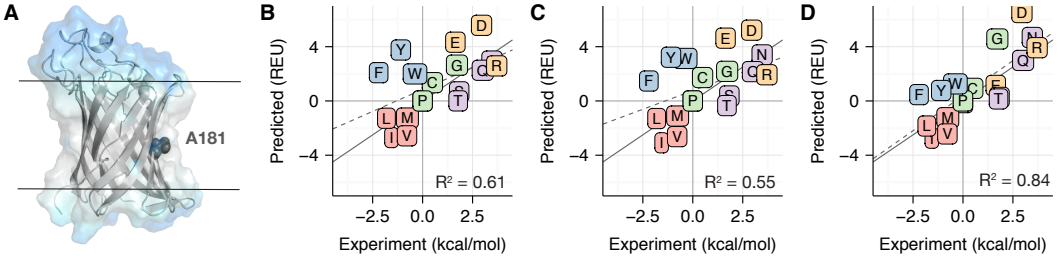

Figure 2.19: Comparison between computationally predicted and experimentally measured $\Delta\Delta G_{\mathbf{mut}}$ values in OmpLA. The experimental values were measured by [99]. For all correlation plots (B-D), proline is not shown due to steric clashes resulting in a large $\Delta\Delta G_{\text{mut}}$ value. The dotted gray line is the line of best fit and the solid gray line is $y = x$. Amino acids are colored according to the following categories: charged (orange), nonpolar (red), aromatic (blue), polar (purple), special case (green). (A) Structure of the OmpLA scaffold (PDB 1qd6) with the mutation site A181 highlighted in dark grey. The implicit solvent phases are colored in a similar manner to Fig. 1 (Main Text). The $\Delta\Delta G_{\text{mut}}$ predictions for mutations in OmpLA by M07, M12, and M19 are shown in panels B, C, and D respectively.

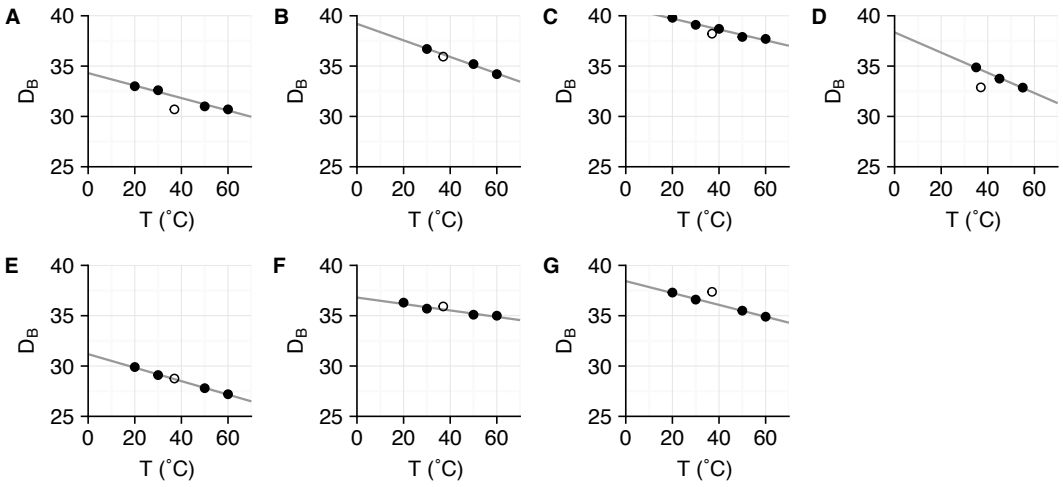

Figure 2.20: Comparison of the membrane thickness computed from simulated water density and measured by X-Ray and neutron scattering experiment. The measurements were taken by Kucerka *et al.* [108, 146, 147] and Jambeck *et al.* [148]. Measured thicknesses are represented by filled circles and thicknesses computed from molecular dynamics trajectories are represented by open circles. The solid line is the line of best fit through the measured values. (A) DLPC (B) DMPC (C) POPC (D) DLPE (E) DLPG (F) DOPG (G) POPG. The calculated values closely follow the thickness vs. temperature trend for each lipid composition.

2.6.7 Supplemental Tables

Table 2.2: Full names of lipid types and abbreviations

Lipid	Full Name	Head Group
DLPC	1,2-dilauroyl-sn-glycero-3-phosphocholine	PC
DMPC	1,2-dimyristoyl-sn-glycero-3-phosphocholine	PC
DOPC	1,2-dioleoyl-sn-glycero-3-phosphocholine	PC
DPPC	1,2-dipalmitoyl-sn-glycero-3-phosphocholine	PC
POPC	1-palmitoyl-2-oleoyl-glycero-3-phosphocholine	PC
DLPE	1,2-dilauroyl-sn-glycero-3-phosphoethanolamine	PE
DMPE	1,2-dimyristoyl-sn-glycero-3-phosphoethanolamine	PE
DOPE	1,2-dioleoyl-sn-glycero-3-phosphoethanolamine	PE
DPPE	1,2-dipalmitoyl-sn-glycero-3-phosphoethanolamine	PE
POPE	1-palmitoyl-2-oleoyl-sn-glycero-3-phosphoethanolamine	PE
DLPG	1,2-dilauroyl-sn-glycero-3-phospho-(1'-rac-glycerol)	PG
DMPG	1,2-dimyristoyl-sn-glycero-3-phospho-(1'-rac-glycerol)	PG
DOPG	1,2-dioleoyl-sn-glycero-3-phospho-(1'-rac-glycerol)	PG
DPPG	1,2-dipalmitoyl-sn-glycero-3-phospho-(1'-rac-glycerol)	PG
POPG	1-palmitoyl-2-oleoyl-sn-glycero-3-phospho-(1'-rac-glycerol)	PG

Table 2.3: Water density parameters fit from all-atom molecular dynamics

Lipid Type	Chain	Thickness (t)	Pseudo Thk (τ)	Steepness (s)	Temp (°C)
DLPC	12:0/12:0	15.35	199.57	0.343	37
DLPE	12:0/12:0	16.45	1538.31	0.446	37
DLPG	12:0/12:0	14.38	457.67	0.413	37
DMPC	14:0/14:0	17.97	390.54	0.343	37
DMPE	14:0/14:0	19.26	7906.16	0.446	37
DOPC	18:1/18:1	18.64	707.00	0.343	37
DOPE	18:1/18:1	19.61	3419.03	0.446	37
DOPG	18:1/18:1	17.97	1233.72	0.413	37
DPPC	16:0/16:0	20.03	925.15	0.343	37
DPPE	16:0/16:0	22.11	13436.10	0.446	37
DPPG	16:0/16:0	18.92	1229.49	0.413	37
POPC	16:0/18:1	19.10	815.94	0.343	37
POPG	16:0/18:1	18.69	2379.13	0.413	37

Table 2.4: Lowest energy peptide orientation, given by tilt angle (θ) and depth (d)

Target	Exp	**M07** d (Å)	**M07** θ (°)	**M12** d (Å)	**M12** θ (°)	**M19** d (Å)	**M19** θ (°)
1a11	11	-20	87	1	3	4	26
1mp6	37	-19	76	0	24	2	43
2nr1	40	-60	33	19	59	-7	42
1pje	16	8	66	-6	19	-1	18
WALP23	25	1	2	0	18	-2	32

Table 2.5: Experimentally measured and predicted $\Delta\Delta G^{mut}$ values in PagP

Mutation	$\Delta\Delta G^{mut}_{exp}$ (kcal/mol) [113]	$\Delta\Delta G^{mut}_{M07}$ (REU)	$\Delta\Delta G^{mut}_{M12}$ (REU)	$\Delta\Delta G^{mut}_{M19}$ (REU)
A	0	0	-0.017	0
C	-0.72	1.49	1.30	0.53
D	2.49	5.17	5.37	3.91
E	1.18	4.00	4.34	0.37
F	-2.44	-0.89	-1.91	-4.03
G	1.64	2.14	2.32	4.00
H	3.32	3.38	2.34	3.44
I	-2.17	-1.80	-1.92	-1.97
K	3.54	3.07	2.03	4.65
L	-2.01	-0.50	-1.41	0.91
M	-1.15	-1.54	-1.78	-0.89
N	-2.95	2.94	3.40	3.00
P	3.82	216.14	215.09	168.83
Q	2.54	1.76	1.49	1.73
R	3.22	2.73	0.45	4.02
S	1.83	1.35	0.92	0.96
T	0.95	0.14	-0.25	-1.34
V	-1.75	-1.95	-1.00	-4.20
W	-2.21	-0.59	-2.39	-2.39
Y	-1.02	0.36	-0.56	-4.35

Table 2.6: Rosetta atom types

Atom Type	Description
CH0	carbon with no hydrogens
CH2	carbon with two hydrogens
CH1	carbon with one hydrogen
CH3	methyl carbon
CNH2	Glu amine carbon
COO	carbonyl carbon
S	sulfur
SH1	sulfur with one hydrogen
aroC	aromatic carbon
Nhis	His nitrogen
Ntrp	Trp and HIs nitrogen
Nlys	Lys nitrogen
NH2O	Glu amine nitrogen
Narg	arginine nitrogen
NtrR	Trp secondary nitrogen
ONH2	Glu amine oxygen
OOC	carbonyl oxygen
OH	hydroxyl oxygen

Table 2.7: Constraint equations for water-to-bilayer transfer energy fit.

Amino Acid	Equation
A	x_{CH3}
C	$x_{\mathrm{CH2}} + x_{\mathrm{SH1}}$
D	$x_{\mathrm{CH2}} + x_{\mathrm{COO}} + 2x_{\mathrm{OOC}}$
E	$2x_{\mathrm{CH2}} + x_{\mathrm{COO}} + 2x_{\mathrm{OOC}}$
F	$x_{\mathrm{CH0}} + x_{\mathrm{CH2}} + 5x_{\mathrm{aroC}}$
G	–
H	$x_{\mathrm{CH0}} + x_{\mathrm{CH2}} + 2x_{\mathrm{aroC}} + x_{\mathrm{Nhis}} + x_{\mathrm{Ntrp}}$
I	$2x_{\mathrm{CH3}} + 2x_{\mathrm{CH2}}$
K	$4x_{\mathrm{CH2}} + x_{\mathrm{Nlys}}$
L	$2x_{\mathrm{CH3}} + x_{\mathrm{CH2}} + x_{\mathrm{CH1}}$
M	$x_{\mathrm{CH3}} + 2x_{\mathrm{CH2}} + x_{\mathrm{S}}$
N	$x_{\mathrm{CH2}} + x_{\mathrm{ONH2}} + x_{\mathrm{CNH2}} + x_{\mathrm{NH2O}}$
P	$x_{\mathrm{Npro}} + 3x_{\mathrm{CH2}}$
Q	$2x_{\mathrm{CH2}} + x_{\mathrm{ONH2}} + x_{\mathrm{CNH2}} + x_{\mathrm{NH2O}}$
R	$3x_{\mathrm{CH2}} + x_{\mathrm{aroC}} + 2x_{\mathrm{Narg}} + x_{\mathrm{NtrR}}$
S	$x_{\mathrm{CH2}} + x_{\mathrm{OH}}$
T	$x_{\mathrm{CH3}} + x_{\mathrm{CH2}} + x_{\mathrm{OH}}$
V	$2x_{\mathrm{CH3}} + x_{\mathrm{CH1}}$
W	$3x_{\mathrm{CH0}} + x_{\mathrm{CH2}} + 5x_{\mathrm{aroC}} + x_{\mathrm{Ntrp}}$
Y	$2x_{\mathrm{CH0}} + x_{\mathrm{CH2}} + 4x_{\mathrm{aroC}} + x_{\mathrm{OH}}$

Table 2.8: Per-atom water-to-bilayer transfer energies, $\Delta G^{\mathrm{atom}}_{\mathrm{w,l}}$

Atom Type	$\Delta G_{\mathrm{w,l}}$, kcal/mol	ΔG_{IMM1}, kcal/mol
CH0	-0.7625	-0.3
CH2	-0.7418	-0.791
CH1	-0.6889	-0.3
CH3	-1.362	-0.3
CNH2	0.9292	0
COO	0.3675	-0.211
S	0.0386	0.612
SH1	-0.2582	0.612
aroC	-0.4532	-0.378
Nhis	2.2556	4.147
Ntrp	3.3449	3.102
Nlys	6.7870	9.305
NH2O	0.9292	2.773
Narg	1.9274	3.311
NtrR	0.9637	3.102
ONH2	0.9292	2.773
OOC	0.7351	4.206
OH	1.4193	3.3

Table 2.9: Residuals for predicted $\Delta\Delta G^{mut}$ values in OmpLA

Mutation	M07 (REU)	M12 (REU)	M19 (REU)
A	0.00	0.01	0.00
C	1.57	1.43	0.88
D	1.90	2.04	1.00
E	2.00	2.23	0.58
F	1.10	0.37	1.12
G	0.35	0.48	1.67
H	0.04	0.69	0.09
I	0.26	0.18	0.14
K	0.33	1.07	0.79
L	1.07	0.43	2.07
M	0.28	0.46	0.18
N	4.09	3.86	4.21
P	–	–	–
Q	0.55	0.75	0.58
R	0.35	1.96	0.56
S	0.34	0.65	0.62
T	0.58	0.85	1.62
V	0.14	0.53	1.73
W	1.15	0.13	0.13
Y	0.98	0.33	2.36

Table 2.10: Weights for membrane energy functions based on `score_12`

Energy Term	Description	M07 [63]	M12 [111]
`fa_atr`	van der Waals attractive energy	0.78	0.8
`fa_rep`	Repulsive energy	0.43	0.44
`fa_intra_rep`	Intra-residue repulsive energy	0.004	0.004
`fa_pair`	Statistical residue-pair interaction energy	0.48	0.49
`fa_dun`	Knowledge-based rotamer energy	0.56	0.56
`fa_mpsolv`	Lazaridis IMM1 membrane solvation energy	0.60	0.35
`fa_mpenv`	Lazaridis IMM1 membrane environment energy	0.48	0.3
`fa_mpenv_smooth`	Knowledge-based membrane environment energy	0	0.5
`ref`	Amino acid reference energy	1.0	1.0
`hbond_lr_bb`	Long-range backbone hydrogen bond energy	1.16	1.17
`hbond_sr_bb`	Short-range backbone hydrogen bond energy	1.16	1.17
`hbond_bb_sc`	Backbone to side-chain hydrogen bond energy	1.16	2.34
`hbond_sc`	Side-chain to side-chain hydrogen bond energy	1.1	2.2
`p_aa_pp`	ϕ, ψ-dependent amino acid propensity	0.64	0.32
`dslf_ss_dst`	Disulfide bonding energy for S-S distance	0.5	0.5
`dslf_cs_ang`	Disulfide bond energy for CSS angle	2	2
`dslf_ss_dih`	Disulfide bond energy for SS dihedral	5	5
`dslf_ca_dih`	Disulfide bond energy for CC dihedral	5	5
`pro_close`	Proline closure energy	1.0	1.0
`rama`	Rakmachandran energy	0.2	0.2
`omega`	ω torsion energy	0.5	0.5

Table 2.11: Weights for membrane energy functions based on `ref2015`

Energy Term	Description	R15 [60, 61]	M19
`fa_atr`	van der Waals attractive energy	1.0	1.0
`fa_rep`	Repulsive energy	0.55	0.55
`fa_sol`	Lazaridis-Karplus solvation energy	1.0	1.0
`fa_intra_sol_xover4`	Intra-residue solvation energy	1.0	1.0
`lk_ball_wtd`	Orientation-dependent solvation energy	1.0	1.0
`fa_intra_rep`	Intra-residue repulsive energy	0.005	0.005
`fa_elec`	Coulomb electrostatics energy	1.0	1.0
`pro_close`	Proline closure energy	1.25	1.25
`fa_dun`	Knowledge-based rotamer energy	0.56	0.56
`hbond_lr_bb`	Long-range backbone hydrogen bond energy	1.0	1.0
`hbond_sr_bb`	Short-range backbone hydrogen bond energy	1.0	1.0
`hbond_bb_sc`	Backbone to side chain hydrogen bond energy	1.0	1.0
`hbond_sc`	Side chain to side chain hydrogen bond energy	1.0	1.0
`dslf_fa13`	Disulfide bonding energy	1.25	1.25
`rama_prepro`	Ramachandran energy	0.45	0.45
`omega`	ω torsion energy	0.5	0.5
`p_aa_pp`	ϕ, ψ-dependent amino acid propensity	0.6	0.6
`fa_dun`	Knowledge-based rotamer energy	0.7	0.7
`yhh_planarity`	Tyrosine χ_3 torsion energy	0.625	0.625
`ref`	Amino acid reference energy	1.0	1.0
`fa_water_to_bilayer`	Water-to-bilayer transfer energy	0.0	1.0

Table 2.12: Lipid composition parameters for α-helical peptide energy landscape calculations.

Target	PDB Code	Conditions	Parameters	Ref.
Acetylcholine M2 segment	1a11	DPC micelles	DLPC, 20°C	[149]
Influenza A M2 channel	1mp6	DMPC vesicles	DMPC, 30°C	[150]
VPU-forming domain HIV-1	1pje	DOPC:DOPG 9:1	DOPC, 30°C	[151]
NMDA receptor segment	2nr1	DPC micelles	DLPC, 20°C	[149]
WALP23	NA	DOPC	DOPC, 30°C	[112, 152]

Chapter 3

Diverse scientific benchmarks for implicit membrane energy functions

This chapter contains material that will be submitted to the *Journal of Chemical Theory and Computation*. If accepted and published, then this chapter will contain material that is reproduced with permission of the American Chemical Society, as per the statement of author rights.

3.1 Overview

Energy functions are fundamental to biomolecular modeling. Their success depends on robust physical formalisms, efficient optimization, and high-resolution data for training and validation. Over the past 20 years, progress in each area has advanced soluble protein energy functions. Yet, energy functions for membrane proteins lag behind due to sparse and low-quality data, leading to overfit tools. To overcome this challenge, we assembled a suite of 12 tests on independent datasets varying in size, diversity, and resolution. The tests probe an energy function's ability to capture membrane protein orientation, stability, sequence, and structure. In this chapter, we

present the tests and use the *franklin2019* energy function to demonstrate them. We then present a vision for transforming these "small" datasets into "big data" that can be used for more sophisticated energy function optimization. The tests are available through the Rosetta Benchmark Server (https://benchmark.graylab.jhu.edu/) and GitHub (https://github.com/rfalford12/Implicit-Membrane-Energy-Function-Benchmark).

3.2 Introduction

Accurate energy functions are critical for biomolecular structure prediction and design. Through physical, empirical, and statistical models of intermolecular interactions, these functions discriminate near-native from non-native conformations and optimize sequences to stabilize structures. Over the past 20 years, an influx of high quality structural data paired with new optimization tools have boosted the accuracy of soluble protein energy functions [61]. A remaining task is to improve energy functions for membrane proteins, a class of molecules that constitutes 30% of all proteins [68] and targets for over 50% of drugs [3].

The heterogeneous lipid bilayer introduces several challenges for membrane protein energy function development. Biomolecular modeling tasks such as docking and design require benchmarking with both thermodynamic data and macromolecular structures. Yet, difficulties in over-expression and purification of membrane proteins have limited the quality and quantity of experimental validation data [153]. For instance, membrane proteins represent less than 2% of structures in the Protein Databank [154] and less than 1% of entries in ProTherm [155]. Additionally, biomolecular modeling programs accelerate calculations with implicit membrane models that

represent the solvent as a continuous medium. This choice obfuscates the comparison between predictions and experimental data measured in a real lipid bilayer.

As a consequence, many membrane protein energy functions are trained for a single task on a small dataset. This strategy has been applied to various membrane protein modeling tools including estimating the $\Delta\Delta G$ of mutation [139], hydrophobic thickness [132], native structure discrimination [114, 138], refinement [156], protein design [140], symmetry [157], and protein-protein docking [158, 159]. These tools enabled a decade of membrane protein modeling; however, their generalizability is unclear. Small quantities of data prevent cross-validation [160]: a technique that ensures performance on targets that are different from the training set. Further, small datasets may be feature-poor. For example, a set of membrane proteins may only contain transmembrane domains and exclude juxta-membrane domains important for function.

Recent advances have enabled energy function development with up to four training and testing sets. In the Rosetta community, this includes two new implicit membrane energy functions. The first model, developed by Weinstein *et al.* [118], was fit to transfer free energies from the dSTβL assay [119] and tested on datasets describing the folding and thermodynamics of single-span dimers. The second model is *franklin2019* [161], our "biologically realistic" implicit membrane model that permits use of parameters for different lipid compositions. This model was fit with the Moon & Fleming hydrophobicity scale [99] and evaluated on four tests describing α-helical and β-barrel membrane proteins with complex topologies. Interestingly, Weinstein *et al.* reported excellent performance on homo-dimers of single transmembrane segments; however, the same model underperformed on our tests. This outcome

demonstrates another important complication in this area: developers use different criteria to evaluate membrane protein energy functions, resulting in ambiguity in performance.

For soluble proteins, these challenges are addressed by using multiple large, qualitatively and quantitatively diverse datasets that aim to fully describe the biomolecular system [116]. For example, inclusion of both small-molecule thermodynamic data along with macromolecule structures from X-Ray crystallography and NMR spectroscopy resulted in significant improvements to Lennard-Jones, electrostatic, and solvation parameters in the Rosetta soluble protein energy function [60]. The CHARMM force field is parameterized with a large collection of biophysical data [162]. The Open Force Field project integrated multiple data sources with a Bayesian statistical framework to improve atom typing [163]. It would be ideal to apply a similar solution for membrane proteins. The closest examples involve parameterization of an anisotropic model for orientation prediction with free energy calculations [164] and explicit lipid force fields for molecular dynamics with a combination of quantum mechanical calculations and experimental thermodynamic data [77]. However, these examples do not yet incorporate benchmarks on macromolecule structures. Further, for membrane proteins there are only multiple small and non-diverse datasets that partially describe the system.

The goal of this work was to overcome this validation challenge by developing a set of sparse and diverse scientific benchmarks for evaluating membrane protein energy functions. We created tests that probe four areas of the membrane protein energy landscape: (1) protein orientation in the bilayer, (2) stability, (3) sequence, and (4) complete structures. The tests rely on a mixture of datasets that range in both size

and quality, resulting in overall feature-rich optimization targets. Importantly, the tests are fast to evaluate to enable multiple iterations for optimization protocols. As a demonstration, we applied the scientific benchmarks to evaluate the accuracy of the *franklin2019* energy function. The tests identified energy function strengths and imperative areas for optimization. These optimization imperatives lay the groundwork for future energy function development and potentially enable use of more sophisticated optimization tools such as deep learning.

3.3 Results

To evaluate implicit membrane energy functions, we developed a set of 12 scientific benchmark tests (Table 3.1) In the following sections, we present each test and demonstrate the analysis with *franklin2019*, a current Rosetta implicit membrane energy function.

3.3.1 Test #1: Orientation of transmembrane peptides

Membrane proteins occupy precise orientations in the lipid bilayer to perform their biological functions. Thus, a key challenge for energy functions is to recapitulate this position during structure prediction and design. This first test verifies that the most stable computed orientation of a transmembrane peptide corresponds to the native orientation. This test is the cornerstone of our benchmark because it was used for validation of early implicit membrane models [64, 89]. Here, the native orientation is defined as the tilt angle measured by solid-state NMR spectroscopy in the context of oriented lipid bilayers [168].

To predict orientation, we developed a protocol to sample all possible orientations

Table 3.1: Membrane protein energy function benchmarks

Test	#	Experiment	Data Ref.
Protein orientation in the bilayer			
Transmembrane peptide tilt angle	1	ssNMR	[47]
Surface-adsorbed peptide rotation angle	2	ssNMR	[47]
Protein tilt & depth	3	PPM Server	[132]
Hydrophobic length	4	PPM Server	[132]
Protein stability			
$\Delta G_{w,l}$ at constant pH	5	Translocon	[165]
$\Delta\Delta G_{w,l}$ with pH shift	6	Trp	[166]
$\Delta\Delta G^{mut}$	7	Trp	[99, 113, 121]
Design			
Sequence recovery	8	X-Ray	[117]
Depth-dependent side chain distribution	9	X-Ray	[117]
Native structure features			
Decoy discrimination	10	X-Ray	[114]
Helix kink identification	11	X-Ray	[167]
Protein-protein interface prediction	12	X-Ray	[158, 159]

of the peptide relative to the implicit membrane within $\pm$ 60 Å of the bilayer center and tilt angles between $\pm$180°(see SI Appendix). The global energy minimum of all sampled positions is defined as the most stable predicted orientation for comparison to the experimental measurements. More generally, based on our biophysical intuition and the observation that transmembrane peptides typically prefer tilt angles between 0-45°, we expect those tilt angles and depths that span the membrane to be lower in energy relative to the aqueous phase or interface.

Dataset. The test set contains seven peptides with a single transmembrane domain (Table 3.4). The first four peptides are segments of biological membrane proteins from Ulmschneider *et al.* [47]. The fifth peptide is the designed WALP23 peptide [112]. Their tilt angles were measured in different lipid compositions including DPC micelles [149], DMPC vesicles [150], mixed DOPC:DOPG bilayers [151], and pure DOPC bilayers [112]. While the experimental uncertainty is not available for all measurements [47],

tilt angle measurements have a typical error range of ± 3-5°. In addition, to evaluate the preference of aromatic side chains for the membrane interface, we added to the set two designed poly-alanine helices with flanking tryptophan and tyrosine residues [120, 169]. Orientations have not been measured for these peptides, but predictions can still be compared to biophysical intuition.

Demonstration & Assessment. Test results with *franklin2019* are shown for a biological and a designed transmembrane peptide in Fig. 3.1a and 3.1b, respectively. The remaining results are shown in Fig. 3.9 and 3.10. We rated performance according to how many predictions fall within ± 10° of the measured value, a little more than the usual experimental error since some cases do not have reported errors.

As previously reported (Fig. 1 in Alford *et al.* [161]), *franklin2019* predicts the tilt angles of WALP and three of four biological peptides within 10°. For the poly-alanine aromatic-flanked peptides, the minimum energy occurs at a low energy tilt angle between 10-20°, which would reasonably expose the aromatic side chains to the aqueous solvent.

3.3.2 Test #2: Orientation of membrane surface adsorbed peptides

Many proteins perform their functions by binding to the membrane surface at a specific orientation. This test verifies that the most stable surface-adsorbed peptide orientation corresponds to the native orientation. We define the native orientation by the rotation of the peptide relative to the helix axis and a specific membrane depth. Similar to **Test #1**, we sampled all pairs of membrane depths and rotation angles (SI Appendix).

Dataset. The dataset includes seven biological peptides [47] and the designed

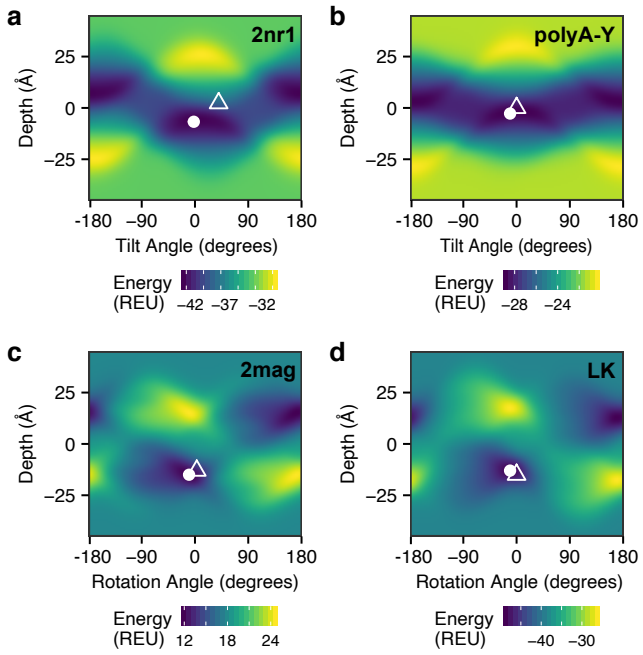

Figure 3.1: Implicit potentials capture the orientation of membrane associated-peptides with biological and designed sequences. A mapping between all sampled orientations and energies for (a) nicotinic acetylcholine receptor segment (b) poly-alanine trp-flanked peptide, (c) magainin, and (d) leucine-lysine repeat peptide. Tilt or rotation angle is on the x-axis and depth relative to the bilayer center is on the y-axis. Each grid point represents a 1 Å and 1°and is colored by *franklin2019* energy, with low (favorable) energies in dark blue and high energies in yellow. The predicted lowest energy orientation is shown as a white circle, and where applicable the experimentally measured orientation is shown as an open triangle.

leucine-lysine (LK) repeat peptide [170] (Table 3.5). The experimental reference data are rotation angles measured by solution NMR in dodecylphosphocholine micelles or trifluoroethanol [171]. In the experiment, rotation angles are reported with an uncertainty of $\pm$ 6-12°[47].

Demonstration & Assessment. The mapping of orientations to energies for magainin and the LK repeat peptide calculated in an assumed DLPC bilayer are shown in Fig. 3.1c and Fig. 3.1d, respectively. The remaining targets are shown in Fig. 3.11. We rated performance according to how many predictions fall within the maximum experimental uncertainty across all of the measurements, i.e., 12°.

Fig. 3.1c-d and Fig. 3.11 show the energy landscapes with the predicted low-energy orientation (white circle) overlaying the measured value (white triangle). The landscapes reveal a repeating pattern of high energy (yellow) and low energy patches (dark blue) near the membrane interfaces ($\pm$ 18-23 Å). This pattern matches the biophysical intuition that the non-polar side of amphipathic peptides is more compatible with the membrane surface than aqueous solvent. Where experimentally measured values are available, the *franklin2019* energy function calculated rotation angles within $\pm$ 12° of the native value for all of the surface-adsorbed peptides where experimentally measured values are available.

3.3.3 Test #3: Orientation of multi-pass α-helical and β-barrel proteins

Accurately predicting peptide tilt angle is an important step toward predicting membrane protein orientation; yet, most membrane proteins have multiple transmembrane segments. Here, we examine how implicit membrane energy functions recapitulate the orientations of α-helical and β-barrel protein domains with complex topologies.

We sample protein orientations (Fig. 3.2a-c) using the protocol described in **Test #1**. Then, because this data set is larger, we summarize the difference between the reference and calculated values across the set by computing the cumulative distribution of residuals.

Dataset This test set was curated by Dutagaci & Feig [132] and includes 18 α-helical and 17 β-barrel proteins (Table 3.7). In the dataset, 60% of proteins reside in the *E. coli* outer membrane and 14% reside in the eukaryotic plasma membrane. The remaining 26% reside in either the mitochondria inner membrane, archea, or the *E. coli* inner membrane.

The most challenging step of this test is choosing reference data. There are various methods for identifying protein tilt angles and penetration depths in lipid bilayers or detergents including chemical modification, spin labeling, NMR, X-Ray scattering, and electron cryo-microscopy [172]. The data vary in quality and have different assumptions and error sources. For this reason, the current gold-standard data source is the Orientations of Proteins in Membranes database of membrane protein structures positioned in a 1,2-dioleoyl-sn-glycero-3-phosphocholine (DOPC) bilayer (OPM [117]). OPM computes the spatial position of a membrane protein using PPM; a method that combines an all-atom representation of the protein, an anisotropic model of the lipid bilayer, and a universal solvation model. The final orientation is determined by minimizing the water-to-bilayer transfer energy, which is computed as a sum of van der Waals, electrostatics, and hydrogen bonding energies [164]. Using uncertainties from multiple original experiments, the estimated accuracy of OPM reference data is $\pm 10°$ for tilt angle and ± 2.5 Å for depth [172].

Demonstration & Assessment. Membrane protein orientations predicted by

franklin2019 in a DOPC bilayer are given in Fig. 3.2d-e and the cumulative distribution of residuals is shown in Fig. 3.2g-h. We rated performance by the number of predictions that fall within the maximum uncertainty ranges of $\pm$ 10° for tilt angle and $\pm$ 2.5 Å for depth. For α-helical proteins, protein depth was correctly predicted for 62.5% of targets. In contrast, predictions were correct for 4% of β-barrel protein targets. Tilt angle prediction was more consistent, with 60% and 70% of protein tilt angles predicted within 10° of the OPM value for α and β proteins respectively. Still, for β-barrel proteins, *franklin2019* predicts several outliers. For example, the predicted tilt angle for the alginate export protein (AlgE, 4afk) was 34°, whereas the OPM predicted value is 3°. The *franklin2019* prediction is likely unrealistic as it buries the pore entry. Overall, the data reveal that *franklin2019* predicts membrane depth more accurately for α-helical proteins than β-barrel proteins.

3.3.4 Test #4: Membrane protein hydrophobic thickness

To overcome unfavorable exposure of non-polar side chains to water, membrane proteins generally have a hydrophobic thickness compatible with the bilayer thickness. Thus, hydrophobic thickness is an important parameter for predicting orientation and stability. In this test, we predict hydrophobic thickness by placing the protein at its OPM orientation and then iteratively rescoring the protein at membrane thickness values ranging from 10-40 Å (Fig. 3.12). The protein hydrophobic thickness is then defined as the bilayer thickness that minimizes the energy. This test uses parameters for a phosphatidylcholine head group.

Dataset. This test uses the same proteins as **Test #3**. Experimentally, hydrophobic thickness is measured using various techniques that often introduce different assumptions and errors. For instance, the experimentally measured hydrophobic

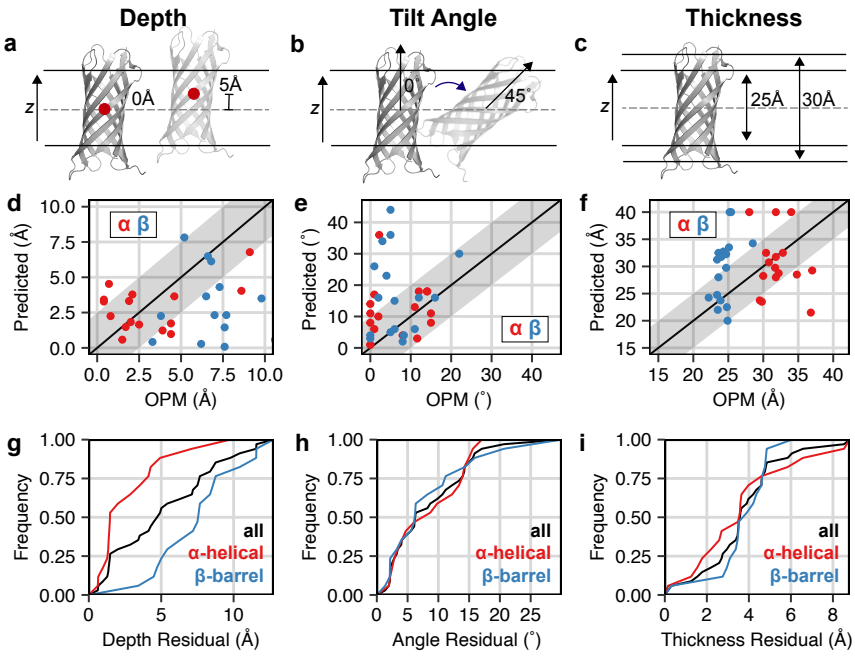

Figure 3.2: Protein orientation predictions of α-helical and β-barrel proteins. Comparison of membrane protein depth (a), tilt angle (b), and hydrophobic length (c) predicted by *franklin2019* relative to values predicted by the OPM anisotropic model [117]. A $y = x$ line is shown in each plot, with a light gray stripe for an error range of 2.5Å, 10° and 5 Å respectively. Targets that are α-helical (β-barrels) are represented as red (blue) points. Cumulative distribution for residuals of (d) membrane protein depth, (e) tilt angle, and (f) hydrophobic thickness. A distribution for all proteins is shown in black, and the distributions for α-helical only and β-barrel only are shown in red and blue respectively. Points at 40 Å indicate that full burial of the protein in the bilayer minimizes the energy.

thickness of OmpX (1qj8) was determined assuming that the protein does not tilt [173]. For this reason, we use predicted hydrophobic thickness values from the OPM database [164] as our gold standard. OPM reports thickness as the bilayer thickness that minimizes the water-to-bilayer transfer energy. The estimated uncertainty for hydrophobic thickness values from OPM is $\pm$ 2.5 Å[172].

Demonstration & Assessment. A comparison of *franklin2019* and OPM is shown in Fig. 3.2f and Fig. 3.2i. The hydrophobic thickness was within 2.5 Å of OPM for only 30% of α-helical proteins and 10% of β-barrel proteins. At 5 Å, accuracy improves for both categories to 75%; however, this threshold is large relative to the thickness differences between varied lipid compositions. For 5 targets, we observed that the energy continued to improve up to the limit of 40 Å. These points are plotted at T=40 Å and indicate that *franklin2019* prefers to completely bury these proteins in the membrane. Overall, prediction of hydrophobic thickness was less reliable than orientation.

To better understand areas for improvement, we examined the outliers in Fig. 3.2f. The most outstanding incorrect prediction is for the bacterial semiSweet transporter (4x5n, Fig. 3.2f). Here, *franklin2019* predicted a hydrophobic thickness value of 21.5 Å whereas OPM predicted a value of 36.8 Å. This suggests error in pore estimation because $franklin$2015 leaves the entry and exit of the pore more exposed than OPM [117]. For five targets, *franklin2019* was unable to find a minimum energy hydrophobic thickness, meaning the minimum was $T = 40$ (the maximum thickness): photosynthetic reaction center (1rzh), potassium channel KcsA (1r3j), opioid delta receptor (4n6h), outer membrane protein A (1qjp), and the hemoglobin binding protease

autotransporter (3aeh). It is less clear why these cases were outliers. Both the photosynthetic reaction center and opioid delta receptor have significant juxta-membrane domains, suggesting *franklin2019*'s implicit membrane interfacial representation may be insufficient to differentiate transmembrane from non-transmembrane segments. Another possibility is that pore estimation further complicates predictions.

3.3.5 Test #5: Stability of transmembrane peptides at neutral pH

In cells, the translocon machinery is responsible for recognizing transmembrane segments and integrating them into the bilayer. Once folded, membrane proteins remain in the bilayer due to a favorable water-to-bilayer transfer free energy. To keep the protein in the membrane, we therefore must accurately estimate the transfer energy from solvent to the bilayer. In **Test #5**, we build on the calculations sapmling all possible peptide orientations from **Test # 1**. Then, we compute the ΔG of insertion as the energy difference between the lowest energy orientation of the peptide in the lipid bilayer phase and in the aqueous phase (see SI Appendix) to compare to experimental insertion energy measurements.

Dataset. The test set includes five poly-leucine peptides designed by Ulmschneider *et al.* [165]. There are four peptides in the set that follow a GL_XRL_XG motif, where $X = 5, 6, 7, 8$ (Table 3.8). The fifth peptide follows a different motif pattern by adding a flanking tryptophan: GWL_6RL_7G. The reference transfer energies are taken from molecular dynamics simulations in POPC bilayers that were validated against intrinsic fluorescence measurements. The experimental uncertainty of the measured ΔG_{ins} values is ± 1.4 kcal mol^{-1}.

Demonstration & Assessment. The *franklin2019* energy function computes the

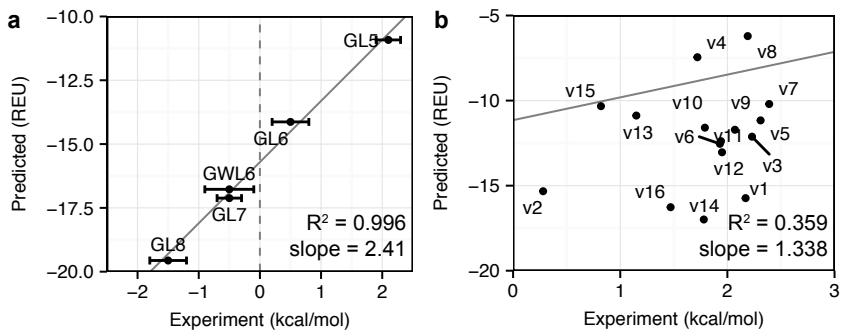

Figure 3.3: Comparison of predicted and experimentally measured peptide insertion energies. (a) Prediction of the $\Delta\Delta G$ of insertion for five designed poly-leucine peptides of varying length and flanking residues from Ulmschneider *et al.* (b) Prediction of the $\Delta\Delta G$ of insertion upon pH shift from pH 8 to 4 for 16 variants of the pH-sensitive low insertion peptide sequence from Weerakkody *et al.* Experimental measurements were taken by intrinsic fluorescence in POPC liposomes and calculations were performed for DLPC.

water-to-bilayer insertion energy using a Gibbs insertion energy approximation. As in many other Rosetta based calculations, we expect this energy function may reproduce trends but not exact values. Thus, we evaluate the ability to reproduce trends using the Pearson correlation coefficient (R^2) between the experimentally measured and predicted values (although as accuracy improves in the future, exact predictions can also be evaluated). In calculating R^2, we use a Grubbs test to eliminate outliers.

A comparison between the *franklin2019* prediction in POPC bilayers and reference ΔG values from molecular dynamics is shown in Fig. 3.3a. Encouragingly, the Pearson correlation coefficient is high (R^2 = 0.996), and no points are outliers. The slope of the best fit line is high (2.41 REU-mol/kcal), revealing that while the relative energies are correct, *franklin2019* overestimates the overall benefit of insertion. Further, the comparison indicates a reference state calibration issue because the ΔG of inserting the GL5 and GL6 peptides is favorable; whereas, the experiment indicates insertion is unfavorable.

3.3.6 Test #6: Stability of transmembrane peptides at acidic pH

The water-to-bilayer transfer energy is influenced by many factors including changing conditions in the intracellular and extracellular environment. Physiologically, extracellular acidity is an important biomarker for tumor growth and development [174]. To benchmark the ability of the energy function to capture pH, we evaluated the prediction of peptide insertion energy when there is a change in pH. The test performs two grid-style searches using the protocol described in **Test #1** with Rosetta-pH [175] to find the best peptide orientation at both pH 4 and 8 (see SI Appendix). Then, the insertion energy difference is computed as the difference between the peptide integrated into the bilayer at pH 4 and in the aqueous phase at pH 8 (i.e., $\Delta\Delta G_{pH,ins} = \Delta G_{ins,pH4} - \Delta G_{ins,pH8}$, see SI Appendix).

Dataset. The test set includes seventeen peptides designed by Weerakkody *et al.* [166] that insert into membranes upon a shift from neutral to acidic pH, called pHLIP peptides (Table 3.9). The reference value is the water-to-bilayer transfer energy measured using titration and fluorescence experiments in the context of POPC liposomes. The experimental uncertainty of the measured $\Delta\Delta G_{\text{pH,ins}}$ values is $\pm 1.0\,\text{kcal mol}^{-1}$.

Demonstration & Assessment. A comparison of the *franklin2019* and experimentally measured values is given in Fig. 3.3b. Similar to **Test #5**, we aim to maximize the Pearson correlation coefficient. In contrast to **Test #5** at neutral pH, the correlation between the experiment and calculation is poor, and the energy function prefers the peptides in solution rather than in the bilayer. There are two areas that we suspect cause gaps in performance. First, the underlying pKa values do not account for the membrane. Second, the *franklin2019* Coulomb term does not account for changes

in the dielectric constant in the membrane. This is a critical area of future energy function optimization because the shifted pKa values in the bilayer affect the stability of membrane proteins at all pH values.

3.3.7 Test #7: $\Delta\Delta G$ of mutation

Test #7 evaluates how changes to the sequence of a membrane protein affect its overall thermostability. This quantity, called $\Delta\Delta G_{\text{mut}}$, is a critical building block for membrane protein design and evaluating the effects of genetic mutations on protein function. To predict $\Delta\Delta G_{\text{mut}}$, we used our previously described fixed-backbone and fixed-orientation protocol [65] that evaluates the difference in total energy between the mutant and wild-type (see Methods).

Dataset. We used three sets of $\Delta\Delta G$ measurements from the Fleming lab. All of the measurements were taken at equilibrium in DLPC vesicles and in the context of a β-barrel protein scaffold. The three datasets are: (1) mutations from alanine to all 19 remaining canonical amino acids at a lipid-exposed site on OmpLA [99] (2) mutations from alanine to all remaining 19 canonical amino acids at a lipid-exposed site on PagP [113] and (3) mutations from alanine to tryptophan, tyrosine, or phenaylanine at different membrane depths on OmpLA [121]. The experimental uncertainty of the measured $\Delta\Delta G_{\text{mut}}$ values is ± 0.6 kcal mol^{-1}.

Demonstration & Assessment. We previously reported the performance of *franklin2019* on the OmpLA and PagP datasets [161]. Here, we focus on the third set which probes the contribution of aromatics to stability [120, 169]. To emulate the experiment we modeled an implicit DLPC bilayer. A comparison of the *franklin2019* and experimentally measured values is shown in Fig. 3.3, focusing on tryptophan and

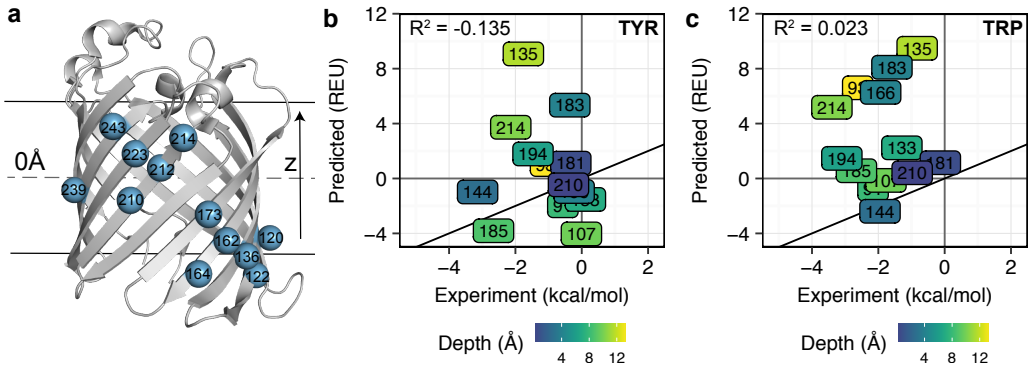

Figure 3.4: Comparison of predicted and experimentally measured depth-dependent $\Delta\Delta G_{\text{mut}}$ values. (a) Outer membrane protein phospholipase A (OmpLA, PDB 1qd6) with each host site highlighted in blue. A comparison of predicted and experimentally measured $\Delta\Delta G_{\text{mut}}$ for mutations to tyrosine and tryptophan are shown in (b) and (c) respectively. Each position is colored by depth relative to the membrane center plane in Å on a scale from blue (closer to the center) to yellow (closer to the interface/water barrier). The $y = x$ line is shown as a bold black line. The experimentally measured values were taken from [121].

tyrosine because both demonstrate strong depth-dependence [121]. Unfortunately, there was no correlation between the predicted and experimentally measured values. The Pearson correlation coefficient was $R^2 = -0.135$ for tyrosine and $R^2 = 0.023$ for tryptophan.

Interestingly, the Pearson correlation coefficient between the measured values and the *franklin2019* water-to-bilayer energy term was higher than that to the full energy function, with $R^2 = 0.451$ for tyrosine and $R^2 = 0.608$ for tryptophan (Fig. 3.13). To explore whether the $\Delta\Delta G$ was driven by factors other than membrane heterogeneity, we mapped the contribution of all component energy terms to the $\Delta\Delta G$ value (Fig. 3.14 and Fig. 3.15 show all values over 0.01 REU). The largest contributions were from rotamer energies, suggesting that steric clashes between guest side chains and neighboring side chains inflated the cost of substitution.

3.3.8 Test #8: Sequence Recovery

The next two tests concern the ability to identify residue types in design calculations. Test #8 probes whether the energy function can recover native membrane protein sequences. To run the test, we perform redesign using Rosetta's Monte Carlo fixed-backbone design protocol [116]. Each protein is initialized in the orientation from the OPM database [117], and the orientation remains fixed. For simplicity, we use a DLPC membrane in our calculations. We compute two metrics: (1) the fraction of amino acids recovered (sequence recovery) and (2) the divergence of the designed amino acid distribution from the native amino acid distribution (Kullback-Leibler divergence). To tailor this test for the membrane, we also compute these metrics for subsets of amino acids exposed to the aqueous phase (outside of membrane or pore facing), lipid phase, and interfacial region. An optimal energy function would maximize sequence recovery and minimize divergence.

Dataset. The test set includes 133 α-helical and β-barrel membrane proteins. The starting dataset was curated by Koehler Leman *et al.* [105] and revised to only include proteins with known sub-cellular localization [161]. In this set, all entries have resolution of 3.0 Å or better, and no two sequences share more than 25% sequence identity. The native and host lipid compositions for these proteins vary widely and include compositions not yet covered by the *franklin2019* lipid parameters. So here for simplicity, we perform all design calculations in a DLPC bilayer.

Demonstration & Assessment. We previously reported the performance of *franklin*2019 on the sequence recovery test (Fig. 4 in Alford *et al.*) [161]. Here, the recovery rate was high (31.8%) and the divergence between designed and native residue distributions was low (KL $= -2.7$). Both metrics improved relative to prior

energy functions.

3.3.9 Test #9: Depth-dependent side chain distribution

Test #9 evaluates whether the energy function captures bilayer depth-dependent features of membrane protein sequences. This test has been used previously for calibrating statistical implicit membrane potentials [118, 119, 176]. To run the test, we first generate redesigned proteins using the same protocol as in **Test #8**. We use a kernel-density estimate to compute the depth-dependent (z-dependent) distribution of amino acids in both the native and redesigned proteins. We then use numerical integration to compute the difference in the area under the curve (AUΔC) between the native and redesigned distributions. An effective implicit membrane energy function qualitatively matches the shape of the distribution and minimizes the AUΔC difference.

Dataset. This test uses the same set of 133 protein structures as in **Test #8**.

Demonstration & Assessment. The depth-dependent amino acid distributions for proteins redesigned with *franklin2019* are shown in Fig. 3.5, and the AUΔC values are shown in Fig. 3.16. The profiles reveal both native-like and non-native-like properties of *franklin2019*. The best predicted amino acid distributions were for polar, non-polar, and some aromatic amino acids, namely T, A, P, F, Y, M, I, N, and G (Fig. 3.16; AUΔC < 0.01). In contrast, leucine and valine were over enriched in the membrane core, resulting in larger AUΔC values of 0.018 and 0.022, respectively. The disparities were larger for charged amino acids. Specifically, the presence of D and E is underestimated, whereas the presence of R and K is overestimated. Further, lack of asymmetry in the distributions reveals that *franklin2019* does not capture the

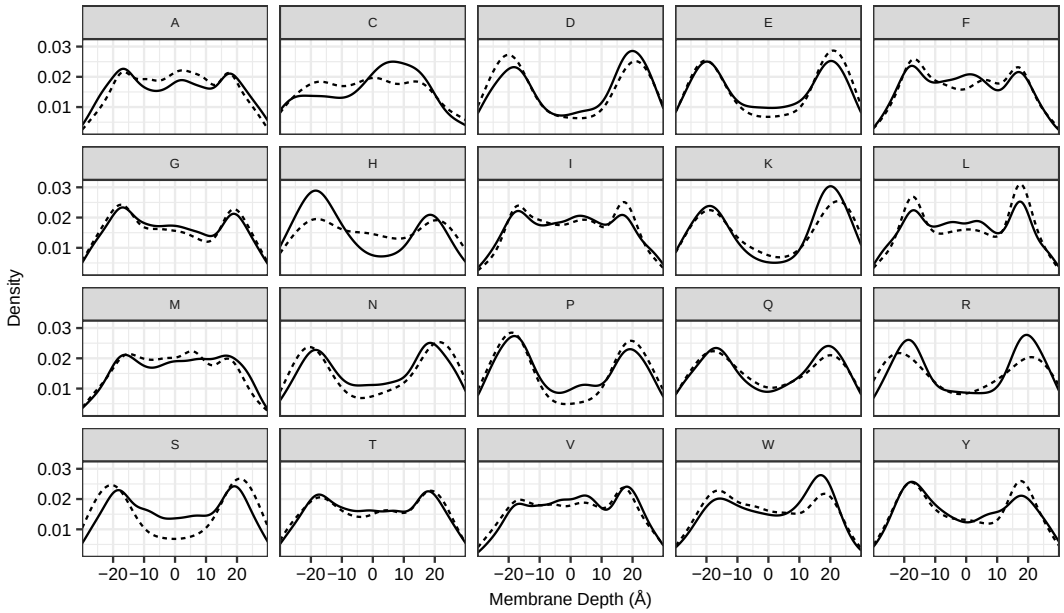

Figure 3.5: Comparison of the depth-dependent side chain distribution in native and designed protein sequences. The native amino acid distribution is shown with a solid line and the designed amino acid distribution is shown with a dotted line. Each panel represents the distribution for one of the twenty canonical amino acids with the membrane depth ranging between -30 Å and 30 Å.

"positive-inside rule", which dictates that cytosolic loops near the bilayer contain more positively charged amino acids [119, 177]. Further, the distribution misses enrichment of positively charged side chains in the inner leaflet. Both of these features have been observed using the Elazar energy function [119].

3.3.10 Test #10: Native decoy discrimination

A key task for membrane protein energy functions is to distinguish near-native from non-native backbone structures. So, the last three tests involve discriminating between alternate structures. In previous work, there were two discrimination studies with implicit membrane models for molecular dynamics [114, 138]. Recently, we also reported structure discrimination results for *franklin2019* [161] Here, we expand

the test by increasing the number and structural diversity of decoy models. The native discrimination test is performed by refining a set of decoy models with Rosetta MPRelax [65] in the context of the candidate energy function. Then, we quantify discrimination using the Boltzmann-weighted average root-mean-squared-deviation (RMSD) over all models (D). We also qualitatively examine the ranking of decoys by score and RMSD. An optimal energy function would exhibit a funnel-like arrangement of decoys, with non-native decoys assigned high energies and near-native decoys assigned low energies.

Dataset. The dataset includes five targets: bacteriorhodopsin (brd7), fumarate reductase (fmr5), lactose permease (ltpa), rhodopsin (rhod), and V-ATPase (vatp). Structural error is related to is the resolution of each crystal structure: 1.8 Å for brd7, 1.78 Å for fmr5, 3.5 Å for ltpa, 2.2 Å for rhod, and 2.1 Å for vatp. Each target is represented by decoys from two datasets: (1) the Dutagaci *et al.* set [114] includes decoys between 4–14Å RMSD from the native crystal structure, and (2) the Yarov-Yarovoy *et al.* set [62] includes decoys between 5–40 Å RMSD.

To increase the number and diversity of decoys for each target, we used RosettaMPRelax to generate five models from each decoy structure to provide 0.5–1.5 Å RMSD of additional variation. Since all of the X-Ray crystal structures were determined in detergents, we performed the calculations in a default lipid composition of DLPC. This bilayer is appropriate because all of the targets were expressed in *E. coli*.

Demonstration & Assessment. Fig. 3.6 summarizes the *franklin2019* native structure discrimination results for all five targets, and Table 3.2 lists the discrimination score for all decoys (D_{all}), Dutagaci decoys (D_{Dut}), and Yarov-Yarovoy decoys (D_{YY}). Consistent with previous results [161], discrimination of Dutagaci decoys for each

Table 3.2: Native structure discrimination by *franklin2019*. D is the Boltzman-weighted average RMSD over all models, with lower values indicating better identification of near-native models.

Target	D_{all} (Å)	D_{Dut} (Å)	D_{YY} (Å)
brd7	7.8	4.6	7.8
fmr5	14.2	5.5	14.2
ltpa	4.8	4.8	13.7
rhod	4.3	4.3	12.7
vatp	4.0	4.3	4.0

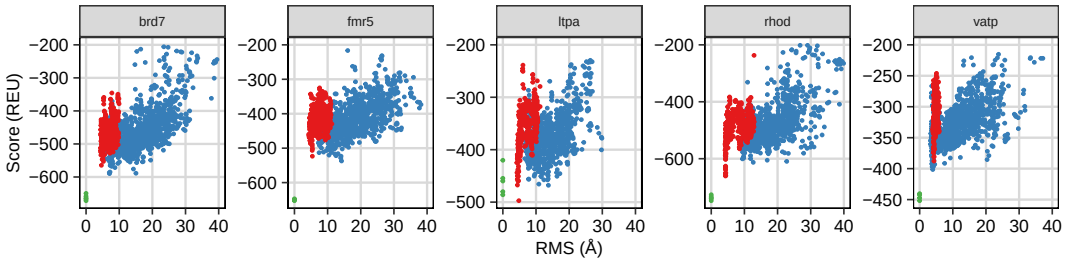

Figure 3.6: Decoy discrimination of five targets by the *franklin2019* implicit membrane potential. Each panel shows the decoys for each target ranked by energy (in REU) and RMSD of the Cα atoms to the native (x-ray) structure. The high resolution (Dut) decoys (1–11 Å) are shown in red, the low resolution (YY) decoys (5–40 Å) are shown in blue, and the refined native structures are shown in green.

target is high and the models form a funnel. Interestingly, structure discrimination worsens with the addition of low-resolution decoys for two targets: bacteriorhodopsin and fumarate reductase. In both cases, there are models near 15 Å that score the same or better than models near 4 Å, suggesting that the energy function requires improvements to recognize native-like helix-helix contacts when there are large differences between possible conformations.

3.3.11 Test #11: Helix kinks

A unique feature of membrane proteins is the distortion of α-helices into kinked and curved conformations [178]. Upon first look, kinked transmembrane helices seem counterintuitive because backbone hydrogen bonds are more stable in the membrane

and kinks will break hydrogen bonds. In reality, there are multiple biochemical possibilities to resolve the hydrogen bonds, including using a proline [179], a vestigial proline [180], and non-canonical backbone hydrogen bonding patterns [181, 182]. To evaluate the energy function's capacity to identify native non-canonical helical conformations, we scored conformational ensembles of membrane proteins with at least two conformational states with known structures where one structure exhibited a kinked helix that straightens in the second structure. First, assuming the system is stabilized by harmonic potentials [183], we generated conformational ensembles using normal mode analysis to explore equilibrium modes. We used KinkFinder [180] to compute the kink angle, and then, to test whether the energy function can discriminate the native conformation, we calculated the energy of each model in the conformational ensemble.

Dataset. The dataset includes three targets: (1) potassium channel KcsA, (2) adiponectin receptor 1, and (3) platelet activating receptor (Table 3.10). The experimental kink measurements are derived from the crystal structure. For these cases, the native bilayer was ambiguous, thus for all calculations we chose a DLPC system.

Demonstration & Assessment. A comparison of energies and kink angles for each state are shown in Fig. 3.7. As an example, we discuss the conformation of transmembrane helix 2 (TM2) in the the potassium channel KcsA (Fig. 3.7a). In the channel's closed state, TM2 is kinked (red), whereas in the open state, TM3 is slightly curved (blue). However, Figure 3.7a shows that the conformations cluster closer to 20° than 40° and assigns these decoys a significantly higher score, indicating that Rosetta prefers to straighten TM2 in the open state, even though both states are realistic. This error also occurs for the second target, adiponectin receptor 1 (Fig.

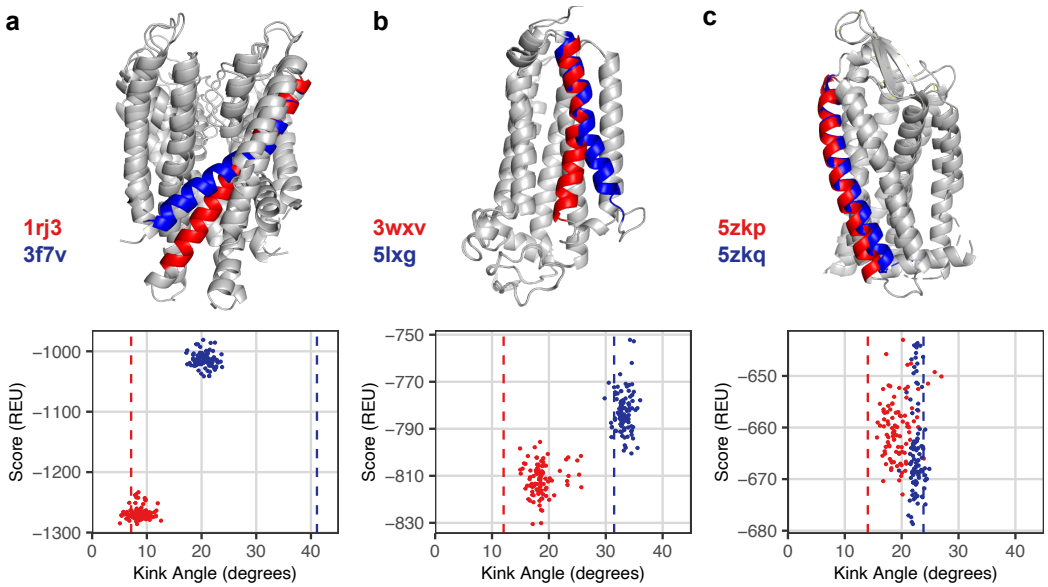

Figure 3.7: Kinked and straight conformations of α helices are not distinguished correctly. A structure discrimination experiment for kinked and straight helix conformations is shown for three targets: the open (3f7v) and closed (1r3j) conformation of the potassium channel KcsA (left), the active (3wxv) and inactive (5lxg) conformation of the adiponectin receptor, and (c) the active (5zkp) and inactive (5zkq) conformation of the platelet activating receptor. The top row shows the lowest energy conformation for both states and the bottom row ranks the energy of each conformation by kink angle relative to the native (denoted by a dotted line).

3.7b). This test demonstrates that improvements are needed to accurately capture helix conformations.

3.3.12 Test #12: Membrane protein-protein interactions

A final challenging task for implicit membrane models is to distinguish near-native from non-native membrane protein-protein interface structures. A range of studies hint toward key features, including the GxxG motif [184], bifurcated C_α hydrogen bonds [185], and apolar side chain packing [115]. However, there have only been a few general efforts to dock membrane proteins [65, 158, 159, 186].

Toward this goal, the final test is membrane protein-protein docking. Here, RosettaMPDock is used to search for the low-energy orientation of the protein partners by performing rigid-body rotations and translations with cycles of side chain repacking and torsion minimization (see Methods). For each target, we generated 5,000 candidate models and then used CAPRI metrics to evaluate the distance to crystal structures [187]. We also computed two additional scoring metrics: (1) the number of near-native decoys in the top 5 scoring decoys, $\langle N5 \rangle$, and (2) the enrichment of high quality models in the top 1% and 10% scoring models [52], $\langle E_{1\%} \rangle$ and $\langle E_{10\%} \rangle$ [66]. Angle brackets denote bootstrapped averages over resampled decoy sets.

Dataset. This test uses three existing benchmark sets. The first dataset comprises 18 homodimers formed by single transmembrane helices [158]. The second dataset comprises 48 homo- and hetero-dimers formed by multi-pass α helical proteins [159]. The third dataset is a subset of the second consisting of nine targets with the starting backbone generated by homology modeling [188] to simulate an "unbound" docking scenario where the starting conformations of the partner are not pre-configured in the bound state. For this test, all calculations were performed in a DLPC bilayer.

Demonstration & Assessment. Fig. 3.8 summarizes results for protein-protein docking with *franklin2019*. First, we examined the efficacy of docking structures from the crystalized bound state (Fig. 3.8a-b). We found that the membrane protein docking routine identifies high quality models for 90% of single-helix homodimer targets and 45% of multi-pass heterodimer targets, as indicated by two-fold enrichment in the top-scoring 1% of models. These data demonstrate that membrane protein docking routines can identify some membrane protein interfaces, yet require improvement. Importantly, these are easy targets because the binding partners are already in the

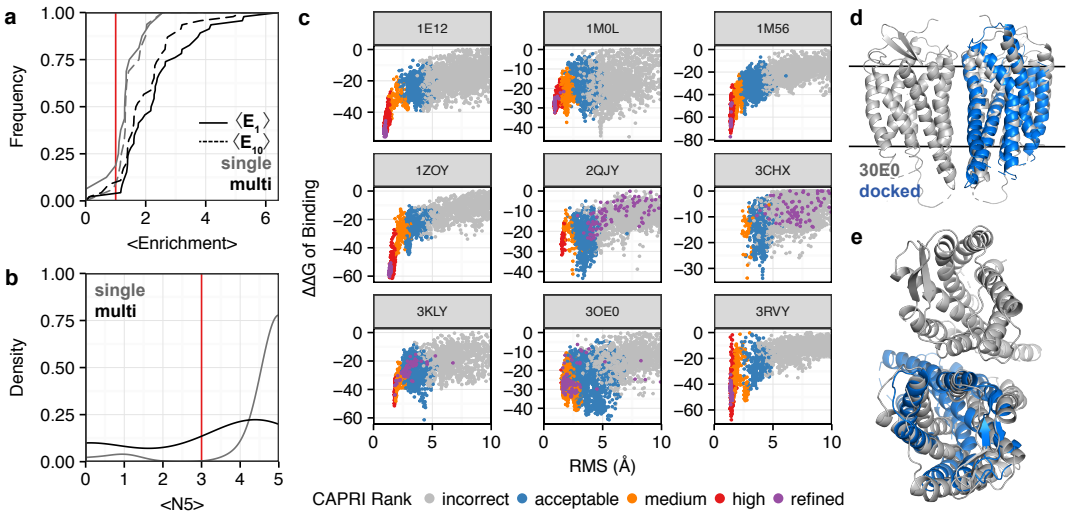

Figure 3.8: Implicit potentials identified native-like membrane protein-protein interfaces for nearly half of challenging targets. A summary of docking performance on bound (easy) targets is shown on the left hand side. (a) Cumulative distribution for the enrichment of high-quality models in the top 1% and 10% scoring models, given as $\langle E_{1\%} \rangle$ (solid line) $\langle E_{10\%} \rangle$ (dashed line) respectively. The distribution for single-transmembrane homodimers is shown in gray (n = 18) and the distribution for multi-pass homo- and heterodimers is shown in black (n = 48). (b) Cumulative distribution for the number of near-native decoys among the five top scoring decoys, called $\langle N5 \rangle$. Again, the distribution for single-transmembrane homodimers is shown in gray and the distribution for multi-pass targets is shown in black. The success cutoff of three models is shown in red. (c) Performance of docking nine challenging (unbound) targets. Each panel ranks models with an interface RMSD in Å between 0 Å and 10 Å. Each model is colored by CAPRI rank [187], with incorrect models in gray, acceptable models in blue, medium quality models in orange, and high quality models in red. The bound refined native models are shown in purple. The CXCR4 chemokine receptor which was unsuccessfully docked is shown in (d) as a membrane view and (e) as a top view. The crystal structure (3OE0) is shown in gray and the best scoring docked model is shown in blue.

right conformation for binding. To evaluate interface recognition in more detail, we need to dock unbound targets.

Fig. 3.8c shows the performance of the nine homology-model docking targets. Each panel plots all 5,000 models by interface RMSD and interface score, with each model colored by CAPRI criteria. In four of the nine cases, the energy landscape has a funnel pattern, with incorrect models scoring high and near-native models receiving the lowest score, showing that the *franklin2019* recognized near-native

interfaces. Further, scores for the refined native structures (purple) are near the bottom of the funnel of sampled docked structures. The four targets are halorhodopsin, cytochrome C oxidase, mitochondrial respiratory complex II, and the NavAB voltage-gated sodium channel. The five best-scoring models are shown in Fig. 3.18 and 3.19.

For the five remaining unbound targets, RosettaMPDock fails to recognize the correct interface. For two cases (3CHX and 3OE0), the docking program did not sample any high-quality models. Amongst the remaining cases (1M0L, 2QJY, and 3KLY), the energy function prefers acceptable or incorrect models over near-native models. One example of a challenging case is the CXCR chemokine receptor (Fig. 3.8d-e, 3OE0), where the low-scoring models have an incorrect bilayer orientation. These targets may be rescued by improved representation of the lipid bilayer.

3.3.13 Summary of *franklin2019* successes and challenges

Above, we described and demonstrated protocols for twelve scientific benchmark tests. To integrate the test results, we established a threshold or optimization goal for the summary metrics (Table 3.3).

Together, the benchmark results reveal strengths and pitfalls of a current energy function. For instance, test #1 demonstrates effective prediction of single-transmembrane helix tilt angles. In addition, test #9 demonstrates the energy function can predict many bilayer depth-dependent amino acid preferences. In contrast, test #5 illuminated the need to capture shifts in proton avidity for titratable sites in the low dielectric bilayer. Test #4 suggests the need for better implicit membrane interfacial representations to accurately predict hydrophobic thickness. Test #11 highlights possible pitfalls in the hydrogen bonding model. Further, tests #4 and #5 probe the balance

Table 3.3: Summary of current benchmark test performance criteria

#	Test	Metrics	Exp. Error	Threshold/Goal
1	Tilt angle	tilt	5°	10°
2	Rotation angle	rotation	12°	12°
3	Protein orientation	tilt/depth	10°/2.5Å	10°/2.5Å
4	Hydrophobic thickness	thickness	2.5 Å	2.5 Å
5	$\Delta G_{\text{w,l}}$ at constant pH	ΔG_{ins}	1.4 kcal/mol	max R^2
6	$\Delta\Delta G_{\text{w,l}}$ with pH shift	$\Delta\Delta G_{\text{pH-ins}}$	0.1 kcal/mol	max R^2
7	$\Delta\Delta G^{\text{mut}}$	$\Delta\Delta G_{\text{mut}}$	0.6 kcal/mol	max R^2
8	Sequence recovery	R_{s}/KL	NA	max R_{s}/min KL
9	Side chain distribution	AUC diff	NA	min AUC diff
10	Decoy discrimination	NA	D	5Å
11	Helix kinks	kink	NA	10°
12	Docking	$\langle N_5 \rangle / \langle E_{1\%} \rangle$	NA	3/2

of forces in the overall energy function. Together, the pitfalls lay the groundwork for the coming decade of membrane energy function optimization.

3.4 Discussion

We developed 12 scientific benchmarks to evaluate energy functions for membrane protein modeling and design. Our approach overcomes the challenge of limited experimental data by bundling many small sets to achieve a large feature-rich dataset. The tests account for effects of the heterogeneous lipid bilayer on protein orientation, stability, sequence, and structure. The tests encompass wide-ranging modeling tasks from $\Delta\Delta G$ calculations to protein-protein docking and design. As a step forward from single-test validation [114, 132, 139, 140] or four-test validation [161], we anticipate that these benchmarks will accelerate development of the next generation of membrane protein energy functions.

An interesting consequence of the membrane is the type of data that can be used for benchmarking. For soluble proteins, energy functions for molecular modeling

and force fields for molecular dynamics rely on a combination of small molecule thermodynamic data and known macromolecular structures. For membrane proteins, all-atom force fields also use physical chemistry data to derive parameters for different lipid types. However, the analogous small molecule data are difficult to obtain for implicit membrane simulations because organic solvents do not sufficiently mimic the properties of heterogeneous biological membranes [95]. Further, it is challenging to rigorously measure thermodynamic properties in lipid bilayers.

Hydrophobic length and membrane protein re-orientation can be observed on short timescales, i.e. it is currently accessible via molecular dynamics [114]. However, molecular dynamics is computationally expensive for modeling long-timescale biological phenomena such as some conformational changes and protein binding. By using a Monte Carlo approach with an implicit biologically-realistic implicit membrane, we enabled fast calculation of both thermodynamic and structural properties. For a single run, the tests require no more than 1,000 CPU hours. As a result, it is practical to iteratively run the tests to maintain reproducibility and for continuous optimization. For this purpose, we have implemented the tests on the Rosetta benchmark server (https://benchmark.graylab.jhu.edu/). In addition, we have distributed the source code through GitHub (https://github.com/rfalford12/Implicit-Membrane-Energy-Function-Benchmark) to make the tests accessible to all membrane protein modeling developers. We hope these resources will help the community share standardized metrics for evaluating membrane protein energy functions.

This first multi-faceted benchmark is a base upon which the quantity and quality of test data can be extended. For quantity, improvements in structure determination will increase the number and diversity of known structures to benefit both sequence

and structure tests. In contrast, the data are still sparse for stability and orientation since these values are not revealed when structures are determined in detergents. The paucity of data limits splitting the data into a training and a testing set, a key practice for demonstrating generalizability of models. On the other hand, quality is determined by various factors including the resolution of crystal and NMR structures, the uncertainty of stability measurements, and the rigor of assumptions made to obtain and analyze the data. The challenge of quality and quantity is well illustrated by choosing a dataset of $\Delta\Delta G$ of mutation measurements. Kroncke *et al.* [139] compiled a large dataset of $\Delta\Delta G$ of mutation measurements. However, the reference state for each measurement varied (e.g., lipid composition, ion concentration in aqueous phase), making it challenging to compare the datasets. As a result, we used a smaller set of $\Delta\Delta G$ measurements to improve quality. Comparing measurements is a consistent challenge of resolving the complexity of membrane proteins performed in different lipid compositions and environments.

In this work, we evaluate energy functions with experimental reference data. By transitivity, the energy function can only be as accurate as this reference data. For soluble proteins, the wealth of biophysical and structural information compensates. As of April 2020, there are more than 160,000 structures deposited in the Protein Databank [141]. Consequently, soluble protein energy functions can be validated on large and diverse datasets [60, 137]. In contrast, membrane protein structures can require up to 160,000 crystallization trials to determine a single structure. A central challenge is that many membrane proteins are not naturally abundant and cannot be reconstituted into a membrane mimetic. For this reason, substantial improvements to the energy function will require both reliable benchmarks and significant advances in

experimental methods.

Important future work includes developing a framework to perform a global optimization. A possible framework is to develop a series of objective functions that define the relationship between the threshold and performance for all targets in the dataset. For example, an objective function to define the performance of the tilt angle test (Test #1) could be

$$f(x) = |x_{\text{calc}} - x_{\text{exp}}| \tag{3.1}$$

$$F_{\text{T1}} = \sum_{i}^{\text{ntargets}} \frac{1}{\theta^2} \begin{cases} 0 & f(x_i) \leq \theta \\ (f(x_i) - \theta)^2 & f(x_i) > \theta \end{cases} \tag{3.2}$$

where x_{calc} is the predicted tilt angle, x_{exp} is the experimentally measured tilt angle, i is an iterator over all targets in the dataset, and $\theta = 10°$ is an allowable amount of error. A quantitative system for rating test performance could fit these benchmarks in a sophisticated optimization framework such as machine learning.

Looking ahead, our approach begs the question about the future role of optimization tools to improve membrane protein energy function accuracy. Deep learning has recently piqued the interest of the structural biology community [189]. Currently, deep learning approaches require large, high-quality datasets. Recently, Wang *et al.* [190] used transfer learning to develop a transmembrane protein structure prediction algorithm that relies on a soluble protein contact prediction algorithm [191] and the Deep CNF transmembrane topology prediction algorithm [192]. Our benchmark data can be used for direct learning, particularly toward incorporating the all-important lipid composition and specificity features to move toward more

accurate and biologically realistic implicit energy functions.

3.5 Appendix

3.5.1 Supplemental Figures

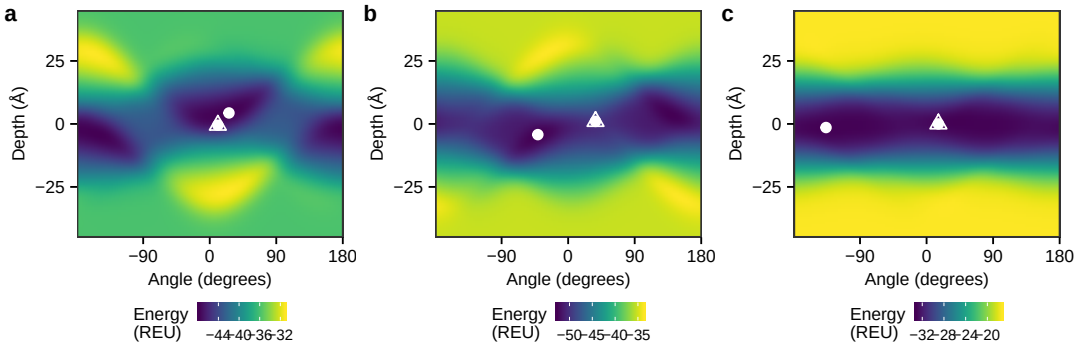

Figure 3.9: Tilt angle prediction for biological peptides with a single transmembrane domain. A mapping between all sampled orientations and energies for (a) Acetylcholine receptor segment M2, (b) Influenza A segment M2, and (c) VPU-forming domain of HIV-1 protein. Here, tilt angle relative to the membrane normal (in degrees) is on the x-axis and depth relative to the membrane center is on the y-axis. Each grid point is colored by *franklin2019* energy, with low energies colored in dark blue and high energies colored in yellow. Further, each grid point represents a 1Å and 1°increment. the lowest energy predicted orientation is shown as a white circle, and where applicable the experimentally measured orientation is shown as a white triangle.

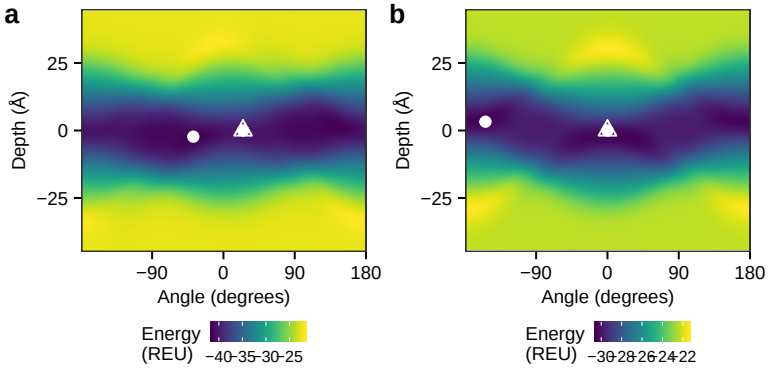

Figure 3.10: Tilt angle prediction for designed peptides with a single transmembrane domain. A mapping between all sampled orientations and energies for (a) WALP23 and (b) a poly-alanine helix with flanking tyrosine residues. Here, tilt angle relative to the membrane normal (in degrees) is on the x-axis and depth relative to the membrane center is on the y-axis. Each grid point is colored by *franklin2019* energy, with low energies colored in dark blue and high energies colored in yellow. Further, each grid point represents a 1Å and 1°increment. the lowest energy predicted orientation is shown as a white circle, and where applicable the experimentally measured orientation is shown as a white triangle.

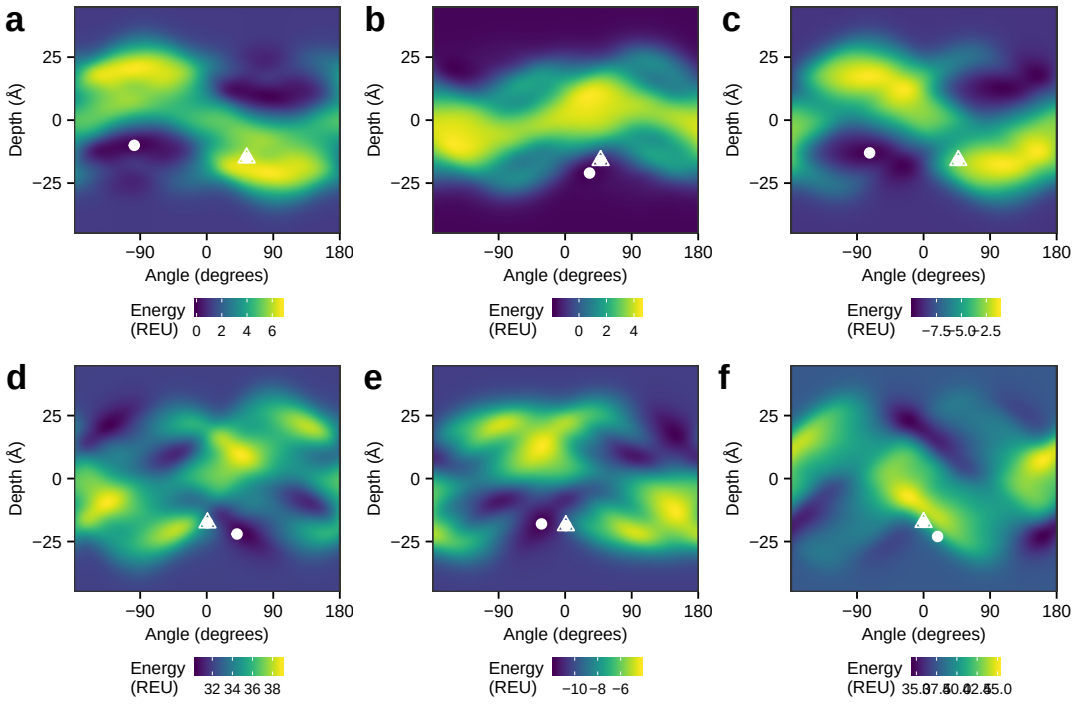

Figure 3.11: Rotation angle prediction for surface-adsorbed biological peptides. A mapping between all sampled orientations and energies for (a) Ovispirin 1 (b) Novispirin G10, (c) Novispirin T2, (d) Magainin-cercopin hybrid, (e) Magainin-cercopin hyrbrid P2, and (f) Magainin-cercopin hybrid P1. Here, rotation angle relative to the membrane surface plane (in degrees) is on the x-axis and depth relative to the membrane center is on the y-axis. Each grid point is colored by *franklin2019* energy, with low energies colored in dark blue and high energies colored in yellow. Further, each grid point represents a 1Å and 1°increment. the lowest energy predicted orientation is shown as a white circle, and where applicable the experimentally measured orientation is shown as a white triangle.

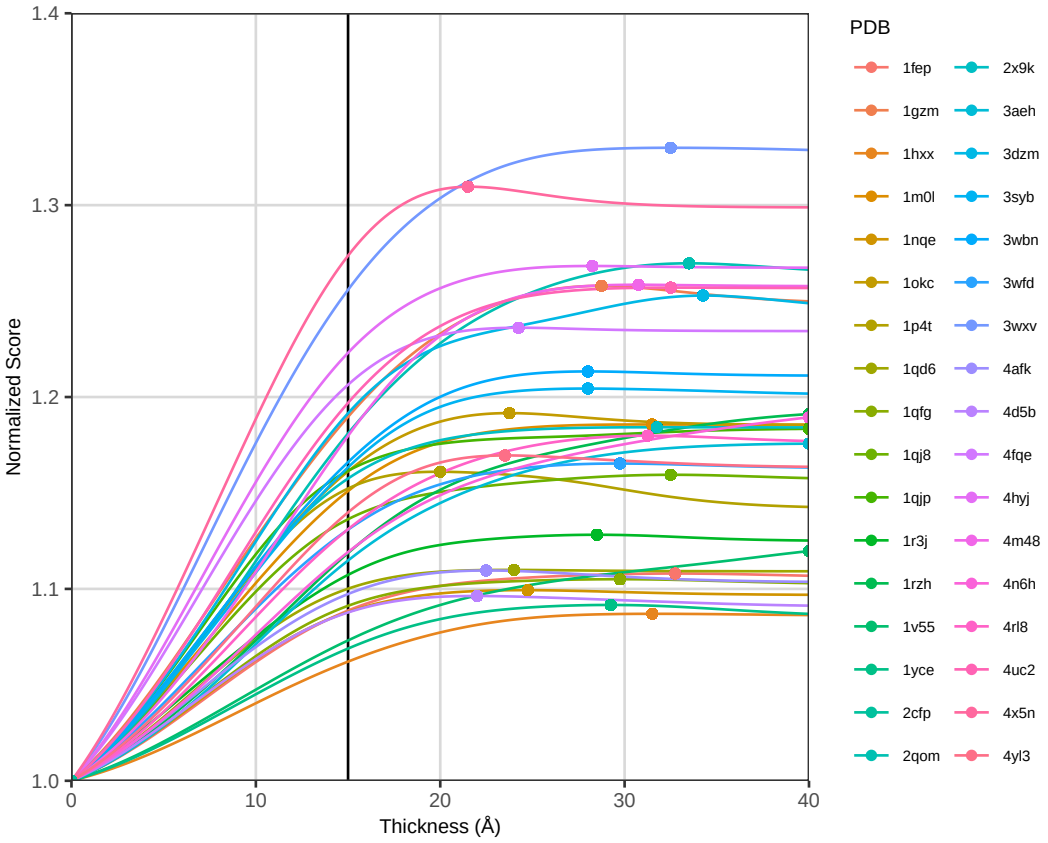

Figure 3.12: Change in energy with different bilayer thickness for hydrophobic length estimate. The energy is normalized relative to the maximum score for the protein. Each curve represents the change in energy with bilayer thickness for a different target. Each point represents the minimum energy bilayer thickness.

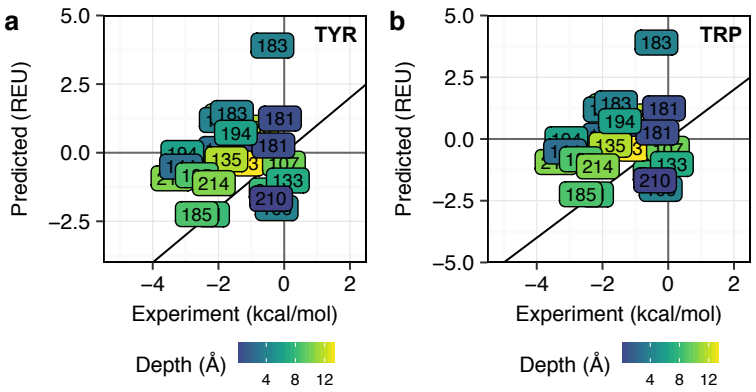

Figure 3.13: Comparison between experimentally measured $\Delta\Delta G^{\mathbf{mut}}$ and *franklin2019* water-to-bilayer score. Values for mutations to tyrosine and tryptophan are shown in (a) and (b) respectively. Each position is colored by depth relative to the membrane center plane in Å on a scale from blue (closer to the center) to yellow (closer to the interface/water barrier). The $y = x$ line is shown as a bold black line. The experimentally measured values were taken from [121].

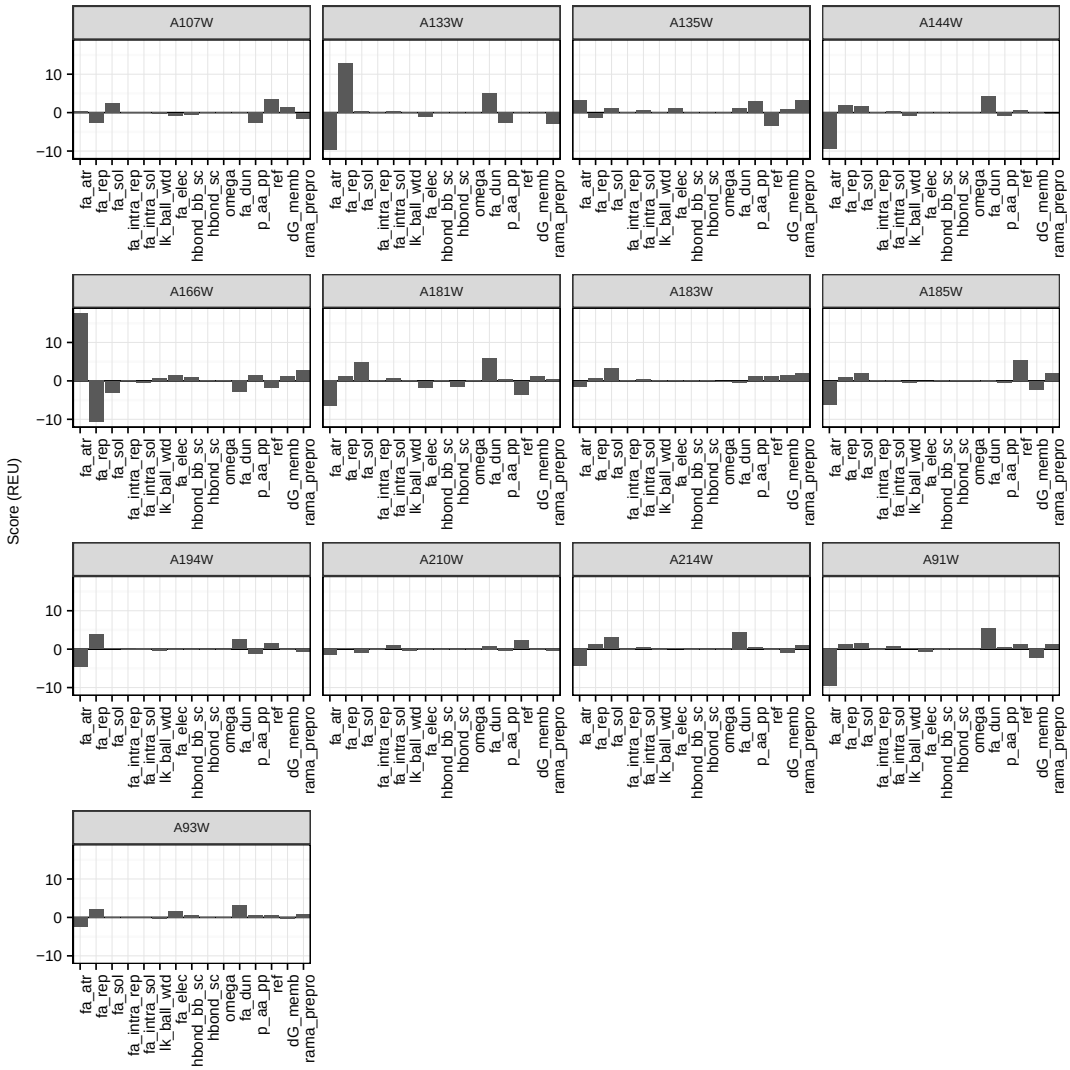

Figure 3.14: Contributions of component energies to the $\Delta\Delta G^{\mathbf{mut}}$ for mutations to tryptophan. Energies are only listed for contributions > 0.1 REU to the $\Delta\Delta G_{\text{mut}}$. These energy terms include the van der Waals attractive energy (fa_atr), repulsive energy (fa_rep), Lazaridis-Karplus solvation energy (fa_sol), intra-residue repulsive energy (fa_intra_rep), intra-residue Lazaridis-Karplus solvation energy (fa_intra_sol), orientation-dependent component of Lazaridis-Karplus solvation energy (lk_ball_wtd), Coulomb electrostatics energy (fa_elec), backbone-side chain hydrogen bonding energy (hbond_bb_sc), side chain to side chain hydrogen bonding energy (hbond_sc), omega torsion energy (omega), Dunbrack rotamer energy (fa_dun), knowledge-based backbone ϕ, ψ energy (rama_prepro, p_aa_pp), amino acid reference energy (ref), and *franklin2019* water-to-bilayer energy (dG_memb).

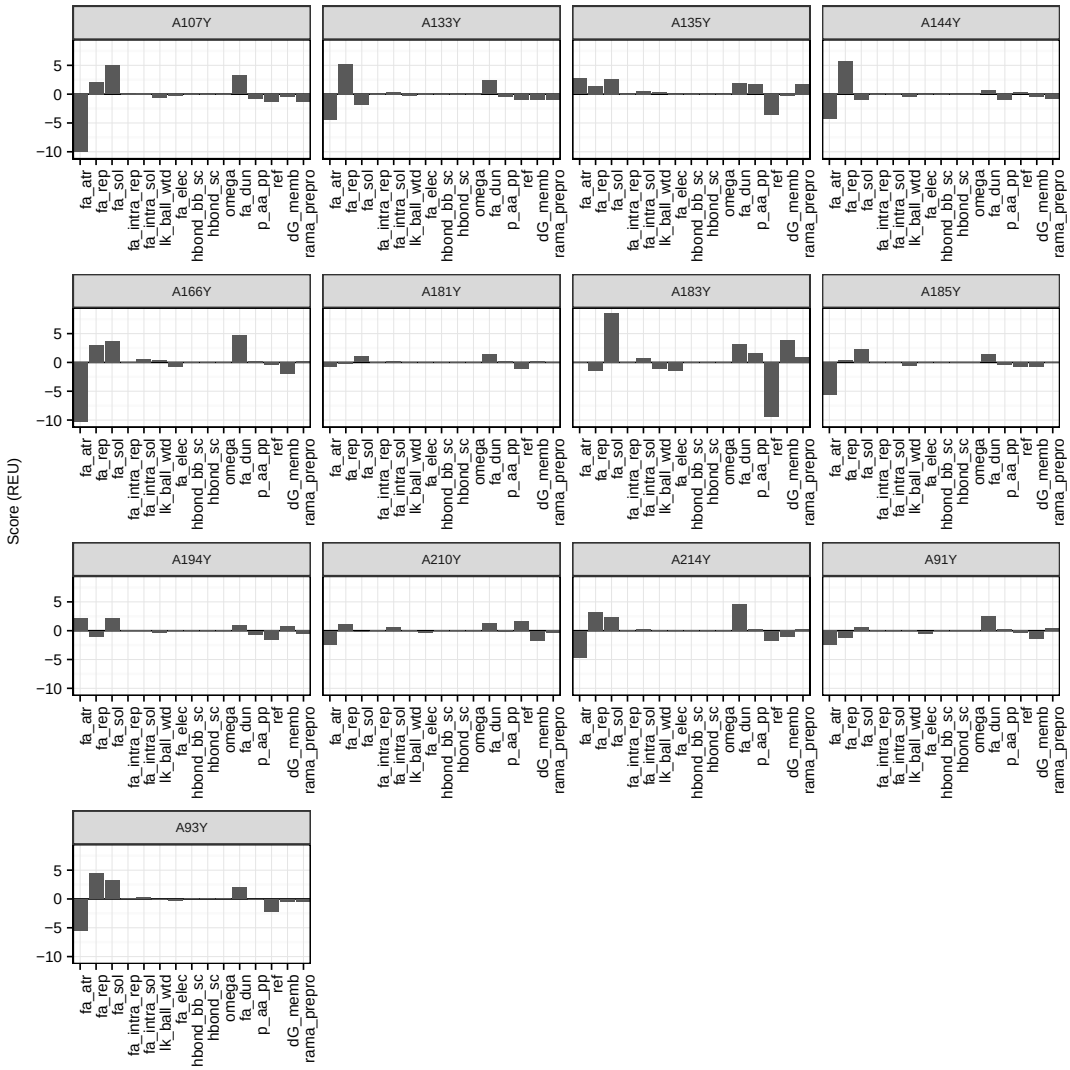

Figure 3.15: Contributions of component energies to the $\Delta\Delta G^{\mathbf{mut}}$ for mutations to tyrosine. Energies are only listed for contributions > 0.1 REU to the $\Delta\Delta G_{\text{mut}}$. These energy terms include the van der Waals attractive energy (fa_atr), repulsive energy (fa_rep), Lazaridis-Karplus solvation energy (fa_sol), intra-residue repulsive energy (fa_intra_rep), intra-residue Lazaridis-Karplus solvation energy (fa_intra_sol), orientation-dependent component of Lazaridis-Karplus solvation energy (lk_ball_wtd), Coulomb electrostatics energy (fa_elec), backbone-side chain hydrogen bonding energy (hbond_bb_sc), side chain to side chain hydrogen bonding energy (hbond_sc), omega torsion energy (omega), Dunbrack rotamer energy (fa_dun), knowledge-based backbone ϕ, ψ energy (rama_prepro, p_aa_pp), amino acid reference energy (ref), and *franklin2019* water-to-bilayer energy (dG_memb).

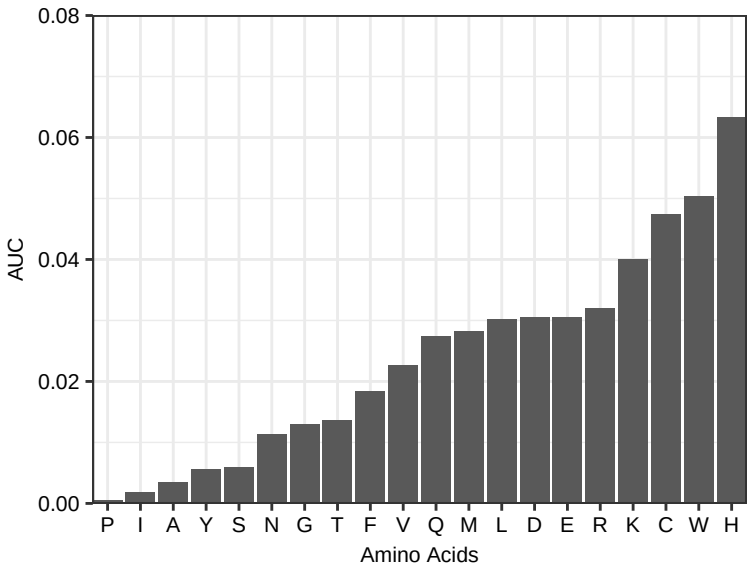

Figure 3.16: Difference in the depth-dependent side chain distribution between native and designed sequences. The difference in distributions is calculated as the difference between the area-under-the-curve for the native and designed amino acid distributions. The area under the curve was computed using a trapezoidal rule.

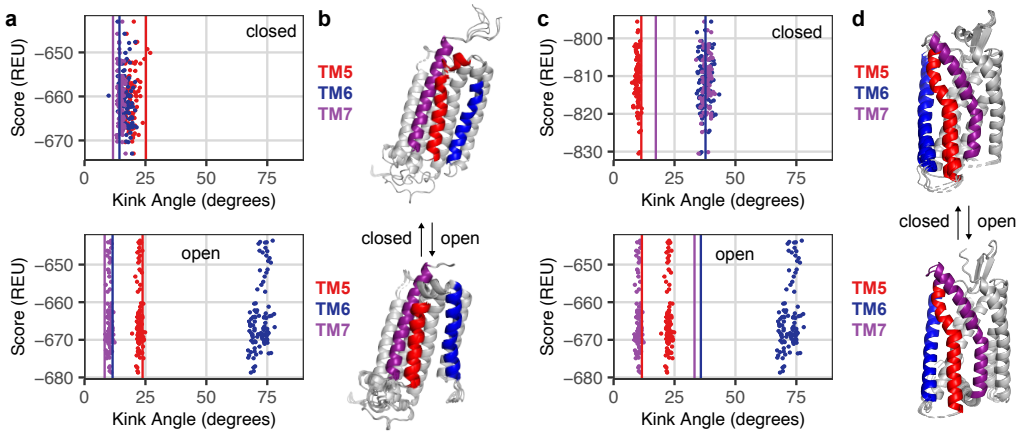

Figure 3.17: Helix kink predictions for Adiponectin receptor 1 and Platelet activating receptor. A structure discrimination experiment for kinked and straight helix conformations is shown for two of four targets: the open (5lxg) and closed (3wxv) conformation of the adiponectin receptor 1 (left) and the active (5zkp) and inactive (5zkq) conformation of platelet activating receptor 1. In (a) and (c), energies and kink angles for transmembrane helix 5 (red), 6 (blue) and 7 (purple). In (b) and (d), Conformation of the five lowest scoring models corresponding to the active (top) and inactive (bottom) conformations.

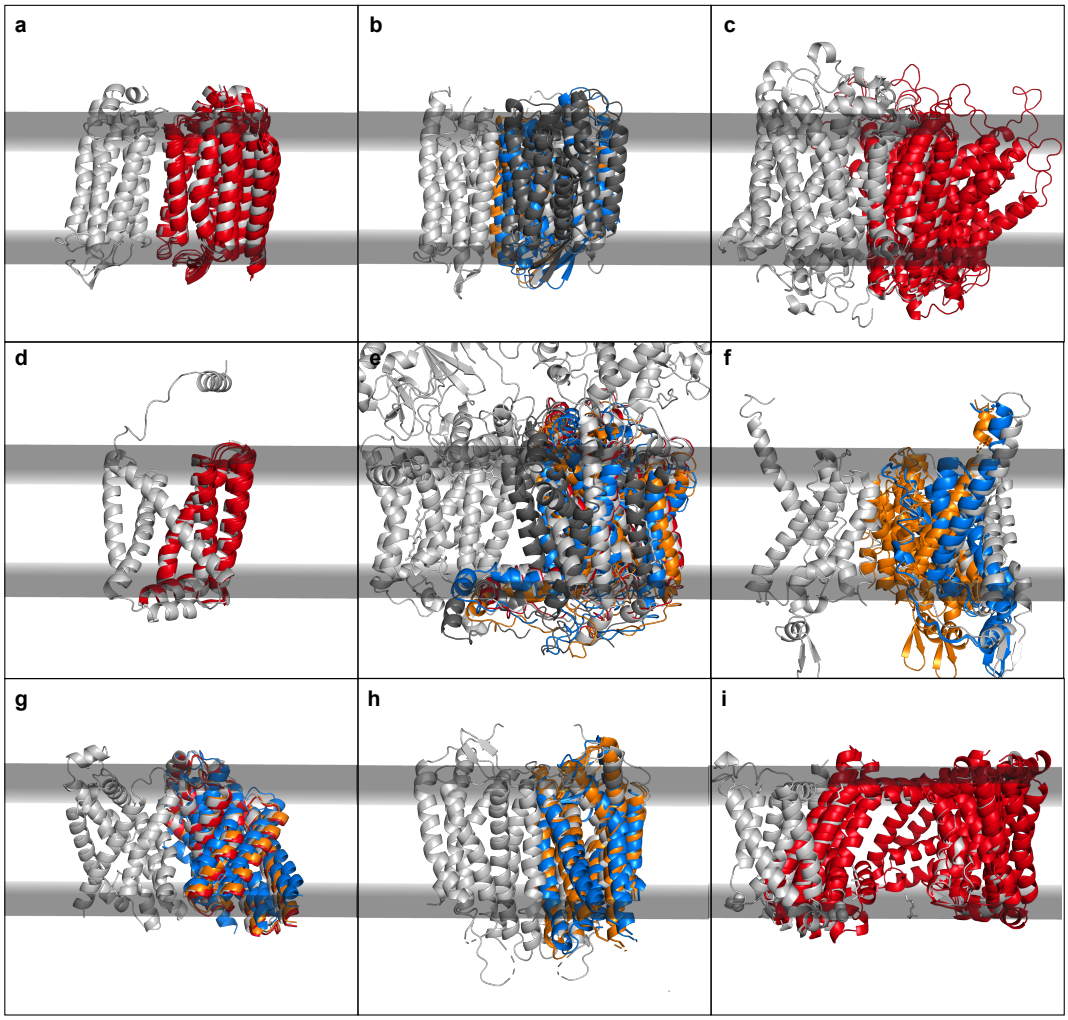

Figure 3.18: Comparison between the native and five lowest scoring docked membrane protein complexes from membrane view. The native membrane protein complex is colored in gray and the docked models are colored by CAPRI criteria. Here, high-quality models are in red, medium-quality models are in orange, acceptable models are in blue, and incorrect models are in dark grey. Each panel shows docked models for one of the nine unbound docking targets: (a) halorhodopsin, (b) bacteriorhodopsin, (c) cytochrome C oxidase, (d) mitochondrial respiratory complex II, (e) cytochrome bc1, (f) methane monooxygenase, (g) pentameric formate channel, (h) CXCR4 chemokine receptor, (i) NavAb voltage-gated sodium channel.

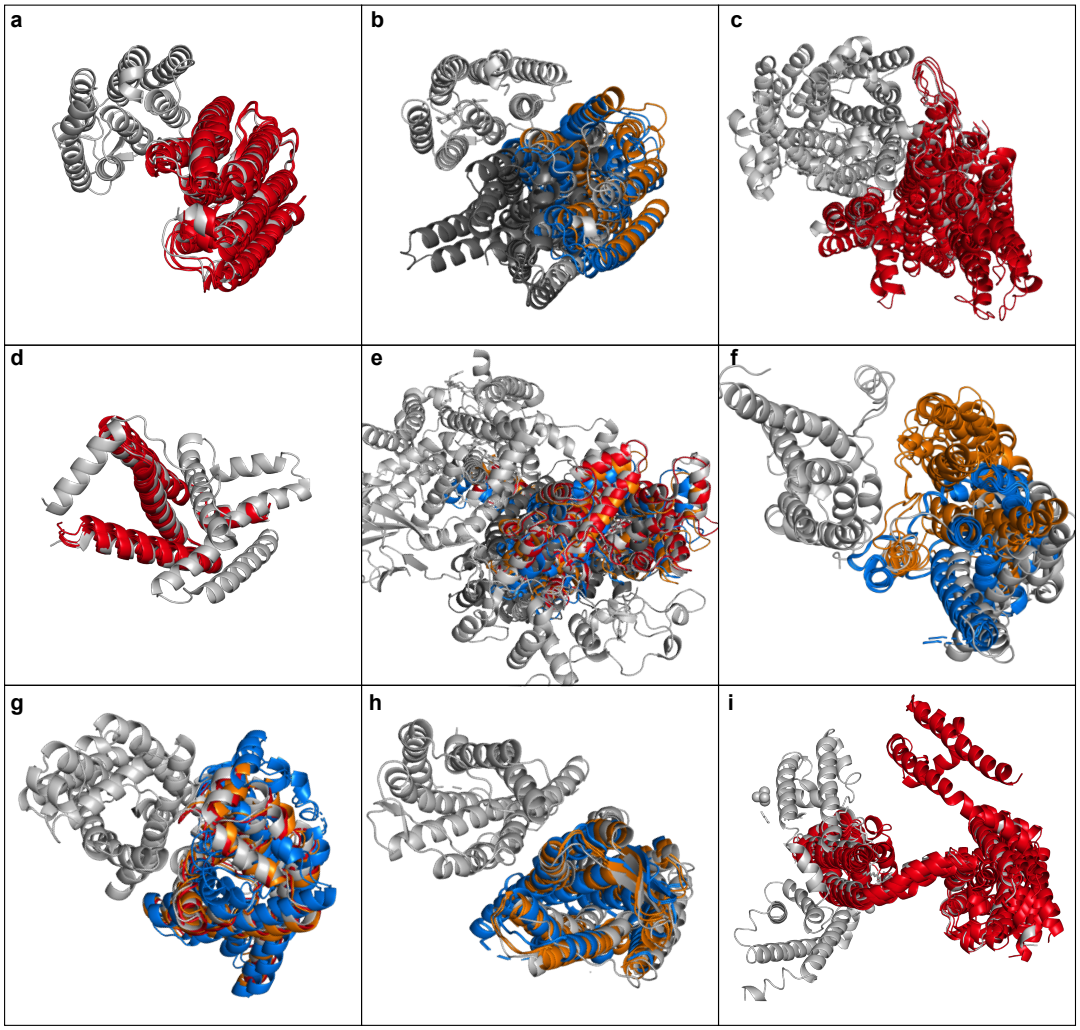

Figure 3.19: Comparison between the native and five lowest scoring docked membrane protein complexes from top view. The native membrane protein complex is colored in gray and the docked models are colored by CAPRI criteria. Here, high-quality models are in red, medium-quality models are in orange, acceptable models are in blue, and incorrect models are in dark grey. Each panel shows docked models for one of the nine unbound docking targets: (a) halorhodopsin, (b) bacteriorhodopsin, (c) cytochrome C oxidase, (d) mitochondrial respiratory complex II, (e) cytochrome bc1, (f) methane monooxygenase, (g) pentameric formate channel, (h) CXCR4 chemokine receptor, (i) NavAb voltage-gated sodium channel.

3.5.2 Supplemental Tables

Table 3.4: Transmembrane peptide targets for tilt angle test

Name	PDB	Membrane	Sequence	Tilt Angle(°)	Ref.
Acetylcholine M2	1a11	DPC	GSEKMSTAISVLLAQAVFLLLTSQR	11	[149]
Influenza A M2	1mp6	DMPC	SSDPLVVAASIIGILHLILWILDRL	38 ± 3	[150]
VPU domain	1pje	DOPC:DOPG	MQPIQIAIVALVVAIIIAIVVWSIVIIEGRGGKKKK	16	[151]
NMDA Receptor	2nr1	DPC	GSNGDALTLSSAMWFSWGVLLNSGIGE	40 ± 2	[149]
WALP23	–	DOPC	GWWLALALALALALALALWWA	24.8	[112]
PolyA-Y	–	–	AAAYAAAAAAAAAAAAAAAYA	–	–
PolyA-W	–	–	AAAWAAAAAAAAAAAAAAAWA	–	–

Table 3.5: Membrane surface-adsorbed peptide targets for rotation angle test

Name	PDB	Membrane	Sequence	Tilt Angle (°)	Ref.
Magainin	2mag	DPC	GIGKFLHSAKKFGKAFVGEIMNSX	87 ± 7	[193]
Ovispirin 1	1hu5	2,2,2-trifluoroethanol	KNLRRIIRKIIHIIKKYG	94 ± 11	[194]
Novispirin G10	1hu6	2,2,2-trifluoroethanol	KNLRRIIRKGIHIIKKYG	88 ± 6	[194]
Novispirin T2	1hu7	2,2,2-trifluoroethanol	KNLRRITRKIIHIIKKYG	87 ± 12	[194]
Magainin-cercopin hybrid	1f0e	DPC micelles	KWKLFKKIPKFLHSAKKFX	91 ± 8	[195]
Magainin-cercopin hybrid P2	1f0f	DPC micelles	KWKLFKKIKFLHSAKKFX	88 ± 4	[195]
Magainin-cercopin hybrid P1	1f0g	DPC micelles	KLKLFKKIGIGKFLHSAKKFX	90 ± 10	[195]
Leucine-lysine repeat	–	–	LKKLLKLLKKLLKLLKKLLKLLKKL	–	[170]

Table 3.6: Multi-pass α-helical and β-barrel proteins for orientation and hydrophobic thickness test

PDB	Protein	Class
1fep	Ferric enterobactin receptor	β
1gzm	Bovine rhodopsin	α
1hxx	OmpF porin channel	β
1m0l	Bacteriorhodopsin	α
1nqe	Cobalambin transporter	β
1okc	Mitochondrial ATP/ADP Carrier	α
1p4t	Neisserial surface protein A	β
1qd6	OMP phospholipase A	β
1qfg	Ferric hydroxamate receptor (FhuA)	β
1qj8	OmpX	β
1qjp	OmpA	β
1r3j	Potassium channek KcsA	α
1rzh	Photosynthetic reaction center	α
1v55	Cytochrome C oxidase	α
1yce	Rotor ring of F-type Na+-ATP-ase	α
2cfp	Sugar-free lactose permease	α
2qom	EspP autotransporter beta-domain	β
2x9k	OmpG	β
3aeh	Autotransporter Hbp	β
3dzm	TtoA	β
3syb	OMP carboxylate channel	β
3wbn	MATE multidrug transporter	α
3wfd	Nitric oxide reductase	α
3wxv	Adopinectin receptor 1	α
4afk	Alginate transporter AlgE	β
4d5b	OMP CymA	β
4fqe	Oligogalacturonate KdgM	β
4hyj	Proteorhodopsin	α
4m48	Dopamine transporter	α
4n6h	Delta opioid receptor	α
4rl8	COG4313 outer membrane channel	β
4uc2	TSPO transporter protein	α
4x5n	SemiSWEET transporter	α
4yl3	mPGES-1 inhibitor complex	α

Table 3.7: Reference OPM values for hydrophobic thickness, tilt angle, and depth

PDB	Protein	Length (Å)	Angle (°)	Depth (Å)
1fep	Ferric enterobactin receptor	24.3	1	12.8
1gzm	Bovine rhodopsin	32.2	11	-0.4
1hxx	OmpF porin	24	0	-6.6
1m0l	Bacteriorhodopsin	31.8	0	-1.7
1nqe	Cobalambin transporter BtuB	23.4	5	9.8
1okc	Mitochondrial ATP/ADP Carrier	29.5	14.1	-4.4
1p4t	Neisserial surface protein A	24.9	22	6.5
1qd6	OmpLA	23.9	0	-5.2
1qfg	Ferric hydroxamate receptor	24.7	5	-12.4
1qj8	OmpX	23.6	12	-7.3
1qjp	OmpA	25.4	11	-3.8
1r3j	Potassium channek KcsA	34.8	0	2.1
1rzh	Photosynthetic reaction center	31.8	2	8.6
1v55	Cytochrome C oxidase	28	0	2.5
1yce	Rotor ring of F-type Na+-ATP-ase	37	0	-4.2
2cfp	Sugar-free lactose permease	31.1	2.2	-4.4
2qom	EspP autotransporter beta-domain	25.1	6	7.7
2x9k	OmpG	24.7	5	-7.6
3aeh	Autotransporter Hbp	25.2	4	-7.6
3dzm	TtoA	28.5	16	11.4
3syb	Carboxylate channel (OpdP)	23.6	8	-6.8
3wbn	MATE multidrug transporter	31.8	8	-0.7
3wfd	Nitric oxide reductase	31.7	11.6	-0.4
3wxv	Adopinectin receptor 1	32.8	15	-2
4afk	Alginate transporter AlgE	24.8	3	7
4d5b	CymA	23.5	8.3	10.6
4fqe	Oligogalacturonate-specific KdgM	22.2	2	3.3
4hyj	Proteorhodopsin	30	15	-1.5
4m48	Dopamine transporter	30.8	12	1.9
4n6h	Delta opioid receptor	34	14	-9.1
4rl8	COG4313	23.4	6	-6.2
4uc2	TSPO transporter protein	30.4	1	4.6
4x5n	SemiSWEET transporter	36.8	1	0.8
4yl3	mPGES-1 inhibitor complex	29.8	0	-3.9

Table 3.8: Sequences and measured insertion energies for designed poly-leucine peptides

Name	Sequence	Membrane	ΔG_{insert}
GL5	GLLLLLRLLLLLG	POPC	2.1
GL6	GLLLLLLRLLLLLLG	POPC	0.5
GL7	GLLLLLLLRLLLLLLLG	POPC	-0.5
GL8	GLLLLLLLLRLLLLLLLLG	POPC	-1.5
GWL6	GWLLLLLLRLLLLLLLG	POPC	-0.5

Table 3.9: Sequences and measured insertion energies for designed pH-sensitivie peptides

Name	Sequence	ΔG_{insert}
v1	ACEDQNPYWARYADWLFTTPLLLLDLALLVDG	2.17
v2	ACEDQNPYWRAYADLFTPLTLLDLLALWDG	0.28
v3	ACDDQNPWRAYLDLLFPTDTLLLDLLW	2.23
v4	ACEEQNPWRAYLELLFPTETLLLELLW	1.72
v5	ACDDQNPWARYLDWLFPTDTLLLDL	2.31
v6	CDNNNPWRAYLDLLFPTDTLLLDW	1.93
v7	ACEEQNPWARYLEWLFPTETLLLEL	2.39
v8	CEEQQPWAQYLELLFPTETLLLEW	2.19
v9	CEEQQPWRAYLELLFPTETLLLEW	2.07
v10	ACEDQNPWARYADWLFPTTLLLLD	1.79
v11	ACEEQNPWARYAEWLFPTTLLLLE	1.94
v12	ACEDQNPWARYADLLFPTTLAW	1.95
v13	ACEEQNPWARYAELLFPTTLAW	1.15
v14	TEDADVLLALDLLLLPTTFLWDAYRAWYPNQECA	1.78
v15	CDDDDDNPNYWARYANWLFTTPLLLLNGALLVEAEET	0.82
v16	CDDDDDNPNYWARYAPWLFTTPLLLLPGALLVEAEET	1.47

Table 3.10: Targets for helix kink prediction

Target	State	PDB
Potassium channel KcsA	closed	1r3j
	open-inactive	3f7v
B2-adrenergic GPCR	inactive	2rh1
	active	3p0g
Adiponectin receptor 1	closed	3wxv
	open	5lxg
Platelet activating receptor	closed	5zkp
	open	5zkq

Chapter 4

An heuristic implicit model for electrostatic interactions in the membrane environment

4.1 Overview

Electrostatics play an intimate role in membrane protein structure and function. However, accurately capturing electrostatic energies in the low-dielectric membrane often requires expensive Poisson-Boltzmann calculations that are not scalable for membrane protein structure prediction and design. In this chapter, we develop a fast-to-compute electrostatics model that considers the lipid bilayer. In proof-of-concept benchmarks, we demonstrate that the updated energy function improves partitioning energy estimates for pH-sensitive transmembrane peptides. These results demonstrate promise for the electrostatic model to improve the accuracy of membrane protein structure prediction and design.

4.2 Introduction

Electrostatic interactions play an intimate role in membrane protein stability, structure, and function. In particular, the hydrophobic core of the bilayer de-screens interactions between charged particles, giving rise to biophysical features that are less frequently observed in the aqueous phase. For instance, hydrogen bonds between C_α and OH groups are more common, have energies up to 3 kcal/mol [196, 197], and facilitate dimerization [185]. To minimize the cost of inserting charged groups into the membrane, arginine and lysine have been observed to snorkel toward the interfacial region [198]. The protonation equilibria of titratable sites are shifted to favor charge-neutral states [199, 200]. Additionally, the non-polar bilayer can increase the strength of traditional hydrogen bonds [201].

Despite their importance, electrostatic forces are challenging to capture during computational modeling. A primary difficulty is the computational cost of sampling both solute and solvent degrees of freedom. To overcome this hurdle, electrostatic calculations are typically based on macroscopic electrodynamics that treat the solvent as a continuous medium and ignores solvent-solvent interactions [202, 203]. In this approach, the dielectric is modeled as a parameter rather than a constant [204, 205].

A common approach to electrostatic calculations of biological systems is to numerically solve the Poisson-Boltzmann (PB) equation [206]. In this formalism, electrostatic forces are expressed as a system of second-order partial differential equations that can be solved for the electric field caused by a collection of charges [88]. The PB equation

is given in Eq. 4.1.

$$-\nabla \cdot [\epsilon(r)\nabla\phi(r)] + \epsilon(r)\kappa^2(r)\sinh[\phi(r)] = \frac{e}{k_B T} 4\pi\rho(r) \tag{4.1}$$

Here, $\phi = e\psi/k_B T$ is the reduced electrostatic potential, ϵ is the dielectric value in different phases (water, membrane, protein), κ is the Debye-Huckel screening parameter, ρ is the charge distribution, and r is the position in three-dimensional space. This model has been used extensively to compute electrostatic features of membrane proteins including pKa values [207], insertion energies [208], and membrane potentials [209]. While reliable, the PB equation is not scalable for structure prediction and design calculations which often require $10^6 - 10^9$ energy calculations per trajectory.

A popular alternative to the Poisson-Boltzmann model is the analytical generalized Born approximation. This method approximates atoms as charged spheres whose internal dielectric is lower than the environment [210, 211]. The screening on each atom is then determined by the local environment: more neighbors indicates an atom will be less screened by water. De-screening (D_{ij}) is computed as a function of the dielectric constant in the solvent ϵ_s, dielectric constant in the protein ϵ_p, and the born radius f_{ij} (Eq. 4.2), as shown in Eq. 4.3.

$$f_{ij} = \sqrt{r_{ij}^2 + \alpha_i \alpha_j \exp\left(\frac{-r_{ij}^2}{4\alpha_i \alpha_j}\right)} \tag{4.2}$$

$$D_{ij} = \left(\frac{1}{\epsilon_p} - \frac{\exp(-k f_{ij})}{\epsilon_s}\right) \tag{4.3}$$

Then, the generalized Born energy for an atom pair is computed as a function of

the de-screening, Born radius, partial atomic charges on atoms i and j, q_i and q_j, and constant k_e, as given by Eq. 4.4.

$$E_{ij}^{\mathrm{GB}} = -k_e D_{ij} \frac{q_i q_j}{f_{ij}} \tag{4.4}$$

The generalized Born approximation is commonly used in molecular dynamics simulations of membrane proteins [89, 143]. Yet, the radius calculation is still expensive in the context of searching both conformational and sequence space. A third possibility is the heuristic Coulomb equation. To account for a variable dielectric, we can introduce a distance-dependent dielectric constant [212]. In Rosetta soluble protein calculations, this model has yielded a significant speedup relative to generalized Born calculations [213] and has improved modeling of hydrogen bonds [137].

In previous work, Lazaridis [64] developed a formalism to account for the dielectric variation with the bilayer. However, this method has not yet been tested in the context of structure prediction and design. In this chapter, I develop a new fast-to-compute Coulomb electrostatics model that considers the lipid bilayer. To account for the low-dielectric membrane, the model extends the Coulomb energy and considers shifted proton avidity for titratable sites. In proof-of-concept benchmarks, the updated energy function improves partitioning energy estimates for pH-sensitive transmembrane peptides. These results demonstrate promise for the electrostatic model to improve the accuracy of membrane protein structure prediction and design.

4.3 Methods

4.3.1 Bilayer-dependent electrostatics energy

I developed a bilayer-dependent electrostatics energy based on Coulomb's inverse-square law for the force between two stationary charged particles.The Coulomb energy, the integral of the force expression, is computed as a function of the distance between atoms i and j (d_{ij}), the partial atomic charges for atoms i and j (q_i,q_j), the dielectric constant ϵ and the Coulomb constant $C_0 = 322\,\text{Å kcal mol}^{-1}e^{-2}$ (Eq. 4.5). The partial atomic charges are taken from CHARMM [162] and adjusted via a group optimization scheme [60].

$$E_{\text{elec},ij} = \frac{C_0 q_i q_j}{\epsilon} \frac{1}{d_{i,j}} \tag{4.5}$$

For soluble proteins, Rosetta uses a modified version of the Coulomb energy with a distance-dependent dielectric [214]. Here, the constant ϵ is substituted by a sigmoidal function $\epsilon(d_{ij})$ that describes the transition between the dielectric constant in the protein core ($\epsilon_{\text{core}} = 6$) and in the solvent ($\epsilon_{\text{solvent}} = 80$) [60]. Additionally, the distance-dependent dielectric dampens long-range electrostatics; thus, the potential is truncated at 5.5 Å and shifted by $1/d_{\text{max}}$ to equal zero at d_{max} [61]. The updated functional form is given in Eq. 4.6.

$$E_{\text{elec}} = \frac{C_0 q_i q_j}{\epsilon(d_{i,j})} \left[\frac{1}{d_{i,j}} - \frac{1}{d_{\text{max}}} \right] \tag{4.6}$$

To accommodate the lipid bilayer, we altered the function $\epsilon(d_{ij})$ to additionally depend on membrane depth. Here, membrane depth is captured by fractional hydration h (called f_{hyd} in Chapter 3) [161]: a function that captures the three-dimensional

shape of the implicit membrane as a dimensionless number that describes the solvent environment given the position of an atomic group. When an atomic group is exposed to lipids, $h = 0$; whereas when an atomic group is exposed to water, $h = 1.0$. The hydration fraction for the atom pair h_{ij} is computed as the geometric average of the hydration fraction for atoms i and j.

We empirically developed a linear mixture equation for $\epsilon(d_{ij}, h_{ij})$ based on the following requirements: (1) for a close atom pair in water, $\epsilon = 20$, (2) for a distant atom pair in water, $\epsilon = 80$, (3) for a close atom pair in the bilayer $\epsilon = 2$, and (4) for a distant atom pair in the bilayer, $\epsilon = 10$ (Fig. 4.1a).

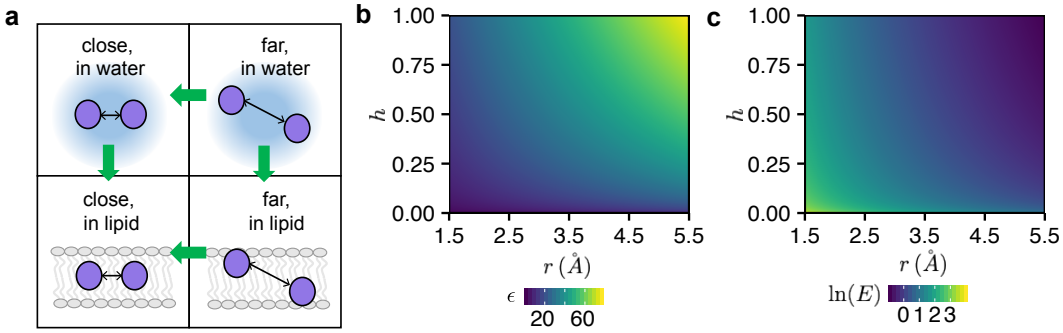

Figure 4.1: Coulomb electrostatics model with a varying dielectric. (a) Requirements for a membrane-dependent electrostatics potential: The energy increases when entering the bilayer and at close atom pair distances. Green arrows indicate the direction of increasing energy. (b) Dependence of the dielectric constant ϵ on fractional hydration h (dimensionless) and atom-pair distance r in Å. Each grid point corresponds to a different dielectric constant, colored from low (dark blue) to high (yellow). (c) Variation of the membrane-dependent electrostatics energy as a function of fractional hydration h (dimensionless) and atom-pair distance r in Å. Each grid point corresponds to a sample energy calculation for point charges with opposing signs, and the energy varies from low (dark blue) to high (yellow). Note, energy is represented on a logarithmic scale.

The resulting equation is given in Eq. 4.7, where D_0 and D are constants. The variation of $\epsilon(d_ij, h_ij)$ with atom-pair distance and fractional hydration is illustrated

as a heatmap in Fig. 4.1b.

$$\epsilon(h_{i,j}, d_{i,j}) = (1 - h_{i,j})D_0 r + h_{i,j} D r \tag{4.7}$$

Finally, we substituted $\epsilon(d_{ij})$ in Eq. 4.6 for Eq. 4.7. The resulting form of the bilayer-dependent electrostatics energy is given in Eq. 4.8. Further, the variation of Eq. 4.8 with atom-pair distance and fractional hydration is illustrated in Fig. 4.1c.

$$E_{\text{elec}} = \frac{C_0 q_i q_j}{\epsilon(h_{i,j}, d_{i,j})} \left[\frac{1}{\epsilon(h_{i,j}, d_{i,j})} - \frac{1}{\epsilon(h_{\text{water}}, d_{\text{max}})} \right] \tag{4.8}$$

4.3.2 Shifting the pK_a in the lipid bilayer

Most macromolecular modeling calculations assume the system is at neutral pH with fixed protonation states for titratable side chains. While this assumption is valid for some systems, it breaks down in a heterogeneous membrane environment. In particular, proton avidity for titratable sites (the pK_a) is influenced by electrostatic interactions within the lipid bilayer [215, 216]. To accommodate, we introduced protonation state sampling and a potential function that accounts for a shifted pK_a in the lipid bilayer.

We began with the Rosetta-pH framework developed by Kilambi & Gray [175]. This framework evaluates protonation probability using a simplified version of the potential developed by Onufriev *et al.* [217]. Here, the probability of protonating an isolated site is given by Eq. 4.9, an expression that is algebraically equivalent to the

Henderson-Hasselbalch sigmoidal titration curve [218].

$$f_{\text{prot}} = \frac{1}{10^{\text{pH - pKa}} + 1} \tag{4.9}$$

In this formalism, the protonation probability is 1/2 when the pK_a of an isolated site is equal to the pH. The pK_a is equal to the unperturbed intrinsic pK_a value of a model compound in solution ($pK_a = 4.0$ for Asp, 4.4 for Glu, 6.3 for His, 10.0 for Tyr, and 10.4 for Lys). Then, the protonation potential is given by Eq. 4.10 where the factor $k_B T$ is assigned a value of 0.59 kcal/mol which corresponds to 298K.

$$E_{\text{pH}} = -k_B T \begin{cases} \ln(f_{\text{prot}}) & \text{if protonated} \\ \ln(1 - f_{\text{prot}}) & \text{if deprotonated} \end{cases} \tag{4.10}$$

To accommodate the bilayer, we substituted the constant pK_a value for a function that depends on the fractional hydration h_i of the titratable site i. We derived the function using constant pH molecular dynamics data from Teixera *et al.* [125] that quantifies the increase or decrease of pK_a along the bilayer normal. The discrete data points were converted to an analytic functional form through non-linear regression to a generalized logistic equation (Eq. 4.11).

$$f_{\text{pKa}} = \frac{pK_{a,\text{max}}}{1 + \exp(-a(h_i - b))} + pK_{a,\text{min}} \tag{4.11}$$

The fitted parameters for the five titratable residue types are given in Table 4.1 and a comparison of the raw data and resulting analytic forms is shown in Fig. 4.2.

To create the bilayer-dependent protonation potential, we simply substitute the constant pK_a value by the bilayer dependent pK_a function (Eq. 4.11).

Table 4.1: Logistic parameters for bilayer-dependent pKa model

AA	a	b	$pK_{a,\text{min}}$	$pK_{a,\text{max}}$
ASP	-3.19	0.44	1.9	6.84
GLU	-3.03	0.44	1.32	7.06
HIS	0.82	2.47	-1.49	5.25
LYS	1.13	0.7	1.27	8.99
CYS	-3.59	0.8	3.34	11.87
TYR	-4.33	0.5	0.47	14.12

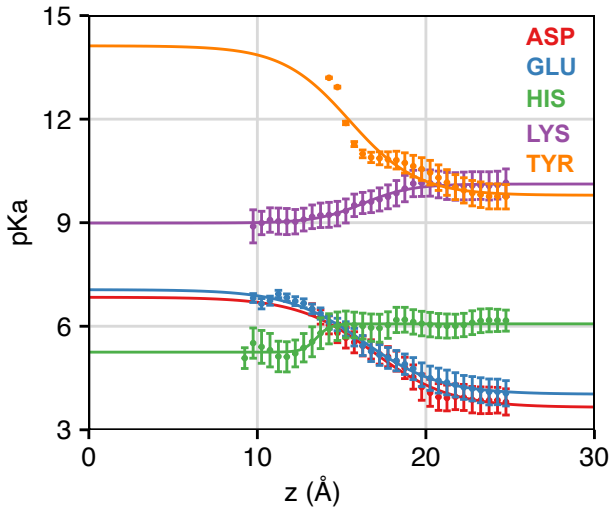

Figure 4.2: Dependence of site pK_a values on the membrane environment Shift in pK_a with bilayer depth for five protonatable side chains: aspartate (red), glutamate (blue), histidine (green), lysine (purple), and tyrosine (orange). Data points from constant pH molecular dynamics simulations are shown as dots with error bars and the analytic fit is shown as a solid line.

4.3.3 Sampling alternate protonation states

To sample alternate protonation states, we designed a task operation that modifies Rosetta's rotamer packing process. Typically, a packing process samples rotamers for the same chemical side chain type. This new task operation, called pHVariantTaskOperation, samples both protonated and de-protonated rotamers for titratable side chains. The sampling algorithm then relies on the energy term (above) to select the appropriate protonation state. The task operation can be easily added to any existing

Rosetta protocol.

4.3.4 Integrating new energy terms with *franklin*

We integrated the new energy terms into the existing *franklin* energy function in the following manner. First, we substituted the standard fa_elec term with our bilayer-dependent electrostatics energy, called fa_imm_elec. We kept the weight fixed at 1.0 to be consistent with the philosophy that molecular mechanics terms should not require weighting. The weight of the membrane-dependent protonation potential called menv_pH was set at 1.0 to ensure that the Henderson-Hasselbalch criteria is satisfied. Finally, we chose to down-weight the water-to-bilayer energy from 0.5 to 0.25 to eliminate potential double counting. This new energy function is called *franklin2020*.

4.4 Results & Discussion

4.4.1 pH-sensitive peptide insertion into lipid bilayers

I first evaluated the electrostatics model using a test that predicts the partitioning energy of pH-sensitive peptides (Test #6 in Chapter 3). We chose to start with this test because the calculation is sensitive to both dielectric and pK_a shifts. The test is modeled after work by Weerakkody *et al.* [166] who rationally designed 16 variants of the wild-type pH low-insertion-peptide (pHLIP) [215]. The authors quantified partitioning energy by intrinsic tryptophan fluorescence in the presence of 1-palmitoyl-2-oleoyl-sn-glycero-3-phosphocholine (POPC) liposomes at high pH (pH 8) and low pH (pH 4-5; Fig. 4.3a). Then, the authors computed the water-to-bilayer transfer energy as the difference in Gibbs free energy (ΔG) of the interaction of variants with the

membrane and low and high pH (in kcal/mol): $\Delta\Delta G_{\mathrm{b,\,pH}} = \Delta G_{\mathrm{b,\,pH\,4}} - \Delta G_{\mathrm{b,\,pH\,8}}$.

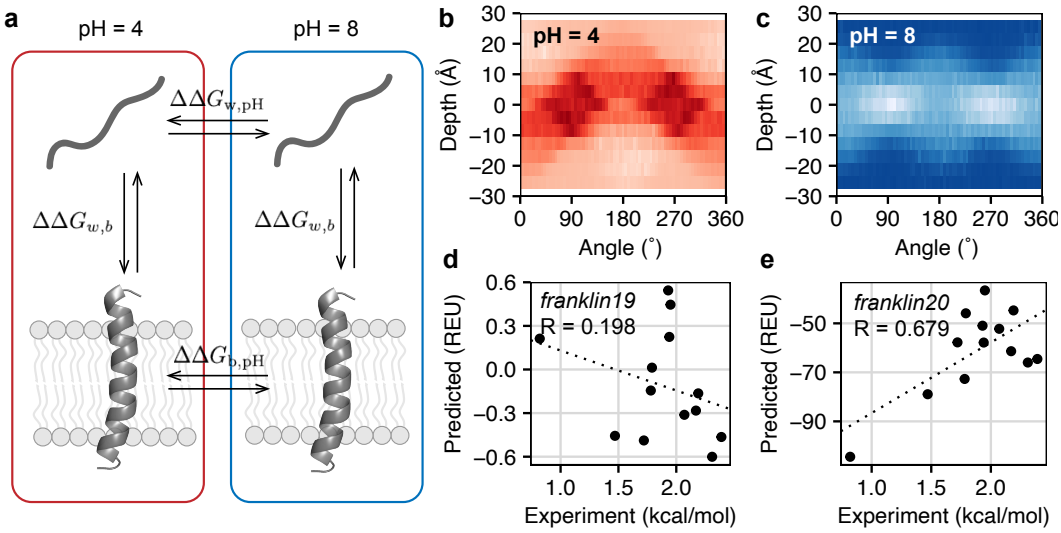

Figure 4.3: Performance of the membrane-aware electrostatics model on predicting bilayer insertion of pHLIP peptides. (a) Weerakkody *et al.* [166] measured the interaction of pHLIP variants with lipid bilayers at high pH (pH = 8) and low pH (pH = 4-5). Intrinsic fluorescence experiments approximate the value of $\Delta\Delta G_{w,b}$: the water-to-bilayer transfer energy. Then, the change in energy upon pH-shift in the bilayer is measured as the difference of $\Delta\Delta G_{w,b}$ and pH 4 and pH 8 (blue). Panels (b) and (c) show a mapping of orientations to energies for pHLIP variant # 4 at pH 4 (red) and pH 8. Light hues correspond to high energies and dark hues correspond to low energies. The bottom right-hand panel shows the performance of (d) *franklin2019* and (e) the updated model on prediction of the $\Delta\Delta G_{b,pH}$ for pHLIP variants. The dotted line is the line of best fit.

To attempt to recapitulate the experimentally measured $\Delta\Delta G_{\mathrm{b,\,pH}}$ values, we generated mappings of all peptide orientations to energies at both pH 4 and pH 8. Orientation is given as a function of tilt angle (°) and bilayer depth (Å). Importantly, the peptide side chains were re-packed at every grid point to allow sampling of the alternative protonation states. This procedure was repeated for all 16 variants and a sample mapping for variant #4 at pH 4 and pH 8 is shown in Fig. 4.3b and Fig. 4.3c, respectively. At pH 8, we found that the peptide preferred the aqueous phase; whereas, at pH 4 the peptide preferred a membrane embedded orientation. This result is consistent with the experimentally observed behavior for pHLIP peptide

insertion.

Next, we computed the partitioning energy as the energy difference between the lowest-scoring embedded conformations at pH 4 and pH 8. The data for predictions with *franklin2019* and the results for the new model *franklin2020* are reported in Fig. 4.3d and Fig. 4.3e respectively. In the previous model, there was no correlation between the experimentally measured and predicted values (R = 0.197). In contrast, the new electrostatics model results in a correlation of R = 0.679. Thus, the new electrostatics and pH-sensitive energy terms significantly improved predictions. Note, both R values exclude variants #3 and #16 as these peptides meet the Grubb's outlier criteria.

4.4.2 Transmembrane peptide insertion and neutral pH

Next, we investigated the performance of the model on the insertion of transmembrane peptides at neutral pH. To evaluate, we ran benchmark test #1 from Chapter 3. In summary, this test generates a mapping of orientations to energies for six transmembrane peptides and then compares the lowest energy tilt angle to the experimental measurement. The results are summarized in Fig. 4.4.

The performance of the new electrostatics model on the test #1 dataset is mixed. For four targets (1a11, 2nr1, poly-W and poly-Y), the peptide preferred a reasonable membrane orientation with a tilt between 0-30°and a depth close to the bilayer center. However, for 1mp6 and 1pje, the tilt angle minimum was closer to 90°. This result suggests that the new energy terms make the model too hydrophobic, thus incorrectly preferring burial of these peptides in the bilayer.

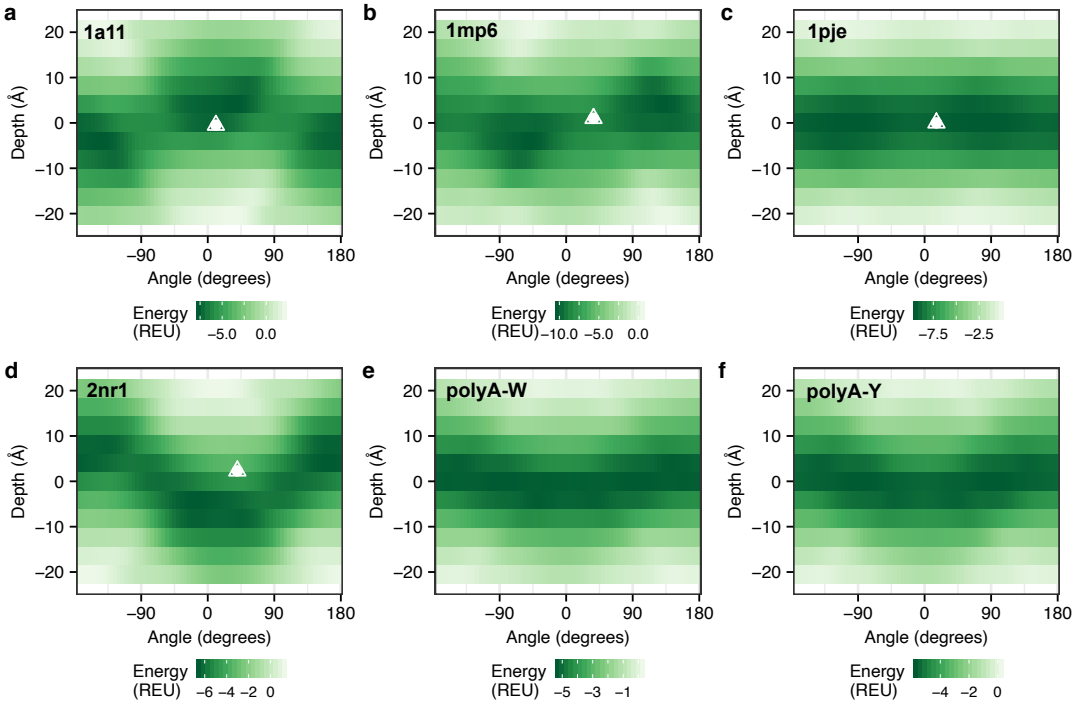

Figure 4.4: Prediction of non-pH dependent transmembrane peptide insertion. Prediction of orientation for six transmembrane peptides: (a) acetylcholine receptor, PDB 1a11, (b) M2 proton channel segment, PDB 1mp6, (c) VPU-forming domain, PDB 1pje (d) NMDA-receptor, PDB 2nr1, (e) designed poly-alanine peptide with flanking tryptophan residues and (f) designed poly-alanine peptide with flanking tyrosine residues. Each grid point represents the energy at a particular orientation, given as a function of tilt angle in degrees and depth in Å. The grid points are colored according to energy, with dark green hues corresponding to low energies and light green hues corresponding to high energies. White green triangles indicate the experimental solid-state NMR measurement of peptide tilt angle when available.

4.5 Conclusion

We have developed a molecular mechanics electrostatics model that considers the influence of the lipid bilayer. To account for the low-dielectric membrane, the model extends the Coulomb energy and considers shifted proton avidity for titratable sites. In proof-of-concept benchmarks, we demonstrated that the updated energy function improves partitioning energy estimates for pH sensitive transmembrane peptides. A next step is to run the remaining 10 benchmarks from Chapter 3 and iteratively

optimize the model. The model provides a starting point for considering two-body solvation effects toward improving the accuracy of membrane protein structure prediction and design.

Chapter 5

An *in silico* method to analyze ZMPSTE24 stability

This chapter includes material from Spear ED, Alford RF, Babatz T, Wood K, Mossberg O, Odinammadu K, Shilgardi K, Gray JJ, and Michaelis S (2019) "A humanized yeast system to analyze cleavage of Prelamin A by ZMPSTE24" *Methods* 157:47-55.

5.1 Overview

Over the past decade, the parity of α-helical bundle and β-barrel membrane proteins has been challenged by an influx of new membrane protein structures from previously unexplored families [219, 220]. A key takeaway is that membrane proteins are not simple cylinders: they occupy wide-ranging folds to perform their functions. For computational tools, capturing sophisticated protein folds further complicates the already difficult task of modeling the protein and bilayer. To learn more about these systems, we embarked on a collaborative study of the Integral Membrane Zinc Metalloprotease (ZMPSTE24). In this chapter, I describe a computational tool that compliments an experimental assay to probe the influence of mutations in ZMPSTE24

on protein stability and function.

5.2 Introduction

The *ZMPSTE24* gene has been associated with several rare diseases characterized by premature aging phenotypes. Mutations in the *LMNA* gene cause the premature aging disorder Hutchinson-Gilford Progeria Syndrome (HGPS) [221–225]. By one year of age, children with HGPS manifest accelerated aging symptoms, including failure to thrive, lipodystrophy, hair loss, join ailments, and cardiovascular disease [221, 226]. Mutations in the *ZMPSTE24* gene cause recessive diseases that share many features with HGPS. Restrictive dermopathy (RD) is a neonatal lethal disease with earlier onset and greater sensitivity than HGPS, whereas mandibuloacral dysplaysia-type B (MAD-B) develops later in life with milder symptoms. RD mutations ablate ZMPSTE24 function while ZMPSTE24 proteins with MAD-B mutations exhibit some residual function [227–229]. Understanding the molecular mechanisms of these premature aging diseases may bring significant insight into human health and longevity.

Previous work has revealed that the ZMPSTE24 protein is responsible for maturation of the nuclear scaffold protein lamin A from its precursor prelamin A. The complete biogenesis pathway of mature lamin A from its precursor, prelamin A, involves four enzymatic steps (Fig. 5.1). Prelamin A terminates with a C-terminal CAAX motif (where "C" is cysteine, "A" is generally an aliphatic amino acid and "X" is any amino acid other than proline). The CAAX motif directs the post-translational processing steps collectively called "CAAX processing" in which the cysteine sulfhydryl is farnesylated, followed by endoproteolytic cleavage of the -AAX tripeptide, and

carboxyl methylation of the farnesylated cysteine residue [229–232]. What distinguishes prelamin A from other CAAX proteins is that following these processing steps, prelamin A undergoes an additional cleavage mediated by ZMPSTE24 [233, 234]. Failure to perform this final cleavage results in accumulation of permanently farnesylated and carboxyl methylated prelamin A. This molecule causes aberrant nuclear morphology and is the culprit in progeroid diseases [221, 224, 235].

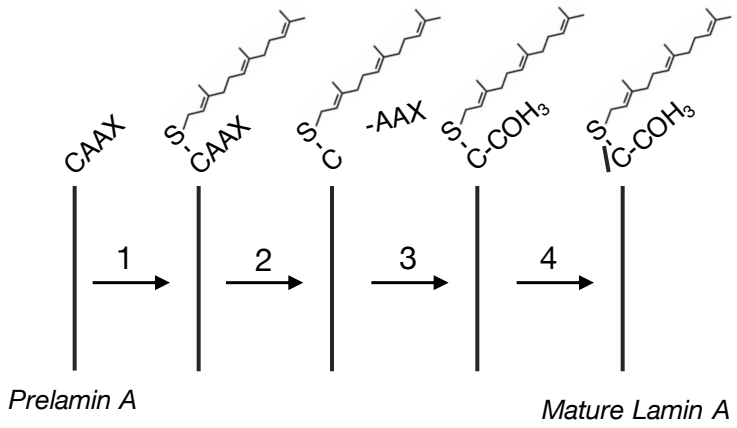

Figure 5.1: Maturation of the nuclear scaffold protein lamin A from the precursor prelamin A. The biogenesis of mature lamin A involves four steps: (1) farnesylation of the CAAX domain, (2) cleavage of -AAX by ZMPSTE24, (3) carboxyl methylation of the cystiene residue, and (4) full cleavage of the farnesyl domain.

ZMPSTE24 is an integral membrane proteins with seven transmembrane spans that is localized to both the inner nuclear membrane as well as the endoplasmic reticulum membrane [236–238]. The recently solved X-ray crystal structures of human ZMPSTE24, and that of the virtually superimposable yeast Ste24, reveal a completely novel and fascinating class of protease [239–241] (Fig. 5.2). The seven transmembrane spans comprise a helical barrel that surrounds a voluminous intra-membrane "hollow" chamber, large enough to accommodate about 450 water molecules. Surprisingly, the HEXXH active site conserved among all zinc metalloproteases does not face the

cytosol or nucleoplasm, but rather resides inside of this barrel in ZMPSTE24/Ste24. Side portals apparent in the structure are likely to provide access into the chamber interior for prelamin A and a-factor proteolytic cleavage.

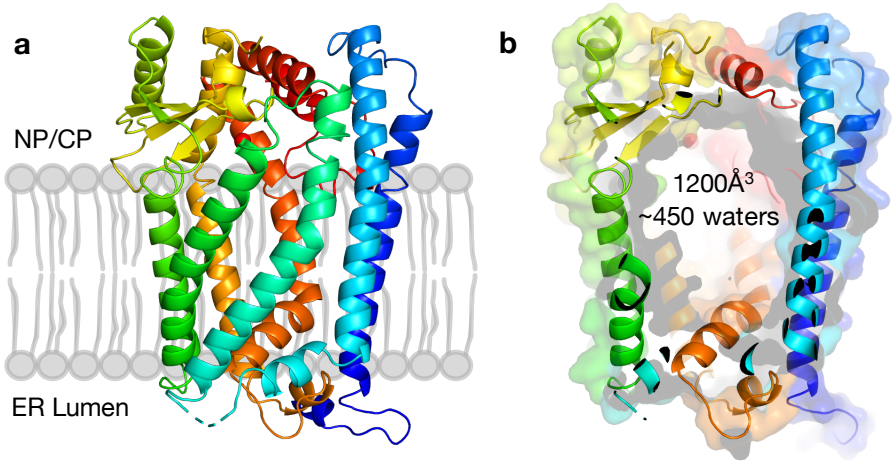

Figure 5.2: Structure of the human integral membrane zinc metalloprotease ZMPSTE24. (a) Crystal structure of the seven transmembrane spanning zinc metalloprotease (PDB 2ypt). (b) Clipped view of ZMPSTE24 revealing the hollow chamber of water.

Recently, Dr. Michaelis and Dr. Spear developed a high-throughput assay to probe structure-function relationships between ZMPSTE24 and its prelamin A substrate [229]. The assay is a fully humanized *Saccharomyces cerevisiae* system that can assess the activity and *in vivo* stability of disease or synthetic alleles of ZMPSTE24 relative to wild type. An example of this analysis for human disease alleles is shown in Fig. 5.3.In this chapter, we describe a complimentary *in silico* protocol to investigate the molecular mechanism underlying these mutations.

5.3 Methods

Our computational analysis was performed using a protocol adapted from the Rosetta $\Delta\Delta G$ protocol with flexible backbones described by Barlow and coworkers [242, 243]:

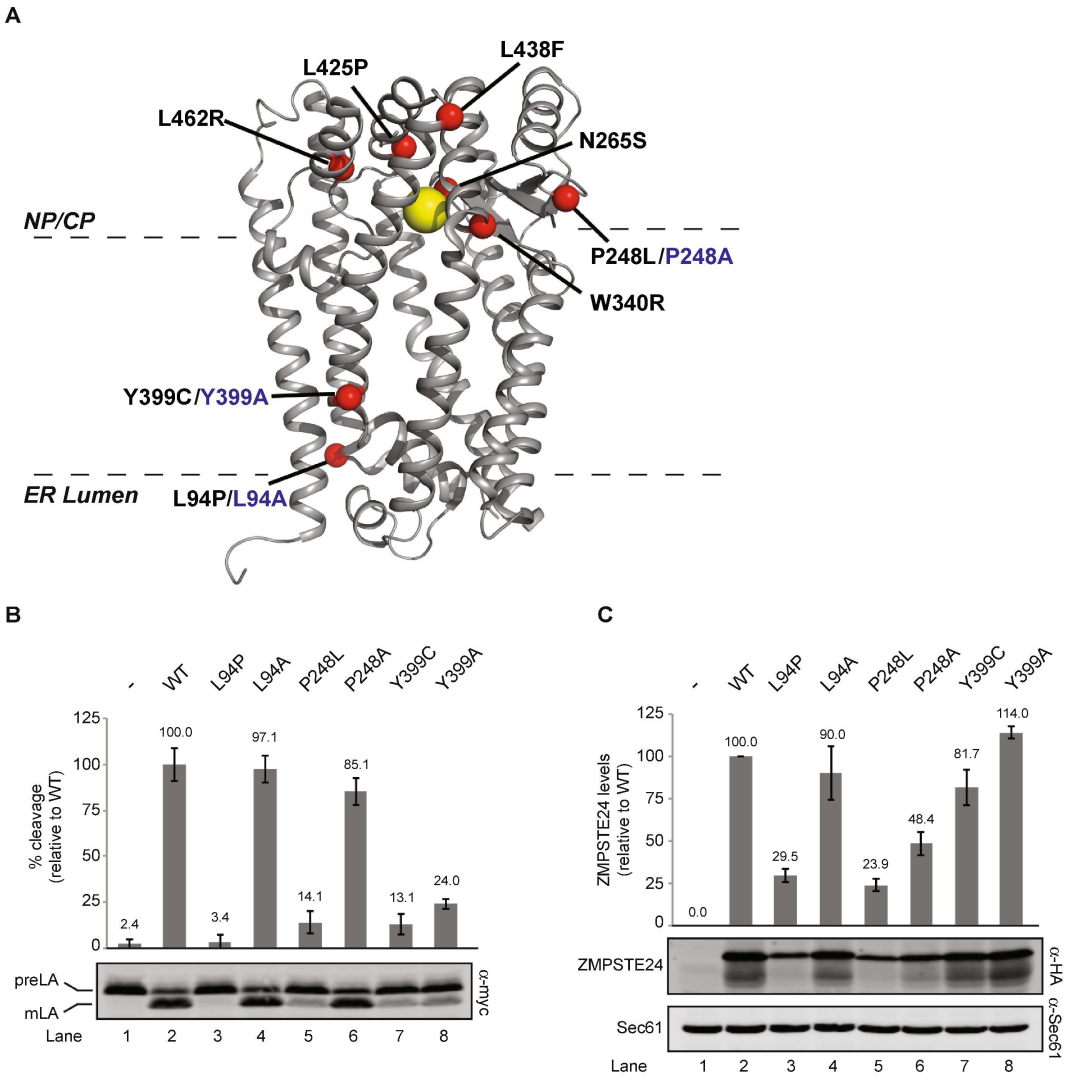

Figure 5.3: Structure-function studies of ZMPSTE24. (A) X-Ray crystal structure of human ZMPSTE24 (PDB entry 2ypt) embedded in the lipid bilayer with zinc indicated by the yellow ball and disease residues indicated with red balls. Disease alleles are labeled in black, with alanine changes in blue. (B) Average cleavage and standard deviation of the mean for three independent experiments is shown, with wild-type ZMPSTE24 activity set to 100% for comparison. (C) ZMPSTE24 protein levels were analyzed by western blotting using anti-HA (normalized to the loading control Sec61). The average and standard deviation of the mean is shown for the same three experiments as in (B). Wild-type ZMPSTE24 protein levels are set to 100% for comparison.

Starting with the crystal structure of ZMPSTE24 (PDB 2YPT) [241], we applied the $\Delta\Delta G$ protocol to generate refined model of both the native and mutated proteins.

Each model is an ensemble of 50 structures representing the most likely conformations. Then, we calculated the change in stability using the Rosetta all-atom energy function [61]. Rosetta calculates macromolecular energies as a linear combination of terms that evaluate van der Waals, electrostatics, solvation, backbone, and side chain energies. Here, we computed the $\Delta\Delta G^{\text{mut}}(X \rightarrow Y)$ as the difference between the average score of the mutant conformation ensemble $\Delta G(X)$ and the native conformation ensemble $\Delta G(Y)$ (Eq. 5.1).

$$\Delta\Delta G^{\text{mut}}(X \rightarrow Y) = \Delta G(X) - \Delta G(Y) \tag{5.1}$$

Further, we evaluated the contribution of individual energies to the using PyRosetta tools described in Chaudhury *et al.* [66].

5.4 Results

We used the Rosetta macromolecular modeling suite [51] to explore if we could generate structure-based hypotheses of each ZMPSTE24 variant's role in stability. Our approach is adapted from the flexible-backbone $\Delta\Delta G$ protocol described in Barlow and coworkers [242, 243]. The goal was to calculate the free-energy change for each mutant as compared to WT ZMPSTE24, since the predicted thermodynamic cost of a mutation might provide insight into the observed changes in *in vivo* stability.

The first step was to compare the calculations to the experimental *in vivo* stability and cleavage measurements from [229] for each variant. The calculated and experimental data are graphed in Fig. 5.4. In general, for this panel of mutants, we observed that the calculated values (y axis), expressed as Rosetta Energy Units (REU), exhibit a strong negative correlation with protein stability (Fig. 5.4A). As the magnitude

of $\Delta\Delta G^{mut}$ decreases, protein expression, which reflects in vivo stability, increases. For instance, the P248L is predicted by Rosetta to be much less thermodynamically stable than WT and Y399A is predicted to be more stable than WT, which roughly match the experimental data. The $\Delta\Delta G^{mut}$ of L94P is an outlier in our dataset. These results indicate that the thermodynamic stability measurements calculated by Rosetta correlate reasonably well with in vivo stability and suggest that what the cellular machinery detects as mis-folding is reflected in the Rosetta energy calculations of thermodynamic stability.

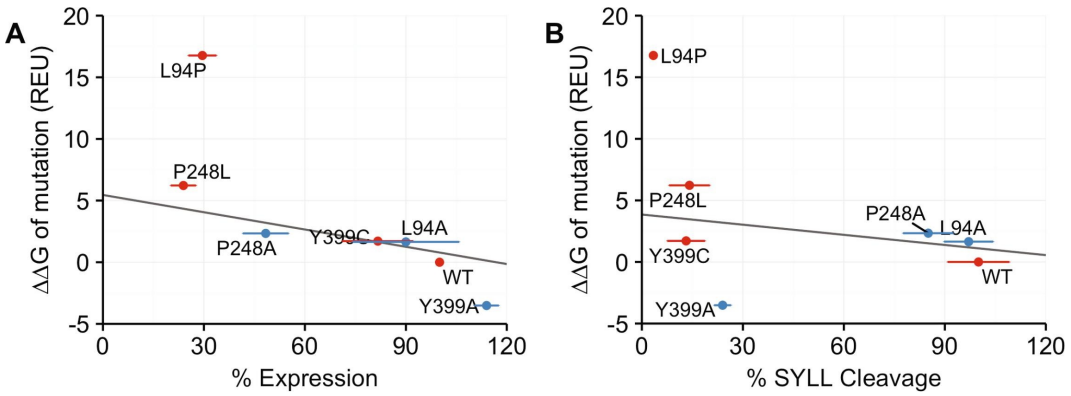

Figure 5.4: Comparison of experimentally measured ZMPSTE24 stability and cleavage with computed $\Delta\Delta G^{mut}$ values for mutant ZMPSTE24. The $\Delta\Delta G^{mut}$ is the predicted difference in free energy of folding between a WT and mutant protein. A) The calculated values in Rosetta Energy Units (REU) (y axis) for the indicated mutant alleles of ZMPSTE24 is compared with the level of ZMPSTE24 stability (denoted as expression; x axis). When the proline mutation L94P is excluded, the correlation coefficient is -0.843. (B) Comparison of calculations (y axis) with percentage of prelamin A cleavage determined in Fig. 4A (x axis). When the proline mutation L94P is excluded, the correlation coefficient is -0.207. Disease variants are in red and additional variants are in blue. Horizontal error bars are the standard deviation of the mean.

In contrast to the stability measurements, the prelamin A cleavage results do not correlate well with the Rosetta predictions (Fig. 5.4B). For instance, the of Y399C is 1.711 REU, while that of Y399A is strikingly low, yet both show strong cleavage defects. This result is not unexpected, because the Rosetta energy function is designed

to capture thermodynamic and not catalytic effects.

To further investigate how the calculated $\Delta\Delta G^{mut}$ values relate to predicted structural changes for these two mutations, we used energy decomposition and structure visualization. The comparison of the energy breakdown and structures for the Y399A/Y399C variants is shown in Fig. 5.5.

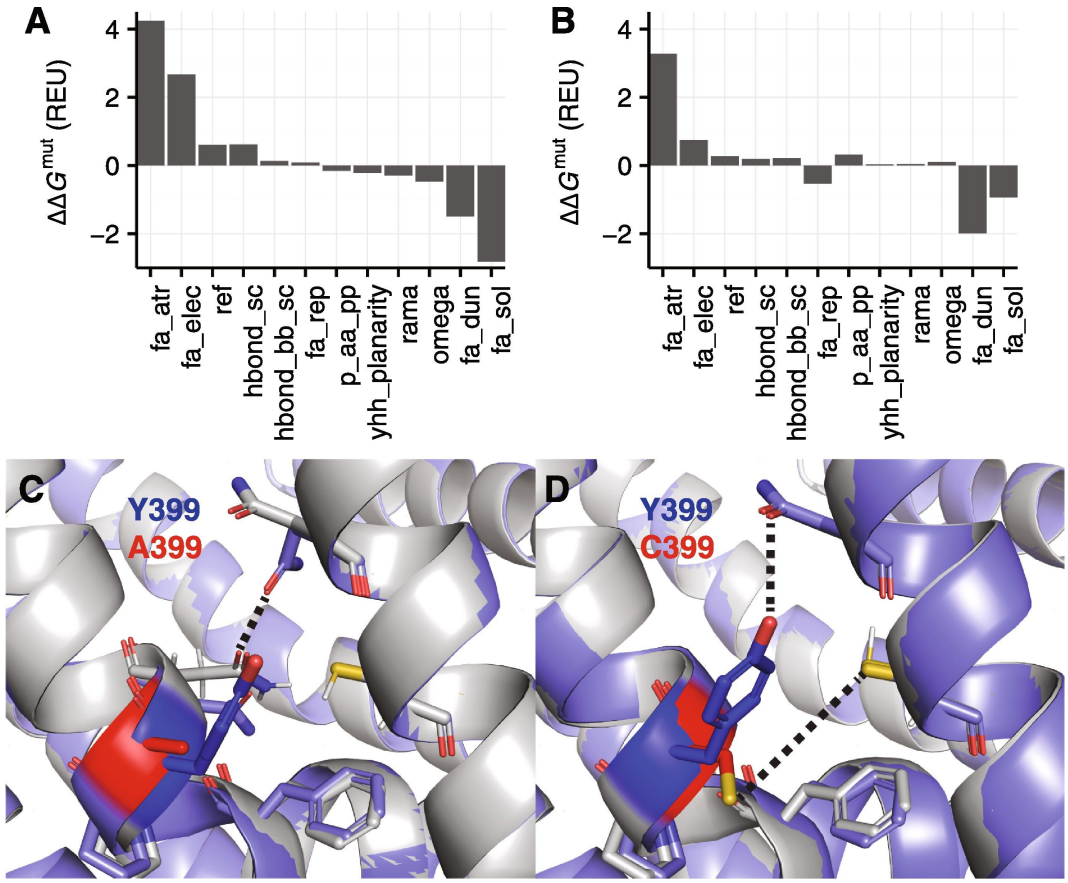

Figure 5.5: Structural and energetic effects of Y399A vs. Y399C in ZMPSTE24. We compared the Y399A and Y399C variants by analyzing the decomposed Rosetta energies and structural ensembles. (A) Decomposed $\Delta\Delta G^{mut}$ of the Y399C ZMPSTE24 variant. (C) Lowest scoring structure in the native ensemble (gray) superimposed onto the lowest scoring structure in the Y399A ensemble (purple). The native tyrosine is highlighted in blue and the mutant alanine is highlighted in red. Side chains within 3.0Å of the mutation are shown. (D) Lowest scoring structure in the native ensemble (gray) superimposed onto the lowest scoring structure in the Y399C ensemble (purple). The native tyrosine is highlighted in blue and the mutant cysteine is highlighted in red. Side chains within 3.0Å of the mutation are shown.

In the Y399A variant, the conformation loses favorable van der Waals attractive and electrostatic interactions, likely due to the loss of a hydroxyl group capable of hydrogen bonding to nearby side chains (Fig. 5.5A). However, this mutation is rescued by favorable side-chain conformations and solvation energies-define these terms briefly. The rotamer score improves because alanine is very small and is easy to fit into a pocket. The solvation score improves because position 399 is buried, thereby minimizing exposure of the hydrophobic alanine to solvent (Fig. 5.5C). In contrast, Y399C also loses favorable van der Waals and electrostatic interactions (Fig. 5.5B). This variant is not rescued by favorable solvation because cysteine is not as hydrophobic as traditional nonpolar residues. For Y399C, the structure is particularly revealing (Fig. 5.5D). There is a cysteine nearby capable of forming a disulfide bond with position 399, further deforming the aqueous cavity and potentially impacting catalytic activity. Overall, this structure-based analysis of Y399A and Y399C provides insight into the mechanism of stability loss and may ultimately be useful to suggest sites for potential therapeutics that rescue activity.

5.5 Discussion

In this work, we developed a computational method to compliment the humanized ZMPSTE24 assay. Our approach yielded in mechanistic models of ZMPSTE24 disease alleles. As a result, we generated model-based hypotheses on how the protein quality control machinery selects and degrades some mis-folded variants, while ignoring others. In addition to ZMPSTE24 insights, this collaborative study also revealed key areas for computational method improvement detailed below.

Proline residues. Proline residues occur frequently in membrane proteins, especially to facilitate kink and hinge formation. In this study, we found that the stability effects of disease alleles involving proline substitutions were not correctly modeled. We hypothesize this occurs because the backrub protocol does not capture the large backbone conformational change involved in accommodating a proline ring. This suggests that additional sampling may be required to accurately capture the change in stability due to proline substitutions.

Implicit membrane model. In this study, we used *ref2015* to capture the energetic costs of single point mutations. This approximation was practical because most mutation sites were exposed to the inside of the aqueous chamber of ZMPSTE24. However, it is more realistic to incorporate the membrane. Rosetta currently uses an implicit membrane model that can capture different pore shapes, however this does not extend to enclosed chambers. This suggests that the pore model will need to become even more flexible in the future.

Large protein size. A third challenge is that many membrane proteins including ZMPSTE24 include more than 500 residues. The large size significantly increases computational cost of the modeling protocol. This suggests a need for more efficient sampling strategies that can accommodate larger proteins.

Overall, this chapter reveals important future challenges for computational methods that model the effects of mutations on membrane protein stability. We anticipate these takeaways will be helpful in guiding future methods development efforts.

Chapter 6

Protein docking and steered molecular dynamics reveal alternative regulatory sites on the SERCA calcium transporter

With permission from the publisher, this chapter includes material from Alford RF, Smolin N, Young HS, Gray JJ, and Robia SL (2020) "Protein docking and steered molecular dynamics suggest alternative regulatory sites on the SERCA calcium transporter" *Journal of Biological Chemistry*

6.1 Overview

The transport activity of the sarco(endo)plasmic reticulum calcium ATPase (SERCA) in cardiac muscle cells is modulated by an inhibitory interaction with a 52-residue transmembrane peptide, phospholamban (PLB). Biochemical studies have revealed that PLB interacts with a specific inhibitory site on SERCA; yet, there is also low-resolution structural evidence that PLB interacts with alternative sites that are distinct from the inhibitory site. High-resolution structures would illuminate the structural determinants of regulation; however, experiments are complicated by the dynamic

nature of the regulatory complex. In this study, we use computational approaches to develop a structural model of SERCA-PLB interactions, toward a mechanistic understanding of SERCA transport regulation by PLB. Steered molecular dynamics (SMD) and membrane protein-protein docking experiments were performed to investigate the apparent affinity of PLB interactions with candidate sites on SERCA. We modeled the relative binding of PLB to several different conformations of SERCA, representing different enzymatic states sampled during the calcium transport catalytic cycle. Overall, the SMD and docking experiments indicate that the canonical binding site of the ideal conformation is preferred, but the binding preference becomes more ambivalent for other conformers. These structural models of SERCA-PLB interactions suggest PLB can interact with many loosely defined binding sites though rotation and translocation, enabling dynamic regulation of Ca^{2+} transport.

6.2 Introduction

The family of sarco(endo)plasmic reticulum Ca2+-ATPases (SERCA) is responsible for sequestering calcium into the sarcoplasmic and endoplasmic reticulum, creating a reservoir for intracellular Ca^{2+} signaling. These transporters are important in all cell types and are tightly controlled such that Ca^{2+} handling can rapidly adjust to changing physiological demands [244, 245]. A prime example is the regulation of the SERCA2a transporter in cardiac muscle cells. Calcium transport is reduced under resting conditions in the unstimulated heart through an inhibitory interaction with a single-span transmembrane peptide, phospholamban (PLB), which decreases the affinity of SERCA for its substrate, Ca^{2+}. The mechanism for this may be slowing the rate of the structural transition that occurs after binding of the first Ca ion [246],

and decreasing the rate of the transition between enzymatic states E1P and E2P [247]. Inhibition of SERCA by PLB is relieved at high Ca^{2+} concentrations or by phosphorylation of PLB by protein kinase A (PKA) [248] or calcium-calmodulin dependent kinase II (CaMKII) [249, 250] after stimulation of the heart by adrenaline [251]. Thus, PLB regulation of SERCA provides an "adrenaline trigger" to increase Ca^{2+} transport and increase cardiac output during exercise. The importance of this regulatory mechanism is underscored by the association of disordered Ca handling and heart disease [252]. This makes SERCA an attractive therapeutic target [253, 254] and motivates investigation of the structural elements that govern SERCA function.

Efforts to elucidate the mechanism by which Ca^{2+} and PLB phosphorylation relieve SERCA inhibition have focused on the relationship between SERCA-PLB binding and Ca^{2+} transport activity. Some studies suggested that SERCA inhibition is relieved by dissociation of the complex [255–257]. However, previous studies by our lab [258–261] and others [262–268] indicate that PLB remains bound after phosphorylation and in high Ca, and relief of inhibition is due to a structural change of the intact regulatory complex. Specifically, we previously hypothesized that the PLB transmembrane domain could become displaced from the canonical PLB-binding cleft and translocate to a non-inhibitory site on SERCA [261].

Structural models have further illuminated the mechanisms of SERCA regulation [269, 270]. Previous X-Ray crystallography studies have mapped out nearly every step in the SERCA transport cycle, revealing the different conformations of the intermediate enzymatic states [271, 272] (Fig. 6.1b) . Among the different states, the cleft formed by transmembrane helices M2, M6, and M9 is relatively more open or closed, structural transitions between SERCA conformers may alter contacts with

PLB. However, high-resolution structures of the SERCA-PLB regulatory complex have been elusive. One X-ray crystallographic structure that reveals aspects of the SERCA-PLB complex (Fig. 6.1a, "4KYT") [255] was obtained by exploiting a mutant form of PLB that greatly increases affinity and inhibitory potency. The degree to which this mutant recapitulates the regulatory complex structure of the wild-type protein is unknown. Moreover, several alternative interactions between SERCA and PLB are suggested by additional studies. X-ray crystallography [273, 274] and modeling [275] studies of closely related P-type ATPase, the sodium/potassium ATPase (NKA) indicated that NKA regulatory subunits, the FXYD family of proteins, bind to the outside of helix M9 (Fig. 6.1a, green). Another accessory binding site was suggested by electron crystallography of SERCA and PLB, which involves an interaction of PLB with transmembrane segment M3 of SERCA (Fig. 6.1a, red) [276–278]. These studies suggest novel regulatory complex configurations, but higher resolution models are required to reveal the mechanistic significance of these alternative modes of PLB binding.

Computational methods offer a promising route to elucidating protein-protein interactions, especially when paired with experimental data. Methods for modeling protein-protein interactions are well-established for soluble proteins [279]; however, progress for membrane proteins has been delayed because of the paucity of known structures [219] and difficulty accounting for the lipid bilayer. One approach is Molecular Dynamics (MD) which simulates the time-evolved behavior of a macromolecular system using Newton's equation of motion. Molecular dynamics most accurately represents the lipid bilayer; however, the large system size requires computationally expensive simulations, even with enhanced sampling techniques. In contrast, protein

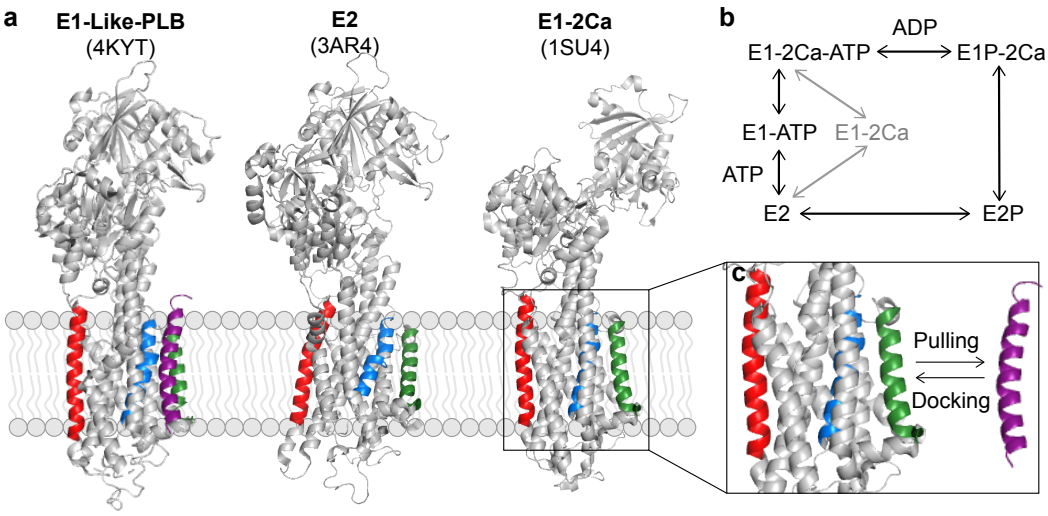

Figure 6.1: Exploring possible binding sites for phospholamban on different enzymatic states of SERCA. In this study, we examined the interaction of PLB with three different enzymatic states of SERCA. The three states are shown in (a): the E1-like state of SERCA bound to PLB (purple) (PDB 4KYT), the E2 calcium-free state (PDB 3AR4), and the E1 calcium bound state (PDB 1SU4). The canonical inhibitory binding site is formed by helices M2, M6 (blue), and M9 (green). The two postulated alternative sites are binding to the outside of helix M9 (green) and M3 (red). The role of each state in the catalytic cycle of ATP-mediated SERCA transport is shown in (b). Panel (c) shows two methods for exploring PLB interactions with SERCA. Steered molecular dynamics simulations pull PLB away from a postulated binding site and quantitate the unbinding force. In contrast, membrane protein docking tests possible interaction sites and quantitates the binding energy.

docking aims to predict the best binding conformation between two macromolecular partners [280]. Recently, a handful of protein-protein docking methods have been adapted to account for the membrane [65, 159, 281]. These methods are faster to compute and can examine both where and how macromolecular partners bind. However, many of the membrane-adapted methods are validated on a small dataset [186] and approximate features of the lipid bilayer.

When performed together, molecular dynamics and protein-protein docking can provide complimentary information about ideal binding conformations. Molecular dynamics approaches can account for explicit lipid-protein interactions; yet require enhanced sampling techniques that bias interactions. On the other hand, protein-protein docking tools can explore potential interactions in an unbiased manner yet approximate the bilayer environment. To overcome these barriers, we used a computational approach that integrates both molecular dynamics and molecular docking to develop a model for PLB interactions with the SERCA2a pump. For molecular dynamics, we chose to employ steered molecular dynamics (SMD)[282]: a well-established technique for examining protein-protein interactions by inducing receptor-ligand unbinding on an accessible timescale (Fig. 6.1c, "pulling"). Importantly, SMD offers the opportunity to quantify the unbinding force required to extract PLB docked to a candidate site in the context of an all-atom lipid bilayer, with peak force taken as an index of the affinity of PLB for that site. For molecular docking, we used RosettaMPDock: a tool that combines soluble Rosetta protein-protein docking [283] with the membrane protein framework that accounts for the position, orientation, and physical chemistry of the lipid bilayer (39) (Fig. 6.1c, "docking"). We applied these techniques to modeling the relative binding of PLB to three conformations of SERCA

(Fig. 6.1a) that represent major intermediates in the calcium transport cycle (Fig. 6.1b). Together, these techniques revealed both where and how PLB binds to the SERCA pump, providing insight into the structural determinants of the regulatory interaction of PLB with different enzymatic states of SERCA.

6.3 Methods

6.3.1 Preparation of starting structures

The SERCA/PLB complex was modeled from crystal structures of SERCA1a, the skeletal muscle isoform for which many conformations are available [272]. This isoform has high homology to the cardiac specific Ca pump, SERCA2a, and the recently published first structure of SERCA2a showed that the known PLB-binding site is highly conserved between these isoforms [284]. Here we generated models starting from three different SERCA1a structures: 1SU4 [285], representing an E1 Ca-bound state; 3AR4 [286], representing an E2 Ca-free state; and 4KYT [255], representing a Ca-free state bound to PLB. The latter Ca-free X-ray crystal structure was designated an E2 structure, but the conformation resembles an E1 structure, and is referred to as "E1-like" in the present study. In that x-ray crystal structural solution, the cytoplasmic domain of PLB was not observed. In addition, 4KYT contains structure of mutated PLB; for experiments that simulate interaction of WT-PLB with SERCA we mutated the residues back to the native sequence.

6.3.2 Steered molecular dynamics simulations

We examined transmembrane domain residues 22-52 of PLB docked in the canonical binding cleft of 4KYT or the equivalent site on 1SU4 or 3AR4. To test the possibility of

PLB binding to the putative alternative sites on SERCA, we created a model of the PLB bound to M9 using as a guide the NKA co-crystal structure with a FXYD protein [274, 275]. PLB was also docked to M3 to test a possible interaction hypothesized from cryo-EM studies of SERCA-PLB co-crystals [277, 278]. Additional models were generated to represent different relative orientations of PLB with respect to the binding interface on SERCA, rotating PLB around its long axis by 90°, 180°, and 270°.

All-atom MD simulations were carried out with the CHARMM 36 force field [287–289] and TIP3P water model [290]. Energy minimization was performed on the crystal structures using the steepest descent method for 1000 steps, then each model was embedded into a POPC lipid bilayer and solvated in a rectangular water box size with dimensions 130 Å by 130 Å by 160 Å. Na^+ and Cl^- ions were added to the solution to neutralize the charge of the system and to produce an ion concentration of 150 mM. The Particle Mesh Ewald method [291, 292] was used to calculate the long-range electrostatic interactions and cut-off of 12 Å was used for the short-range. Van der Waals interactions were reduced to zero by switch truncation applied from 8 to 12 Å. Simulations were carried out with an integration time step of 2 fs. To reach the target temperature (300 K) and pressure (1 bar) the Berendsen method was used with relaxation times of 0.1 ps [293]. After 1 ns equilibration, the production run was performed in the NPT ensemble using the Nose-Hoover thermostat [294, 295] and the Parrinello-Rahman barostat [296, 297] with relaxation times of 1.0 ps. The atomic coordinates of the trajectories were saved every 1 ps. The steered molecular dynamics (SMD) runs were carried out for 5 ns each.

To test the reproducibility of the experiments, three independent SMD runs were

performed for each orientation of PLB. Pulling force was applied with a spring constant of 1000 kJ/mol/nm with a constant pulling velocity of 0.001 nm/ps. Increasing the pulling speed increases the rupture force [298], but does not change the relative "stickiness" of candidate binding sites. Hence, this approach is useful for comparing the relative affinities of different binding modes. For these computationally intensive experiments we found that a pulling speed of 0.001nm/ps is an ideal compromise that allows sufficient time for side chain and lipid motions. Force was applied to backbone atoms of PLB transmembrane residues (ASN27 - ILE48), pulling PLB away from the candidate SERCA binding site along line connecting the SERCA binding site and TM region of PLB. During SMD run positions of SERCA Ca^{2+} atoms were constrained and atoms of PLB were allowed to move only in XY direction (in the membrane plane), and not along Z axis (normal to the membrane plane). During SMD runs we recorded pulling force values as a function of time, recording the peak force (rupture force) as an index of the affinity of PLB for the candidate binding site.

6.3.3 Protein-protein docking simulations

A search for SERCA-PLB interaction sites was performed using global and local docking. Each crystal structure was first refined using RosettaMPRelax [65] to erase artifacts from crystallization and prior binding ligands. To accomplish this, the protocol performs cycles of small backbone torsion moves followed by side-chain repacking and energy minimization of all torsion angles (ϕ, ψ, χ) [145]. For each starting structure, 50 PLB orientations were generated, and the lowest energy conformation was used as the next starting pose. Next, the ClusPro Fast-Fourier Transform (FFT)-based rigid-body docking server [299, 300] was used to perform a global search for SERCA-PLB binding sites. Then, the following criteria were used to filter solutions

from the best-scoring clusters: (1) the conformers are in the correct direction (e.g. V49G) and (2) the conformers span the membrane.

Following global docking, RosettaMPDock [65] was used to locally search for PLB binding orientations. RosettaMPDock an adaptation of the RosettaDock [283] minimization protocol that locally searches for docked PLB orientations through two stages (a) a coarse-grained stage to quickly identify favorable orientations and (b) an all-atom refinement stage that optimizes the rigid body position and side-chain rotamers. To account for the membrane environment, RosettaMPDock samples the protein-membrane orientation and represents the bilayer using an implicit membrane model. An implicit approach represents the solvent as a continuous medium rather than individual "explicit" solvent molecules. In this work, we used the Lazaridis Implicit Membrane Model (IMM1/EEF1) [63, 64] which captures the membrane environment as three phases: an isotropic water phase, an isotropic hydrophobic phase, and an anisotropic phase corresponding to the interfacial region. The IMM1 model is 30Å thick which is similar to the thickness of the endoplasmic reticulum membrane [6].

For each starting pose, 5,000 PLB orientations were generated. Then, the interface analyzer protocol [301] was used to compute two properties: (a) Axial Angle – the angle between the second principal axis of the 4KYT PLB conformation and the candidate PLB conformation and (b) $\Delta\Delta G_{bind}$ - the change in Rosetta energy when the chains are separated versus when they are in complex.

6.3.4 Z-score analysis

To quantify the significance of each major mode of SERCA-PLB binding, we computed two scores that measure the similarity of binding conformations, with values of zero indicating the conformations are identical, and larger values corresponding to greater differences. The first score called z_{all} evaluates the relationship of a particular binding conformation relative to the mean of all possible binding conformations. The second score, called z_{site} , computes the same quantity but relative to the mean of all structures interacting with a specific site (e.g. M3, M6/M9 or the outside of M9). For docking, the mean was computed from the top 5% of structures ranked by $\Delta\Delta G$ of binding.

6.4 Results

To test whether PLB may bind to putative alternative sites, we performed steered molecular dynamics and protein-protein docking of PLB to different conformations of SERCA. These conformations are sampled as SERCA progresses through the catalytic cycle (Fig. 6.1b), binding Ca ions from the cytoplasm and transporting them into the lumen of the sarcoplasmic reticulum. In this study, we examined three key SERCA conformations (Fig. 1A): (1) the calcium-free E1-like state bound by PLB (represented by 4KYT) [255], the calcium-free E2 state (represented by 3AR4) [286], which is characterized by a more open PLB-binding groove compared to 4KYT, and (3) the calcium-bound E1 state (represented by 1SU4) [285]. The starting structure of the PLB TM domain was taken from the PLB-SERCA complex 4KYT. The cytoplasmic domain of PLB was not detected in this X-ray structure and was omitted from the SMD simulations. Previous biochemical studies have demonstrated that the transmembrane domain is sufficient for binding and inhibition of SERCA [302].

6.4.1 Steered Molecular Dynamics (SMD) Simulations

To perform SMD simulations, the SERCA residue Cα atoms positions were first restrained by applying a spring force to each Cα atom, preventing significant deviations from the starting position. Pulling force was applied uniformly toCαresidues of PLB, with force directed away from the center of mass of the SERCA TM domain. Fig. 6.2a quantifies the force applied to PLB (vs. time) for three repeated simulations of PLB interacting with the canonical cleft of 4KYT beginning with the original orientation of PLB in the crystal structure. As the simulation progressed, the number of interacting residues decreased until the interaction was broken. As pulling progressed, force increased to a maximum, then rapidly declined to a non-zero plateau. The peak force represents the point at which the PLB-SERCA complex ruptured and was quantified as an index of binding affinity. The plateau force was due to viscous drag of the lipid bilayer after the loss of the protein-protein contacts.

For the equilibrated PLB-SERCA crystal structure (4KYT), we determined a peak force of 1292$\pm$69 kJ/mol/nm (error is standard deviation for n = 3). The simulation was then repeated for four different PLB orientations, rotating the helix around its long axis by 90°, 180°, and 270°. Simulations of alternative axial orientations showed 30% lower peak force (Table 6.1), Fig. 6.2b-c), which is consistent with the native orientation of PLB in the X-ray crystal structure being the most stable configuration. Z-score analysis is given in Supplementary Table 6.3.

6.4.1.1 SMD of PLB Docked to Alternative Sites

We performed SMD experiments comparing PLB bound to the canonical M6/M9 site with PLB bound to alternative sites to M3 or to the outside of M9, with three repeated

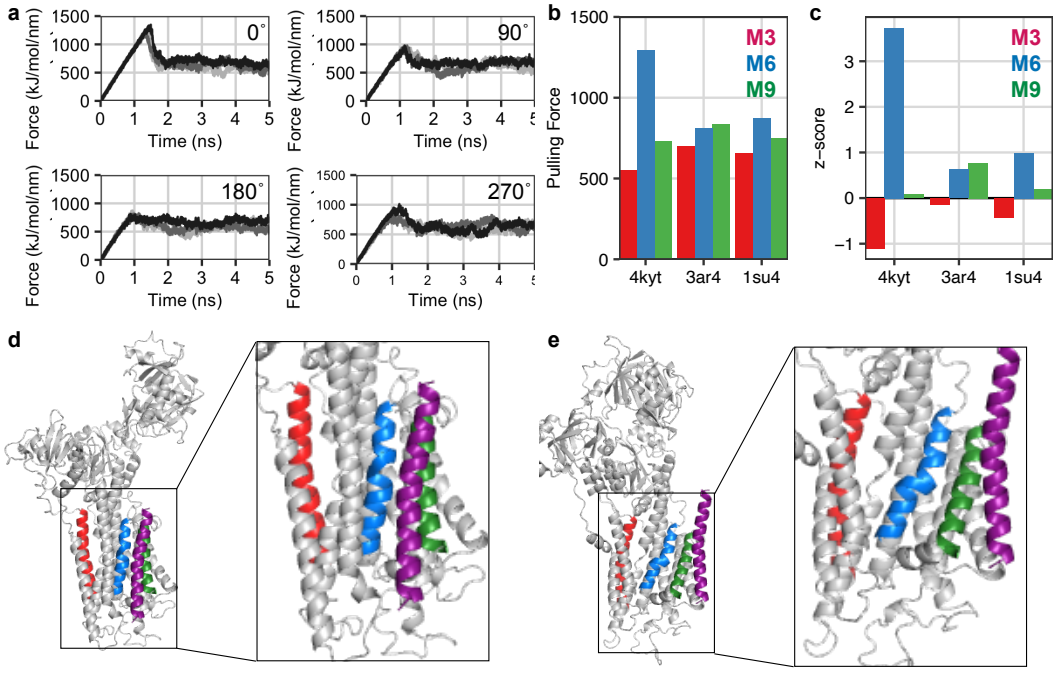

Figure 6.2: Steered molecular dynamics simulations of PLB interactions with different sites on three enzymatic states of SERCA. (a) Quantification of force that developed as PLB was pulled away from the canonical cleft of the E1-like-PLB state of SERCA. Data are three repeated measures of force for the original orientation of the X-Ray crystal structure (PDB 4KYT) and after axial rotation of PLB by 90°, 180°, and 270°. (b) Peak unbinding force from SERCA in kJ/mol/nm upon dissociation with transmembrane (TM) helix 3 (M3; red), or the canonical cleft formed by TM helices 6 and 9 (M6/M9; blue), or the outside of TM helix 9 (M9; green). (c) Z-score analysis of peak unbinding forces relative to the mean pulling force at the M3 (red), canonical (blue) and outside M9 (green) sites. Structural models of key interactions with non-canonical sites are shown in the bottom row. (d) Interaction of PLB (purple) with the canonical binding site formed by helices M6 (red) and M9 (green) in the E1-calcium bound state of SERCA (PDB 1SU4). (e) Interaction of PLB (purple) with the M9 accessory site (green) in the E2 calcium free state of SERCA (PDB 3AR4).

Table 6.1: Summary of PLB interactions with different SERCA states quantified by steered molecular dynamics

State	Site	Mean Rupture Force (kJ/mol/nm)			
		0°	90°	180°	270°
4KYT	M3	546 ± 53	526 ± 41	485 ± 38	550 ± 27
	M6/M9	1292 ± 69	982 ± 3	838 ± 31	914 ± 84
	M9	686 ± 46	731 ± 45	688 ± 27	616 ± 44
3AR4	M3	544 ± 20	640 ± 52	698 ± 14	572 ± 9
	M6/M9	848 ± 29	814 ± 22	729 ± 40	720 ± 94
	M9	658 ± 40	580 ± 87	811 ±12	838 ±108
1SU4	M3	606 ± 49	655 ± 23	629 ± 25	601 ± 39
	M6/M9	871 ± 25	775 ± 97	833 ± 81	766 ± 15
	M9	682 ± 32	681 ± 55	736 ± 88	749 ± 60

trajectories simulated for each orientation (Supplementary Fig. 6.7). The average peak force associated with the alternative sites was reduced by approximately 50% compared to the canonical site. Binding to M3 or the outside of M9 was modestly improved by axial rotation of the PLB transmembrane domain by 270° or 90°, respectively (Table 6.1; Fig. 6.2b-c) but rupture forces were still lower than those observed for various axial orientations of PLB at the canonical site. The data suggest that PLB binds best to the M6/M9 site in the E1-like conformation captured in the SERCA-PLB crystal structure. When bound to the canonical site, PLB interacts with side chains of SERCA helices M4, M6, and M9. In contrast, when docked to the outside of M9 in the manner of binding of FXYD proteins with M9 of the sodium/potassium ATPase [274, 275], PLB had interactions with M9 only which accounts for the lower rupture force of this configuration.

6.4.1.2 SMD of Different SERCA Conformations

Next, we measured the relative binding of PLB to different conformations of SERCA to test how PLB affinity might change as a result of SERCA structural transitions

during the catalytic cycle. Repeated SMD simulations revealed that peak rupture force for PLB bound to the canonical binding site (Fig. 6.2b-c, Supplementary Fig. 6.8) of the calcium-free E2 state (3AR4) structure was 34% lower than that observed for the E1-like state (4KYT). Interestingly, the rupture force for PLB bound to the hypothetical alternative site outside M9 in a 270° orientation (Fig. 6.2d) was slightly improved for E2 compared to the binding of PLB to the outside of M9 of the E1-like structure. Thus, due to improved binding to the outside of M9 and worsened binding to the canonical M6/M9 site, the two alternative sites then showed similar maximal rupture forces (838±108 and 848±29 kJ/mol/nm, respectively). The Ca-bound E1 structure (1SU4) yielded a peak force that was 33% lower than that observed for E1-like state (Fig. 6.2e, Supplementary Fig. 6.9). E1-Ca also showed a decrease in the rupture force deficit between the M6/M9 site and the proposed site outside M9 compared to the E1-like structure (4KYT). The magnitude of the difference in rupture forces observed for 4KYT (Ca-free) vs. 1SU4 (Ca-bound) is in harmony with our previous physical measurements that suggested a 41% difference in apparent binding for the SERCA-PLB complex in low and high Ca conditions [261]. Overall, the data indicate that there is a clear preference for the E1-like PLB-bound state captured by the crystal structure. However, for other enzymatic states, PLB may bind with similar affinity to the canonical site and the putative site on the outside of M9. This result is broadly compatible with the hypothesis of diverse modes of interaction between PLB and SERCA.

6.4.2 Membrane Protein-Protein Docking of the SERCA-PLB complex

Our molecular docking strategy involves two steps: (1) a global-docking step to explore possible PLB binding sites in an unbiased manner and (2) a local docking

step to optimize possible SERCA-PLB binding poses in the context of the lipid bilayer. We required two steps because there are currently no global docking strategies that account for the membrane. For step one, we used fast-Fourier transform (FFT)-based global docking (48) to identify possible binding sites on different enzymatic states of SERCA (represented by structures 4KYT, 3AR4, and 1SU4). For each structure, the FFT method identified 30-50 overall docked SERCA-PLB complexes, ranked by an energy function that uses desolvation and electrostatic energy terms, and filtered based on the requirement for PLB to span the membrane in the correct orientation. Using these criteria, we obtained eight SERCA-PLB complexes for the calcium-free E1-like state of SERCA (4KYT) (Fig. 6.3a,d), five for the calcium-free E2 state (3AR4) (Fig. 6.3b,e), and six for the calcium-bound E1 state (1SU4) (Fig. 6.3c,f).

Several docking solutions included PLB bound to the M6/M9 canonical site; while the remaining solutions included PLB docked at the M3 accessory site. This result contrasts with the SMD experiments, which showed no appreciable affinity of PLB for this site. Moreover, while the SMD experiments suggested some affinity of PLB for the putative binding site on the outside of helix M9, the unbiased protein-protein docking experiments did not yield M9-docked structures among the most favorable solutions. Additional comparison of the complementary methods is provided in the Discussion section below.

6.4.2.1 Docking of Different Axial Orientations of PLB

After obtaining initial docked SERCA-PLB complexes, we used RosettaMPDock [65] to optimize high-ranking PLB orientations within the membrane environment. RosettaMPDock is an adaptation of the RosettaDock [283] protocol that locally searches for docked structures in two stages. First, the algorithm performs a coarse-grained

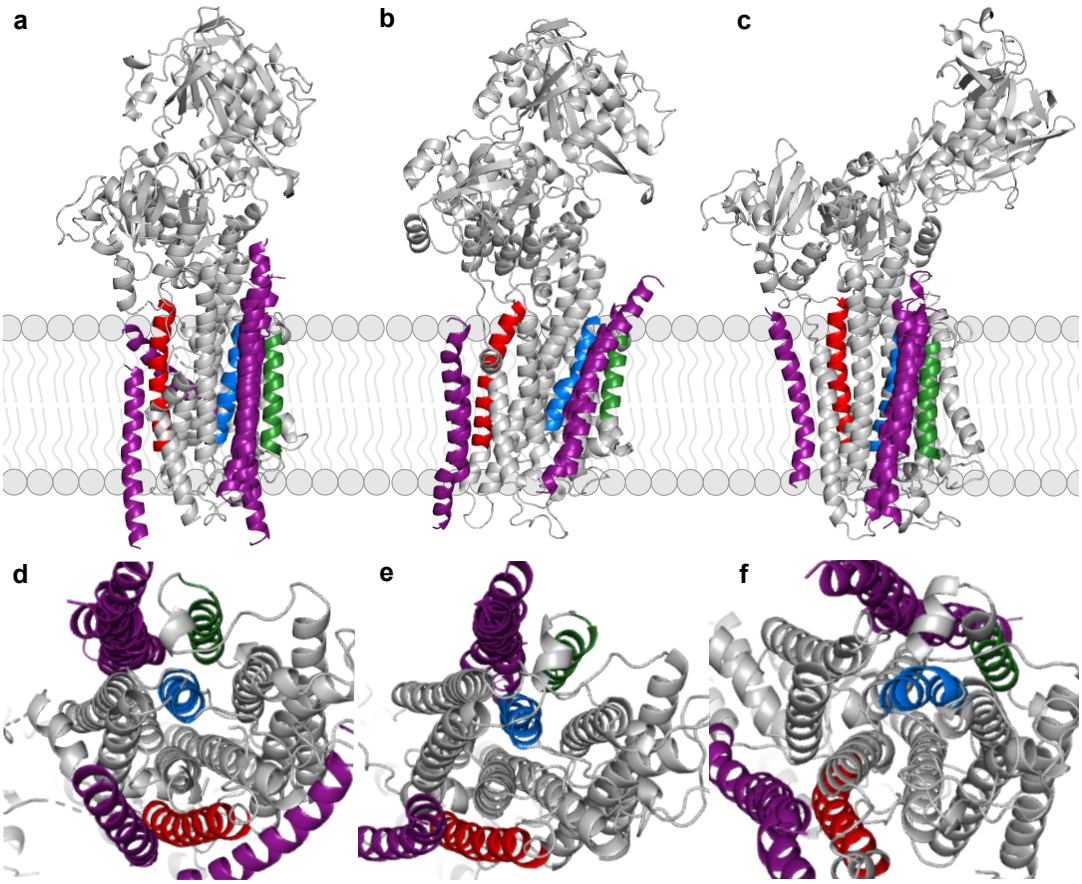

Figure 6.3: Global protein-protein docking solutions for PLB interaction with different enzymatic states of SERCA. For each enzymatic state of SERCA, we used a fast-Fourier transform (FFT) based global docking program to find possible binding sites and conformations of PLB at those sites. PLB binding solutions (purple) are shown bound to each enzymatic-state of SERCA in a membrane-facing view (top row) and luminal view (bottom row): (a,d) 4KYT, (b,e) 3AR4, and (c,f) 1SU4. The canonical cleft is highlighted with M6 in blue and M9 in green and the alternative sites are highlighted with M3 in red and M9 in green.

search with random rigid-body rotations and translations. Then, an all-atom stage includes side-chain optimization and minimization along side chain torsion degrees of freedom. RosettaMPDock uses an implicit model to represent the bilayer: meaning the heterogeneous lipid bilayer is represented as a continuous medium rather than individual "explicit" solvent molecules. In the context of this study, an important consequence of an implicit model is that we cannot capture interactions between the protein and specific lipids. Therefore, any displacement of PLB relative to SERCA is due to changes in the protein conformation and any interchain interactions.

For each of the 19 SERCA-PLB docked complex starting structures we generated 5,000 high-resolution candidate structures. The resulting structures were ranked by PLB angle of rotation around its long axis, tilt angle relative to the membrane normal, and the $\Delta\Delta G$ of binding to SERCA. Importantly, RosettaMPDock follows the premise that the observed complex is almost always in a low free-energy state [58]. Therefore, the resulting complexes represent snapshots rather than dynamics of SERCA-PLB interactions in energy minima. A summary of the strongest interactions of PLB with each structural state of SERCA is provided in Table 6.2 and the full list of SERCA-PLB interactions is provided in Supplementary Table 6.4.

Table 6.2: Summary of top ranking PLB interactions with different SERCA states identified through protein docking

State	Site	#	Start (°)	Axial (°)	Energy (REU)	z_{site}	z_{all}
E1-2Ca (1SU4)	M6/M9	0	11	6	-53.1	-4.3	-6.1
		1	46	25	-56.9	-5.8	-2.8
	M3	9	280	273	-46.2	-3.5	-4.5
E2 (3AR4)	M6/M9	1	319	321	-49.3	-2.7	-2.8
		17	89	87	-47.4	-2.0	-2.0
	M3	6	335	334	-45.1	-3.0	-0.9
E1-Like-PLB (4KYT)	M6/M9	2	347	6	-53.8	-4.6	-4.8
		5	277	267	-54.8	-5.0	-5.2
	M3	6	278	298	-45.2	-3.0	-1.0

For the E1-like state of SERCA (4KYT), we observed two SERCA-PLB complexes at the M6/M9 site with strong binding affinity with rotational axial angles of 6° and 267°. Both structures exhibit a strong binding funnel (Fig. 6.4a), meaning that the conformations with the lowest $\Delta\Delta G$ of binding are concentrated at a specific PLB axial rotation angle. Further, both z-scores indicated strong and specific interactions, with z_{all} of -4.3 for the 6° PLB orientation and -5.2 for the 267° orientation. These docked complexes are represented in Fig. 6.4b in red and blue, respectively. The first orientation was closest to the SERCA-PLB crystal structure (4KYT) with an all-atom root-mean-squared-deviation (RMSD) between PLB from the crystal structure and PLB from the model of 0.89 Å (Fig. 6.4b). Fig. 6.4c shows a helical wheel representation of PLB, highlighting key residues in the interface with SERCA for the 6° (red) and 267° (blue) orientations, and residues that are common to the interfaces of both orientations (orange). The docking results implicating this face of the PLB helix are in harmony with previous biochemical and cross-linking studies [303, 304] and are consistent with the interpretation of the SERCA-PLB co-crystal X-ray structure [255]. Global docking also identified a PLB rotational orientation that interacted with the M3 accessory site, though the apparent binding affinity was weaker than those observed for binding to the M6/M9 canonical site (Supplementary Fig. 6.11). M3-binding yielded interface energy of -45.2 Rosetta energy units (REU) and both z-scores indicated weaker binding (Table 6.2, Supplementary Table 6.4). Note, the Rosetta Energy Unit is an arbitrary unit that approximates a kcal/mol. Overall, the binding affinity for the M6/M9 is only modestly better (21% improvement in REU) than the M3 site, suggesting that M3 is a reasonable alternative interface for PLB.

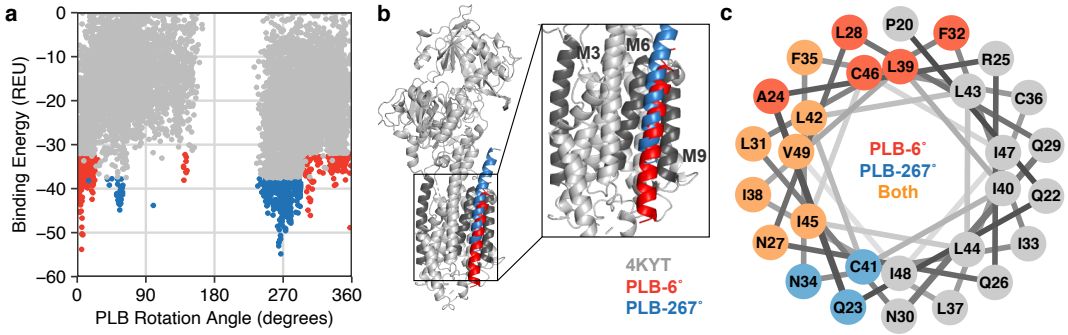

Figure 6.4: High-resolution model of PLB interaction with the SERCA 4KYT canonical cleft. Molecular docking identified two PLB orientations interacting with the 4KYT canonical cleft, characterized by axial rotation angles of 6° and 267°. (a) Ranking of PLB orientations by axial rotation angle and binding energy. The top 5% scoring points are colored in red for the 6° conformation and blue for the 267° conformation. (b) Conformation of the SERCA-PLB regulatory complex, with a 2x zoomed view of the transmembrane domains. The 6° PLB orientation is shown in red and then 267° orientation is shown in blue, with the M3, M6, and M9 helices highlighted in dark gray. (c) Helical wheel diagram showing the PLB interface residues. Positions unique to the 6° orientation are shown in red, positions unique to the 267° conformation are shown in blue, and mutual positions are colored in orange.

6.4.2.2 Docking of PLB to different SERCA states

The global docking results were also consistent with a multiplicity of interactions between PLB and other conformations of SERCA. Interestingly, there were two strong binding interactions between PLB and the E2 conformation. The first was PLB binding to M6/M9 at 321° with a binding affinity of -49.3 REU (Supplementary Fig. 6.12a-c) and the second was PLB interacting with the alternative M3 site at 334° with a binding affinity of -45.1 REU (Table 6.2, Fig. 6.5a and Fig. 6.5d). While the gap between binding affinities to the canonical cleft and M3 site was 10 REU for the E1-like-PLB state (4KYT), the gap narrowed in the E2 (3AR4) state to only 4 REU. Further, the interaction z-scores were suggestive of a significant interaction with this site.

Finally, we also examined the affinity of PLB for different sites of the Ca-bound structure of SERCA (1SU4). Overall, we found that PLB bound the most tightly

to the M6/M9 canonical site for two rotation angles, 6° and 25° (Supplementary Fig. 6.12d-f). Both sites exhibited strong binding funnels with z_{all} scores of -6.1 and -2.8 respectively. Interestingly, the first conformation was the same binding angle as the low energy E1-like M6/M9 structure, suggesting that face of the helix encodes an important sequence for SERCA interaction. PLB also bound to the M3 site at an angle of 280° (Fig. 6.5b,e), a similar angle for which moderate binding was predicted for docking to the E1-like structure. These data emphasize the role of M3 as an important site for PLB binding. Binding to M3 of SERCA has been observed for both PLB [277] and SLN [305] and is hypothesized to play a role in regulating the maximal activity (Vmax) of SERCA [277, 306]. The docked complexes are most similar to our model for PLB [277] where SERCA residues such as Val^{269} and Trp^{272} appear to stabilize the interaction. In the recent model for the SERCA-SLN complex [305], SLN sits directly along M3 though residues such as Val^{269} are predicted to interact in all cases.

6.4.2.3 Comparison of WT-PLB and PLB4 Binding to SERCA

To investigate the contribution of specific key side chains to the energetics of the PLB-SERCA regulatory complex, we repeated the protein-protein docking experiments with the quadruple mutant PLB4 (N27A, N30C, L37A, V49G) that was used to obtain the 4KYT X-ray crystal structure (Supplementary Table 6.5). This super-inhibitory mutant binds more avidly than the WT sequence [307]. Interestingly, PLB4 docking solutions did not include significant binding to the alternative site on SERCA helix M3. At the canonical M6/M9 site, we observed similar docking for WT-PLB and PLB4, with a narrow binding funnel and interface energies ranging between -54 and -57 REU (Table 6.5, Fig. 6.6a), but the interface energy was slightly more favorable for docking of PLB4. In addition, there were fewer favorable orientations for PLB4

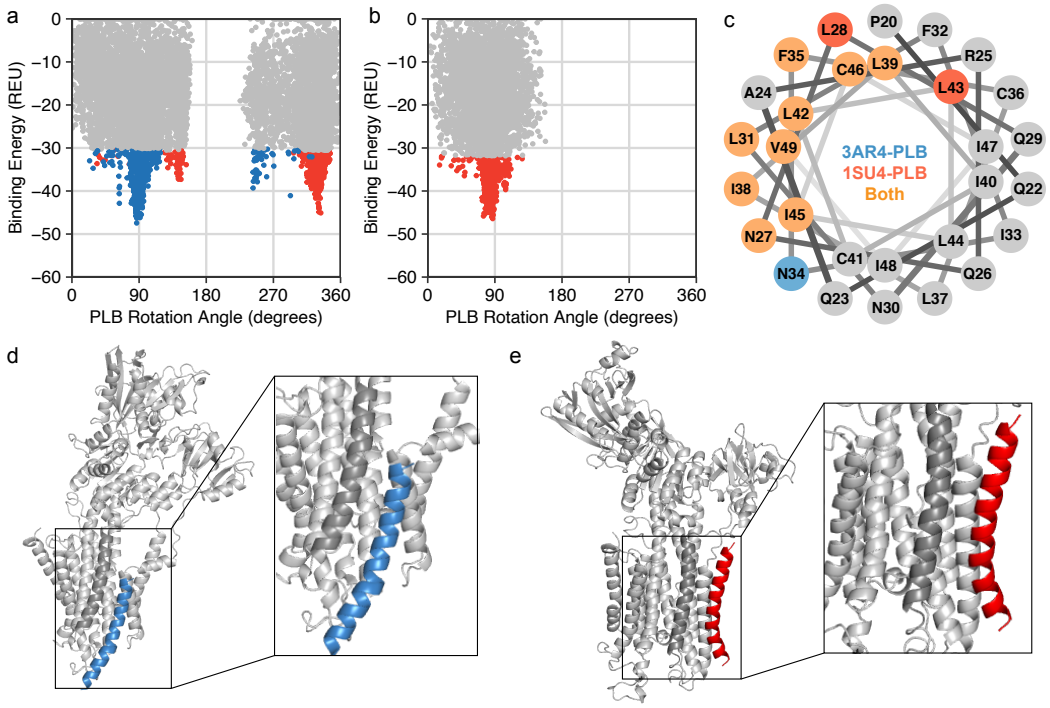

Figure 6.5: High-resolution models of PLB interaction with the M3 accessory site in the E1 and E2 enzymatic states of SERCA. . Molecular docking identified PLB interaction with the M3 helix of the 3AR4 (E2) and 1SU4 (E1-2Ca) enzymatic states of SERCA. Panels (a) and (b) show a ranking of PLB orientations by axial rotation and binding energy, with the top 5% scoring points shown in blue and red for 3AR4 and 1SU4 respectively. (c) Helical wheel diagram showing PLB interface residues: side chains only interacting with 3AR4 are shown in blue, positions only interacting with 1SU4 are shown in red, and mutual positions are shown in orange. Panels (d) and (e) show structural models for PLB interactions with 3AR4 and 1SU4 respectively. PLB is highlighted in red or blue, and a 2x zoomed representation of the transmembrane domain is shown to the right of the full SERCA model.

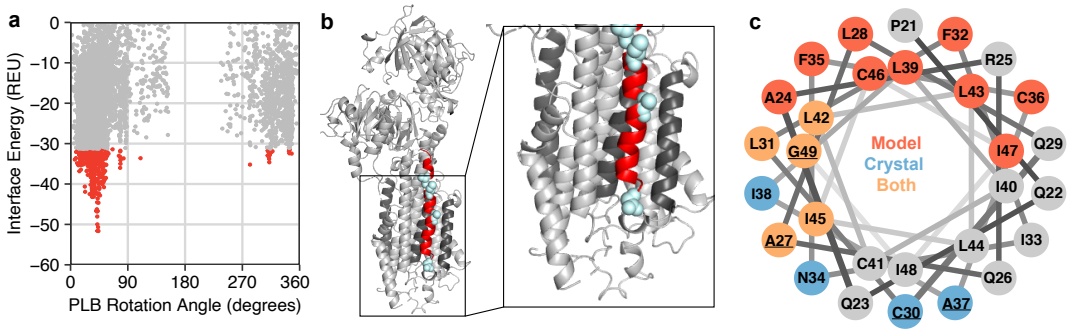

Figure 6.6: Interactions between SERCA and the PLB4 variant. Protein-protein docking identified interactions between the PLB4 variant (N27A, N30C, L37A, V49G) and the canonical cleft of the E1-Like state of SERCA. Panel (a) shows a ranking of PLB4 orientations by axial rotation and binding energy with the top 5% scoring points shown in red. (b) Structural model of PLB4 interaction with the canonical cleft of 4KYT. PLB4 is highlighted in red with mutation positions colored in light blue. A 2x zoomed representation of the transmembrane domain is shown to the right of the full SERCA model. (c) Helical wheel diagram showing PLB4 interfaces with different enzymatic states of SERCA. The PLB4 mutant sites are underlined. Positions colored in red are part of the docking model interface, positions in blue are part of the crystal structure interface, and positions in orange are common to both.

(Fig. 6.6a) than for WT (Fig. 6.4a). The data suggest that the mutations that enhance PLB binding to SERCA increase the specificity of the interface with regard to the range of favorable axial rotational angles of PLB and the preference for the M6/M9 cleft of SERCA. We noted that the SERCA-binding interface was different from WT, and surprisingly, several of the mutated residues faced the bilayer, rather than the SERCA-PLB interface. Only the N27A and V49G mutant residues participated in direct interactions with SERCA (Fig. 6.6b-c).

6.5 Discussion

The goal of this study was to test the hypothesis that PLB may interact with alternative binding sites on SERCA and determine how the population of the alternative sites by PLB may shift with the transporter's changing structural poise. The motivation for the present computational study comes from consideration of previous physical

measurements: a) SERCA-PLB binding affinity changes with SERCA conformational changes [261], but PLB remains bound to SERCA throughout the enzymatic cycle [261, 263, 264] b) cryo-EM studies showed densities attributable to PLB near SERCA TM helix M3 [277, 308]; c) X-ray crystallography of an analogous transporter, NKA, showed its cognate regulatory peptide bound to the outside of TM helix M9. We investigated modes of SERCA-PLB interaction through a combined strategy of hypothesis-driven steered molecular dynamics and unbiased protein-protein docking. Overall, the data support the hypothesis for multiple, loosely defined binding sites. The results provide new insight into the diverse modes of interaction for the PLB-SERCA regulatory complex.

6.5.1 Structural Determinants of the SERCA-PLB Regulatory Complex

The most important point of comparison for the present results is with the high-resolution structure of SERCA co-crystalized with PLB (4KYT) [255]. While that structure did not resolve the PLB cytoplasmic domain, it did reveal details of an interface between the PLB transmembrane domain and SERCA. PLB was found at the expected location, in the canonical binding cleft comprising SERCA helices 2, 6, and 9. Residues that were identified as important for the PLB-SERCA interaction in that structure and previous biochemical studies [303, 304] also emerged as key elements in the SMD and unbiased protein-protein docking analysis performed here. Key binding residues identified by biochemistry and crystallography include N27*, N30*, L31, N34, L37*, I38, L42, I45, and V49* (residues marked with asterisks indicate residues mutated to create the superinhibitory mutant PLB4) [253]. Those residues were the majority of the interface observed by docking SERCA E1-like conformers with the most favorable PLB rotational orientations (Fig. 6.4c). Those residues also partially

overlapped with other PLB binding interfaces observed from protein-protein docking (Fig. 6.5c) and SMD. The other major surface of PLB that repeatedly appeared in docking experiments was the upper left quadrant of the helical wheel (Figs. 6.4c, 6.5c, and 6.6c). Engagement of this surface was frequently associated with a significantly different binding position for PLB, suggesting movement of the regulatory peptide either through an upward shift in the membrane (Fig. 6.5d and 6.5e), or translocation to a completely different alternative site (Fig. 6.2e). The involvement of residues near the top of the helical wheel was also favored for the E1 Ca-bound conformation of SERCA (1SU4, Fig. 6.5e), consistent with the concept that SERCA conformational changes alter the nature of the binding of PLB, or, alternatively, that different modes of PLB binding are important for different enzymatic states in the SERCA transport cycle. The data may reconcile apparently contradictory studies of the calcium dependence of chemical cross-linking and FRET experiments. PLB-SERCA FRET is maintained in high Ca, suggesting the complex is intact [261, 263, 264], but cross-linking of PLB is lost in high Ca [256, 257, 304, 309]. If the rotational angle and vertical register of PLB changes with the E2-E1 transition it is not surprising that crosslinking of specific residues is greatly diminished.

In this regard, it is instructive to compare the results of docking of wild-type PLB to SERCA with docking of the high affinity, super-inhibitory quadruple mutant PLB4. The latter interacts very avidly with SERCA [256] and provided a sufficiently stable regulatory complex to achieve co-crystallization for X-ray studies [255]. Plots of the interface energies of PLB rotational orientations show similar landscapes, with PLB4 funnels (Fig. 6.6a) appearing at similar axial angles as those manifested by WT-PLB (Fig. 6.4a). However, the WT sequence yields more deep funnels (Fig. 6.4a and

Supplementary Fig. 6.10), suggesting the WT helix has more docking options that are energetically acceptable. Therefore, we hypothesize that PLB mutations that caused tighter binding to SERCA [303] and yielded well-ordered structures for crystallization [255] tailored PLB to bind in a specific orientation to a specific (canonical) binding site of a specific SERCA conformer.

6.5.2 Alternative Modes of Binding of PLB to SERCA

Protein docking studies identified transmembrane segment M3 in both the E1-2CA and E2 states of SERCA as a potential interaction interface. Of the docked complexes between SERCA and the wild-type PLB monomer, one of the solutions (model #6) is similar to the previously described MD simulations of the SERCA-PLB pentamer complex based on electron crystallography [277]. The docked complex is not identical to the previous complex, though this is likely due to the PLB pentamer used in the prior docking and MD simulations. In addition, that previous study used the human PLB sequence (in which residue 27 is a lysine), while the present docking analysis follows the X-ray crystallography study in using the canine PLB (with an asparagine at position 27). Nonetheless, the PLB monomer in the docked complex (Fig. 6.5) interacts with M3, but it is located more toward transmembrane segment M1 of SERCA and it is shifted upward by one turn of the helix. The interaction interface between SERCA and PLB is similar in the two models, with key residues such as F32 and I45 of PLB and K26 and Y272 of SERCA contributing. In the docked complex, N34 interacts with E258. This fits with the previous conclusion that electrostatic interactions, at least in part, draw PLB into this region of SERCA. The negatively charged residues include D254 and E255 on M3 and additional residues on M1 (e.g. D59 and E58). Finally, it is interesting to note that the protein docking of the PLB4

variant used in the X-ray crystal structure of the SERCA-PLB complex did not yield a docked complex at the M3 accessory site of SERCA. Only the wild-type PLB yielded satisfactory docking to M3 of SERCA. As discussed above, the results suggest the mutations increased the selectivity of PLB4 binding to the canonical binding site on M6.

6.5.3 Complementary Approaches for Interrogating Membrane Protein Complexes

Steered molecular dynamics and protein-protein docking provided complementary perspectives in evaluating PLB-SERCA binding interactions. SMD offers an all-atom view of SERCA's behavior in a biologically realistic membrane, quantifying rupture forces as an index of protein-protein binding affinity. On the other hand, protein-protein docking provides an unbiased strategy. RosettaMPDock, in particular, is one of a few specialized docking methods that can efficiently and inexpensively explore new conformations while considering the physical properties of the surrounding lipid bilayer. Overall, the results from the two types of experiments were in harmony. Most notably, both suggested that the canonical binding cleft is the most favorable site for PLB binding.

On the other hand, the methods provided different insights into the interactions between PLB and alternative sites, and the binding of PLB to different SERCA conformers. Both SMD and protein-protein docking simulations suggest that M3 is a plausible alternative site. Docking yielded a favorable PLB orientation at 298° binding with weak-to-moderate affinity (Fig. 6.5). By SMD, the best M3 binding is seen for the 180° and 90° orientations, yielding a rupture force that was 1 or 2 standard deviations from the mean rupture force, respectively. Interestingly, the 180° orientation

that showed relatively weak affinity by SMD (1 standard deviation above the mean). This configuration did not appear among high-scoring docking results, suggesting it is not a preferred orientation. In contrast, there was an 80° PLB orientation with weak binding affinity (-35 REU). We regard the 80° value (from docking) and 90° value (from SMD) as representing a similar possible orientation of PLB bound to M3. Another difference between the experiments is that the 298° orientation observed in docking was not tested by SMD, because those experiments systematically evaluated fixed PLB orientations at 90° intervals. The identification of a favorable "in-between" orientation at 298° demonstrates the added value of an unbiased docking strategy for identifying new quaternary arrangements that may be important for regulating SERCA transport function.

Conversely, SMD provided insight into a possible interaction that was not detected by docking. SMD experiments showed binding to hypothetical site on the outside of M9 was relatively strongly site- and orientation-specific for PLB in for the E1-like Ca-free (3AR4) conformation of SERCA. The 180° and 270° orientations of PLB bound to M9 yielded rupture forces that appeared equally favorable to the canonical cleft. However, despite this apparent site selectivity, it was a moderately weak binder overall, as compared to all other interactions. Thus, the site was not ranked highly enough to be discovered by protein-protein docking. On the basis of the SMD experiments, we suspect that the outside of M9 may be populated by PLB for some conformations of SERCA, such as the E2 Ca-free state represented by 3AR4 (Fig. 6.2). An analogous interaction is that of the sodium/potassium ATPase, which binds FXYD proteins on the outside of M9 of the NKA alpha (catalytic) subunit. This regulatory complex also benefits from the contribution of additional contacts between the FXYD

extracellular residues with the NKA beta subunit [274], accounting for the apparently stable occupation of that position in the crystal structure. Overall, the disparity between the SMD and docking results underscores the value of complementary approaches for evaluating metastable interactions that may be biologically significant. A possible future step is to use global docking poses as input to SMD to further integrate information from these approaches

6.5.4 Challenges for modeling of protein-protein interactions in the membrane

In this study, we applied two complementary strategies to investigate a physiologically important integral membrane interaction. This dual strategy enabled the computational feasibility of exploring the wide protein-protein interaction space for a large target (>1,000 residues) while also considering the context of a heterogeneous membrane environment. This is an exciting study in membrane protein structural biology because specialized methods for exploring membrane protein-protein interactions are still in their infancy. In particular, there are many open questions about the biophysical questions driving protein-protein interactions in the nonpolar membrane environment. With this, these specialized methods require improvement in several areas. For instance, the protein-protein docking program kept the backbone of both SERCA and PLB fixed. However, it is likely that PLB bends or straightens to enhance shape complementarity with its binding partner. This is especially notable because transmembrane membrane helices are notorious for kinks and curvature [310]. Programs for incorporating backbone flexibility have emerged for soluble proteins [52, 311] and these developments will soon translate to membrane proteins. Another challenge is incorporating the effect of bilayer deformations induced by the protein

that influence the landscape of available protein-protein complex conformations. Further, the all-atom membrane in SMD only included one lipid type, whereas biological membranes include hundreds of different lipid types [6]. While building membrane models with complex lipid compositions is computationally expensive due to a long equilibration time, improved computing capabilities will make these models within reach.

6.5.5 Implications for our understanding of SERCA-PLB interactions

This study represents a shift for our understanding of regulation of cardiac calcium handling. The reasonable first assumption about the regulatory complex of SERCA with PLB was that there was a simple, specific, lock-and-key mechanism where PLB occupies a single stringent binding site with a fixed orientation and a well-defined binding interface. Previous physical measurements have gradually undermined this simplistic model. FRET measurements suggested additional binding interfaces, characterized by different binding affinities [261]. Additional interfaces were also demonstrated by cryo-Electron Microscopy [277, 308]. Moreover, a number of non-specific hydrophobic peptide sequences were shown to functionally inhibit SERCA [312], indicating a looser specificity than was previously appreciated. The present results may reconcile these previous findings, as they suggest PLB can bind SERCA at three alternative sites using several different favorable orientations. The preference among these sites and orientations is determined by the enzymatic poise of the structurally dynamic SERCA pump, which may explain ligand-dependent changes in site-specific chemical cross-linking of PLB to SERCA [256, 313]. The structural details revealed by the present study may suggest new binding interfaces that could be explored with cross-linking, mutagenesis, or other physical experiments. Finally, the

results reveal a possible mechanism for the gain-of-function of PLB4, a superinhibitory mutant of PLB [307].

6.5.6 Summary

In conclusion, we find that PLB-SERCA binding interactions are more diverse than can be appreciated from previous studies that suggested PLB binds with a fixed orientation to a single site on a specific SERCA conformer. Instead, the present data are consistent with spectroscopic results that suggest PLB interacts with all SERCA enzymatic states and structural data that suggest additional alternative binding sites. We propose PLB equilibrates between different modes of binding. Some of these mode changes are minor shifts of PLB within a binding pocket (e.g. rotation about the PLB long axis, or normal translations in the bilayer), while others involve translocation to completely different sites (e.g. to the outside of M9 or to M3). Based on the increased apparent specificity of the superinhibitory PLB4 mutant for the M6/M9 site, we conclude that the canonical binding mode mediates functional inhibition, and we presume that the other sites are non-inhibitory, or possibly even stimulatory [247, 277, 306]. Thus, PLB transitions between different structural poises may deliver different functional outcomes as is appropriate for the varying demands of different physiological conditions.

6.6 Appendix

6.6.1 Supplementary Tables

Table 6.3: Summary of z-scores for PLB conformations explored by steered molecular dynamics

State	Site	Angle (°)	Force (kJ/mol/nm)	z_{site}	z_{all}
4kYT	M3	0	546	-1.13	-0.68
		90	526	-1.26	-1.01
		180	485	-1.52	-1.68
		270	550	-1.1	-0.61
	M6/M9	0	1292	3.73	2.77
		90	982	1.71	0.76
		180	838	0.77	-0.18
		270	914	1.27	0.32
	M9	0	686	-0.21	-0.25
		90	731	0.08	0.36
		180	688	-0.2	-0.22
		270	616	-0.67	-1.2
3AR4	M3	0	544	-1.14	-0.71
		90	640	-0.51	0.86
		180	698	-0.14	1.8
		270	572	-0.96	-0.25
	M6/M9	0	848	0.84	-0.11
		90	814	0.62	-0.33
		180	729	0.07	-0.89
		270	720	0.01	-0.95
	M9	0	658	-0.4	-0.63
		90	580	-0.9	-1.7
		180	811	0.6	1.47
		270	838	0.77	1.84
1SU4	M3	0	606	-0.74	0.3
		90	655	-0.42	1.1
		180	629	-0.59	0.68
		270	601	-0.77	0.22
	M6/M9	0	871	0.99	0.04
		90	775	0.36	-0.59
		180	833	0.74	-0.21
		270	766	0.31	-0.65
	M9	0	682	-0.24	-0.3
		90	681	-0.25	-0.31
		180	736	0.11	0.44
		270	749	0.2	0.61

Table 6.4: Summary of PLB binding conformers in complex with different states of SERCA

State	Site	#	Start (°)	Axial (°)	Energy (REU)	z_{site}	z_{all}
1SU4	M6/M9	0	11.41	5.85	-53.091	-4.26	-6.13
		1	45.57	25.15	-56.9	-5.82	-2.83
		2	250.55	266.67	-49.41	-2.77	-2.19
		3	35.53	55.75	-47.93	-2.15	0.58
		5	298.32	303.334	-41.64	-0.42	-1.52
	M3	9	279.61	272.93	-46.15	-3.49	-4.45
3AR4	M6/M9	1	319.01	321.477	-49.33	-2.72	-2.8
		2	336.29	341.806	-44.7	-0.83	-0.77
		17	88.58	86.711	-47.43	-1.95	-1.97
	M3	6	335.41	333.569	-45.09	-2.99	-0.94
		10	142.1	131.42	-41.31	-1.57	-0.72
1SU4	M6/M9	0	49.82	52.63	-46.23	-1.46	-1.44
		1	29.93	36.52	-43.77	-0.45	-0.36
		2	346.97	5.734	-53.8	-4.55	-4.76
		3	57.03	287.873	-47.82	-2.11	-2.14
		4	252.61	255.553	-44.2	-0.63	-0.54
		5	276.54	266.95	-54.83	-4.97	-5.22
	M3	6	277.7	298.45	-45.2	-3.03	-0.98
		7	292.29	69.44	-41.45	-1.61	0.66

Table 6.5: Summary of PLB4 binding conformers in complex with different states of SERCA

State	Site	#	Start (°)	Axial (°)	Energy (REU)	z_{site}	z_{all}
1SU4	M6/M9	1	17.47	17.501	-53.77	-3.15	-2.97
	M3	2	102.32	56.8	-42.49	-0.75	-0.04
3AR4	M6/M9	1	322.12	324.08	-49.53	-2.289	-1.87
		2	337.69	338.96	-49.46	-2.28	-1.85
		3	57.17	59.62	-52.76	-3.57	-2.71
	M3	4	115.47	329.37	-38.75	0.283	0.92
4KYT	M6/M9	1	25.25	24.49	-56.62	-3.73	-3.71
		2	28.71	43.8	-51.64	-2.718	-2.41
	M3	3	60.93	65.29	-44.91	-1.41	-0.674
		4	55.25	52.68	-45.2	-1.49	-0.75

6.6.2 Supplementary Figures

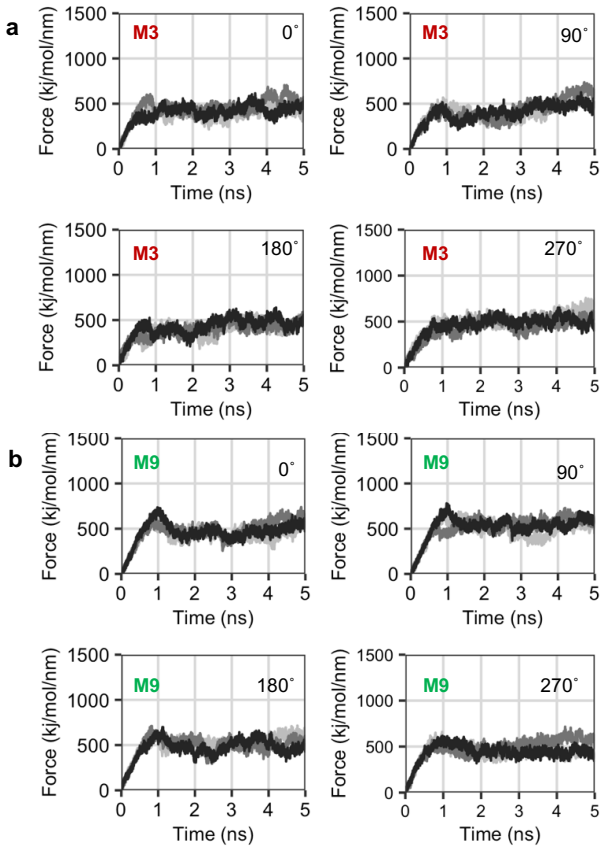

Figure 6.7: SMD simulations of the E1-Like-PLB state of SERCA with PLB. Quantification of force that developed as PLB was pulled from the canonical cleft of the E1-like-PLB state of SERCA (represented by 4KYT). Data are three repeated measures of force for the original orientation of the X-Ray crystal structure (PDB 4KYT) and after axial rotation of PLB by 90°, 180°, and 270°. The data are shown for interaction with the M3 (a) and M9 (b) helices of SERCA.

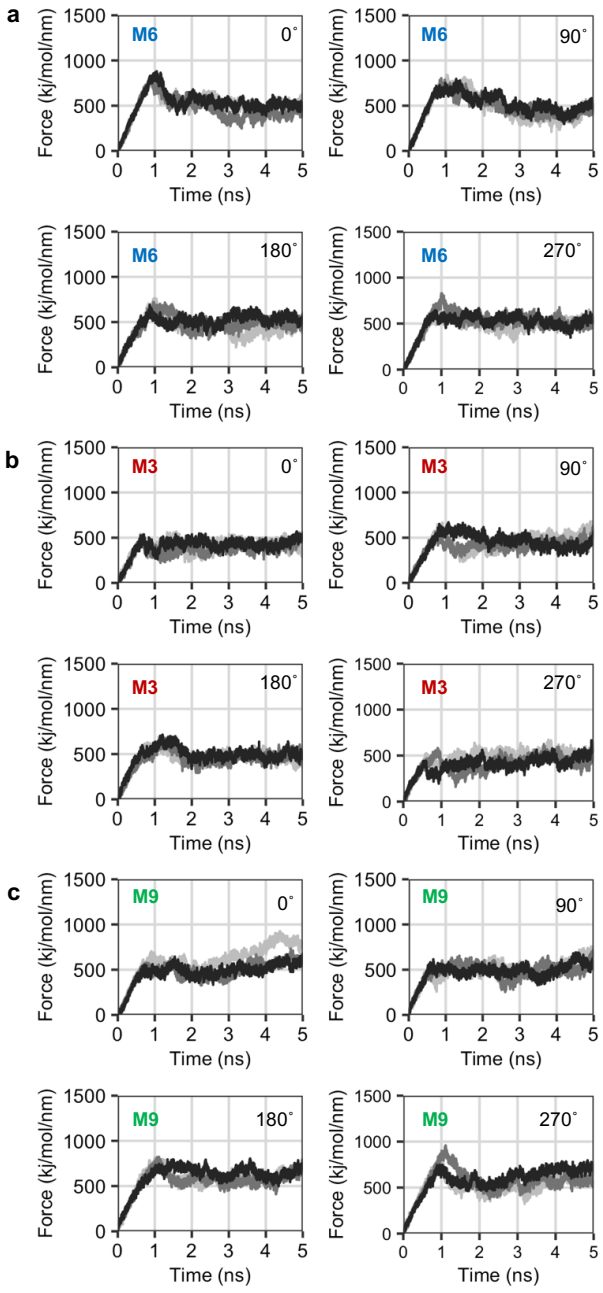

Figure 6.8: SMD simulations of the E2 state of SERCA with PLB. Quantification of force that developed as PLB was pulled from the canonical cleft of the E2 state of SERCA (represented by 3AR4). Data are three repeated measures of force for the original orientation of the X-Ray crystal structure (PDB 4KYT) and after axial rotation of PLB by 90°, 180°, and 270°. The data are shown for interaction with the M6/M9 (a) M3 (b) and M9 (c) helices of SERCA.

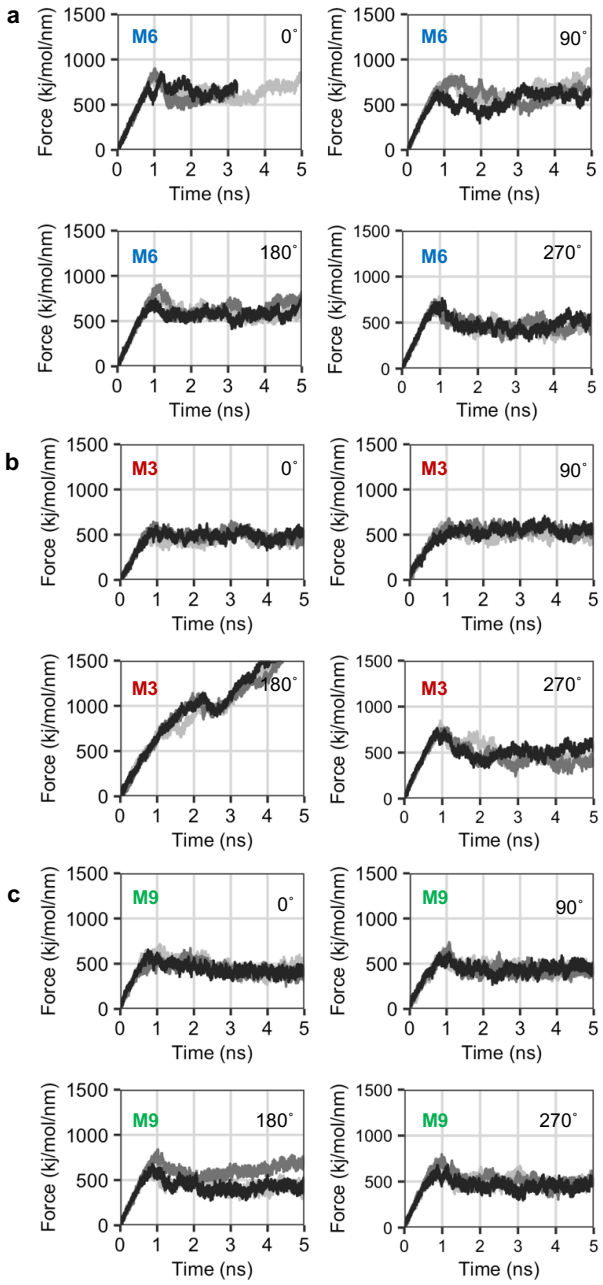

Figure 6.9: SMD simulations of the E1-2Ca state of SERCA with PLB. Quantification of force that developed as PLB was pulled from the canonical cleft of the E1-2Ca state of SERCA. Data are three repeated measures of force for the original orientation of the X-ray crystal structure (PDB 4KYT) and after axial rotation of PLB by 90°, 180°, and 270°. The data are shown for interaction with the M6/M9 (a) M3 (b) and M9 (c) helices of SERCA.

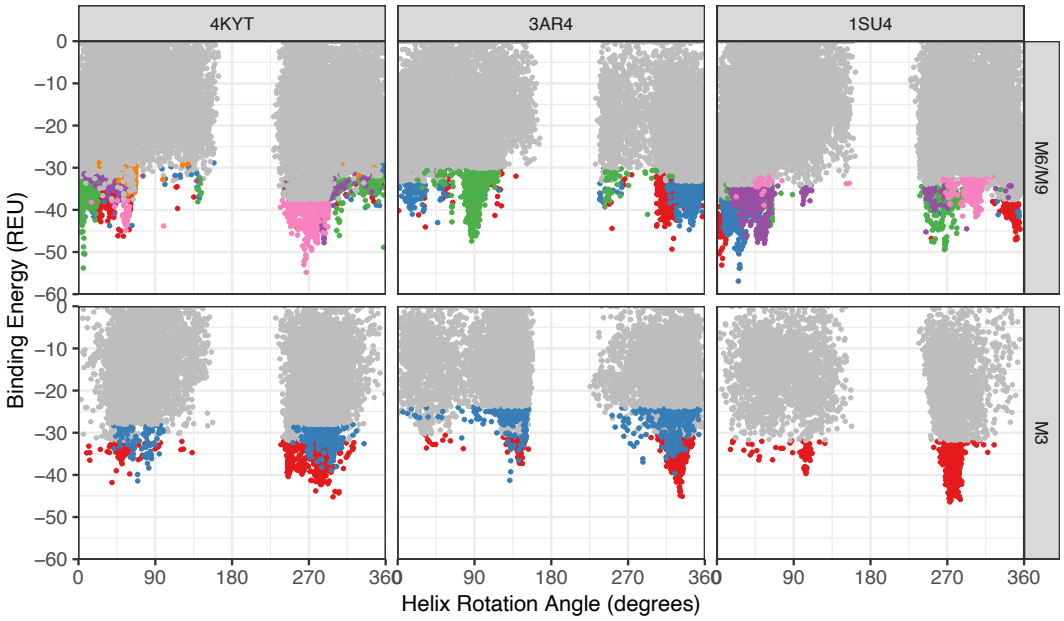

Figure 6.10: Ranking of all PLB conformers from all global docking solutions. Each SERCA-PLB complex model is ranked by axial rotation and binding energy, with each subpanel corresponding to a particular enzymatic state (4KYT, 3AR4, or 1SU4) and binding site (canonical cleft M6/M9 or M3). The top 5% scoring points are shown in red, blue, orange, green, pink or purple. A different color indicates the model was generated from a different global docking solution.

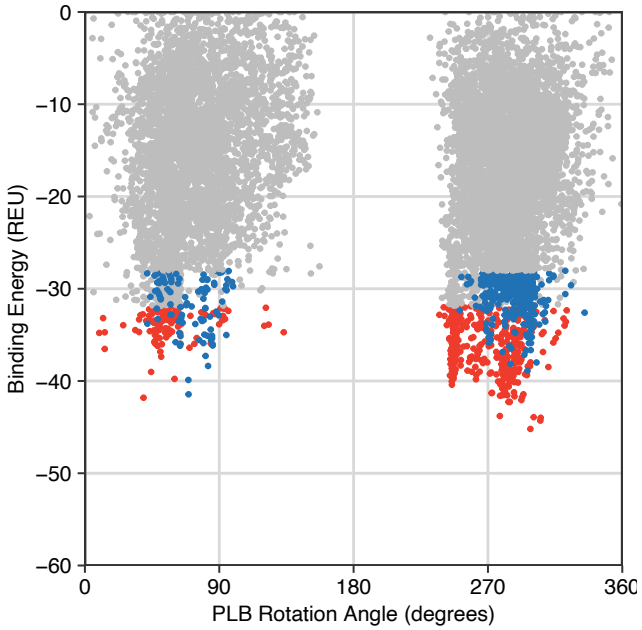

Figure 6.11: Ranking of all PLB conformers from docking the E1-Like-PLB state of SERCA with the M3 accessory site. Each SERCA-PLB complex model is ranked by axial rotation and binding energy and the top 5% scoring points are shown in red or blue. A different color indicates the model was generated from a different global docking solution.

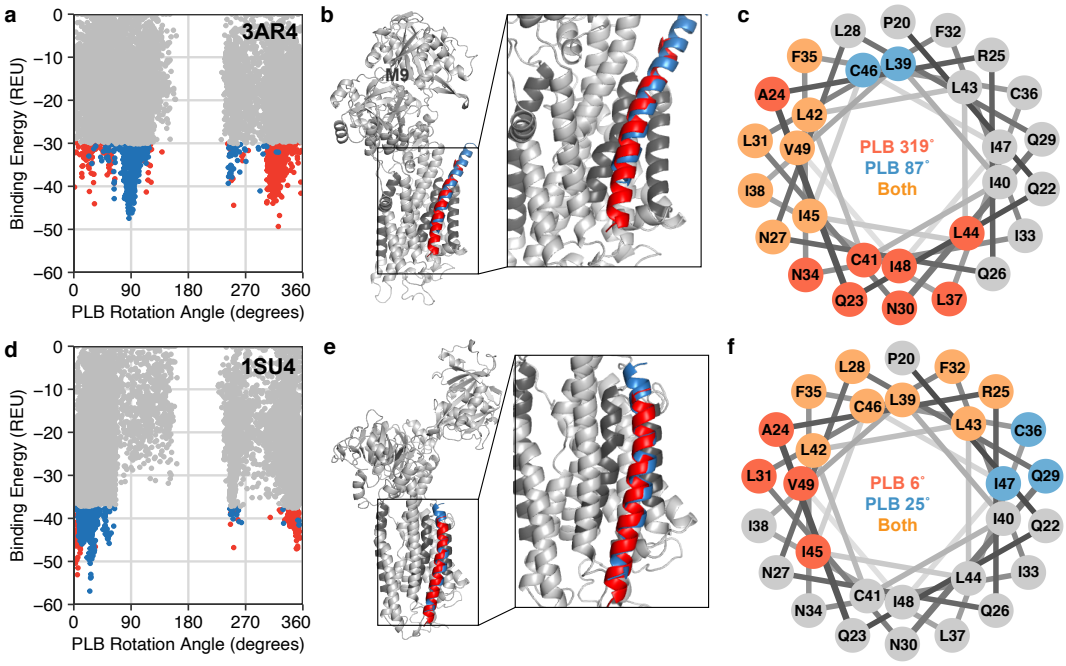

Figure 6.12: High resolution models of PLB interactions with the canonical cleft of the E2 and E1-2Ca states of SERCA. The model of the E2 state (represented by 3AR4) is shown in the top row and the model of the E1-2Ca state (represented by 1SU4) is shown in the bottom row. (a,d) Ranking of each SERCA-PLB complex model by axial rotation and binding energy. The top 5% scoring points are shown in red or blue, with a different color indicating the model was generated from a different global docking solution. (b,e) High resolution model of two possible PLB conformers interacting with SERCA shown in red and blue, corresponding to the colors in panels (a,d). A 2x zoomed view of the transmembrane domain is shown to the right of the SERCA model. (c,f) Helical wheel demonstrating PLB conformer interface residues. Positions colored in red correspond to the first conformer, positions in blue correspond to the second conformer, and mutual positions are in orange.

Chapter 7

Computational design of a self-assembling transmembrane protein pore

7.1 Overview

Nanoscale channels are critical for directed transport within living systems. Within synthetic biology, channels have potential applications in diagnostics, therapeutics, and smart materials. Previous studies have engineered channels from DNA nanotubes with various chemical modifications that enable membrane insertion. However, none of these solutions guarantee both reliable assembly and insertion. In this chapter, I explore an alternative route of designing channels from protein helical bundles. First, I generate helical bundles with varying pore radii and point symmetries from 40-residue poly-alanine α-helices. I apply a symmetric fixed-backbone design protocol that searches for low energy sequences that also satisfy the design criteria. Then, I evaluate monomer stability in the bilayer, a prerequisite state for insertion. Finally, I identify a single viable sequence and outline next steps for experimental testing.

7.2 Introduction

A major goal of synthetic biology is to develop a portfolio of engineered biological circuits inspired by living systems [314]. These circuits can be integrated into nano-devices for diagnostics, therapeutics, and smart materials. One circuit of interest is membrane protein channels that facilitate directed transport of water, ions, or other molecules through otherwise impermeable walls [315]. Such channels can enable wide ranging processes driven by ion flux such as pumps, rotary motors, and transport proteins.

DNA origami is an enticing material for synthetic biology design tasks because carefully programmed DNA monomers have been shown to reliably fold into non-arbitrary two- and three-dimensional shapes [316]. Synthesis of DNA nanotubes is well established [317], and nanotubes provide an excellent scaffold for a channel. In the past decade, several channel prototypes have been constructed from DNA origami nanotubes. Thus far, the main challenge has been integrating the negatively charged DNA nanopore into the non-polar membrane. Several chemical modifications have been applied to improve compatibility including the addition of cholesterol [318], ethyl protected phosphorothiolates [319], porphryn tags [320], tocepherol tags and modification with streptavidin and biotin [321]. These approaches have achieved one of two feats but not both: (1) fast assembly into the bilayer, and (2) stability in the bilayer relative to the aqueous phase.

Proteins are a promising alternative because their sequences can be programmed to insert and form stable folds in the bilayer. Further, there are examples of synthetic pores, such as pPorA: a 40-amino-acid α-helical peptide that self-assembles into a stable membrane channel called Porin Acj [322]. There has also been limited success

engineering naturally ocuring membrane proteins to act as pores including the cWza octomer [71] and redesigned OmpF [72].

To select for various materials, it would be ideal to design a pore with a customized radius and height. This task requires *de novo* design: generating new proteins from physical principles with novel sequences [54]. *De novo* design has already been used to create a wide array of tools outside of what biology has already provided such as for drug delivery [323] and process control [53, 324]. For membrane proteins, there have been two significant *de novo* milestones. DeGrado and coworkers designed the PRIME and ROCKR alternating access transporters formed by two tightly interacting pairs of helices [70, 325]. And Lu *et al.* achieved *de novo* design of helical bundles that insert into the membrane [75]. Yet, the field overall is still in its infancy relative to the designs produced by DNA origami.

In this chapter, I aim to computationally design a protein pore that can be used to transport material from a DNA nanotube into another membrane-enclosed compartment. I explore backbone geometries with varying pore radii and evaluate the ability of the design to self-insert and self-assemble within the bilayer. Then, I aim to propose sequences that can be synthesized and tested in the wet lab. While the design goal is challenging, I believe this synthetic biology problem will provide many insights into needed improvements for the design process.

7.3 Methods

7.3.1 Helical bundle generation

I used the BundleGridSampler application to generate starting backbones [326]. For each backbone, the monomer unit was 40 alanine residues long. Helical bundles were

generated for four cyclic point symmetries: C_4, C_6, C_8, C_{10}. For all bundles, I sampled three values for the ω_0 parameter ($\omega_0 = -0.05, 0, 0.05$) and three values for the δ_0 parameter ($\delta_0 = 0.33, 0.66, 1.00$). The following ranges in Å Ire chosen for r_0 given the symmetry n: $C_4 = [4.5, 7.5]$, $C_6 = [6, 9]$ $C_8 = [10, 15]$, $C_10 = [12, 17]$. For each symmetry, I sampled 27 bundle geometries and chose the lowest scoring scaffolds without clashes and unique Crick parameters to proceed in the next step.

7.3.2 Adapting *franklin2019* for membrane proteins with cyclic point symmetry

The Rosetta program uses a general framework for modeling arbitrary symmetric macromolecular systems [327]. Symmetric systems are abundant in nature; yet, they are also large and computationally expensive to model. The Rosetta symmetry framework improves efficiency by sampling only symmetric degrees of freedom and explicitly simulating a subset of the interacting monomers. Unsurprisingly, the symmetry framework requires that a macromolecular system is completely symmetric. This constraint has important implications for modeling membrane proteins with pores and cavities because the current method described in Chapter 2 is intrinsically asymmetric. To adapt this method for symmetric proteins, I simplified the method to assume the pore is a cylinder (Fig. 7.1).

The simplified pore representation follows a similar formalism to that described by Lazaridis *et al.* [109]. Here, the geometry of a pore is represented by a circle with radius r and center coordinates (x_0, y_0) (7.1).

$$g_{\text{radius}} = \frac{1}{r}\sqrt{\big(x - x_0(z)\big)^2 + \big(y - y_0(z)\big)^2} \tag{7.1}$$

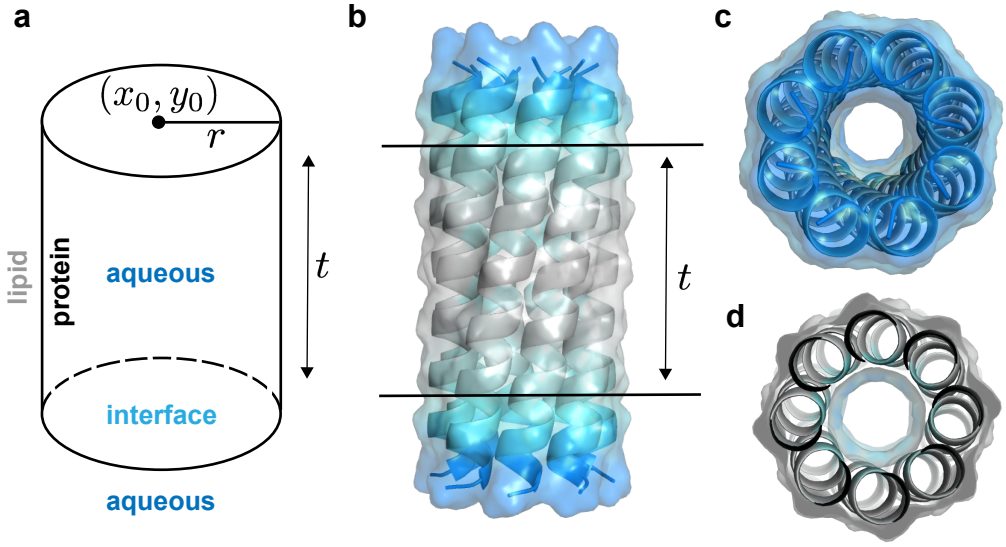

Figure 7.1: Architecture of a symmetrical helical bundle pore. The architecture of a symmetric membrane protein pore is simplified relative to the pore estimation strategies for non-symmetric proteins. (a) The pore is a cylinder with a center (x_0, y_0), a radius r, and height t equal to the thickness of the transmembrane region. (b) Projection of the symmetric architecture onto a generic helical bundle with C_8 point symmetry in membrane view. Side chains exposed to the aqueous phase are colored in blue, side chains exposed to the interface are colored in teal, and side chains exposed to the lipid phase are colored in gray. Panels (c) and (d) show a cytoplasm facing view of the pore with the same color scheme as in (b). Panel (d) is a clipped view showing the pore at $z = 0$Å.

Then, the the hydration fraction f_{hyd} is described as a function of g_{radius} and the transition steepness n as given in Eq. 7.2.

$$f_{\text{pore}} = 1 - \frac{g_{\text{radius}}^n}{1 + g_{\text{radius}}^n} \tag{7.2}$$

7.3.3 Backbone redesign

To explore the sequence space for helical bundles with different pore radii, I used a fixed backbone design protocol that performs side chain repacking and minimization with the *franklin2019* energy function.

7.3.4 Bilayer-dependent monomer energy landscape

I evaluated the bilayer stability of the monomer by searching for the low-free energy orientation in the bilayer. The purpose of this step is to ensure the design scaffold can exist in both the monomer and oligomer state. Here, orientation is defined by two coordinates: (1) distance between the membrane center and peptide center of mass, d and (2) angle between the membrane normal and helical axis, θ. To search for the low energy orientation, I first apply side-chain packing and minimization to resolve steric clashes. Then, I apply rigid-body moves to sample all combinations of θ and d values. Membrane depths were sampled between -60 Å and 60 Å with a 1 Å step size and tilt angles were sampled between $0° - 360°$ with a $1°$ step size.

7.4 Results

7.4.1 Design strategy

The overall goal is to design a protein channel fused to a DNA nanotube that will insert into the membrane and self-assemble. DNA nanotube assembly is a well-established process [317]; thus, this chapter will focus on design of the protein component. At the outset, I proposed the following mechanism (Fig. 7.2). The initial state is an unfolded polypeptide chemically fused to a DNA tile. The polypeptide is driven into the membrane by a favorable water-to-bilayer transfer energy. Upon insertion, the peptide folds into an α-helix to satisfy hydrogen bonds within the non-polar lipid bilayer. Then, in excess of monomers, the subunits will assemble into an oligomeric pore. Our design strategy was to engineer the final oligomer state and then work backward to test viability of the monomer.

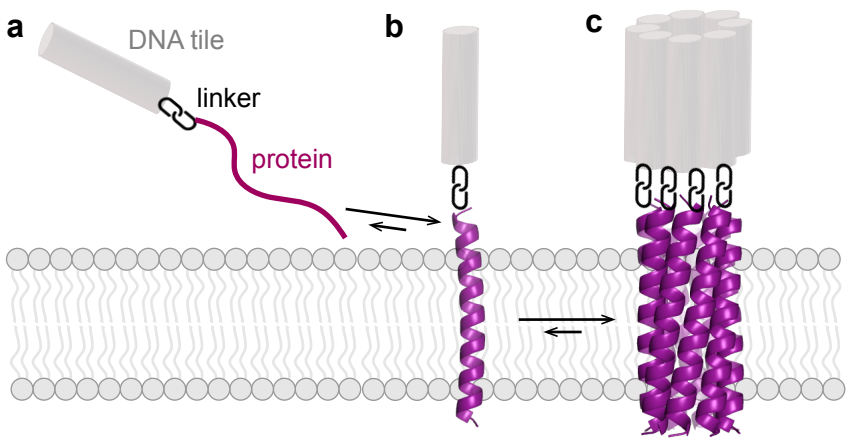

Figure 7.2: Proposed mechanism for insertion and assembly of a DNA-protein channel. (a) The starting conformation is an unfolded peptide (purple) linked to a DNA tile segment (grey) in the aqueous phase. (b) Next, membrane insertion is driven by a favorable water-to-bilayer transfer energy. Upon insertion, the polypeptide folds into an α-helix to resolve unsatisfied hydrogen bonds. (c) Then, multiple monomer segments self-assemble into a protein pore linked to the self-assembled DNA-nanotube.

7.4.2 Generating helical bundles with variable pore radii

The starting point for oligomer design is a helical bundle: a coiled coil of two or more helices supercoiled around a central axis [328]. This geometry is described by the parametric Crick equations which describe a bundle of n helices with supercoil twist ω_0, α-helical twist ω_1, supercoil radius R_0, helix phases $\psi_1, \psi_2, ..., \psi_n$, and helix offsets $z_1, z_2, ..., z_n$ [329]. For this design problem, helical bundles are advantageous for two main reasons. First, the parametric description enables generation of backbones with multiple symmetries and pore radii. Second, helical bundles are very stable folds [330] and have been previously shown to insert into lipid bilayers [75].

I used the BundleGridSampler [326] to generate helical bundle backbones. For each backbone, the monomer was a 40 residue poly-alanine helix. I chose to use an extra-long helix to ensure the monomer spans the membrane even if "coiling" shortens the effective length. I generated 27 bundles for four symmetries: C_4, C_6, C_8, C_10 (total

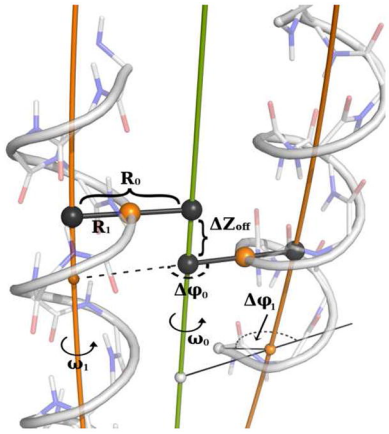

Figure 7.3: Representation of Crick coil-coil parameters. Geometrical meanings of the superhelical radius (R_0), the helical radius (R_1), the superhelical frequency (ω_0), the helical frequency (ω_1), chain axial offset (ΔZ_{off}), chain superhelical phase offset ($\Delta\psi_0$), and starting helical phase ($\Delta\psi_1$). The interfacial axis is shown in green, local helical axes are shown in orange, and the helical curve that passes through C_α atoms is shown in gray. The distance along the interfacial axis between an inward-facing point (orange) and its closest counterpart on the opposite helix is defined as ΔZ_{off}. *This figure is reproduced with permission from "Grigoryan G & DeGrado WF (2011) Probing designability via a generalized model of helical bundle geometry" J Mol Biol. 405(4):1079-1100.*

108 designs). Then, I chose the best backbones in each symmetry group as models with unique parameters, no clashes ($E < 0$), and the lowest energy. The resulting bundle geometries are summarized in Table 7.1 and shown in Fig. 7.4. Overall, the pore radii r range between 5.75-17 Å.

Table 7.1: Crick parameters for low energy helical bundles

C_n	r (Å)	ω (rad)	δ (rad)
4	5.75	0.05	0.66
4	7.5	-0.05	0.66
6	9	0.05	0.33
8	12.5	0.05	0.33
8	15	0.05	1
10	14.5	0.05	0.33
10	17	0.05	1

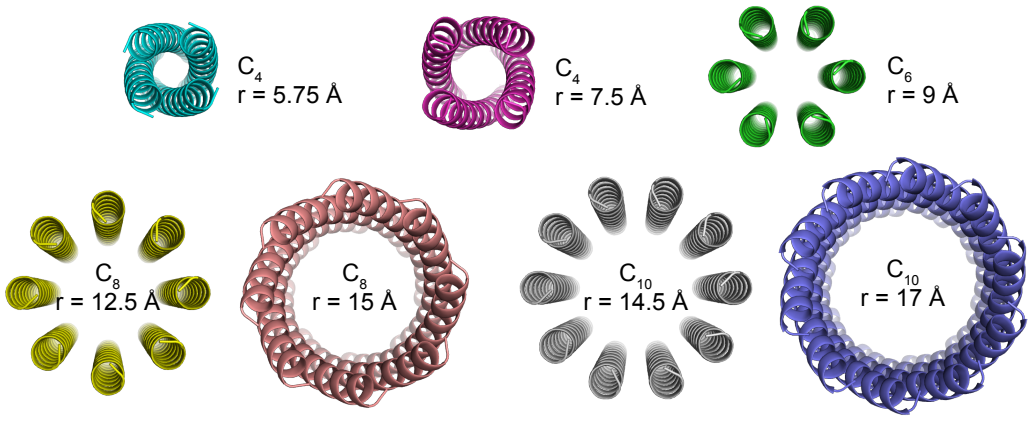

Figure 7.4: Low energy helical bundles with variable radi I used the BundleGridSampler application to search for low energy helical bundle backbones with four point symmetries: C_4, C_6, C_8, and C_{10}. Backbone conformations with unique parameters and no clashes ($E < 0$) were selected for further design. The resulting seven scaffolds are shown here.

7.4.3 Symmetric bundle design

Next, I applied a symmetric design protocol to search for low energy sequences. First, each protein was set up as a symmetric system and then initialized in the *franklin2019* implicit membrane. Then, I used a Monte Carlo fixed-backbone design protocol to sample possible sequences. The protocol uses a full protein-and-rotamer sequence optimization and multi-cool annealer simulated annealing protocol to explore sequence space. The resulting monomer sequence for each backbone is listed in Table 7.2.

Table 7.2: Designed sequences for each pore radius

C_n	r (Å)	Sequence
4	5.75	DEAGKKAGILAAIAAIIAGIIAGILAAIAAIIGALLAGKS
4	7.5	DEDEAKIILILLLIAIILLLIAIILNILATLETLKGLKKS
6	9	DEDGKKIAIAIIIAAILITLAILIAAIYTLIGLLLAAKSS
8	12.5	EEDAKKTAIAIIIAAILETLARLIAAIYKLIADILSARSS
8	15	EEEEKLTLIALIIAYIILAILLAIAYIIIILIAIILKAKS
10	14.5	DEAAKLTAIALIIAAILIAIALIIKAIYLAIAAILSARSS
10	17	DEEAKSAIKAAIALAIALAIAYILAAIALAIALAIASKKS

I evaluated the designs by generating a sequence logo frequency plot (Fig. 7.7) that represents the position-specific frequency of different amino acids. All of the sequences have a hydrophobic stretch of amino acids between positions 8-31. Outside this range, the amino acids are predominantly charged and polar. This pattern signals that the designs are well-matched to the hydrophobic thickness of the bilayer.

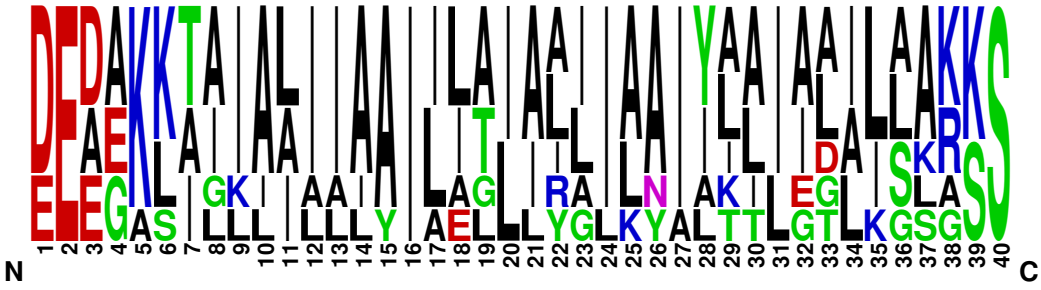

Figure 7.5: Sequence logo of designed monomers. Sequence logo frequency plot demonstrating the diversity of amino acids at each position within the 40 amino acid monomer. Amino acids are colored according to the following scheme: positively charged (blue), negatively charged (red), non-polar (black), polar (green), and special (pink).

I expected that many designs would include polar or charged residues in the transmembrane region to accommodate an aqueous pore. Interestingly, this was not the case for all designs except the C_8 symmetric 12.5Å pore. The C_8 design includes four charged or polar residues per monomer: T7, E14, R18, and K27. To visualize the relative placement of polar, charged, and non-polar side chains, I generated a helical wheel diagram of the monomer in Fig. 7.6b. Helical wheels for the remaining sequences are shown in Fig. 7.8.

The helical wheel shows that the helix is amphipathic, with hydrophobic side chains on the left and polar/charged side chains on the bottom right. This is ideal because the hydrophobic moment can orient the helix during oligomer assembly. These properties suggest that C_8 would be viable in both the oligomer and monomer

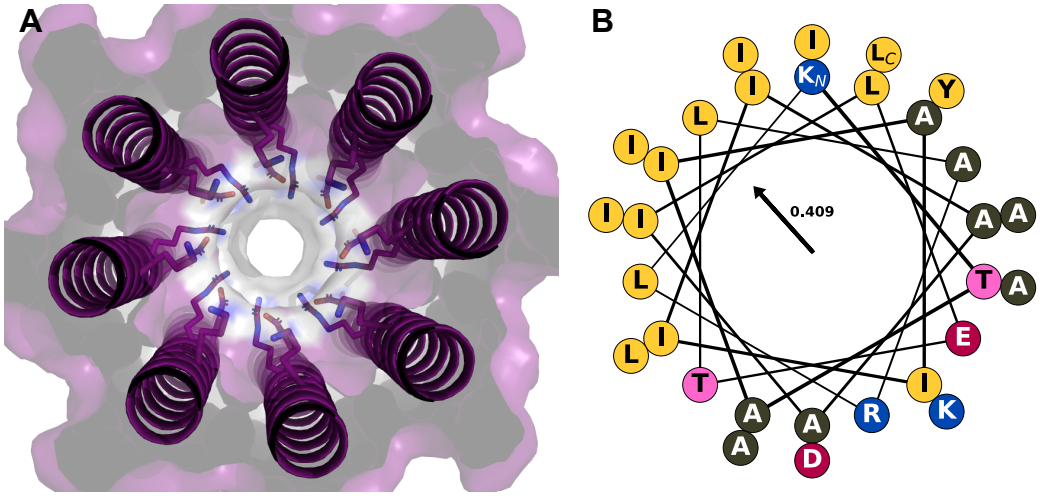

Figure 7.6: Analysis of 12.5ÅC_8 design. (A) Lumen-side view of the C_8 symmetric helical bundle design with a 12.5Åpore radius. The backbone is shown in cartoon representation and polar/charged side chains T7, E14, R18, and K27 are shown as sticks. (B) Helical wheel representation of the monomer sequence from position 5-35. The charged termini are excluded to represent side chains that contact the interfacial or lipid phase of the bilayer. Amino acids are colored according to category, with non-polar amino acids in yellow, positively charged amino acids in blue, negatively charged amino acids in red, polar amino acids in pink, and special case amino acids in brown. The hydrophobic moment is indicated in the center of the wheel.

states. I therefore test this hypothesis in the next section.

7.4.4 Membrane stability of the C_8 monomer

Finally, I computationally evaluate the stability of the monomeric state in the membrane. To explore this question, I use the MembraneEnergyLandscapeSampler [161] to generate a mapping of energies to all possible orientations of the monomer in the bilayer. The resulting map is shown in Fig. 7.7.

In the energy landscape, I observed two low-energy wells at (0 Å, 30°) and (0 Å, 330°). These orientations correspond to helices that span the membrane with realistic tilt angles. The water-to-bilayer transfer free energy of the monomer is -9 REU, indicating a strong preference for the bilayer. These results support that the monomer

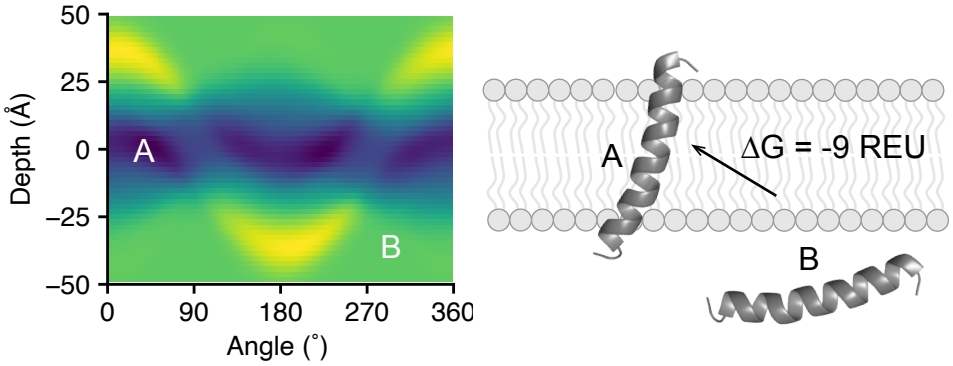

Figure 7.7: Stability the C_8 monomers in the membrane. (Left) The mapping of protein orientations to energies computed by *franklin2019* is shown for the C_8 12.5 Ådesign. Each point represents a different orientation and the color corresponds to the energy, with low energy points colored in blue and high energy points colored in green. (Right) Important conformations in the energy landscape diagram: (A) the lowest energy orientation spans the bilayer, whereas (B) the highest energy orientation is outside the membrane. The water to bilayer transfer energy from state B to A is -9 REU.

would be stable and insert into the bilayer as well as in the oligomeric form.

7.5 Discussion

In this work, I computationally designed a membrane protein pore that self-inserts and self-assembles from amphipathic monomers. The assembled pore is a C_8 symmetric helical bundle with a pore radius of 12.5 Å. This design was the only monomer that was sufficiently amphipathic for directional assembly. I believe that the design process and the resulting sequence provides an excellent starting point for further *in silico* and experimental testing.

This study was enabled by two recent milestones in membrane protein design. First, Lu *et al.* [75] successfully demonstrated that helical bundle backbones could be redesigned to embed in the membrane. This is the first example of fully *de novo* designed membrane proteins. Second, I previously developed *franklin2019* which is

the first all-atom implicit membrane energy function that captures aqueous pores with variable geometries [161]. As a result, I was able to easily construct backbones with variable pore lengths. This design study demonstrates the importance of advancing methods for membrane protein design. Before these advances, I could not have tackled a problem of this complexity.

This study was proof-of-principle. To demonstrate the concepts at low computational cost, I under-sampled backbone space and sequence space. Therefore, future work should expand the scope of the study. Further, the C_8 sequence is encouraging; yet, it remains a model. Thus, experimental testing is essential to ensure the designs are practical and overcome unforeseen challenges of cell-free synthesis.

7.6 Appendix

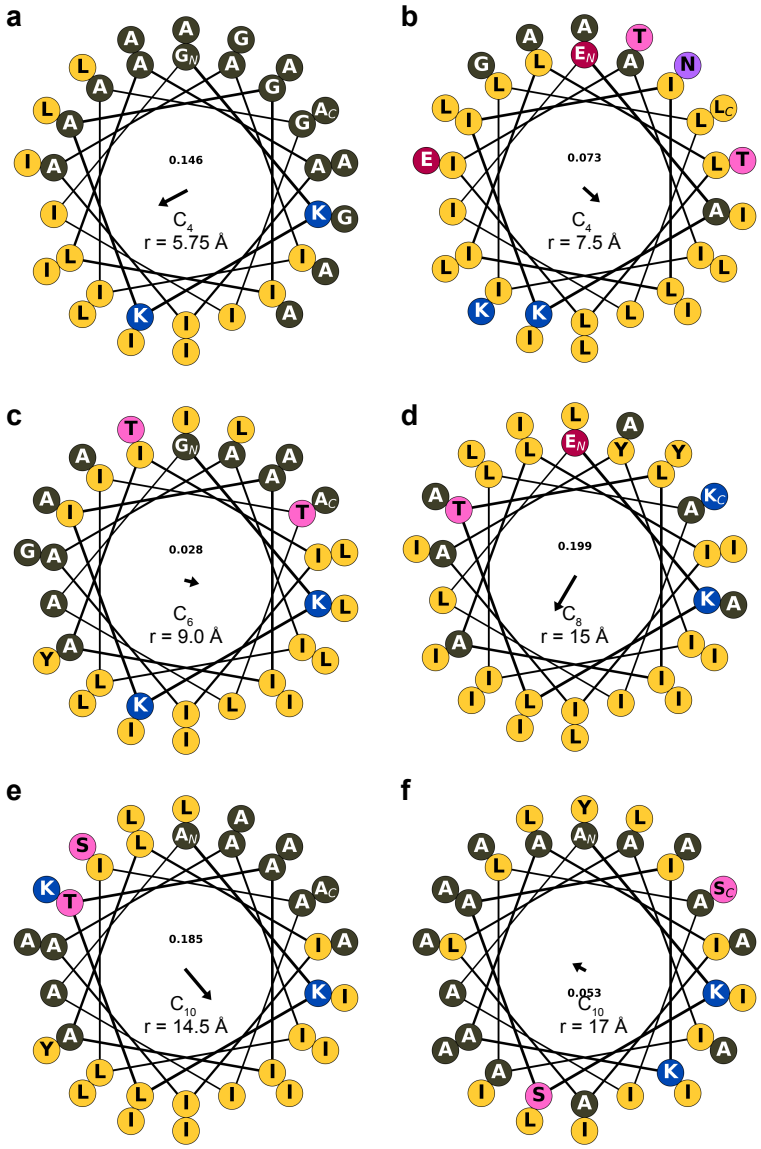

Figure 7.8: Helical wheel representations of monomer sequences. Helical wheel representations are shown for the remaining six designs: (a) C_4, $r = 5.75$Å, (b) C_4, $r = 7.5$Å, (c) C_6, $r = 9.0$Å, (d) C_8, $r = 15$Å, (e) C_{10}, $r = 14.5$Å, (f) C_{10}, $r = 17$Å.The charged termini are excluded to represent side chains that contact the interfacial or lipid phase of the bilayer. Amino acids are colored according to category, with non-polar amino acids in yellow, positively charged amino acids in blue, negatively charged amino acids in red, polar amino acids in pink, and special case amino acids in brown. The hydrophobic moment is indicated in the center of the wheel.

Chapter 8

Conclusions and Future Directions

8.1 My contributions

Structural studies of proteins provide a blueprint for cellular function, an understanding of how misshapen molecules make us sick, and insights into drug development. Over the past 50 years, structural biologists have developed a collection of tools to elucidate biomolecular structures including X-Ray crystallography, NMR spectroscopy, and cryo electron microscopy. While these tools have been fruitful for proteins in solution, experimental difficulties have delayed progress for membrane proteins. Further, many of these tools are protein-centric and cannot capture the heterogeneous lipid bilayer. Computational approaches that provide atomistic models of proteins coupled with the lipid bilayer can compliment experimental structures and provide mechanistic insight into function. Yet, computational models of the membrane are either too expensive to compute or not biologically realistic. In this dissertation, my main contribution is a membrane model that is fast to compute and more biologically realistic. My model can be effectively used for structure prediction and design. I also investigated three challenging systems involving membrane proteins to explore the next steps needed to advance computational tools.

8.1.1 From non-polar slabs to phospholipid bilayers

The first membrane models were implemented into the Rosetta macromolecular modeling suite in 2007. These models laid the foundation for a decade of computational membrane protein structural studies; yet, they encountered critical challenges. The membrane model resembled a hydrophobic slab of fixed thickness, which is inconsistent with our current knowledge of biological membranes. In Chapter 2, I developed a new implicit membrane model that captures the anisotropic structure and nanoscale dimensions of phospholipid bilayers. This is an important step forward because biological membranes are predominantly composed of phospholipids. The model is called *franklin2019*, and it improved the accuracy of structure prediction and design tasks relative to prior models. In this chapter, I also demonstrated protein design tied to different lipid compositions. As a result, including details of the lipid composition is now standard for Rosetta calculations. This advance enabled simulations to be more aligned with experiments, and it is consistent with the membrane literature that emphasizes the importance of lipid composition in protein structure and function.

8.1.2 From one test to many

A significant challenge in membrane protein structural biology is collecting sufficient experimental data to accurately describe membranes and their resident proteins. This challenge is important because computational models are only as accurate as the experimental data available to validate them. When I began my dissertation research, the most common validation approach was to check a single application against a single dataset. This approach led to many specialized applications; however, accurate membrane models are necessarily general models. In Chapter 3, I developed a set

of 12 diverse scientific benchmarks for evaluating implicit membrane models. The tests probe four key areas: stability, orientation, sequence, and structure. The tests are available to the public for use with Rosetta and other macromolecular modeling packages. The tests are an important contribution to the field because they will facilitate the development of more accurate and general energy functions for diverse applications.

8.1.3 From intra-residue to inter-residue

An important conclusion from Chapters 2 and 3 is that while *franklin2019* has yielded progress, there are also many areas for improvement. A particular area of interest is capturing electrostatics in the bilayer, as electrostatic interactions play an intimate role in membrane protein function and protein-protein interactions. In Chapter 4, I developed a Coulomb electrostatics model that accounts for the low-dielectric membrane environment. In addition, the model accounts for a shift in proton avidity in the membrane core and subsequently samples relevant protonation states of titratable amino acids. In preliminary tests, the model demonstrates significant improvement for predicting the partitioning energies of pH-sensitive peptides. This proof-of-concept model lays an important foundation for capturing electrostatic interactions in the membrane and serves as a starting point for continued energy function development.

8.1.4 From safety to the wild west

When asked to generate a structural model with a given tool, computational biologists think deeply about a tool's limitations. A common experience is to realize that biological systems are far more complex than what tools can handle. Through developing methods, I realized these complex systems spotlighted opportunities to

push the boundaries of current methods and outline future steps. In my dissertation, I applied this principle to explore two biological systems involving membrane proteins. In Chapter 5, I examined the stability effects of mutations in the integral zinc metalloprotease with a voluminous aqueous chamber. In this study, I helped develop a hybrid computational-experimental assay for investigating stability effects in this unique protein. Here, I learned that the geometry is too complex for current implicit models and requires more flexible cavity representations. Then, in Chapter 6, I explored interactions between the SERCA integral membrane calcium pump and the regulatory transmembrane segment phospholamban. This interaction is physiologically important in cardiac response to stress such as exercise. My docking studies support experimental evidence for a transient interaction mechanism, while also demonstrating needed work in modeling protein flexibility within the bilayer.

8.1.5 From prediction to design

The penultimate chapter of my thesis describes a first attempt to design a membrane protein in the context of a real nanotechnology problem (Chapter 7): design of nanoscale channels for transport. Design is the ultimate application for a membrane model because it asks if we can reproduce the rules for membrane protein structure and stability. In this chapter, I identified a viable sequence for experimental testing. Further, I learned important lessons for design problems including considering the starting scaffold and including customized pore definitions. This design chapter is a starting point for future design problems with *franklin2019*.

8.2 Future directions

In Chapter 2, I demonstrated that implicit membrane models that capture different phospholipid compositions improve structure prediction and design. Thus far, I have developed model parameters for single-component phospholipid bilayers. A next step is to develop parameters for more complex lipid mixtures. This work is especially important as biological plasma membranes contain hundreds of chemically distinct lipid types [19, 331] that are heterogeneous on the length scale of proteins and small protein clusters (1-10 nm) [127, 332]. One possibility is to generate parameters for membranes with specific mean-field features, such as asymmetric lipid distributions [333] and anionic head-groups [126]. A second area is to consider cholesterol, a sterol that constitutes 20-40% of animal cell membranes [334]. Cholesterol tunes bilayer rigidity and may induce lateral pressure on the protein [335].

Importantly, some lipids facilitate protein function through explicit interactions. For instance, cholesterol and phosphatidylinositol (PIP) lipids are tied to specific conformational states of G-protein coupled receptors [336], and PIP lipids facilitate dimerization of Bruton's tyrosine kinase [337]. These biological examples suggest that an exclusively implicit representation may not always be appropriate. One solution is a hybrid implicit-explicit model, such as the Highly Mobile Membrane Mimetic (HMMM) [131] that represents head-groups explicitly and the hydrophobic core implicitly. An alternate path is to leverage the framework developed by Labonte *et al.* [338] to represent a few lipids explicitly. Most likely, both implementations may be useful.

Biological membranes also exhibit changes in morphology: rather than a rigid slab, the bilayer can curve, bend, stretch, and compress in response to the environment

[339]. An important future direction is to consider these changes during structure prediction and design. First, membrane proteins sculpt the lipid bilayer, such as the sodium-aspartate symporter reshaping the bilayer during conformational change [340] and rows of F-ATPase dimers forming christea in the inner mitochondrial membrane [341]. In these cases, evaluating hydrophobic mismatch may help tune the shape of the implicit membrane model. Second, mechanical properties of the bilayer also affect the protein. For instance, gramicidin dimerizes upon changes in hydrophobic thickness [342] and mechano-sensitive channels open and close in response to osmotic stress [133]. To address this challenge, several elasticity models have been proposed [24]. Yet, previous work has also demonstrated that implicit elastic models are insufficient to reproduce experimental results [135]. This suggests the possible importance of a hybrid implicit-explicit model.

A prevailing question in membrane protein structural biology is how mimetics used for structure determination alter the native structure. Recent work has highlighted differences between structures of the same protein determined by X-Ray crystallography and NMR spectroscopy [343]. Accordingly, structural integrity can be preserved in membrane mimetics, yet function may be compromised [344]. Could parameters be derived to differentiate features of mimetics such as micelles, bicelles, and nano-discs? A possible application is to use refinement protocols to resolve structural differences invoked by mimetic environments. These models may lead us toward a better understanding of membrane protein structures in their natural environments.

Another important area to examine is the generalizability of the biologically realistic implicit membrane model. In Chapter 2, I compared the performance of

franklin2019 with implicit membrane models already implemented in Rosetta. However, there are alternate implicit models in several molecular modeling packages. One technical challenge is that modeling packages choose different atom and residue parameters. For instance, a tyrosine and serine hydroxyl group may be equivalent to one package but not the other [61]. Recently, the Open Force Field project has suggested new tools for resolving such differences [163]. Adopting these techniques may facilitate comparisons, enabling a critical evaluation of membrane models outside the context of a particular program.

Finally, energy functions can only be as accurate as available experimental validation data. This principle poses a special challenge for membrane protein energy functions due to sparse data. Recent advances in biophysical techniques and structure prediction have increased the number of thermodynamic measurements [345] and known structures. Nonetheless, critical future work involves considering how to better leverage existing experimental data and obtain new data points. An important direction is to collaborate with experimentalists to design experiments for direct energy function calibration. Another area is to apply meta-, active- or transfer learning to appropriately leverage sparse data. These techniques have been successfully applied to therapeutic peptide design [346] and may also be useful for energy function optimization.

References

1. Editorial. Cellular gatekeepers. *Nature Structural and Molecular Biology* **23,** 463 (2016).
2. Wallin, E. & Heijne, G. V. Genome-wide analysis of integral membrane proteins from eubacterial, archaean, and eukaryotic organisms. *Protein Science* **7,** 1029–1038 (2008).
3. Overington, J. P., Al-Lazikani, B. & Hopkins, A. L. How many drug targets are there? *Nature Reviews Drug Discovery* **5,** 993–996 (2006).
4. Bill, R. M., Henderson, P. J. F., Iwata, S., Kunji, E. R. S., Michel, H., Neutze, R., Newstead, S., Poolman, B., Tate, C. G. & Vogel, H. Overcoming barriers to membrane protein structure determination. *Nature Biotechnology* **29,** 335–340 (2011).
5. Koehler Leman, J., Ulmschneider, M. & Gray, J. Computational modeling of membrane proteins. *Proteins: Structure, Function, and Bioinformatics* **83,** 1–24 (2015).
6. Harayama, T. & Riezman, H. Understanding the diversity of membrane lipid composition. *Nature Reviews Molecular Cell Biology* **19,** 281–296 (2018).
7. White, S. H. & Wimley, W. C. Membrane protein folding and stability: Physical principles. *Annual Review of Biophysics and Biomolecular Structure* **28,** 319–365 (1999).
8. Langosch, D. & Heringa, J. Interaction of transmembrane helices by a knobs into holes packing characteristic of soluble coiled coils. *Proteins: Structure, Function, and Bioinformatics* **31,** 150–159 (1998).
9. Alberts, B., Johnson, A., Lewis, J., Raff, M., Roberts, K. & Walter, P. in *Molecular Biology of the Cell* 4th Edition (Garland Science, 2002).
10. Arkin, I. T., Brünger, A. T. & Engelman, D. M. Are there dominant membrane protein families with a given number of helices? *Proteins* **28,** 465–466 (1997).
11. Faham, S., Yang, D., Bare, E., Yohannan, S., Whitelegge, J. P. & Bowie, J. U. Side-chain contributions to membrane protein structure and stability. *Journal of Molecular Biology* **335,** 297–305 (2004).

12. Efremov, R. G. & Sazanov, L. A. Structure of Escherichia coli OmpF porin from lipidic mesophase. *Journal of Structural Biology* **178,** 311–318 (2012).

13. Meer, G. V., Voelker, D. R., Feigenson, G. W., van Meer, G., Voelker, D. R. & Feigenson, G. W. Membrane lipids : where they are and how they behave. *Nature reviews. Molecular cell biology* **9,** 112–124 (2008).

14. Singer, S. J. & Nicolson, G. L. The Fluid Mosaic Model of the Structure of Cell Membranes. *Science* **175,** 720–731 (1972).

15. Johansson, A. C. V. & Lindahl, E. Protein contents in biological membranes can explain abnormal solvation of charged and polar residues. *Proceedings of the National Academy of Sciences* **106,** 15684–15689 (2009).

16. Engelman, D. M. Membranes are more mosaic than fluid. *Nature* **438,** 578–580 (2005).

17. Veatch, S. L., Cicuta, P., Sengupta, P., Honerkamp-Smith, A., Holowka, D. & Baird, B. Critical fluctuations in plasma membrane vesicles. *ACS Chemical Biology* **3,** 287–293 (2008).

18. Sud, M, Fahy, E, Cotter, D, Brown, A, Dennis, E. A., Glass, C. K., Merrill Jr., A. H., Murphy, R. C., Raetz, C. R., Russell, D. W. & Subramaniam, S. LMSD: LIPID MAPS structure database. *Nucleic Acids Res* **35,** D527–32 (2007).

19. Sampaio, J. L., Gerl, M. J., Klose, C., Ejsing, C. S., Beug, H., Simons, K. & Shevchenko, A. Membrane lipidome of an epithelial cell line. *Proceedings of the National Academy of Sciences* **108,** 1903–1907 (2011).

20. Baumgart, T., Hammond, A. T., Sengupta, P., Hess, S. T., Holowka, D. A., Baird, B. A. & Webb, W. W. Large-scale fluid/fluid phase separation of proteins and lipids in giant plasma membrane vesicles. *Proceedings of the National Academy of Sciences* **104,** 3165–3170 (2007).

21. Simons, K. & Ikonen, E. Functional rafts in cell membranes. *Nature* **387,** 569–572 (1997).

22. Dumas, F., Lebrun, M. C. & Tocanne, J.-F. Is the protein/lipid hydrophobic matching principle relevant to membrane organization and functions? *FEBS Letters* **458,** 271–277 (1999).

23. Harroun, T. A., Heller, W. T., Weiss, T. M., Yang, L. & Huang, H. W. Experimental evidence for hydrophobic matching and membrane-mediated interactions in lipid bilayers containing gramicidin. *Biophysical Journal* **76,** 937–945 (1999).

24. Andersen, O. S. & Koeppe, R. E. Bilayer thickness and membrane protein function: An energetic perspective. *Annual Review of Biophysics and Biomolecular Structure* **36,** 107–130 (2007).

25. McMahon, H. T. & Boucrot, E. Membrane curvature at a glance. *Journal of Cell Science* **128,** 1065–1070 (2015).

26. Haswell, E. S., Phillips, R. & Rees, D. C. Mechanosensitive channels: What can they do and how do they do it? *Structure* **19,** 1356–1369 (2011).

27. Perutz, M. F., Rossmann, M. G., Cullis, A. F., Muirhead, H., Will, G. & North, A. C. T. Structure of Hæmoglobin: A three-dimensional fourier synthesis at 5.5Å resolution, obtained by X-ray analysis. *Nature* **185,** 416–422 (1960).

28. Kendrew, J. C., Dickerson, R. E., Strandberg, B. E., Hart, R. G., Davies, D. R., Phillips, D. C. & Shore, V. C. Structure of myoglobin: A three-dimensional fourier synthesis at 2Å resolution. *Nature* **185,** 422–427 (1960).

29. Deisenhofer, J, Epp, O, Miki, K, Huber, R & Michel, H. Structure of the protein subunits in the photosynthetic reaction centre of Rhodopseudomonas viridis at 3Å resolution. *Nature* **318,** 618–624 (1985).

30. Berman, H. M., Battistuz, T., Bhat, T. N., Bluhm, W. F., Bourne, P. E., Burkhardt, K., Feng, Z., Gilliland, G. L., Iype, L., Jain, S., Fagan, P., Marvin, J., Padilla, D., Ravichandran, V., Schneider, B., Thanki, N., Weissig, H., Westbrook, J. D. & Zardecki, C. The protein data bank. *Acta Crystallographica Section D: Biological Crystallography* **58,** 899–907 (2002).

31. Picknett, T. M. & Brenner, S. in *Encyclopedia of Genetics* 2154 (Elsevier, 2001).

32. Carpenter, E. P., Beis, K., Cameron, A. D. & Iwata, S. Overcoming the challenges of membrane protein crystallography. *Current opinion in structural biology* **18,** 581–6 (2008).

33. Rasmussen, S. G., Choi, H. J., Rosenbaum, D. M., Kobilka, T. S., Thian, F. S., Edwards, P. C., Burghammer, M., Ratnala, V. R., Sanishvili, R., Fischetti, R. F., Schertler, G. F., Weis, W. I. & Kobilka, B. K. Crystal structure of the human β2 adrenergic G-protein-coupled receptor. *Nature* **450,** 383–387 (2007).

34. Granier, S. & Kobilka, B. A new era of GPCR structural and chemical biology. *Nature Chemical Biology* **8,** 670–673 (2012).

35. Howard, M. Protein NMR spectroscopy. *Current Biology* **8,** 331–333 (1998).

36. Nietlispach, D. & Gautier, A. Solution NMR studies of polytopic α-helical membrane proteins. *Current Opinion in Structural Biology* **21,** 497–508 (2011).

37. Zhou, H.-X. & Cross, T. A. Influences of Membrane Mimetic Environments on Membrane Protein Structures. *Annual Review of Biophysics* **42,** 361–392 (2013).

38. Andronesi, O. C., Becker, S., Seidel, K., Heise, H., Young, H. S. & Baldus, M. Determination of membrane protein structure and dynamics by magic-angle-spinning solid-state NMR spectroscopy. *Journal of the American Chemical Society* **127,** 12965–12974 (2005).

39. Yao, Y., Fujimoto, L. M., Hirshman, N., Bobkov, A. A., Antignani, A., Youle, R. J. & Marassi, F. M. Conformation of BCL-XL upon membrane integration. *Journal of Molecular Biology* **427,** 2262–2270 (2015).

40. Milne, J. L. S., Borgnia, M. J., Bartesaghi, A., Tran, E. E. H., Earl, L. A., Schauder, D. M., Lengyel, J., Pierson, J., Patwardhan, A. & Subramaniam, S. Cryo-electron microscopy - A primer for the non-microscopist. *FEBS Journal* **280,** 28–45 (2013).

41. Henderson, R & Unwin, P. N. T. Three-dimensional model of purple membrane obtained by electron microscopy. *Nature* **257,** 28–32 (1975).

42. Kuhlbrandt, W. The resolution revolution. *Science* **343,** 1443–1444 (2014).

43. Becker, T., Bhushan, S., Jarasch, A., Armache, J. P., Funes, S., Jossinet, F., Gumbart, J., Mielke, T., Berninghausen, O., Schulten, K., Westhof, E., Gilmore, R., Mandon, E. C. & Beckmann, R. Structure of monomeric yeast and mammalian Sec61 complexes interacting with the translating ribosome. *Science* **326,** 1369–1373 (2009).

44. Liao, M., Cao, E., Julius, D. & Cheng, Y. Structure of the TRPV1 ion channel determined by electron cryo-microscopy. *Nature* **504,** 107–112 (2013).

45. Meyerson, J. R., Kumar, J., Chittori, S., Rao, P., Pierson, J., Bartesaghi, A., Mayer, M. L. & Subramaniam, S. Structural mechanism of glutamate receptor activation and desensitization. *Nature* **514,** 328–334 (2014).

46. Cheng, Y. Membrane protein structural biology in the era of single particle cryo-EM. *Current Opinion in Structural Biology* **52,** 58–63 (2018).

47. Ulmschneider, M. B., Sansom, M. S. P. & Di Nola, A. Evaluating tilt angles of membrane-associated helices: comparison of computational and NMR techniques. *Biophysical journal* **90,** 1650–60 (2006).

48. Marcoline, F. V., Bethel, N., Guerriero, C. J., Brodsky, J. L. & Grabe, M. Membrane Protein Properties Revealed through Data-Rich Electrostatics Calculations. *Structure* **23,** 1526–1537 (2015).

49. Simons, K. T., Kooperberg, C, Huang, E & Baker, D. Assembly of protein tertiary structures from fragments with similar local sequences using simulated annealing and Bayesian scoring functions. *Journal of molecular biology* **268,** 209–25 (1997).

50. Rohl, C. A., Strauss, C. E. M., Misura, K. M. S. & Baker, D. Protein structure prediction using Rosetta. *Methods in Enzymology* **383,** 66–93 (2004).

51. Leaver-Fay, A., Tyka, M., Lewis, S. M., Lange, O. F., Thompson, J., Jacak, R., Kaufman, K. W., Renfrew, P. D., Smith, C. A., Sheffler, W., Davis, I. W., Cooper, S., Treuille, A., Mandell, D. J., Richter, F., Ban, Y.-E. A., Fleishman, S. J., Corn, J. E., Kim, D. E., Lyskov, S., Berrondo, M., Mentzer, S., Popovic, Z., Havranek, J. J., Karanicolas, J., Das, R., Meiler, J., Kortemme, T., Gray, J. J., Kuhlman, B., Baker, D. & Bradley, P. Rosetta3: An Object-Oriented Software Suite for the Simulation and Design of Macromolecules. *Methods in enzymology* **487,** 545–574 (2011).

52. Marze, N. A., Roy Burman, S. S., Sheffler, W. & Gray, J. J. Efficient Flexible Backbone Protein-Protein Docking for Challenging Targets. *Bioinformatics* **34,** 3461–3469 (2018).

53. Langan, R. A., Boyken, S. E., Ng, A. H., Samson, J. A., Dods, G., Westbrook, A. M., Nguyen, T. H., Lajoie, M. J., Chen, Z., Berger, S., Mulligan, V. K., Dueber, J. E., Novak, W. R. P., El-Samad, H. & Baker, D. De novo design of bioactive protein switches. *Nature* **572,** 205–210 (2019).

54. Huang, P. S., Boyken, S. E. & Baker, D. The coming of age of de novo protein design. *Nature* **537,** 320–327 (2016).

55. Labonte, J. W., Aldof-Bryfogle, J, Schief, W. R. & Gray, J. J. Residue-centric modeling and design of saccharide and glycoconjugate structures. *Journal of Computational Chemistry* **38,** 276–287 (2017).

56. Das, R. & Baker, D. Automated de novo prediction of native-like RNA tertiary structures. *Proceedings of the National Academy of Sciences* **104,** 14664–14669 (2007).

57. Anfinsen, C. B. Principles that govern the folding of protein chains. *Science* **181,** 223–30 (1973).

58. Baker, D., Sohl, J. L. & Agard, D. A. A protein-folding reaction under kinetic control. *Nature* **356,** 263–265 (1992).

59. Das, R. & Baker, D. Macromolecular modeling with rosetta. *Annual review of biochemistry* **77,** 363–382 (2008).

60. Park, H., Bradley, P., Greisen, P., Liu, Y., Mulligan, V. K., Kim, D. E., Baker, D. & Dimaio, F. Simultaneous Optimization of Biomolecular Energy Functions on Features from Small Molecules and Macromolecules. *Journal of Chemical Theory and Computation* **12,** 6201–6212 (2016).

61. Alford, R. F., Leaver-Fay, A., Jeliazkov, J. R., O'Meara, M. J., DiMaio, F. P., Park, H., Shapovalov, M. V., Renfrew, P. D., Mulligan, V. K., Kappel, K., Labonte, J. W., Pacella, M. S., Bonneau, R., Bradley, P., Dunbrack, R. L., Das, R., Baker, D., Kuhlman, B., Kortemme, T. & Gray, J. J. The Rosetta All-Atom Energy Function for Macromolecular Modeling and Design. *Journal of Chemical Theory and Computation* **13,** 3031–3048 (2017).

62. Yarov-Yarovoy, V., Schonbrun, J. & Baker, D. Multipass membrane protein structure prediction using Rosetta. *Proteins: Structure, Function, and Bioinformatics* **62,** 1010–1025 (2005).

63. Barth, P, Schonbrun, J & Baker, D. Toward high-resolution prediction and design of transmembrane helical protein structures. *Proceedings of the National Academy of Sciences* **104,** 15682–15687 (2007).

64. Lazaridis, T. Effective energy function for proteins in lipid membranes. *Proteins: Structure, Function, and Genetics* **52,** 176–192 (2003).

65. Alford, R. F., Koehler Leman, J., Weitzner, B. D., Duran, A. M., Tilley, D. C., Elazar, A. & Gray, J. J. An integrated framework advancing membrane protein modeling and design. *PLoS Computational Biology* **11,** e1004398 (2015).

66. Chaudhury, S., Lyskov, S. & Gray, J. J. PyRosetta: a script-based interface for implementing molecular modeling algorithms using Rosetta. *Bioinformatics* **26,** 689–691 (2010).

67. Fleishman, S. J., Leaver-Fay, A., Corn, J. E., Strauch, E.-M., Khare, S. D., Koga, N., Ashworth, J., Murphy, P., Richter, F., Lemmon, G., Meiler, J. & Baker, D. RosettaScripts: A Scripting Language Interface to the Rosetta Macromolecular Modeling Suite. *PLoS One* **6,** e20161 (2011).

68. Tan, S., Tan, H. T. & Chung, M. C. M. Membrane proteins and membrane proteomics. *Proteomics* **8,** 3924–32 (2008).

69. Barth, P. & Senes, A. Toward high-resolution computational design of the structure and function of helical membrane proteins. *Nature Structural and Molecular Biology* **23,** 475–480 (2016).

70. Joh, N. H., Wang, T., Bhate, M. P., Acharya, R., Wu, Y., Grabe, M., Hong, M., Grigoryan, G. & DeGrado, W. F. De novo design of a transmembrane Zn2+-transporting four-helix bundle. *Science* **346,** 1520–1524 (2014).

71. Mahendran, K. R., Niitsu, A., Kong, L., Thomson, A. R., Sessions, R. B., Woolfson, D. N. & Bayley, H. A monodisperse transmembrane α-helical peptide barrel. *Nature Chemistry* **9,** 411–419.

72. Chowdhury, R., Ren, T., Shankla, M., Decker, K., Grisewood, M., Prabhakar, J., Baker, C., Golbeck, J. H., Aksimentiev, A., Kumar, M. & Maranas, C. D. PoreDesigner for tuning solute selectivity in a robust and highly permeable outer membrane pore. *Nature Communications* **9,** 3661 (2018).

73. Young, M, Dahoun, T, Sokrat, B, Arber, C, Chen, K. M., Bouvier, M & Barth, P. Computational design of orthogonal membrane receptor-effector switches for rewiring signaling pathways. *Proceedings of the National Academy of Sciences* **115,** 7051–7056 (2018).

74. Feng, X., Ambia, J., Chen, K.-Y. M., Young, M. & Barth, P. Computational design of ligand-binding membrane receptors with high selectivity. *Nature Chemical Biology* **13,** 715–723 (2017).

75. Lu, P., Min, D., DiMaio, F., Wei, K. Y., Vahey, M. D., Boyken, S. E., Chen, Z., Fallas, J. A., Ueda, G., Sheffler, W., Mulligan, V. K., Xu, W., Bowie, J. U. & Baker, D. Accurate computational design of multipass transmembrane proteins. *Science* **359,** 1042–1046 (2018).

76. Dickson, C. J., Rosso, L., Betz, R. M., Walker, R. C. & Gould, I. R. GAFFlipid: a General Amber Force Field for the accurate molecular dynamics simulation of phospholipid. *Soft Matter* **8,** 9617–9627 (2012).

77. Klauda, J. B., Venable, R. M., Freites, J. A., O'Connor, J. W., Tobias, D. J., Mondragon-Ramirez, C., Vorobyov, I., Alexander D. MacKerell, J. & Pastor, R. W. Update of the CHARMM All-Atom Additive Force Field for Lipids: Validation on Six Lipid Types. *Journal of Physical Chemistry B* **114,** 7830–7843 (2010).

78. Schmid, N., Eichenberger, A. P., Choutko, A., Riniker, S., Winger, M., Mark, A. E. & van Gunsteren, W. F. Definition and testing of the GROMOS force-field versions 54A7 and 54B7. *European Biophysics Journal* **40,** 843–856 (2011).

79. Phillips, J. C., Sun, Y., Jain, N., Bohm, E. J. & Kale, L. V. Mapping to irregular torus topologies and other techniques for petascale biomolecular simulation. *SC14: International Conference for High Performance Computing, Networking, Storage and Analysis,* 81–91 (2014).

80. Marrink, S. J., Corradi, V., Souza, P. C., Ingólfsson, H. I., Tieleman, D. P. & Sansom, M. S. Computational Modeling of Realistic Cell Membranes. *Chemical Reviews* **119,** 6184–6226 (2019).

81. Marrink, S. J., Risselada, H. J., Yefimov, S., Tieleman, D. P. & de Vries, A. H. The MARTINI Force Field: Coarse grained model for biomolecular simulations. *Journal of Physical Chemistry B* **111,** 7812–7824 (2007).

82. Barrera, E. E., Frigini, E. N., Porasso, R. D. & Pantano, S. Modeling DMPC lipid membranes with SIRAH force-field. *Journal of Molecular Modeling* **23,** 259 (2017).

83. Baoukina, S., Rozmanov, D. & Tieleman, D. P. Composition Fluctuations in Lipid Bilayers. *Biophysical Journal* **113,** 2750–2761 (2017).

84. Warshel, A. & Russell, S. T. Calculations of electrostatic interactions in biological systems and in solutions. *Quarterly Reviews of Biophysics* **17,** 283–422 (1984).

85. Grossfield, A. Chapter 5: Implicit Modeling of Membranes. *Current Topics in Membranes* **60,** 131–157 (2008).

86. Ulmschneider, J. P. & Ulmschneider, M. B. Sampling efficiency in explicit and implicit membrane environments studied by peptide folding simulations. *Proteins* **75,** 586–597 (2009).

87. Davis, M. E. & McCammon, J. A. Electrostatics in biomolecular structure and dynamics. *Chemical Reviews* **90,** 509–521 (1990).

88. Baker, N. A., Sept, D, Joseph, S, Holst, M. J. & McCammon, J. A. Electrostatics of nanosystems: application to microtubules and the ribosome. *Proceedings of the National Academy of Sciences* **98,** 10037–10041 (2001).

89. Im, W., Lee, M. S. & Brooks, C. L. Generalized born model with a simple smoothing function. *Journal of Computational Chemistry* **24,** 1691–1702 (2003).

90. Spassov, V. Z., Yan, L. & Sándor, S. Introducing an implicit membrane in Generalized Born/Solvent Accessibility continuum solvent models. *Journal of Physical Chemistry B* **106,** 8726–8738 (2002).

91. Panahi, A. & Feig, M. Dynamic Heterogeneous Dielectric Generalized Born (DHDGB): An Implicit Membrane Model with a Dynamically Varying Bilayer Thickness. *Journal of Chemical Theory and Computation* **9,** 1709–1719 (2013).

92. Radzicka, A. & Wolfenden, R. Comparing the polarities of the amino acids: side-chain distribution coefficients between the vapor phase, cyclohexane, 1-octanol, and neutral aqueous solution. *Biochemistry* **27,** 1664–1670 (1988).

93. Nepal, B., Leveritt, J. & Lazaridis, T. Membrane Curvature Sensing by Amphipathic Helices: Insights from Implicit Membrane Modeling. *Biophysical Journal* **114,** 2128–2141 (2018).

94. Franks, N. P., Abraham, M. H. & Lieb, W. R. Molecular organization of liquid n-octanol: an X-ray diffraction analysis. *Journal of Pharmaceutical Sciences* **82,** 466–70 (1993).

95. MacCallum, J. L., Bennett, W. F. D. & Tieleman, D. P. Distribution of amino acids in a lipid bilayer from computer simulations. *Biophysical Journal* **94,** 3393–3404 (2008).

96. Senes, A., Chadi, D. C., Law, P. B., Walters, R. F. S., Nanda, V. & DeGrado, W. F. Ez, a Depth-dependent potential for assessing the energies of insertion of amino acid side-chains into membranes: Derivation and applications to determining the orientation of transmembrane and interfacial helices. *Journal of Molecular Biology* **366,** 436–448 (2007).

97. Schramm, C. A., Hannigan, B. T., Donald, J. E., Keasar, C., Saven, J. G., Degrado, W. F. & Samish, I. Knowledge-based potential for positioning membrane-associated structures and assessing residue-specific energetic contributions. *Structure* **20,** 924–935 (2012).

98. Hsieh, D., Davis, A. & Nanda, V. A knowledge-based potential highlights unique features of membrane α-helical and β-barrel protein insertion and folding. *Protein Science* **21,** 50–62 (2012).

99. Moon, C. P. & Fleming, K. G. Side-chain hydrophobicity scale derived from transmembrane protein folding into lipid bilayers. *Proceedings of the National Academy of Sciences* (2011).

100. Lamy-Freund, M. T. & Riske, K. A. The peculiar thermo-structural behavior of the anionic lipid DMPG. *Chemistry and Physics of Lipids* **122,** 19–32 (2003).

101. Leonenko, Z. V., Finot, E, Ma, H, Dahms, T. E. S. & Cramb, D. T. Investigation of temperature-induced phase transitions in DOPC and DPPC phospholipid bilayers using temperature-controlled scanning force microscopy. *Biophysical Journal* **86,** 3783–3793 (2004).

102. Jo, S., Lim, J. B., Klauda, J. B. & Im, W. CHARMM-GUI Membrane Builder for Mixed Bilayers and Its Application to Yeast Membranes. *Biophysical Journal* **97,** 50–58 (2009).

103. Phillips, J. C., Braun, R, Wang, W, Gumbart, J, Tajkhorshid, E, Villa, E, Chipot, C, Skeel, R. D., Kale, L & Schulten, K. Scalable molecular dynamics with NAMD. *J Comput Chem* **26,** 1781–1802 (2005).

104. Michaud-Agrawal, N., Denning, E. J., Woolf, T. B. & Beckstein, O. MDAnalysis: A toolkit for the analysis of molecular dynamics simulations. *Journal of Computational Chemistry* **32,** 2319–2327 (2011).

105. Koehler Leman, J., Lyskov, S. & Bonneau, R. Computing structure-based lipid accessibility of membrane proteins with mp_lipid_acc in RosettaMP. *BMC Bioinformatics* **18,** 115 (2017).

106. Kuhlman, B & Baker, D. Native protein sequences are close to optimal for their structures. *Proceediings of the National Academy of Science* **97,** 10383–10388 (2000).

107. Khachiyan, L. G. & Todd, M. J. On the complexity of approximating the maximal inscribed ellipsoid for a polytope. *Mathematical Programming* **61,** 137–159 (1993).

108. Kučerka, N., Nieh, M.-P. & Katsaras, J. Fluid phase lipid areas and bilayer thicknesses of commonly used phosphatidylcholines as a function of temperature. *Biochimica et Biophysica Acta (BBA) - Biomembranes* **1808,** 2761–2771 (2011).

109. Lazaridis, T. Structural Determinants of Transmembrane β-Barrels. *Journal of Chemical Theory and Computation* **1,** 716–722 (2005).

110. Pellegrini-Calace, M., Maiwald, T. & Thornton, J. M. PoreWalker: A Novel Tool for the Identification and Characterization of Channels in Transmembrane Proteins from Their Three-Dimensional Structure. *PLoS Computational Biology* **5,** e1000440 (2009).

111. Yarov-Yarovoy, V., Decaen, P. G., Westenbroek, R. E., Pan, C.-Y., Scheuer, T., Baker, D. & Catterall, W. A. Structural basis for gating charge movement in the voltage sensor of a sodium channel. *Proceedings of the National Academy of Sciences* **109,** E93–E102 (2012).

112. Holt, A, Koehorst, R. B., Rutters-Meijneke, T, Gelb, M. H., Rijkers, D. T., Hemminga, M. A. & Killian, J. A. Tilt and Rotation Angles of a Transmembrane Model Peptide as Studied by Fluorescence Spectroscopy. *Biophysical Journal* **97,** 2258–2266 (2009).

113. Marx, D. C. & Fleming, K. G. Influence of Protein Scaffold on Side-Chain Transfer Free Energies. *Biophysical Journal* **113,** 597–604 (2017).

114. Dutagaci, B., Wittayanarakul, K., Mori, T. & Feig, M. Discrimination of Native-like States of Membrane Proteins with Implicit Membrane-based Scoring Functions. *Journal of Chemical Theory and Computation* **13,** 3049–3059 (2017).

115. Mravic, M., Thomaston, J. L., Tucker, M., Solomon, P. E., Liu, L. & DeGrado, W. F. Packing of apolar side chains enables accurate design of highly stable membrane proteins. *Science* **363,** 1418–1423 (2019).

116. Leaver-Fay, A., O'Meara, M. J., Tyka, M., Jacak, R., Song, Y., Kellogg, E. H., Thompson, J., Davis, I. W., Pache, R. A., Lyskov, S., Gray, J. J., Kortemme, T., Richardson, J. S., Havranek, J. J., Snoeyink, J., Baker, D. & Kuhlman, B. Scientific benchmarks for guiding macromolecular energy function improvement. *Methods in Enzymology* **523,** 109–143 (2013).

117. Lomize, M. A., Pogozheva, I. D., Joo, H., Mosberg, H. I. & Lomize, A. L. OPM database and PPM web server: resources for positioning of proteins in membranes. *Nucleic Acids Research* **40,** D370–D376 (2012).

118. Weinstein, J. Y., Elazar, A. & Fleishman, S. J. A lipophilicity-based energy function for membrane-protein modelling and design. *PLOS Computational Biology* **15,** e1007318 (2019).

119. Elazar, A., Weinstein, J., Biran, I., Fridman, Y., Bibi, E. & Fleishman, S. J. Mutational scanning reveals the determinants of protein insertion and association energetics in the plasma membrane. *eLife* **5,** e12125 (2016).

120. Wallin, E., Tsukihara, T., Yoshikawa, S., Heijne, G. V. & Elofsson, A. Architecture of helix bundle membrane proteins: An analysis of cytochrome c oxidase from bovine mitochondria. *Protein Science* **6,** 808–815 (1997).

121. McDonald, S. K. & Fleming, K. G. Aromatic Side Chain Water-to-Lipid Transfer Free Energies Show a Depth Dependence across the Membrane Normal. *Journal of the American Chemical Society* **138,** 7946–7950 (2016).

122. Peters, C. & Elofsson, A. Why is the biological hydrophobicity scale more accurate than earlier experimental hydrophobicity scales? *Proteins: Structure, Function, and Bioinformatics* **82,** 2190–2198 (2014).

123. Robertson, J. L. We choose to go to the membrane. *Proceedings of the National Academy of Sciences* **108,** 10027–10028 (2011).

124. Popot, J. L. & Engelman, D. M. Membrane protein folding and oligomerization: the two-stage model. *Biochemistry* **29,** 4031–4037 (1990).

125. Teixeira, V. H., Vila-Viçosa, D., Reis, P. B. & MacHuqueiro, M. PKa Values of Titrable Amino Acids at the Water/Membrane Interface. *Journal of Chemical Theory and Computation* **12,** 930–934 (2016).

126. Lazaridis, T. Implicit solvent simulations of peptide interactions with anionic lipid membranes. *Proteins: Structure, Function, and Bioinformatics* **58,** 518–527 (2004).

127. Ingólfsson, H. I., Melo, M. N., van Eerden, F. J., Arnarez, C., Lopez, C. A., Wassenaar, T. A., Periole, X., de Vries, A. H., Tieleman, D. P. & Marrink, S. J. Lipid organization of the plasma membrane. *Journal of the American Chemical Society* **136** (2014).

128. Rothman, J. E. & Lenard, J. Membrane asymmetry. *Science* **195,** 743–53 (1977).

129. Jarsch, I. K., Daste, F. & Gallop, J. L. Membrane curvature in cell biology: An integration of molecular mechanisms. *The Journal of Cell Biology* **214,** 375–387 (2016).

130. Lai, J. K., Ambia, J., Wang, Y. & Barth, P. Enhancing Structure Prediction and Design of Soluble and Membrane Proteins with Explicit Solvent-Protein Interactions. *Structure* **25,** 1758–1770.e8 (2017).

131. Vermaas, J. V., Pogorelov, T. V. & Tajkhorshid, E. Extension of the Highly Mobile Membrane Mimetic to Transmembrane Systems through Customized in Silico Solvents. *Journal of Physical Chemistry B* **121,** 3764–3776 (2017).

132. Dutagaci, B. & Feig, M. Determination of Hydrophobic Lengths of Membrane Proteins with the HDGB Implicit Membrane Model. *Journal of Chemical Information and Modeling* **57,** 3032–3042 (2017).

133. Perozo, E., Cortes, D. M., Sompornpisut, P., Kloda, A. & Martinac, B. Open channel structure of MscL and the gating mechanism of mechanosensitive channels. *Nature* **418,** 942–948 (2002).

134. Choe, S., Hecht, K. A. & Grabe, M. A continuum method for determining membrane protein insertion energies and the problem of charged residues. *Journal of General Physiology* **131,** 563–73 (2008).

135. Argudo, D., Bethel, N. P., Marcoline, F. V., Wolgemuth, C. W. & Grabe, M. New Continuum Approaches for Determining Protein-Induced Membrane Deformations. *Biophysical Journal* **112,** 2159–2172 (2017).

136. Jorgensen, W. L., Maxwell, D. S. & Tirado-Rives, J. Development and Testing of the OPLS All-Atom Force Field on Conformational Energetics and Properties of Organic Liquids. *Journal of the American Chemical Society* **118,** 11225–11236 (1996).

137. O'Meara, M. J., Leaver-Fay, A., Tyka, M. D., Stein, A., Houlihan, K., DiMaio, F., Bradley, P., Kortemme, T., Baker, D., Snoeyink, J. & Kuhlman, B. Combined covalent-electrostatic model of hydrogen bonding improves structure prediction with Rosetta. *Journal of Chemical Theory and Computation* **11,** 609–22 (2015).

138. Yuzlenko, O. & Lazaridis, T. Membrane protein native state discrimination by implicit membrane models. *Journal of Computational Chemistry* **34,** 731–738 (2013).

139. Kroncke, B. M., Duran, A. M., Mendenhall, J. L., Meiler, J., Blume, J. D. & Sanders, C. R. Documentation of an Imperative To Improve Methods for Predicting Membrane Protein Stability. *Biochemistry* **55,** 5002–5009 (2016).

140. Duran, A. M. & Meiler, J. Computational design of membrane proteins using RosettaMembrane. *Protein Science* **27,** 341–355 (2018).

141. Berman, H. M., Westbrook, J., Feng, Z., Gilliland, G., Bhat, T. N., Weissig, H., Shindyalov, I. N. & Bourne, P. E. The Protein Data Bank. *Nucleic Acids Research* **28,** 235–242 (2000).

142. Kellogg, E. H., Leaver-Fay, A. & Baker, D. Role of conformational sampling in computing mutation-induced changes in protein structure and stability. *Proteins* **79,** 830–838 (2011).

143. Feig, M. Implicit membrane models for membrane protein simulation. *Methods in Molecular Biology* **443,** 181–196 (2008).

144. Bhardwaj, G., Mulligan, V. K., Bahl, C. D., Gilmore, J. M., Harvey, P. J., Cheneval, O., Buchko, G. W., Pulavarti, S. V. S. R. K., Kaas, Q., Eletsky, A., Huang, P.-S., Johnsen, W. A., Greisen, P. J., Rocklin, G. J., Song, Y., Linsky, T. W., Watkins, A., Rettie, S. A., Xu, X., Carter, L. P., Bonneau, R., Olson, J. M., Coutsias, E., Correnti, C. E., Szyperski, T., Craik, D. J. & Baker, D. Accurate de novo design of hyperstable constrained peptides. *Nature* **538,** 329–335 (2016).

145. Tyka, M. D., Keedy, D. A., Andre, I, Dimaio, F, Song, Y, Richardson, D. C., Richardson, J. S. & Baker, D. Alternate states of proteins revealed by detailed energy landscape mapping. *Journal of Molecular Biology* **405,** 607–618 (2011).

146. Kučerka, N., Holland, B. W., Gray, C. G., Tomberli, B. & Katsaras, J. Scattering Density Profile Model of POPG Bilayers As Determined by Molecular Dynamics Simulations and Small-Angle Neutron and X-ray Scattering Experiments. *The Journal of Physical Chemistry B* **116,** 232–239 (2012).

147. Kucerka, N., van Oosten, B., Pan, J., Heberle, F. A., Harroun, T. A. & Katsaras, J. Molecular Structures of Fluid Phosphatidylethanolamine Bilayers Obtained from Simulation-to-Experiment Comparisons and Experimental Scattering Density Profiles. *The Journal of Physical Chemistry B* **119,** 1947–1956 (2015).

148. Jämbeck, J. P. M. & Lyubartsev, A. P. Derivation and systematic validation of a refined all-atom force field for Phosphatidylcholine lipids. *The Journal of Physical Chemistry B* **116,** 3164–3179 (2012).

149. Opella, S., Marassi, F., Gesell, J., Valente, A., Kim, Y., Oblatt-Montal, M. & Montal, M. Structures of the M2 channel-lining segments from nicotinic acetylcholine and NMDA receptors by NMR spectroscopy. *Nature Structural Biology* **6,** 374–379 (1999).

150. Wang, J., Kim, S., Kovacs, F. & Cross, T. A. Structure of the transmembrane region of the M2 protein H+ channel. *Protein Science* **10,** 2241–2250 (2008).

151. Park, S. H., Mrse, A. A., Nevzorov, A. A., Mesleh, M. F., Oblatt-Montal, M., Montal, M. & Opella, S. J. Three-dimensional structure of the channel-forming trans-membrane domain of virus protein "u" (Vpu) from HIV-1. *Journal of Molecular Biology* **333,** 409–424 (2003).

152. Strandberg, E., Ozdirekcan, S., Rijkers, D. T. S., van der Wel, P. C. A., Koeppe, R. E., Liskamp, R. M. J., Killian, J. A. & Killian, J. A. Tilt angles of transmembrane model peptides in oriented and non-oriented lipid bilayers as determined by 2H solid-state NMR. *Biophysical Journal* **86,** 3709–3721 (2004).

153. Moraes, I., Evans, G., Sanchez-Weatherby, J., Newstead, S. & Stewart, P. D. Membrane protein structure determination - The next generation. *Biochimica et Biophysica Acta - Biomembranes* **1838,** 78–87 (2014).

154. White, S. Membrane Proteins of Known Structure (2018).

155. Abdulla Bava, K, Gromiha, M. M., Uedaira, H., Kitajima, K. & Sarai, A. ProTherm, version 4.0: thermodynamic database for proteins and mutants. *Nucleic Acids Research* **32,** 120–121 (2004).

156. Dutagaci, B., Heo, L. & Feig, M. Structure refinement of membrane proteins via molecular dynamics simulations. *Proteins: Structure, Function and Bioinformatics* **86,** 738–750 (2018).

157. Aleksandrova, A. A., Sarti, E. & Forrest, L. R. MemSTATS: A benchmark set of membrane protein symmetries and pseudo-symmetries. *Journal of Molecular Biology* **432,** 597–604 (2020).

158. Lomize, A. L. & Pogozheva, I. D. TMDOCK: An Energy-Based Method for Modeling α-Helical Dimers in Membranes. *Journal of Molecular Biology* **429,** 390–398 (2017).

159. Hurwitz, N., Schneidman-Duhovny, D. & Wolfson, H. J. Memdock: an α-helical membrane protein docking algorithm. *Bioinformatics* **32,** 2444–2450 (2016).

160. Shao, J. Linear model selection by cross-validation. *Journal of the American Statistical Association* **88,** 486–494 (1993).

161. Alford, R. F., Fleming, P. J., Fleming, K. G. & Gray, J. J. Protein Structure Prediction and Design in a Biologically Realistic Implicit Membrane. *Biophysical Journal* **118,** 2042–2055 (2019).

162. Brooks, B. R., Brooks, C. L., Mackerell, A. D., Nilsson, L., Petrella, R. J., Roux, B., Won, Y., Archontis, G., Bartels, C., Boresch, S., Caflisch, A., Caves, L., Cui, Q., Dinner, A. R., Feig, M., Fischer, S., Gao, J., Hodoscek, M., Im, W., Kuczera, K., Lazaridis, T., Ma, J., Ovchinnikov, V., Paci, E., Pastor, R. W., Post, C. B., Pu, J. Z., Schaefer, M., Tidor, B., Venable, R. M., Woodcock, H. L., Wu, X., Yang, W., York, D. M. & Karplus, M. CHARMM: The biomolecular simulation program. *Journal of Computational Chemistry* **30,** 1545–1614 (2009).

163. Zanette, C., Bannan, C. C., Bayly, C. I., Fass, J., Gilson, M. K., Shirts, M. R., Chodera, J. D. & Mobley, D. L. Toward Learned Chemical Perception of Force Field Typing Rules. *Journal of Chemical Theory and Computation* **15,** 402–423 (2019).

164. Lomize, A. L., Pogozheva, I. D. & Mosberg, H. I. Anisotropic Solvent Model of the Lipid Bilayer. 1. Parameterization of Long-Range Electrostatics and First Solvation Shell Effects. *Journal of Chemical Information and Modeling* **51,** 918–929 (2011).

165. Ulmschneider, M. B., Ulmschneider, J. P., Schiller, N., Wallace, B. A., von Heijne, G. & White, S. H. Spontaneous transmembrane helix insertion thermodynamically mimics translocon-guided insertion. *Nature Communications* **5** (2014).

166. Weerakkody, D, Moshnikova, A, Thakur, M. S., Moshnikova, V, Daniels, J, Engelman, D. M., Andreev, O. A. & Reshetnyak, Y. K. Family of pH (low) insertion peptides for tumor targeting. *Proceedings of the National Academy of Science* **110,** 5834–5839 (2013).

167. Li, S., Wu, B. & Han, W. Parametrization of MARTINI for modeling hinging motions in membrane proteins. *Journal of Physical Chemistry B* **123,** 2254–2269 (2019).

168. Opella, S. J. & Marassi, F. M. Structure Determination of Membrane Proteins by NMR Spectroscopy. *Chemical Reviews* **104,** 3587–3606 (2004).

169. Schiffer, M, Chang, C. H. & Stevens, F. J. The functions of tryptophan residues in membrane proteins. *Protein Engineering* **5,** 213–214 (1992).

170. DeGrado, W. F. & Lear, J. D. Induction of peptide conformation at apolar water interfaces - a study with model peptides of defined hydrophobic periodicity. *Journal of the American Chemical Society* **107,** 7684–7689 (1985).

171. Bechinger, B, Zasloff, M & Opella, S. J. Structure and orientation of the antibiotic peptide magainin in membranes by solid-state nuclear magnetic resonance spectroscopy. *Protein Science* **2,** 2077–84 (1993).

172. Lomize, A. L., ID, P., Lomize, M. A. & HI, M. Positioning of proteins in membranes: A computational approach. *Protein Science* **15,** 1318–1333 (2006).

173. Fernández, C., Hilty, C., Wider, G. & Wüthrich, K. Lipid-protein interactions in DHPC micelles containing the integral membrane protein OmpX investigated by NMR spectroscopy. *Proceedings of the National Academy of Sciences* **99,** 13533–13537 (2002).

174. Corbet, C. & Feron, O. Tumour acidosis: From the passenger to the driver's seat. *Nature Reviews Cancer* **17,** 577–593 (2017).

175. Kilambi, K. P. & Gray, J. J. Rapid calculation of protein pKa values using Rosetta. *Biophysical Journal* **103,** 587–595 (2012).

176. Koehler Leman, J., Bonneau, R. & Ulmschneider, M. B. Statistically derived asymmetric membrane potentials from α-helical and β-barrel membrane proteins. *Scientific Reports* **8,** 4446 (2018).

177. VonHeijne, G. Control of topology and mode of assembly of a polytopic membrane protein by positively charged residues. *Nature* **341,** 456–458 (1989).

178. Bowie, J. U. Membrane protein twists and turns. *Science* **339,** 398–399 (2013).

179. Von Heijne, G. Proline kinks in transmembrane alpha-helices. *Journal of Molecular Biology* **218,** 499–503 (1991).

180. Law, E. C., Wilman, H. R., Kelm, S., Shi, J. & Deane, C. M. Examining the conservation of kinks in alpha helices. *PLoS One* **11,** e0157553 (2016).

181. Cao, Z. & Bowie, J. U. Shifting hydrogen bonds may produce flexible transmembrane helices. *Proceedings of the National Academy of Sciences* **109,** 8121–8126 (2012).

182. Cao, Z., Hutchison, J. M., Sanders, C. R. & Bowie, J. U. Backbone Hydrogen Bond Strengths Can Vary Widely in Transmembrane Helices. *Journal of the American Chemical Society* **139,** 10742–10749 (2017).

183. Atilgan, A. R., Durell, S. R., Jernigan, R. L., Demirel, M. C., Keskin, O & Bahar, I. Anisotropy of fluctuation dynamics of proteins with an elastic network model. *Biophysical Journal* **80,** 505–515 (2001).

184. Lemmon, M. A., Treutlein, H. R., Adams, P. D., Brünger, A. T. & Engelman, D. M. A dimerization motif for transmembrane alpha-helices. *Nature Structural Biology* **1,** 157–163 (1994).

185. Senes, A, Ubarretxena-Belandia, I & Engelman, D. M. The Ca - HO hydrogen bond: A determinant of stability and specificity in transmembrane helix interactions. *Proceedings of the National Academy of Sciences* **98,** 9056–9061 (2001).

186. Koukos, P. I., Faro, I., van Noort, C. W. & Bonvin, A. M. A Membrane Protein Complex Docking Benchmark. *Journal of Molecular Biology* **430,** 5246–5256 (2018).

187. Lensink, M. F. & Wodak, S. J. Docking and scoring protein interactions: CAPRI 2009. *Proteins: Structure, Function and Bioinformatics* **78,** 3073–3084 (2010).

188. Kelm, S., Shi, J. & Deane, C. M. MEDELLER: homology-based coordinate generation for membrane proteins. *Bioinformatics* **26,** 2833–2840 (2010).

189. AlQuraishi, M. AlphaFold at CASP13. *Bioinformatics* (2019).

190. Wang, S., Fei, S., Wang, Z., Li, Y., Xu, J., Zhao, F. & Gao, X. PredMP: A web server for de novo prediction and visualization of membrane proteins. *Bioinformatics* **35,** 691–693 (2019).

191. Wang, S., Li, W., Liu, S. & Xu, J. RaptorX-Property: a web server for protein structure property prediction. *Nucleic acids research* **44,** W430–W435 (2016).

192. Wang, S., Weng, S., Ma, J. & Tang, Q. DeepCNF-D: Predicting protein order/disorder regions by weighted deep convolutional neural fields. *International Journal of Molecular Sciences* **16,** 17315–30 (2015).

193. Gesell, J., Zasloff, M. & Opella, S. J. Two-dimensional H NMR experiments show that the 23-residue magainin antibiotic peptide is an alpha-helix in dodecylphosphocholine micelles, sodium dodecylsulfate micelles, and trifluoroethanol-water solution. *Journal of Biomolecular NMR* **9,** 127–135 (1997).

194. Sawai, M. V., Waring, A. J., Kearney, W. R., McCray, P. B., Forsyth, W. R., Lehrer, R. I. & Tack, B. F. Impact of single-residue mutations on the structure and function of ovispirin/novispirin antimicrobial peptides. *Protein Engineering* **15,** 225–232 (2002).

195. Oh, D, Shin, S. Y., Lee, S, Kang, J. H., Kim, S. D., Ryu, P. D., Hahm, K. S. & Kim, Y. Role of the hinge region and the tryptophan residue in the synthetic antimicrobial peptides, cecropin A(1-8)-magainin 2(1-12) and its analogues, on their antibiotic activities and structures. *Biochemistry* **39,** 11855–11864 (2000).

196. Vargas, R., Garza, J., Dixon, D. A. & Hay, B. P. How strong is the C(α)-H···O=C hydrogen bond? *Journal of the American Chemical Society* **122,** 4750–4755 (2000).

197. Scheiner, S., Kar, T. & Gu, Y. Strength of the CαH··O Hydrogen Bond of Amino Acid Residues. *Journal of Biological Chemistry* **276,** 9832–9837 (2001).

198. Öjemalm, K., Higuchi, T., Lara, P., Lindahl, E., Suga, H. & Von Heijne, G. Energetics of side-chain snorkeling in transmembrane helices probed by non-proteinogenic amino acids. *Proceedings of the National Academy of Sciences* **113,** 10559–10564 (2016).

199. Villinger, S., Briones, R., Giller, K., Zachariae, U., Lange, A., De Groot, B. L., Griesinger, C., Becker, S. & Zweckstetter, M. Functional dynamics in the voltage-dependent anion channel. *Proceedings of the National Academy of Sciences* **107,** 22546–22551 (2010).

200. Rui, H., Lee, K. I., Pastor, R. W. & Im, W. Molecular dynamics studies of ion permeation in VDAC. *Biophysical Journal* **100,** 602–610 (2011).

201. Cao, Z., Hutchison, J. M., Sanders, C. R. & Bowie, J. U. Backbone Hydrogen Bond Strengths Can Vary Widely in Transmembrane Helices. *Journal of the American Chemical Society* **139,** 10742–10749 (2017).

202. Landau, L., Bell, J., Kearsley, M. & Pitaevskii, L. *Electrodynamics of continuous media* (2013).

203. Honig, B. & Nicholls, A. Classical electrostatics in biology and chemistry. *Science* **268,** 1144–1149 (1995).

204. Schutz, C. N. & Warshel, A. What are the dielectric "constants" of proteins and how to validate electrostatic models? *Proteins: Structure, Function and Genetics* **44,** 400–417 (2001).

205. Nakamura, H, Sakamoto, T & Wada, A. A theoretical study of the dielectric constant of protein. *Protein Engineering* **2,** 177–183 (1988).

206. Zhou, Y. C., Feig, M. & Wei, G. W. Highly accurate biomolecular electrostatics in continuum dielectric environments. *Journal of Computational Chemistry* **29,** 87–97 (2008).

207. Bashford, D. & Gerwert, K. Electrostatic calculations of the pKa values of ionizable groups in bacteriorhodopsin. *Journal of Molecular Biology* **224,** 473–486 (1992).

208. Ben-Tal, N., Ben-Shaul, A., Nicholls, A. & Honig, B. Free-energy determinants of α-helix insertion into lipid bilayers. *Biophysical Journal* **70,** 1803–1812 (1996).

209. Roux, B. & MacKinnon, R. The cavity and pore helices in the KcsA K+ channel: Electrostatic stabilization of monovalent cations. *Science* **285,** 100–102 (1999).

210. Onufriev, A., Bashford, D. & Case, D. A. Modification of the generalized born model suitable for macromolecules. *Journal of Physical Chemistry B* **104,** 3712–3720 (2000).

211. Onufriev, A., Bashford, D. & Case, D. A. Exploring Protein Native States and Large-Scale Conformational Changes with a Modified Generalized Born Model. *Proteins: Structure, Function and Genetics* **55,** 383–394 (2004).

212. Gabb, H. A., Jackson, R. M. & Sternberg, M. J. Modelling protein docking using shape complementarity, electrostatics and biochemical information. *Journal of Molecular Biology* **272,** 106–120 (1997).

213. Morozov, A. V., Kortemme, T. & Baker, D. Evaluation of models of electrostatic interactions in proteins. *Journal of Physical Chemistry B* **107,** 2075–2090 (2003).

214. Warshel, A & Levitt, M. Theoretical studies of enzymic reactions: dielectric, electrostatic and steric stabilization of the carbonium ion in the reaction of lysozyme. *Journal of Molecular Biology* **103,** 227–49 (1976).

215. Hunt, J. F., Rath, P., Rothschild, K. J. & Engelman, D. M. Spontaneous, pH-dependent membrane insertion of a transbilayer alpha-helix. *Biochemistry* **36,** 15177–15192 (1997).

216. Fendos, J., Barrera, F. N. & Engelman, D. M. Aspartate embedding depth affects pHLIP's insertion pKa. *Biochemistry* **52,** 4595–4604 (2013).

217. Onufriev, A., Case, D. A. & Ullmann, G. M. A novel view of pH titration in biomolecules. *Biochemistry* **40,** 3413–3419 (2001).

218. Po, H. N. & Senozan, N. M. The Henderson-Hasselbalch Equation: Its History and Limitations. *Journal of Chemical Education* **78,** 1499–1503 (2001).

219. Hendrickson, W. A. Atomic-level analysis of membrane-protein structure. *Nature Structural and Molecular Biology* **23,** 464–467 (2016).

220. Kloppmann, E., Punta, M. & Rost, B. Structural genomics plucks high-hanging membrane proteins. *Current Opinion in Structural Biology* **22,** 326–332 (2012).

221. Gordon, L. B., Rothman, F. G., López-Otín, C. & Misteli, T. Progeria: A paradigm for translational medicine. *Cell* **156,** 400–407 (2014).

222. De Sandre-Giovannoli, A., Bernard, R., Cau, P., Navarro, C., Amiel, J., Boccaccio, I., Lyonnet, S., Stewart, C. L., Munnich, A., Le Merrer, M. & Lévy, N. Lamin A truncation in Hutchinson-Gilford progeria. *Science* **300,** 2055 (2003).

223. Capell, B. C. & Collins, F. S. Human laminopathies: Nuclei gone genetically awry. *Nature Reviews Genetics* **7,** 940–952 (2006).

224. Davies, B. S. J., Fong, L. G., Yang, S. H., Coffinier, C. & Young, S. G. The Post-translational Processing of Prelamin A and Disease. *Annual Review of Genomics and Human Genetics* **10,** 153–174 (2009).

225. Eriksson, M., Brown, W. T., Gordon, L. B., Glynn, M. W., Singer, J., Scott, L., Erdos, M. R., Robbins, C. M., Moses, T. Y., Berglund, P., Dutra, A., Pak, E., Durkin, S., Csoka, A. B., Boehnke, M., Glover, T. W. & Collins, F. S. Recurrent de novo point mutations in lamin A cause Hutchinson-Gilford progeria syndrome. *Nature* **423,** 293–298 (2003).

226. Merideth, M. A., Gordon, L. B., Clauss, S., Sachdev, V., Smith, A. C., Perry, M. B., Brewer, C. C., Zalewski, C., Kim, H. J., Solomon, B., Brooks, B. P., Gerber, L. H., Turner, M. L., Domingo, D. L., Hart, T. C., Graf, J., Reynolds, J. C., Gropman, A., Yanovski, J. A., Gerhard-Herman, M., Collins, F. S., Nabel, E. G., Cannon, R. O., Gahl, W. A. & Introne, W. J. Phenotype and course of Hutchinson-Gilford progeria syndrome. *New England Journal of Medicine* **358,** 592–604 (2008).

227. Barrowman, J., Wiley, P. A., Hudon-Miller, S. E., Hrycyna, C. A. & Michaelis, S. Human ZMPSTE24 disease mutations: residual proteolytic activity correlates with disease severity. *Human Molecular Genetics* **21,** 4084–4093 (2012).

228. Navarro, C. L., Esteves-Vieira, V., Courrier, S., Boyer, A., Duong Nguyen, T., Huong, L. T. T., Meinke, P., Schröder, W., Cormier-Daire, V., Sznajer, Y., Amor, D. J., Lagerstedt, K., Biervliet, M., Van Den Akker, P. C., Cau, P., Roll, P., Lévy, N., Badens, C., Wehnert, M. & De Sandre-Giovannoli, A. New ZMPSTE24 (FACE1) mutations in patients affected with restrictive dermopathy or related progeroid syndromes and mutation update. *European Journal of Human Genetics* **22,** 1002–1011 (2014).

229. Spear, E. D., Hsu, E. T., Nie, L., Carpenter, E. P., Hrycyna, C. A. & Michaelis, S. ZMPSTE24 missense mutations that cause progeroid diseases decrease prelamin a cleavage activity and/or protein stability. *DMM Disease Models and Mechanisms* **11,** dmm033670 (2018).

230. Michaelis, S. & Hrycyna, C. A. A protease for the ages. *Science* **340,** 1529–1530 (2013).

231. Michaelis, S & Barrowman, J. Biogenesis of the Saccharomyces cerevisiae Pheromone a-Factor, from Yeast Mating to Human Disease. *Microbiology and Molecular Biology Reviews* **76,** 626–651 (2012).

232. Worman, H. J. & Michaelis, S. Permanently Farnesylated Prelamin A, Progeria, and Atherosclerosis. *Circulation* **138,** 283–286 (2018).

233. Bergo, M. O., Gavino, B., Ross, J., Schmidt, W. K., Hong, C., Kendall, L. V., Mohr, A., Meta, M., Genant, H., Jiang, Y., Wisner, E. R., Van Bruggen, N., Carano, R. A. D., Michaelis, S., Griffey, S. M. & Young, S. G. Zmpste24 deficiency in mice causes spontaneous bone fractures, muscle weakness, and a prelamin A processing defect. *Proceedings of the National Academy of Sciences* **99,** 13049–13054 (2002).

234. Pendás, A. M., Zhou, Z., Cadiñanos, J., Freije, J. M. P., Wang, J., Hultenby, K., Astudillo, A., Wernerson, A., Rodríguez, F., Tryggvason, K. & López-Otín, C. Defective prelamin A processing and muscular and adipocyte alterations in Zmpste24 metalloproteinase-deficient mice. *Nature Genetics* **31,** 94–99 (2002).

235. Worman, H. J., Fong, L. G., Muchir, A. & Young, S. G. Laminopathies and the long strange trip from basic cell biology to therapy. *Journal of Clinical Investigation* **119,** 1825–1836 (2009).

236. Barrowman, J., Hamblet, C., George, C. M. & Michaelis, S. Analysis of prelamin A biogenesis reveals the nucleus to be a CaaX processing compartment. *Molecular Biology of the Cell* **19,** 5398–5408 (2008).

237. Barrowman, J. & Michaelis, S. ZMPSTE24, an integral membrane zinc metalloprotease with a connection to progeroid disorders. *Biological Chemistry* **390,** 761–773 (2009).

238. Tam, A., Schmidt, W. K. & Michaelis, S. The Multispanning Membrane Protein Ste24p Catalyzes CAAX Proteolysis and NH2-terminal Processing of the Yeast a-Factor Precursor. *Journal of Biological Chemistry* **276,** 46798–46806 (2001).

239. Clark, K. M., Jenkins, J. L., Fedoriw, N. & Dumont, M. E. Human CaaX protease ZMPSTE24 expressed in yeast: Structure and inhibition by HIV protease inhibitors. *Protein Science* **26,** 242–257 (2017).

240. Pryor, E. E., Horanyi, P. S., Clark, K. M., Fedoriw, N., Connelly, S. M., Koszelak-Rosenblum, M., Zhu, G., Malkowski, M. G., Wiener, M. C. & Dumont, M. E. Structure of the integral membrane protein CAAX protease Ste24p. *Science* **340,** 1600–1604 (2013).

241. Quigley, A., Dong, Y. Y., Pike, A. C. W., Dong, L., Shrestha, L., Berridge, G., Stansfeld, P. J., Sansom, M. S. P., Edwards, A. M., Bountra, C., Von Delft, F., Bullock, A. N., Burgess-Brown, N. A. & Carpenter, E. P. The structural basis of ZMPSTE24-dependent laminopathies. *Science* **340,** 1604–1607 (2013).

242. Barlow, K. A., Ó Conchúir, S., Thompson, S., Suresh, P., Lucas, J. E., Heinonen, M. & Kortemme, T. Flex ddG: Rosetta Ensemble-Based Estimation of Changes in Protein-Protein Binding Affinity upon Mutation. *The Journal of Physical Chemistry B* **122,** 5389–5399 (2018).

243. Smith, C. A. & Kortemme, T. Backrub-Like Backbone Simulation Recapitulates Natural Protein Conformational Variability and Improves Mutant Side-Chain Prediction. *Journal of Molecular Biology* **380,** 742–756 (2008).

244. Primeau, J. O., Armanious, G. P., Fisher, M. L. E. & Young, H. S. The sarcoendoplasmic reticulum calcium ATPase. *Subcellular Biochemistry* **87,** 229–258 (2018).

245. Chen, J., Sitsel, A., Benoy, V., Sepúlveda, M. R. & Vangheluwe, P. Primary Active Ca 2+ Transport Systems in Health and Disease. *Cold Spring Harbor Perspectives in Biology* **12,** a035113 (2020).

246. Cantilina, T., Sagara, Y., Inesi, G. & Jones, L. R. Comparative studies of cardiac and skeletal sarcoplasmic reticulum ATPases. Effect of a phospholamban antibody on enzyme activation by Ca2+. *Journal of Biological Chemistry* **268,** 17018–17025 (1993).

247. Mahaney, J. E., Albers, R. W., Waggoner, J. R., Kutchai, H. C. & Froehlich, J. P. Intermolecular conformational coupling and free energy exchange enhance the catalytic efficiency of cardiac muscle SERCA2a following the relief of phospholamban inhibition. *Biochemistry* **44,** 7713–7724 (2005).

248. Tada, M., Kirchberger, M. A., Repke, D. I. & Katz, A. M. The stimulation of calcium transport in cardiac sarcoplasmic reticulum by adenosine 3′:5′ monophosphate dependent protein kinase. *Journal of Biological Chemistry* **249,** 6174–6180 (1974).

249. Movsesian, M. A., Nishikawa, M. & Adelstein, R. S. Phosphorylation of phospholamban by calcium-activated, phospholipid-dependent protein kinase. Stimulation of cardiac sarcoplasmic reticulum calcium uptake. *Journal of Biological Chemistry* **259,** 534–540 (1984).

250. Kirchberger, M. A. & Antonetz, T. Calmodulin-mediated regulation of calcium transport and (Ca2+ + Mg2+)-activated ATPase activity in isolated cardiac sarcoplasmic reticulum. *Journal of Biological Chemistry* **257,** 5685–5691 (1982).

251. Kranias, E. G. & Solaro, R. J. Phosphorylation of troponin I and phospholamban during catecholamine stimulation of rabbit heart. *Nature* **249,** 709–714 (1982).

252. Zima, A. V., Bovo, E., Mazurek, S. R., Rochira, J. A., Li, W. & Terentyev, D. Ca handling during excitation-contraction coupling in heart failure. *Pflugers Archiv European Journal of Physiology* **466,** 1129–1137 (2014).

253. Gorski, P. A., Ceholski, D. K. & Hajjar, R. J. Altered myocardial calcium cycling and energetics in heart failure - A rational approach for disease treatment. *Cell Metabolism* **21,** 183–194 (2015).

254. Stroik, D. R., Ceholski, D. K., Bidwell, P. A., Mleczko, J., Thanel, P. F., Kamdar, F., Autry, J. M., Cornea, R. L. & Thomas, D. D. Viral expression of a SERCA2a-activating PLB mutant improves calcium cycling and synchronicity in dilated cardiomyopathic hiPSC-CMs. *Journal of Molecular and Cellular Cardiology* **138,** 59–65 (2020).

255. Akin, B. L., Hurley, T. D., Chen, Z & Jones, L. R. The structural basis for phospholamban inhibition of the calcium pump in sarcoplasmic reticulum. *Journal of Biological Chemistry* **288,** 30181–30191 (2013).

256. Chen, Z, Akin, B. L. & Jones, L. R. Ca2+ binding to site I of the cardiac Ca2+ pump is sufficient to dissociate phospholamban. *Journal of Biological Chemistry* **285,** 3253–3260 (2010).

257. Chen, Z, Stokes, D. L., Rice, W. J. & Jones, L. R. Spatial and dynamic interactions between phospholamban and the canine cardiac Ca2+ pump revealed with use of heterobifunctional cross-linking agents. *Journal of Biological Chemistry* **278,** 48348–48356 (2003).

258. Abrol, N., De Tombe, P. P. & Robia, S. L. S. Acute inotropic and lusitropic effects of cardiomyopathic R9C mutation of phospholamban. *Journal of Biological Chemistry* **290,** 7130–7140 (2015).

259. Pallikkuth, S., Blackwell, D., Hu, Z., Hou, Z., Zieman, D., Svensson, B., Thomas, D. & Robia, S. Phosphorylated phospholamban stabilizes a compact conformation of the cardiac calcium-ATPase. *Biophysical Journal* **105,** 1812–1821 (2013).

260. Hou, Z., Kelly, E. & Robia, S. Phosphomimetic mutations increase phospholamban oligomerization and alter the structure of its regulatory complex. *Journal of Biological Chemistry* **283,** 28996–29003 (2008).

261. Bidwell, P., Blackwell, D. J., Hou, Z., Zima, A. V. & Robia, S. L. Phospholamban binds with differential affinity to calcium pump conformers. *Journal of Biological Chemistry* **286,** 35044–35050 (2011).

262. Dong, X & Thomas, D. D. Time-resolved FRET reveals the structural mechanism of SERCA-PLB regulation. *Biochemical and Biophysical Research Communications* **449,** 196–201 (2014).

263. Karim, C. B., Zhang, Z, Howard, E. C., Torgersen, K. D. & Thomas, D. D. Phosphorylation-dependent conformational switch in spin-labeled phospholamban bound to SERCA. *Journal of Molecular Biology* **358,** 1032–1040 (2006).

264. Mueller, B, Karim, C. B., Negrashov, I. V., Kutchai, H & Thomas, D. D. Direct detection of phospholamban and sarcoplasmic reticulum Ca-ATPase interaction in membranes using fluorescence resonance energy transfer. *Biochemistry* **43,** 8754–8765 (2004).

265. Negash, S, Yao, Q, Sun, H, Li, J, Bigelow, D. J. & Squier, T. C. Phospholamban remains associated with the Ca2+- and Mg2+-dependent ATPase following phosphorylation by cAMP-dependent protein kinase. *Biochemistry* **351,** 195–205 (2000).

266. Gustavsson, M, Verardi, R, Mullen, D. G., Mote, K. R., Traaseth, N. J., Gopinath, T & Veglia, G. Allosteric regulation of SERCA by phosphorylation-mediated conformational shift of phospholamban. *Proceedings of the National Academy of Sciences* **110,** 17338–17343 (2013).

267. Li, J, Bigelow, D. J. & Squier, T. C. Conformational changes within the cytosolic portion of phospholamban upon release of Ca-ATPase inhibition. *Biochemistry* **43,** 3870–3879 (2004).

268. Martin, P. D., James, Z. M. & Thomas, D. D. Effect of Phosphorylation on Interactions between Transmembrane Domains of SERCA and Phospholamban. *Biophysical Journal* **114,** 2573–2583 (2018).

269. Autry, J. M., Thomas, D. D. & Espinoza-Fonseca, L. M. Sarcolipin Promotes Uncoupling of the SERCA Ca2+ Pump by Inducing a Structural Rearrangement in the Energy-Transduction Domain. *Biochemistry* **55,** 6083–6086 (2016).

270. Fernández-De Gortari, E. & Espinoza-Fonseca, L. M. Structural basis for relief of phospholamban-mediated inhibition of the sarcoplasmic reticulum Ca2+-ATPase at saturating Ca2+ conditions. *Journal of Biological Chemistry* **293,** 12405–12414 (2018).

271. Dyla, M., Hansen, S. B., Nissen, P. & Kjaergaard, M. Structural dynamics of P-type ATPase ion pumps. *Biochemical Society Transactions* **47,** 1247–1257 (2019).

272. Moller, J. V., Olesen, C, Winther, A. M. & Nissen, P. The sarcoplasmic Ca2+-ATPase: Design of a perfect chemi-osmotic pump. *Quarterly Reviews of Biophysics* **43,** 501–566 (2010).

273. Ogawa, H, Shinoda, T, Cornelius, F & Toyoshima, C. Crystal structure of the sodium-potassium pump (Na+,K+-ATPase) with bound potassium and ouabain. *Proceedings of the National Academy of Sciences* **106,** 13742–13747 (2009).

274. Shinoda, T, Ogawa, H, Cornelius, F & Toyoshima, C. Crystal structure of the sodium-potassium pump at 2.4Å resolution. *Nature* **459,** 446–450 (2009).

275. Teriete, P, Thai, K, Choi, J & Marassi, F. M. Effects of PKA phosphorylation on the conformation of the Na,K-ATPase regulatory protein FXYD1. *Biochimica et Biophysica Acta* **1788,** 2462–2470 (2009).

276. Stokes, D. L., Pomfret, A. J., Rice, W. J., Glaves, J. P. & Young, H. S. Interactions between Ca2+-ATPase and the pentameric form of phospholamban in two-dimensional co-crystals. *Biophysical Journal* **90,** 4213–4223 (2006).

277. Glaves, J. P., Primeau, J. O., Espinoza-Fonseca, L. M., Lemieux, M. J. & Young, H. S. The Phospholamban Pentamer Alters Function of the Sarcoplasmic Reticulum Calcium Pump SERCA. *Biophysical Journal* **116,** 633–647 (2019).

278. Glaves, J. P., Trieber, C. A., Ceholski, D. K., Stokes, D. L. & Young, H. S. Phosphorylation and mutation of phospholamban alter physical interactions with the sarcoplasmic reticulum calcium pump. *Journal of Molecular Biology* **405,** 707–723 (2011).

279. Lensink, M. F., Velankar, S. & Wodak, S. J. Modeling protein-protein and protein-peptide complexes: CAPRI 6th edition. *Proteins: Structure, Function and Bioinformatics* **85,** 359–377 (2017).

280. Salmaso, V. & Moro, S. Bridging molecular docking to molecular dynamics in exploring ligand-protein recognition process: An overview. *Frontiers in Pharmacology* **9,** 923 (2018).

281. Viswanath, S., Dominguez, L., Foster, L. S., Straub, J. E. & Elber, R. Extension of a Protein Docking Algorithm to Membranes and Applications to Amyloid Precursor Protein Dimerization. *Proteins: Structure, Function, and Bioinformatics* **83,** 2170–2185 (2015).

282. Izrailev, S., Stepaniants, S., Isralewitz, B., Kosztin, D., Lu, H., Molnar, F., Wriggers, W. & Schulten, K. Steered Molecular Dynamics. *Computational molecular dynamics: Challenges, Methods, Ideas,* 39–65 (1999).

283. Gray, J. J., Moughon, S, Wang, C, Schueler-Furman, O, Kuhlman, B, Rohl, C. A. & Baker, D. Protein-protein docking with simultaneous optimization of rigid-body displacement and side-chain conformations. *Journal of Molecular Biology* **331,** 281–299 (2003).

284. Sitsel, A., De Raeymaecker, J., Drachmann, N. D., Derua, R., Smaardijk, S., Andersen, J. L., Vandecaetsbeek, I., Chen, J., De Maeyer, M., Waelkens, E., Olesen, C., Vangheluwe, P. & Nissen, P. Structures of the heart specific SERCA2a Ca 2+ ATPase. *The EMBO Journal* **38,** e100020 (2019).

285. Toyoshima, C, Nakasako, M, Nomura, H & Ogawa, H. Crystal structure of the calcium pump of sarcoplasmic reticulum at 2.6Å resolution. *Nature* **405,** 647–655 (2000).

286. Toyoshima, C, Yonekura, S, Tsueda, J & Iwasawa, S. Trinitrophenyl derivatives bind differently from parent adenine nucleotides to Ca2+-ATPase in the absence of Ca2+. *Proceedings of the National Academy of Sciences* **108,** 1833–1838 (2011).

287. MacKerell, A. D., Feig, M & Brooks, C. L. Extending the treatment of backbone energetics in protein force fields: Limitations of gas-phase quantum mechanics in reproducing protein conformational distributions in molecular dynamics simulations. *Journal of Computational Chemistry* **25,** 1400–1415 (2004).

288. MacKerell, A. D., Feig, M & Brooks, C. L. Improved treatment of the protein backbone in empirical force fields. *Journal of the American Chemical Society* **126,** 698–699 (2004).

289. Foloppe, N & MacKerell, A. D. All-atom empirical force field for nucleic acids: I. Parameter optimization based on small molecule and condensed phase macromolecular target data. *Journal of Computational Chemistry* **21,** 86–104 (2000).

290. Jorgensen, W. L., Chandrasekhar, J, Madura, J. D., Impey, R. W. & Klein, M. L. Comparison of Simple Potential Functions for Simulating Liquid Water. *Journal of Chemical Physics* **79,** 926–935 (1983).

291. Darden, T, York, D & Pedersen, L. Particle Mesh Ewald - an N.Log(N) Method for Ewald Sums in Large Systems. *Journal of Chemical Physics* **98,** 10089–10092 (1993).

292. Essmann, U, Perera, L, Berkowitz, M. L., Darden, T, Lee, H & Pedersen, L. G. A Smooth Particle Mesh Ewald Method. *Journal of Chemical Physics* **103,** 8577–8593 (1995).

293. Berendsen, H. J. C., Postma, J. P. M., van Gunsteren, W. F., DiNola, A & Haak, J. R. Molecular dynamics with coupling to an external bath. *The Journal of Chemical Physics* **81,** 3684–3690 (1984).

294. Hoover, W. G. Canonical Dynamics - Equilibrium Phase-Space Distributions. *Physical Review A* **31,** 1695–1697 (1985).

295. Nose, S. A Molecular-Dynamics Method for Simulations in the Canonical Ensemble. *Molecular Physics* **52,** 255–268 (1984).

296. Nose, S & Klein, M. L. Constant Pressure Molecular-Dynamics for Molecular-Systems. *Molecular Physics* **50,** 1055–1076 (1983).

297. Parrinello, M & Rahman, A. Polymorphic Transitions in Single-Crystals - a New Molecular-Dynamics Method. *Journal of Applied Physics* **52,** 7182–7190 (1981).

298. Guzmán, D. L., Roland, J. T., Keer, H., Kong, Y. P., Ritz, T., Yee, A. & Guan, Z. Using steered molecular dynamics simulations and single-molecule force spectroscopy to guide the rational design of biomimetic modular polymeric materials. *Polymer* **49,** 3892–3901 (2008).

299. Kozakov, D, Hall, D. R., Xia, B, Porter, K. A., Padhorny, D, Yueh, C, Beglov, D & Vajda, S. The ClusPro web server for protein-protein docking. *Nature Protocols* **12,** 255–278 (2017).

300. Kozakov, D, Brenke, R, Comeau, S. R. & Vajda, S. PIPER: an FFT-based protein docking program with pairwise potentials. *Proteins* **65,** 392–406 (2006).

301. Stranges, P. B. & Kuhlman, B. A comparison of successful and failed protein interface designs highlights the challenges of designing buried hydrogen bonds. *Protein Science* **22,** 74–82 (2013).

302. Kimura, Y, Kurzydlowski, K, Tada, M & MacLennan, D. H. Phospholamban regulates the Ca2+-ATPase through intramembrane interactions. *Journal of Biological Chemistry* **271,** 21726–21731 (1996).

303. Akin, B. L. & Jones, L. R. Characterizing phospholamban to sarco(endo)plasmic reticulum Ca2+-ATPase 2a (SERCA2a) protein binding interactions in human cardiac sarcoplasmic reticulum vesicles using chemical cross-linking. *Journal of Biological Chemistry* **287,** 7582–7593 (2012).

304. Chen, Z, Akin, B. L., Stokes, D. L. & Jones, L. R. Cross-linking of C-terminal residues of phospholamban to the Ca2+ pump of cardiac sarcoplasmic reticulum to probe spatial and functional interactions within the transmembrane domain. *Journal of Biological Chemistry* **281,** 14163–14172 (2006).

305. Glaves, J. P., Primeau, J. O., Gorski, P. A., Espinoza-Fonseca, L. M., Lemieux, M. J. & Young, H. S. Interaction of a Sarcolipin Pentamer and Monomer with the Sarcoplasmic Reticulum Calcium Pump, SERCA. *Biophysical Journal* **118,** 518–531 (2020).

306. Reddy, L. G., Cornea, R. L., Winters, D. L., McKenna, E. & Thomas, D. D. Defining the molecular components of calcium transport regulation in a reconstituted membrane system. *Biochemistry* **42,** 4585–4592 (2003).

307. Akin, B. L., Chen, Z. & Jones, L. R. Superinhibitory phospholamban mutants compete with Ca2+ for binding to SERCA2a by stabilizing a unique nucleotide-dependent conformational state. *Journal of Biological Chemistry* **285,** 28540–28552 (2010).

308. Glaves, J., Gorski, P., Trieber, C., Stokes, D. & Young, H. Two dimensional crystallization of calcium transport regulatory complexes. *Acta Crystallographica Section A Foundations and Advances* **70,** c1066 (2014).

309. Jones, L. R., Cornea, R. L. & Chen, Z. Close proximity between residue 30 of phospholamban and cysteine 318 of the cardiac Ca2+ pump revealed by intermolecular thiol cross-linking. *Journal of Biological Chemistry* **277,** 28319–28329 (2002).

310. Bowie, J. U. Solving the membrane protein folding problem. *Nature* **438,** 581–589 (2005).

311. Roy Burman, S. S., Nance, M. L., Jeliazkov, J. R., Labonte, J. W., Lubin, J. H., Biswas, N., Gray, J. J., Burman, S. S. R., Nance, M. L., Jeliazkov, J. R., Labonte, J. W., Lubin, J. H., Biswas, N. & Gray, J. J. Novel sampling strategies and a coarse-grained score function for docking homomers, flexible heteromers, and oligosaccharides using Rosetta in CAPRI Rounds 37-45. *bioRxiv,* 749317 (2019).

312. Afara, M. R., Trieber, C. A., Ceholski, D. K. & Young, H. S. Peptide inhibitors use two related mechanisms to alter the apparent calcium affinity of the sarcoplasmic reticulum calcium pump. *Biochemistry* **47,** 9522–9530 (2008).

313. Chen, Z, Akin, B. L. & Jones, L. R. Mechanism of reversal of phospholamban inhibition of the cardiac Ca2+-ATPase by protein kinase A and by anti-phospholamban monoclonal antibody 2D12. *Journal of Biological Chemistry* **282,** 20968–20976 (2007).

314. Committee on Science, Technology, and Law Affairs, P., Global & Sciences. Synthetic Biology: Science and Technology for the New Millennium. *Board on Life Sciences, Division on Earth and Life Engineering, National Academy of Council, National Research* (2013).

315. Hille, B. *Ion Channels of Excitable Membranes* Third Edition (Sinauer Associates, Inc., 2011).

316. Rothemund, P. W. K. Folding DNA to create nanoscale shapes and patterns. *Nature* **440,** 297–302 (2006).

317. Rothemund, P. W., Ekani-Nkodo, A., Papadakis, N., Kumar, A., Fygenson, D. K. & Winfree, E. Design and characterization of programmable DNA nanotubes. *Journal of the American Chemical Society* **126,** 16344–16352 (2004).

318. Langecker, M., Arnaut, V., Martin, T. G., List, J., Renner, S., Mayer, M., Dietz, H. & Simmel, F. C. Synthetic lipid membrane channels formed by designed DNA nanostructures. *Science* **338,** 932–936 (2012).

319. Burns, J. R., Stulz, E. & Howorka, S. Self-assembled DNA nanopores that span lipid bilayers. *Nano Letters* **13,** 2351–2356 (2013).

320. Burns, J. R., Gopfrich, K., Wood, J. W., Thacker, V. V., Stulz, E., Keyser, U. F. & Howorka, S. Lipid-Bilayer-Spanning DNA Nanopores with a Bifunctional Porphyrin Anchor. *Angewandte Chemie International Edition* **52,** 12069–12072 (2013).

321. Krishnan, S., Ziegler, D., Arnaut, V., Martin, T. G., Kapsner, K., Henneberg, K., Bausch, A. R., Dietz, H. & Simmel, F. C. Molecular transport through large-diameter DNA nanopores. *Nature Communications* **7,** 1–7 (2016).

322. Krishnan, S., Satheesan, R., Puthumadathil, N., Kumar, K. S., Jayasree, P. & Mahendran, K. R. Autonomously Assembled Synthetic Transmembrane Peptide Pore. *Journal of the American Chemical Society* **141,** 2949–2959 (2019).

323. King, N. P., Sheffler, W., Sawaya, M. R., Vollmar, B. S., Sumida, J. P., André, I., Gonen, T., Yeates, T. O. & Baker, D. Computational design of self-assembling protein nanomaterials with atomic level accuracy. *Science* **336,** 1171–1174 (2012).

324. Humphris, E. L. & Kortemme, T. Design of multi-specificity in protein interfaces. *PLoS Computational Biology* **3,** 1591–1604 (2007).

325. Korendovych, I. V., Senes, A., Kim, Y. H., Lear, J. D., Fry, H. C., Therien, M. J., Blasie, J. K., Walker, F. A. & Degrado, W. F. De novo design and molecular assembly of a transmembrane diporphyrin-binding protein complex. *Journal of the American Chemical Society* **132,** 15516–15518 (2010).

326. Dang, B., Wu, H., Mulligan, V. K., Mravic, M., Wu, Y., Lemmin, T., Ford, A., Silva, D. A., Baker, D. & DeGrado, W. F. De novo design of covalently constrained mesosize protein scaffolds with unique tertiary structures. *Proceedings of the National Academy of Sciences* **114,** 10852–10857 (2017).

327. DiMaio, F., Leaver-Fay, A., Bradley, P., Baker, D. & André, I. Modeling Symmetric Macromolecular Structures in Rosetta3. *PLoS One* **6,** e20450 (2011).

328. Grigoryan, G. & Degrado, W. F. Probing designability via a generalized model of helical bundle geometry. *Journal of Molecular Biology* **405,** 1079–1100 (2011).

329. Offer, G., Hicks, M. R. & Woolfson, D. N. Generalized Crick equations for modeling noncanonical coiled coils. *Journal of Structural Biology* **137,** 41–53 (2002).

330. Huang, P. S., Oberdorfer, G., Xu, C., Pei, X. Y., Nannenga, B. L., Rogers, J. M., DiMaio, F., Gonen, T., Luisi, B. & Baker, D. High thermodynamic stability of parametrically designed helical bundles. *Science* **346,** 481–485 (2014).

331. Gerl, M. J., Sampaio, J. L., Urban, S., Kalvodova, L., Verbavatz, J. M., Binnington, B., Lindemann, D., Lingwood, C. A., Shevchenko, A., Schroeder, C. & Simons, K. Quantitative analysis of the lipidomes of the influenza virus envelope and MDCK cell apical membrane. *Journal of Cell Biology* **196,** 213–221 (2012).

332. Lyman, E., Hsieh, C.-L. & Eggeling, C. From Dynamics to Membrane Organization: Experimental Breakthroughs Occasion a Modeling Manifesto. *Biophysical Journal* **115,** 595–604 (2018).

333. Markones, M., Drechsler, C., Kaiser, M., Kalie, L., Heerklotz, H. & Fiedler, S. Engineering Asymmetric Lipid Vesicles: Accurate and Convenient Control of the Outer Leaflet Lipid Composition. *Langmuir* **34,** 1999–2005 (2018).

334. Cooper, R. A. Influence of increased membrane cholesterol on membrane fluidity and cell function in human red blood cells. *Journal of Supramolecular Structure* **8,** 413–430 (1978).

335. Cantor, R. S. Lipid composition and the lateral pressure profile in bilayers. *Biophysical Journal* **76,** 2625–2639 (1999).

336. Sejdiu, B. I. & Tieleman, D. P. Lipid-Protein Interactions Are a Unique Property and Defining Feature of G Protein-Coupled Receptors. *Biophysical Journal* **118,** 1887–1900 (2020).

337. Wang, Q., Pechersky, Y., Sagawa, S., Pan, A. C. & Shaw, D. E. Structural mechanism for Bruton's tyrosine kinase activation at the cell membrane. *Proceedings of the National Academy of Sciences* **116,** 9390–9399 (2019).

338. Labonte, J. W., Adolf-Bryfogle, J., Schief, W. R. & Gray, J. J. Residue-centric modeling and design of saccharide and glycoconjugate structures. *Journal of Computational Chemistry* **38,** 276–287 (2017).

339. Argudo, D., Bethel, N. P., Marcoline, F. V. & Grabe, M. Continuum descriptions of membranes and their interaction with proteins: Towards chemically accurate models. *Biochimica et Biophysica Acta - Biomembranes* **1858,** 1619–1634 (2016).

340. Zhou, W., Fiorin, G., Anselmi, C., Karimi-Varzaneh, H. A., Poblete, H., Forrest, L. R. & Faraldo-Gómez, J. D. Large-scale state-dependent membrane remodeling by a transporter protein. *eLife* **8,** e50576 (2019).

341. Davies, K. M., Anselmi, C., Wittig, I., Faraldo-Gómez, J. D. & Kühlbrandt, W. Structure of the yeast F 1F o-ATP synthase dimer and its role in shaping the mitochondrial cristae. *Proceedings of the National Academy of Sciences* **109,** 13602–13607 (2012).

342. Urry, D. W. The gramicidin A transmembrane channel: a proposed pi(L,D) helix. *Proceedings of the National Academy of Sciences* **68,** 672–676 (1971).

343. Koehler Leman, J., D'Avino, A. R., Bhatnagar, Y. & Gray, J. J. Comparison of NMR and crystal structures of membrane proteins and computational refinement to improve model quality. *Proteins: Structure, Function, and Bioinformatics* **86,** 57–74 (2018).

344. Frey, L., Lakomek, N.-A., Riek, R. & Bibow, S. Micelles, Bicelles, and Nanodiscs: Comparing the impact of membrane mimetics on membrane protein backbone dynamics. *Angewandte Chemie International Edition* **56,** 380–383 (2017).

345. Kulandaisamy, A, Sakthivel, R & Gromiha, M. M. MPTherm: Database for Membrane Protein Thermodynamics for Understanding Folding and Stability. *Briefings in Bioinformatics,* bbaa064 (2020).

346. Barrett, R. & White, A. D. Iterative Peptide Modeling With Active Learning And Meta-Learning. arXiv: 1911.09103 (2019).

REBECCA F. ALFORD

Department of Chemical & Biomolecular Engineering
Johns Hopkins University
3400 N. Charles Street, Baltimore, Maryland 21218

EDUCATION

Johns Hopkins University — Baltimore, MD
Ph.D. Chemical and Biomolecular Engineering — *Expected June 2020*

Carnegie Mellon University — Pittsburgh, PA
B.S. Chemistry, Department and College Honors — *2016*

RESEARCH EXPERIENCE

Johns Hopkins University, Baltimore, MD — 2016–Present
Ph.D. Candidate
Advisors: Dr. Jeffrey J. Gray & Dr. Karen G. Fleming
Topic: Biologically-realistic membrane protein structure prediction and design

Johns Hopkins University, Baltimore, MD — 2013–2016
Undergraduate Research Assistant
Advisor: Dr. Jeffrey J. Gray
Topic: Modernized scoring and sampling routines for membrane protein modeling in Rosetta3.

New York University, New York, NY — 2011–2013
High School Student Research Assistant
Advisor: Dr. Richard Bonneau
Topic: Classification of disease-linked mutations using structure prediction and machine learning.

Stony Brook University, Stony Brook, NY — 2009–2010
High School Student Research Assistant
Advisor: Dr. Maurice Kernan
Topic: Functional implications of mutations in the Drosophila TRPM gene.

FELLOWSHIPS

Hertz Foundation Fellowship	2016–2020
National Science Foundation Graduate Research Fellowship	2016–2020
Johns Hopkins Whiting School of Engineering Nicholas P. Jones Fellowship	2016–2019
Johns Hopkins Whiting School of Engineering William Schwartz Fellowship	2016–2017

PUBLICATIONS

RESEARCH ARTICLES

14. Koehler Leman J, Lewis S, Lyskov S, Loshbaugh A, **Alford RF**, Smith S, Jeliazkov J, DiMaio F, Burman SS, Theiker D, Mulligan V, Bonneau R (2020) "Enabling reproducibility through large-scale continuous scientific benchmarks for applications in the Rosetta macromolecular modeling and design suite" *In Preparation* - Submit September 2020.

13. **Alford RF** & Gray JJ (2020) "A heuristic implicit model for electrostatics in the membrane environment" *In Preparation* - Submit to *PeerJ* in June 2020.

12. **Alford RF** & Gray JJ (2020) "Diverse scientific benchmarks for implicit membrane energy functions" *In Preparation* - Submit to *JCTC* in June 2020.

11. **Alford RF**, Smolin N, Young HS, Gray JJ, Robia SL (2020) "Protein docking and steered molecular dynamics reveal alternative regulatory sites on the SERCA calcium transporter" *Journal of Biological Chemistry – Accepted*.

10. **Alford RF**, Fleming P, Fleming KG, Gray JJ (2020) "Protein structure prediction and design in a biologically-realistic implicit membrane" *Biophysical Journal* 118(8):2024-2055.

9. Spear ED, **Alford RF**, Babatz T, Wood K, Mossberg O, Odinammadu K, Shilgardi K, Gray JJ, Michaelis S (2019) "A humanized yeast system to analyze cleavage of Prelamin A by ZMPSTE24" *Methods* 157: 47-55.

8. Baugh EH, Simmons-Elder R, Muller CL, **Alford RF**, Volovsky N, Lash A, Bonneau R (2016) "Robust classification of protein variation using structural modeling and large-scale data integration," *Nucleic Acids Res* 44(6): 2501-2513.

7. **Alford RF***, Koehler Leman J*, Weitzner BD, Duran AM, Tilley DC, Elazar A, Gray JJ (2015) "An integrated framework advancing membrane protein modeling and design," *PLoS Comput. Biol.* 11(9): e1004398 (*equal contribution).

REVIEWS

6. **Alford RF** & Gray JJ (2020) "Membrane protein engineering" *Methods in Molecular Biology Computational Membrane Protein Design - In Press*.

5. Koehler J, Weitzner BD, Lewis SM, Aldof-Bryfogle J, Alam N, **Alford RF**, Aprahamian M, Baker D, *et al.* (total 108 authors) (2020) "Macromolecular modeling and design in Rosetta: New methods and frameworks." *Nature Methods*

4. Koehler J, Weitzner BD, Renfrew PD, Lewis SM, Moretti R, Watkins AM, Mulligan VK, Lyskov S, Adolf-Bryfogle J, Labonte JW, Krys J, RosettaCommons Consortium*, *et al.*

(2020) "Better together: Elements of successful scientific software development in a distributed collaborative community" *PLoS Comput Biol* 16(5): e1007507. (*Part of the RosettaCommons Consortium listed in Table S1)

3. **Alford RF**, Leaver-Fay A, Jeliazkov JR, O'Meara MJ, DiMaio FP, Park H, Shapovalov MV, Renfrew PD, Mulligan VK, Kappel K, Labonte JW, Pacella MS, Bonneau R, Bradley P, Dunbrack RL, Das R, Baker D, Kuhlman B, Kortemme T, Gray JJ (2017) "The Rosetta all-atom energy function for macromolecular structure prediction and design" *J Chem. Theory Comput.*. 13(6): 3031-3048.

BIOPHYSICS EDUCATION

2. Le KH, Adolf-Bryfogle J, Klima JC, Lyskov S, Labonte J, Weitzner B, Maguire J, Rangan R, Adrianowycz MA, **Alford RF**, Adal A, Nance M, Das R, Scheif W, Gray JJ "PyRosetta Jupyter Notebooks Teach Biomolecular Structure Prediction and Design" (2020) *Under Review - The Biophysicist*.

1. **Alford RF**, Leaver-Fay A, Gonzales L, Dolan EL, Gray JJ (2017) "A cyber-linked summer research program in computational biomolecular structure prediction and design" *PLoS Comput. Biol.* 13(12): e1005837.

SELECTED HONORS AND AWARDS

Third Place - JHU for NanoBiotechnology Student Research Competition	2019
Rosetta Commons Service Award (for contributions to diversity & inclusion efforts)	2016
Dr. J. Paul Fugassi and Linda Monteverde Award	2016
Carnegie Mellon Women's Association Scholarship	2016
Arthur E. Handlos Award (for excellence in chemistry research)	2016
Ruth Welch Walker Scholarship	2012–2016
Grace Hopper Conference Scholarship	2014
Selected Student Speaker–TEDxCMU	2013
Intel International Science and Engineering Fair–Best Biochemistry Project	2012
Intel Science Talent Search Semifinalist	2012

INVITED TALKS AND SEMINARS

5. **Alford RF** (May 2019) "Protein structure prediction and design in a biologically-realistic implicit membrane" *D.E. Shaw Research - Graduate Student and Postdoc Forum*, New York, NY.

4. **Alford RF** (August 2018) "An accurate energy function for membrane protein modeling and design from thermodynamic building blocks" *Institute for Disease Modeling*, Bellevue, WA.

3. **Alford RF** (July 2017) "A deep-dive into the Rosetta all-atom energy function for macromolecular modeling and design" *Lectures in Computational Biophysics, Johns Hopkins University*, Baltimore, MD.

2. **Alford RF** (June 2017) "A deep-dive into the Rosetta all-atom energy function for macromolecular modeling and design" *Flatiron Institute, Center for Computational Biology, Simons Foundation*, New York, NY.

1. **Alford RF** (March 2015) **Keynote:** "Decoding Biology – Using computers to understand disease" *Winter Rosetta Conference*, Burlington, VT.

CONTRIBUTED SCIENTIFIC TALKS

10. **Alford RF** & Gray JJ (February 2020) "Big data from sparse data: Diverse scientific benchmarks reveal optimization imperatives for implicit membrane energy functions" *Winter Rosetta Conference*, New York, NY.

9. **Alford RF** & Gray JJ (November 2019) "Big data from sparse data: Diverse scientific benchmarks reveal optimization imperatives for implicit membrane energy functions" *Annual meeting of the American Institute of Chemical Engineers*, Orlando, FL.

8. **Alford RF**, Fleming P, Fleming KG, Gray JJ (July 2019) "Protein structure prediction and design in a biologically-realistic implicit membrane" *Gordon Research Conference - Membrane Protein Folding*, Easton, MA

7. **Alford RF**, Fleming P, Fleming KG, Gray JJ (April 2019) "Protein structure prediction and design in a biologically-realistic implicit membrane" *Institute for NanoBiotechnology Student Seminar Series, Johns Hopkins University*, Baltimore, MD.

6. **Alford RF**, Fleming P, Fleming KG, Gray JJ (February 2019) "Protein structure prediction and design in a biologically-realistic implicit membrane" *Rosetta Conference*, Philadelphia, PA.

5. **Alford RF**, Fleming P, Fleming KG, Gray JJ (October 2018) "An accurate energy function for membrane protein modeling and design from thermodynamic building blocks" *American Institute of Chemical Engineers Annual Meeting*, Pittsburgh, PA.

4. **Alford RF**, Fleming P, Fleming KG, Gray JJ (August 2018) "An accurate energy function for membrane protein modeling and design from thermodynamic building blocks" *Summer Rosetta Conference*, Leavenworth, WA.

3. **Alford RF** (August 2017) "What's in Pandora's box? A guide to the Rosetta all-atom energy function" *Rosetta Conference*, Leavenworth, WA.

2. **Alford RF**, Baugh EH (July 2014) "Real-time visualization of Rosetta membrane simulations using the PyMOL viewer" *Summer Rosetta Conference, Developer's Meeting*, Seattle, WA.

1. **Alford RF** (February 2014) "RosettaMP - An object-oriented framework for modeling and design of membrane proteins in Rosetta" *Winter Rosetta Conference*, San Francisco, CA.

SCIENTIFIC POSTERS

14. **Alford RF**, Fleming P, Fleming KG, Gray JJ (November 2019) "Protein structure prediction and design in a biologically-realistic implicit membrane" *Annual meeting of the American Institute of Chemical Engineers*, Orlando, FL.

13. **Alford RF**, Fleming P, Fleming KG, Gray JJ (2019) "Protein structure prediction and design in a biologically-realistic implicit membrane" *Gordon Research Conference on Membrane Protein Folding*, Easton, MA.

12. **Alford RF**, Fleming P, Fleming KG, Gray JJ (2019) "Protein structure prediction and design in a biologically-realistic implicit membrane" *Biophysical Society Meeting*, Baltimore, MD.

11. **Alford RF**, Fleming P, Fleming KG, Gray JJ (2018) "Scientific benchmarks guide improvements to membrane energy functions" *University of Delaware Membrane Symposium*, Newark, DE.

10. **Alford RF**, Fleming P, Fleming KG, Gray JJ (2018) "Scientific benchmarks guide improvements to energy functions for membrane protein modeling and design" *Biophysical Society Meeting*, San Francisco, CA.

9. **Alford RF**, Fleming P, Fleming KG, Gray JJ (2017) "Quantifying the membrane energy landscape" *Summer Rosetta Conference*, Leavenworth, WA.

8. **Alford RF**, Leaver-Fay A, Jeliazkov JR, Kuhlman B, Kortemme T, Gray JJ (2017) "A deep-dive into the Rosetta energy function for biological macromolecules" *Biophysical Society Meeting*, New Orleans, LA.

7. **Alford RF**, Fleming KG, Gray JJ (2016) "Evaluating the performance of Rosetta's membrane energy functions" *Summer Rosetta Conference*, Leavenworth, WA.

6. **Alford RF**, Fleming P, Fleming KG, Gray JJ (2015) "Toward an all-atom energy function for membrane protein modeling in bilayers of different lipid composition" *Rosetta Conference*, Leavenworth, WA.

5. **Alford RF**, Fleming KG, Gray JJ (2015) "Validation of the implicit membrane model in RosettaMP" *Gordon Research Conference – Membrane Protein Folding*, Waltham, MA.

4. **Alford RF**, Koehler Leman J, Weitzner BD, Gray JJ (2014) "An object-oriented framework for modeling and design of membrane proteins" *Grace Hopper Conference for Women in Computing*, Phoenix, AZ.

3. **Alford RF**, Koehler Leman J, Weitzner BD, Gray JJ (2014) "A new object-oriented framework for modeling and design of membrane proteins in Rosetta" *Summer Rosetta Conference*, Leavenworth, WA.

2. **Alford RF**, Koehler Leman J, Gray JJ (2013) "Redesigning the framework for membrane protein modeling in Rosetta" *Summer Rosetta Conference*, Leavenworth, WA.

1. **Alford RF**, Simmons-Elder R, Poultney C, Halvorsen L, Bonneau R (2012) "A machine-learning based approach to predicting functional effects of mutations in membrane proteins" *Summer Rosetta Conference*, Leavenworth, WA.

TEACHING EXPERIENCE

Preparing Future Faculty Program, Fellow — 2017–2018
Center for Educational Resources — Johns Hopkins University

I completed a certificate program that educates students in pedagogy, research-informed teaching, backward design, developing a lecture, leading labs, engaging students, and active learning. I completed 22 hours of course-based learning and six hours of teaching (see ChemBE 414/614).

Computational Protein Structure Prediction and Design (ChemBE 414/614) — 2017–2019
Dept. Chemical & Biomolecular Engineering — Johns Hopkins University

This graduate level course introduces fundamental concepts in biophysics, optimization, and informatics that have enabled breakthroughs in structural biology. Students then apply these concepts to biomolecular modeling puzzles using PyRosetta. I have held various instructional roles in the course:

- Spring 2017: Guest lecture on membrane protein modeling
- Spring 2018: Teaching Assistant, Lectures on python programming, energy functions, loop modeling, membrane protein modeling
- Spring 2019: Guest lectures on protein geometry, energy functions, and membrane proteins

Modeling & Statistical Analysis of Data, Teaching Assistant — Fall 2017
Dept. of Chemical & Biomolecular Engineering — Johns Hopkins University

This upper level undergraduate course teaches computing and data anlysis skills. In the first part, students apply MATLAB/Octave to Chemical Engineering problems from Process Analysis, Thermodynamics, Transport, and Kinetics. Then, students apply these skills to data analysis and hypothesis testing. I taught two lectures, reviewed and graded course material, and provided support to students through TA sessions.

Rosetta Code School — 2014–2019
RosettaCommons — Baltimore, MD

This intensive workshop is designed to teach 15-20 graduate students and post-doctoral fellows concepts in applying the Rosetta modeling suite to addressing a wide range of biological questions. I have held various instructional roles in the course:

- Summer 2014: Instructor for C++ based workshop, 15-20 graduate and post-doctoral trainees
- Summer 2015: Instructor for C++ based workshop, adapted for undergraduates
- Summer 2016: Instructor for C++ based workshop, adapted for undergraduates
- Winter 2019: Instructor for the first python-based Rosetta code school

---

MENTORING EXPERIENCE

1. Priya Prathima, JHU ChemBE Undergraduate 2019-Present
   Topic: *In silico modeling of protein-protein interactions within the membrane.*

2. Margaret Luo, JHU ChemBE Undergraduate 2018–2019
   Topic: Capturing pH and electrostatic effects in the membrane environment

3. Ashton Omdhal, JHU Biomedical Engineering Rotation Student Summer 2019
   Topic: Design of membrane protein pores that dock to DNA nanotubes for smart materials

4. Aleexsan Adal, JHU ChemBE Undergraduate Spring 2018
   Topic: Improving the interface of RosettaMP within the PyRosetta toolkit

5. Brittany Lasher, JHU ChemBE Masters Student 2017-2019
   Topic: Engineering membrane-anchored enzymes for increased catalytic activity (see poster #12)

6. Morgan Beckett, JHU Biophysics Rotation Student Fall 2017
   Topic: Assessment of membrane environment hydrogen bonding potentials

7. Peter J. Murray, JHU ChemBE Undergraduate Fall 2017
   Topic: Modeling of interactions between membrane anchored proteins and the membrane interface

8. Brita Ostermeier, UW Madison Biochemistry Undergraduate Summer 2017
   Topic: Analysis of kinks and curves in α-helical transmembrane proteins

9. Cameron White, JHU ChemBE Undergraduate Summer 2016
   Topic: Analysis of kinks and curves in α-helical transmembrane proteins